

**Scattering of Elastic Waves in Layered Media:
A Boundary Integral—Normal Mode Method**

by

Ronald T. Kessel
B.A.Sc., University of Waterloo, 1984
M.Sc., University of Waterloo, 1989

A Dissertation Submitted in Partial Fulfillment of the
Requirements for the Degree of

Doctor of Philosophy

in the Department of Physics

We accept this dissertation as conforming
to the required standard

Dr. Trevor W. Dawson, Supervisor (Adjunct Professor, Dept. of Physics and Astronomy)

Dr. John Weaver, Supervisor (Dean of Science, Dept. of Physics and Astronomy)

Dr. Robert W. Stewart, Departmental Member (Adjunct Professor, Dept. of Physics and Astronomy)

Dr. Pauline Van Den Driessche, ~~Outside Member~~ (Department of Mathematics)

Dr. Henrik Schmidt, External Examiner (~~Dept.~~ of Ocean Engineering, Massachusetts Institute of Technology)

© Ronald T. Kessel, 1996
University of Victoria

All rights reserved. This dissertation may not be reproduced in whole or in part, by photocopying or other means without the permission of the author.

Supervisor: Dr. Trevor W. Dawson

Abstract

Elastic waves are used in geoaoustics to identify remote objects and events. Computer models for such applications are being pressed to handle propagation in three dimensions, and scattering from penetrable objects of arbitrary shape. One approach approximates earth and ocean as horizontally stratified media into which the features of interest are embedded. Here the Boundary Integral Equation (BIE) method for harmonic elastic wave scattering is applied to layered media with penetrable fluid or solid inclusions. A new indirect method is used to evaluate singular and poorly convergent BIE coefficients, the numerically troublesome coefficients being inferred from free-field solutions of the integral equation in the absence of scattering. The new model is very flexible. Multiple inclusions that are penetrable or impenetrable, passive or actively vibrating, are permitted. Inclusions may have edges, and may pass through interfaces between layers. A combined equation method is used to over-determine the solution in the event of numerical instability. Comprehensive numerical tests recommended for all BIE scattering models are described. Central to the model is a new normal mode model of propagation, now packaged under the name SAMPLE, an acronym for Seismo-Acoustic Mode Program for Layered Environments. Designed for the rigorous demands of the BIE method, SAMPLE computes the total elastic field (displacement vector and stress tensor) for general point forces and force couples (with and without moment), using an complete mode series that is valid in both the near field and far. Modes are found using a stable scattering matrix method together with singular value decomposition (SVD), in a robust root-finding routine. The search includes all mode types: P-SV and SH; propagating and evanescent; proper and improper (on any Riemann sheet); and interface and duct modes. Close mode pairs (double roots) in multiple channels are easily identified and resolved during the search. Little-known properties of modes that were discovered when using SAMPLE are also reported.

Examiners:

Dr. Trevor W. Dawson, Supervisor
(Adjunct Prof., Dept. of Physics and Astronomy)

Dr. John. Weaver, Supervisor
(Dean of Science, Dept. of Physics and Astronomy)

Dr. Robert W. Stewart, Departmental Member
(Adjunct Prof., Dept. of Physics and Astronomy)

Dr. Pauline Van Den Driessche, Outside Member
(Department of Mathematics)

Dr. Henrik Schmidt, External Examiner
(Dept. of Ocean Engineering,
Massachusetts Institute of Technology)

Contents

| | |
|---|------------|
| List of Figures | vii |
| List of Tables | x |
| Acknowledgments | xi |
| Dedication | xii |
| 1 Introduction | 1 |
| 1.1 Motivation | 4 |
| 1.1.1 Need for stratified media | 4 |
| 1.1.2 Need for solid media | 5 |
| 1.1.3 Need for three-dimensional models | 5 |
| 1.2 Two cardinal difficulties in scattering | 6 |
| 1.3 Background for the BIE method | 7 |
| 1.3.1 Review of recent developments | 7 |
| 1.3.2 BIE method in perspective | 8 |
| 1.3.3 A new indirect BIE method | 10 |
| 1.3.4 A flexible combined BIE method | 11 |
| 1.4 A complete Green's function for layered media | 14 |
| 1.4.1 History | 15 |
| 1.4.2 A new normal mode program: SAMPLE | 16 |
| 1.5 Model verification | 18 |
| 1.6 Summary | 19 |
| 2 Waves in elastic media | 21 |
| 2.1 Fundamental equations | 21 |
| 2.2 Plane waves and energy absorption | 25 |
| 2.3 Field continuity and boundary conditions | 27 |
| 2.3.1 Solid-solid interface | 27 |
| 2.3.2 An interface with a fluid | 28 |
| 2.3.3 Impenetrable boundaries | 29 |
| 2.3.4 Infinite domains | 30 |
| 2.4 Somigliana's Identity | 30 |
| 2.5 Huygens' principle | 35 |

| | | |
|----------|---|-----------|
| 2.6 | The boundary integral perspective | 38 |
| 2.7 | Determining the boundary fields | 39 |
| 2.7.1 | A combined equation method | 41 |
| 3 | The indirect BIE method | 43 |
| 3.1 | Numerical approximation of the boundary integral | 43 |
| 3.2 | A flexible combined equation method | 46 |
| 3.2.1 | Surface-field equations | 47 |
| 3.2.2 | Null-field equations | 47 |
| 3.2.3 | Combined equation method | 48 |
| 3.2.4 | Compressing the BIE coefficient matrix | 50 |
| 3.2.5 | A modular approach to the combined equation method | 51 |
| 3.2.6 | Specifying the scattering problem in a flexible way | 52 |
| 3.3 | A consistency test using Huygens' principle | 53 |
| 3.4 | Troublesome integral coefficients | 54 |
| 3.5 | Using Huygens' principle to evaluate troublesome integral coefficients indirectly | 55 |
| 3.5.1 | Several troublesome elements | 57 |
| 3.5.2 | The particular solutions | 58 |
| 3.5.3 | The importance of the residue term | 58 |
| 3.5.4 | Nonunique indirect coefficients | 59 |
| 3.6 | Using Huygens' principle to test the entire BIE method: the free-field test | 60 |
| 3.7 | Testing the boundary field: the null-field test | 61 |
| 3.8 | Measuring error in numerical tests | 61 |
| 3.9 | Example: Plane wave scattering by spheres | 62 |
| 3.9.1 | Plane wave scattering from a rigid sphere in a fluid | 63 |
| 3.9.2 | Fluid sphere in a fluid | 68 |
| 3.9.3 | Solid sphere in a solid | 68 |
| 4 | The field from a point source in layered media | 76 |
| 4.1 | The two-point boundary value problem | 77 |
| 4.1.1 | Transformation to stress-displacement vectors | 79 |
| 4.1.2 | Transformation to wave vectors | 81 |
| 4.1.3 | The solution to the homogeneous equation | 83 |
| 4.2 | The scattering matrix method | 85 |
| 4.2.1 | Scattering matrix for a homogeneous layer | 85 |
| 4.2.2 | Scattering matrix for an interface between layers | 87 |
| 4.2.3 | Scattering matrix for impenetrable boundaries | 91 |
| 4.2.4 | Scattering matrix for an infinite half space and the importance of Riemann sheets | 94 |
| 4.2.5 | Point Sources | 95 |
| 4.3 | Ladder diagram for the global matrix method | 98 |
| 4.4 | A single source and receiver | 101 |
| 4.5 | Recovery of the total elastic field | 106 |

| | | |
|----------|--|------------|
| 5 | Modes in layered media | 112 |
| 5.1 | The discrete and continuous spectrum | 113 |
| 5.2 | The condition for modes | 117 |
| 5.2.1 | Singular value decomposition (SVD) | 118 |
| 5.2.2 | The channel matrix method | 119 |
| 5.3 | The search for modes | 120 |
| 5.3.1 | Restricting the search area | 120 |
| 5.3.2 | Using SVD to search for modes | 122 |
| 5.3.3 | Weakly coupled channels | 124 |
| 5.3.4 | Searching for SH modes | 125 |
| 5.4 | Verifying the mode search | 125 |
| 5.4.1 | Node counting | 127 |
| 5.4.2 | Contour Integration | 127 |
| 5.4.3 | Continuity and boundary conditions | 128 |
| 5.4.4 | Rayleigh's Principle | 128 |
| 5.5 | Five properties of modes | 129 |
| 5.5.1 | Rayleigh's principle | 130 |
| 5.5.2 | Mode orthogonality | 130 |
| 5.5.3 | Group velocity | 131 |
| 5.5.4 | Mode excitation | 132 |
| 5.5.5 | Mode normalization | 134 |
| 5.6 | Vertical energy flow in a mode | 134 |
| 5.7 | The Green's function for bounded waveguides by modal summation | 137 |
| 5.7.1 | The mode series | 137 |
| 5.7.2 | Series convergence | 139 |
| 5.7.3 | The Green's function singularity | 139 |
| 5.8 | Model verification | 141 |
| 5.8.1 | Arctic ocean model | 141 |
| 5.8.2 | Gutenberg earth model | 150 |
| 6 | Catalogue of normal modes | 159 |
| 6.1 | Modes as cylindrical waves | 160 |
| 6.1.1 | Propagating modes | 161 |
| 6.1.2 | Evanescient modes | 161 |
| 6.1.3 | Proper and improper modes | 163 |
| 6.1.4 | Vertical energy flux | 168 |
| 6.2 | Mode trapping mechanisms | 171 |
| 6.2.1 | Modes trapped by constructive reflection | 171 |
| 6.2.2 | Modes in bounded waveguides | 178 |
| 6.2.3 | Interface modes | 181 |
| 6.3 | Identifying channels in the channel matrix method | 186 |
| 6.4 | Deep bounded waveguides—Theory | 187 |
| 6.4.1 | Radiation modes close to the EJP branch lines | 187 |
| 6.4.2 | The spacing of radiation modes | 190 |
| 6.4.3 | Estimating the number of radiation modes | 191 |

CONTENTS

vi

| | | |
|----------|---|------------|
| 6.4.4 | Correspondence with the unbounded waveguide | 192 |
| 6.5 | Weakly coupled sound channels—Theory | 195 |
| 7 | BIE method for layered media | 204 |
| 7.0.1 | Constraints due to element size | 204 |
| 7.0.2 | Constraints due to mode proliferation | 205 |
| 7.1 | The particular solutions for layered media | 206 |
| 7.2 | Interfaces and edges | 207 |
| 7.3 | Demonstration of the BIE method for layered media | 208 |
| 7.3.1 | Hemispherical cavity in an ice plate | 209 |
| 7.3.2 | Rigid sphere half buried in sand | 229 |
| 7.3.3 | Circular ice dome | 241 |
| 8 | Conclusions | 255 |
| 8.1 | Conclusions regarding layered media | 256 |
| 8.1.1 | Schematic ladder diagram | 256 |
| 8.1.2 | Normal modes and SVD | 257 |
| 8.1.3 | The mode search program SAMPLE | 257 |
| 8.1.4 | The properties of modes | 259 |
| 8.2 | The indirect BIE method | 261 |
| 8.2.1 | Future research | 262 |
| 8.3 | Closing Remarks | 263 |
| | Bibliography | 264 |

List of Figures

| | | |
|------|--|-----|
| 2.1 | The volume and surface of integration in Betti's reciprocity relation. | 32 |
| 2.2 | Huygens' principle for wavefront reconstruction. | 36 |
| 3.1 | Quadrilateral boundary element and nodes. | 45 |
| 3.2 | Boundary elements for the rigid sphere. | 65 |
| 3.3 | Polar plot of the scattered field due to the rigid sphere. | 67 |
| 3.4 | Boundary elements for the fluid and solid spheres. | 70 |
| 3.5 | Polar plot of the scattered field due to the fluid sphere. | 71 |
| 3.6 | Polar plot of the scattered field due to the solid sphere. | 73 |
| 3.7 | Plot of the total field surrounding the solid sphere, $kr = 2.0$ | 74 |
| 3.8 | Plot of the total field inside and outside the solid sphere, $kr = 2.0$ | 75 |
| 4.1 | EJP branch cuts for vertical slowness. | 84 |
| 4.2 | Two-port scattering matrix network. | 86 |
| 4.3 | Scattering matrix network for a homogeneous layer. | 88 |
| 4.4 | Scattering matrix network for an interface | 90 |
| 4.5 | Scattering network for an impenetrable plane boundary. | 92 |
| 4.6 | Summation operator for a point source. | 98 |
| 4.7 | The schematic ladder diagram. | 102 |
| 4.8 | The global matrix. | 103 |
| 4.9 | Components in the schematic diagram can be combined in different ways. | 104 |
| 4.10 | Two scattering networks connected together. | 105 |
| 4.11 | The waveguide reduced to its simplest form. | 107 |
| 4.12 | A single source and receiver. | 108 |
| 5.1 | The slowness integral in the Fourier-Bessel transform. | 115 |
| 5.2 | "L"-shaped region covering the EJP branch cuts. | 121 |
| 5.3 | The search surface w_1 resembles a conical hole close to a mode. | 123 |
| 5.4 | Searching for a close mode pair. | 126 |
| 5.5 | The search function for modes in the Arctic waveguide. | 144 |
| 5.6 | P-SV mode locations for the Arctic waveguide. | 145 |
| 5.7 | Vertical mode functions for P-SV modes in the Arctic waveguide | 146 |
| 5.8 | Vertical dependence of integrand in contour integral representation of τ_{zz} | 147 |
| 5.9 | The normal stress τ_{zz} as a function of range in the Arctic waveguide. | 148 |
| 5.10 | The vertical displacement u_z as a function of range in the ice. | 149 |

| | | |
|------|---|-----|
| 5.11 | Wave speed and density profile for the Gutenberg earth model. | 152 |
| 5.12 | Search function for modes in the Gutenberg earth model. | 153 |
| 5.13 | P-SV mode locations for the Gutenberg earth model. | 154 |
| 5.14 | Vertical mode functions for the Gutenberg earth model. | 155 |
| 5.15 | Vertical dependence of integrand in contour integral representation of u_z | 156 |
| 5.16 | The displacement u_z as a function of range in the Gutenberg earth model. | 157 |
| 5.17 | Dispersion of the Rayleigh interface wave in the Gutenberg earth model. | 158 |
| | | |
| 6.1 | P-SV and SH modes for a free ice plate. | 164 |
| 6.2 | Evanescent P-SV modes in the Arctic waveguide. | 165 |
| 6.3 | P-SV modes in a 3 m thick floating ice plate at 750 Hz. | 166 |
| 6.4 | Upward energy flow in an infinite basement layer. | 170 |
| 6.5 | P-SV mode locations for the two-layer leaky mode environment. | 176 |
| 6.6 | Vertical mode functions for proper S-leaky modes. | 177 |
| 6.7 | Mode locations in the unbounded and deep bounded waveguides. | 180 |
| 6.8 | Proper leaky mode in the unbounded waveguide and its radiation counterpart in the bounded. | 182 |
| 6.9 | P-SV modes for the two-layer model of Arvelo et al.. | 185 |
| 6.10 | The reduced schematic ladder diagram for a deep basement layer. | 189 |
| 6.11 | Normal stress τ_{zz} as a function of range, in the infinitely deep waveguide and the corresponding deep bounded waveguide | 196 |
| 6.12 | The reduced schematic ladder diagram for a waveguide supporting two weakly coupled channels at once. | 197 |
| 6.13 | Resonant modes in the almost symmetric waveguide. | 201 |
| 6.14 | Transfer of sound energy between weakly coupled modes. | 202 |
| | | |
| 7.1 | Boundary elements for the hemispherical cavity. | 211 |
| 7.2 | 428 sources generating particular solutions outside the hemispherical cavity. | 212 |
| 7.3 | The relative strength of modes in the mode series. | 213 |
| 7.4 | Free-field test for the ice cavity with incident P-SV waves. | 215 |
| 7.5 | Null-field test for the ice cavity. | 217 |
| 7.6 | Incident field generated by a vertical point force at the surface of the ice. | 218 |
| 7.7 | Scattered field due to the cavity in the ice with incident P-SV waves. | 219 |
| 7.8 | Polar plot of the scattered field in a horizontal plane: incident P-SV waves. | 220 |
| 7.9 | Displacement field along a line over the cavity: incident P-SV waves. | 221 |
| 7.10 | Free-field test for the ice cavity with incident SH waves. | 222 |
| 7.11 | Incident field generated by a a horizontal twisting source in the ice. | 223 |
| 7.12 | Scattered field due to the cavity in the ice with incident SH waves | 224 |
| 7.13 | Polar plot of the scattered field in a horizontal plane: incident SH waves. | 225 |
| 7.14 | Displacement field along a line over the cavity: incident SH waves. | 226 |
| 7.15 | Total field at the surface of the ice. | 227 |
| 7.16 | Vertical component of the scattered field u_z at the ice surface. | 228 |
| 7.17 | Schematic diagram of half-buried rigid sphere. | 231 |
| 7.18 | Boundary elements for the half-buried sphere. | 232 |

| | |
|---|-----|
| 7.19 Point source locations generating the particular solutions for the half-buried sphere. | 233 |
| 7.20 P-SV modes for the shallow ocean with a sand layer. | 234 |
| 7.21 SH modes for the sand layer. | 235 |
| 7.22 Free-field test for the half-buried sphere. | 236 |
| 7.23 Scattered field due to the half-buried sphere in the vertical plane. | 237 |
| 7.24 Total field in a horizontal plane at the top of the sand layer. | 238 |
| 7.25 Scattered field in a horizontal plane at the top of the sand layer. | 239 |
| 7.26 Plot of the scattered field at the top of the sand layer. | 240 |
| 7.27 Schematic diagram of an ice dome in a 3m ice plate. | 242 |
| 7.28 Boundary elements for the ice dome. | 244 |
| 7.29 SH modes for the Arctic waveguide at 20 Hz. | 245 |
| 7.30 Interior null-field point locations for the ice dome. | 246 |
| 7.31 Sources generating particular solutions for perspective 0 (waveguide). | 247 |
| 7.32 Sources generating particular solutions for perspective 1 (ice dome). | 248 |
| 7.33 Free-field test for perspective 0 (waveguide). | 249 |
| 7.34 Free-field test for perspective 1 (ice dome). | 250 |
| 7.35 Incident and total field in a horizontal plane at the ice surface. | 251 |
| 7.36 Scattered field and its vertical component u_z in a horizontal plane at the ice surface. | 252 |
| 7.37 Radial u_r and azimuthal u_ϕ components of the scattered field. | 253 |
| 7.38 Polar plot of the scattered field at the ice surface. | 254 |

List of Tables

| | | |
|-----|---|-----|
| 3.1 | Setup for scattering from a rigid sphere. | 64 |
| 3.2 | Free-field test summary for rigid sphere boundary. | 66 |
| 3.3 | Setup for scattering from a fluid sphere. | 69 |
| 3.4 | Setup for plane wave scattering from a solid sphere. | 72 |
| 5.1 | Arctic profile with floating ice layer. | 143 |
| 5.2 | The Gutenberg earth model. | 151 |
| 6.1 | 10 m sand layer on a limestone sea floor. | 171 |
| 6.2 | Two-layer leaky mode environment. | 178 |
| 6.3 | A simple deep bounded waveguide. | 179 |
| 6.4 | The two-layer leaky mode environment of Arvelo et al. | 184 |
| 6.5 | Almost symmetric fluid waveguide. | 203 |
| 7.1 | Setup for scattering from a hemispherical cavity in an ice plate. | 210 |
| 7.2 | Setup for scattering from a rigid sphere half buried in a sand layer. | 229 |
| 7.3 | Setup for scattering ice dome in a floating ice plate. | 243 |

Acknowledgments

I thank Dr. Trevor Dawson for exemplary guidance through so many mathematical and computational difficulties. I thank the Canadian Department of National Defence for financial support throughout this work, through the Defence Research Establishment Pacific (DREP) and through the Esquimalt Defence Research Detachment (EDRD), and I thank the scientists there who helped through many fruitful discussions and administrative support, especially Dr. John Ozard, Dr. Dave Thomson, and Dr. Gary Brooke. I thank the members of my examining committee, Dr. John Weaver, Dr. Pauline van den Driessche, Dr. Robert Stewart, and Dr. Henrik Schmidt for their helpful criticism and encouragement.

*I dedicate this publication to my parents, in the year of
their forty-first wedding anniversary.*

Chapter 1

Introduction

The ocean is an extremely complicated acoustic medium.

That is how Brekovskikh and Lysanov begin their introductory text for ocean acoustics [17]. It is perhaps as much a warning to the confident acoustician as to the beginner, for although the laws of acoustic wave motion can be expressed rather simply, their application to realistic environments takes on daunting complexity, mainly because the ocean is highly variable over the distances of interest. The warning is appropriate here as well, where the goal is to predict the way sound interacts with solid objects in the ocean, such as features of bottom topography, sub-bottom structure, or a surface ice canopy. Solid media complicate the analysis because elastic waves in solids must be calculated using vector fields rather than scalar fields, and because the actual properties of the sea bed and ice canopy—important parameters for the analysis—can only be determined with difficulty.¹ When ocean acoustics includes solid media this way, it is often called *geoacoustics* to distinguish it from the traditional strictly fluid case, while emphasizing its affinity with geophysics.²

When analytically intractable, the theory of elastic wave motion can nevertheless

¹For example, see Clay and Medwin [28] who review methods of measuring the properties of the sea bed; Hamilton [54] who reports the elastic properties of many different kinds of sediments; and Brooke and Ozard [18] who report the elastic properties of sea ice.

²The affinity with geophysics is widely accepted. Tolstoy and Clay [128, p.269] conclude that “Ocean acoustics is, in the final analysis, a branch of geophysics.” Jensen et al. [66, p.40] define a *geoacoustic model* as “a model of the real seafloor with emphasis on measured, extrapolated, and predicted values of those material properties important for the modelling of sound transmission.”

be applied to realistic geoacoustic environments using computer models whose computations implement the governing equations. The models now in use are the result of continual efforts to improve realism and computation speed.³ The two goals are usually incompatible because greater realism engenders greater model complexity, and therefore greater execution time, except where matched by marked improvements in computer hardware and software. The added complication of solid media is just one example of this. When we speak of realism, it need hardly be mentioned that all models are for the most part abstractions of reality, in which a myriad unaccountable physical properties are idealized by just a few dominant ones. Moreover, it is the judicious simplification of the real world that makes a model especially useful and insightful. Thus, the realism of a model can be posed most concisely in reverse, by citing a model's few abstractions rather than its long list of omissions.

The goal of this thesis, then, is to include three important properties of the ocean: horizontal stratification, solid features, and wave propagation in three dimensions. Each of these have been modeled to some degree independently, but only recently have researchers attempted to unite all three in a full-wave scattering model. That is my objective here.

By "full-wave," I mean that the model undertakes to solve the full scattering problem, posed mathematically as a boundary value problem, without making theoretically motivated approximations from the outset, such as the high frequency approximation of ray theory [66, chapt. 3], or the horizontal forward propagation of the parabolic equation method [66, chapt. 6]. In principle, the aim of a full-wave model is to solve the boundary value problem exactly, though in practice, of course, a numerical solution always entails approximation and error to some extent, and at times these may be disastrous. Progress in full-wave scattering models has advanced along two main fronts, using the Finite Difference (FD) and Boundary Integral Equation (BIE) methods, whose relative advantages and disadvantages will be compared below. I have chosen the BIE method because it is favored for scattering in large domains [88] [27] such as the ocean and earth.

Three-dimensional scattering models of any kind tend to be difficult to use, and

³Many applications of ocean acoustics that use computer models are reviewed by Clay and Medwin [28], including echo ranging, monitoring biological life, and measurement of sea bed properties. More recently, an acoustic method for detecting changes in the average temperature of the ocean has been developed to address concerns about global warming [93]. Active and passive sonar are of great importance in undersea warfare [59] [120].

one always hopes there may be a simpler approach based on some efficacious approximation. But a rigorous full-wave model is in many ways a step towards improved approximate models because it permits freehanded experimentation that is rarely, if ever, possible with physical experiments. It permits, for example, examination of the wave field everywhere in the problem to identify where helpful approximations might be made, and it permits variation of the problem itself to identify its most important features. A full-wave model also provides a benchmark to judge the accuracy of faster but approximate “short-cut” methods.

The scattering of geoacoustic waves is a vast topic and one cannot hope to touch its many sides in a single project. My treatment of scattering is therefore restricted in three important ways. First, I only consider *deterministic* scattering, in which the shape and elastic properties of the scattering features are completely specified; in contrast to *statistical* scattering, arguably of equal importance, in which small-scale random roughness is handled statistically. But just as deterministic models have served as the basis for a statistical treatment of impenetrable roughness [37] [102], my own model might serve for penetrable roughness, though I do not explore the possibility here. Secondly, I only consider harmonic (constant frequency) wave scattering because the BIE method solves just one frequency at a time, and that in itself is a considerable undertaking. In principle, however, the model could be extended to transient waves using Fourier synthesis in the frequency domain as others have done [67][50]. Thirdly, the emphasis will be on shallow oceans, in which the sound is likely to interact significantly with the sea bed, at acoustic frequencies less than 1 kHz, for which sea water is essentially transparent,⁴ though some geophysical applications at much lower frequency are also included. Among the problems I attempt here are

- normal mode computations in an Arctic ocean model, and the Gutenberg earth model from geophysics;
- scattering of plane waves from rigid, fluid, and solid spheres for which analytic solutions are available;
- scattering (750 Hz) from a hemispherical cavity on the floor of a 3 m ice plate at 750 Hz;

⁴The absorption rate of sound below 1 kHz is less than 0.1 dB/km [17].

- scattering (200 Hz) from a 1.193 m rigid sphere half buried in sand in 50 m of water;
- scattering (20 Hz) from an ice dome in a floating ice layer in the Arctic ocean.

But the new model is likely to find applications wherever the scattering of waves in layered media is of interest, in geophysical prospecting⁵, nondestructive testing using ultrasonics, and electromagnetics for example.

Geoacoustic modeling has grown out of three great fields of study: elastic wave propagation, ocean acoustics, and geophysics. It is impossible to survey its manifold history here. Chin-Bing et al. [26], for example, catalogue thirty-six research-oriented computer models in ocean acoustics alone, and these are classified according to seven main model types,⁶ whose underlying theory is given in an excellent companion publication by Jensen et al. [66]. Detailed reviews of roughly the same number of geophysical models have been edited by Doornbos [39], Bolt [14], and Chin et al. [25]. More to our purpose, in this introductory chapter I will review the motivation for the main features of the model, then introduce the main difficulties facing every full-wave scattering model, then survey recent developments concerning the BIE method and layered media, and then outline how the new model will be verified.

1.1 Motivation

1.1.1 Need for stratified media

Geoacoustic waves depend on the disturbance that causes them and the elastic parameters of the medium they traverse. In the ocean, the elastic parameters vary continuously almost everywhere according to the water salinity, temperature, and pressure [17], and they may jump suddenly as at the transition from fluid to solid at the ocean floor. In the absence of distinct scattering features, the length scale of the horizontal variation is

⁵Seismic waves have been used by oil geologists in the search for distinct porous sedimentary structures, such as a Pinnacle reef, that can signify an oil reservoir [117, sect. 23.6].

⁶The seven main model types used by Chin-Bing et al. are the ray, parabolic equation, normal mode, contour integral, coupled mode, finite element and finite difference models. Oddly enough, the BIE method for scattering was not included. Presumably this is because BIE models for geoacoustics are fairly recent, and so far only their inventors use them with confidence. Jensen et al. [66] include a discussion of BIE methods for two-dimensional fluid media.

often much greater than that of the vertical, and greater than the acoustic wavelengths of interest, so it is usual to treat the ocean as a horizontally stratified waveguide made up of homogeneous layers; the elastic parameters of each layer approximating the vertical variation in stepwise fashion [16] [44] [66] [70] [128]. The vertical reverberation that dominates geoacoustic data can be realistically modeled this way. Features of bottom topography or surface ice can then be modeled as penetrable elastic inclusions embedded in the layered waveguide. Of course, not all models assume horizontally invariant media, such as the finite element, finite difference, parabolic equation and geometric ray models, for example. Nevertheless, a locally stratified model is almost always used in practice, if only because the horizontal variation of the ocean is rarely known with certainty.

1.1.2 Need for solid media

Early models in ocean acoustics consisted of strictly fluid layers, with solids included approximately simply as fluids, by omitting shear stresses altogether.⁷ Increasingly, however, attention has been given to low frequency propagation and shallow ocean environments, for which the importance of shear waves in solid media to transmission loss in shallow oceans, reverberation, and scattering is now well established [17] [66] [77] [42]. To omit them often precludes important resonance effects and energy loss mechanisms, and at times the dominant part of the physical reality.⁸

1.1.3 Need for three-dimensional models

A two-dimensional propagation model assumes a high degree of symmetry in the wave field so that the field in three dimensions is completely determined by its values in a single vertical plane. In *planar* symmetry, the media, source, and wave field are all assumed to be invariant in one horizontal direction; the representative plane being any plane perpendicular to the direction of invariance. The planar approach is often inadequate

⁷The review of earlier numerical models for ocean acoustics by DiNapoli and Davenport (1979) [38] deals entirely with fluid media, although they mention that a solid bottom could be included by terminating the water column below using the equivalent reflection coefficient for solid sediment layers.

⁸Scholte interface waves on the sea floor, for example, do not occur in strictly fluid media (see Section(6.2.3)).

because 1) the elementary source is a uniform line source lying parallel to the direction of invariance, which is not typical of the compact sources encountered in reality; 2) because spherical spreading for body waves, and cylindrical spreading for trapped waves (normal modes) cannot occur; and 3) because out-of-plane scattering is precluded by the assumed symmetry. These limitations have been overcome to some degree using “two-and-a-half”-dimensional models, in which the field due to a single point source is constructed using a Fourier transform of the planar field, while the elastic media remains invariant in one direction. Fawcett and Dawson [46] applied the method to a planar BIE model of acoustic wave scattering in fluid waveguides, and Schmidt has since applied it to solid layers [110]. Scattering from compact three-dimensional inclusions cannot be treated this way.

In *axial* symmetry, the media, source, and wave field are rotationally symmetric about a common vertical axis, and the representative plane is a half plane with one edge along the vertical axis. Cylindrical models are sometimes used as “building blocks” to assemble larger non-symmetric domains in a piecewise manner [45] [66, sect. 5.10], but the extension to solid media has yet to be made. Here again, an important instance of out-of-plane scatter, mode conversion between vertically (P-SV) and horizontally (SH) polarized wave motion, is precluded by the assumed symmetry.

In general, the scattering problem does not suit either the planar or axial idealization and a full three-dimensional treatment is required.

1.2 Two cardinal difficulties in scattering

A geoacoustic scattering model faces two fundamental difficulties. The first is that of extreme length scales. To represent the interaction of waves with the shape and sudden contrast of the inclusion, the model must replicate the equation of motion and boundary conditions in its vicinity on a scale much less than the inclusion’s dimensions and the geoacoustic wavelength. At the same time, the model must propagate waves over very large distances, whether to distant receivers or from distant sources. Handling both scales at once is rather like measuring very small and very large distances with the same meter stick; the stick may be well-suited to measuring one length scale or the other, but

not to both at once. The disparity can be very severe in ocean acoustics when the inclusion lies in unconsolidated sediments where the shear (S) wavelength—the length of the meter stick—can be very small. I am not aware of any full-wave scattering model (including my own developed here) that purports to include shear wave scattering in such extreme cases.

The second fundamental difficulty is that of completeness, for the model must have access to all nine components of the elastic wave field—three components of displacement and six unique components of stress—to match boundary conditions on an arbitrary interface between solid media in three dimensions. Such rigor is uncommon in propagation modeling. Usually only part of the field is required, perhaps the normal stress in ocean acoustics, or the displacement vector in seismology.

1.3 Background for the BIE method

1.3.1 Review of recent developments

Among the recent developments in the BIE method for ocean acoustics are contributions by Schuster and Smith (1985) [112] whose BIE method for rigid objects in a two-dimensional fluid media includes reverberant interactions between the scattering inclusion and the layered media approximately using a Born series. Seybert and Casey (1988) [115] were possibly the first to apply the BIE method to penetrable domains with a view towards ocean acoustics, although they considered unbounded homogeneous domains rather than layered. Seybert and Wu (1988) [116] applied the BIE method to a homogeneous fluid halfspace. Lu (1989) [86] used his hybrid ray-mode method for layered media in a two-dimensional BIE method for strictly fluid media including penetrable scatterers. Dawson and Fawcett (1990) [31] considered scattering in two-dimensions by impenetrable deformations in a strictly fluid waveguide, which they later (1990) extended to “two-and-one-half” dimensions [46] as cited earlier, and which Dawson (1991) [32] extended to long repeated boundary deformations using scattering matrices. Dawson (1991) [33] then developed a three-dimensional BIE method for impenetrable inclusions in a strictly fluid waveguide. Gerstoft and Schmidt (1991) [50] developed the first two-dimensional BIE method for arbitrarily layered elastic media following the method of Kawase (1988) [67] in geophysics,

who computed the time domain response of a canyon in a homogeneous solid half space in two dimensions, and Schmidt (1993) [110] later extended their model to “two-and-one-half” dimensions as cited earlier. Xu and Yan (1993) [135] considered two-dimensional scattering in the elementary oceanic waveguide using normal modes,⁹ which they later used for source localization in a shallow ocean with a large rigid inclusion (1994) [136]. Wu (1993) [132] considered three-dimensional scattering in the elementary oceanic waveguide using both the method of images and normal modes. Eliseevnin and Tuzhilkin (1995) [41] apply Kirchhoff’s approximation to the BIE method for rectangular vertical screens in the elementary oceanic waveguide. It remains to develop a three-dimensional BIE method for layered media involving solids.

1.3.2 BIE method in perspective

Perhaps the best-known numerical methods for boundary value problems are the Finite Difference (FD) and Finite Element (FE) methods. In each case the elastic domain is subdivided into volume elements whose dimensions are small compared with both the scattering inclusion and the wavelength, and whose corners are nodes at which the unknown field variables are to be computed. The field at each node is related to its neighbors using a numerical approximation to the equation of motion. This gives a sparse banded system of equations, whose solution yields the field variables at every node throughout the volume. The methods are very flexible because the scattering body can have any shape and the elastic parameters can vary almost arbitrarily.

The main disadvantage of the FD and FE method is that a very large number of nodes are needed to span a large domain, especially in three dimensions. In geoacoustics the domain is reasonably assumed to be infinitely large, but the grid of nodes must be terminated somewhere, by a boundary contrived to minimize any effect on the wave propagation, thereby making a seamless connection to the omitted unbounded domain. Being imperfect, these false boundaries must be kept as far apart as possible, hence the domain spanned by the grid of nodes must be as large as possible. The FD and FE methods have

⁹The elementary oceanic waveguide consists of a single homogeneous fluid layer bounded above and below by free and rigid boundaries, respectively.

therefore been limited to two-dimensional models [40] [66] [47], or to short range (less than ten wavelengths) three-dimensional models [20] [19]. In light of the first cardinal difficulty of scattering, that of handling incongruous distances, it would appear that the FD and FE methods are well-suited for short range propagation in the vicinity of the scattering inclusion, but they face considerable difficulties in the far field due to computer limitations. The second difficulty, that of completeness, must be resolved by the finite difference or element scheme relating each node to its neighbors. Interested readers can consult the references.

The Boundary Integral Equation (BIE) method is an alternative approach in which only the boundary of the scattering body need be subdivided into small surface elements, rather than the entire domain [8]. Associated with each element are nodes, also on the boundary where the field is to be computed. The field at each node is related to that at all the others through a boundary integral representation of the field, giving a full system of equations whose solution yields the field at all nodes simultaneously. The field can then be computed at points off the boundary, once again using its integral representation. As we will see, the method is a realization of Huygens' principle for wave reconstruction, in which the field within a domain is represented as the sum of wavelets radiated from secondary sources on a boundary. The field radiated by each wavelet is the Green's function for a suitably chosen domain in the absence of scattering.¹⁰ In an unbounded domain, the Green's function propagates a wavelet over large distances in a single evaluation, without an intervening grid of nodes as in the FD and FE methods. This is why the BIE method can accommodate unbounded domains. The two cardinal difficulties of scattering are therefore relegated to the Green's function; for it must propagate a wavelet over arbitrary distances — between nearby nodes on the boundary, or from the boundary to distant receivers — and it must be complete, returning all components of the elastic field for a wavelet.

The main advantage over the FD and FE methods, then, is a considerable reduction in the number of nodes, from a grid spanning a large three-dimensional domain, to a grid spanning a finite two-dimensional domain of the boundary of the scattering inclusion.

¹⁰A Green's function is the field due to a fundamental point source. The fundamental source in the BIE method for elastic waves is a point force, which makes the Green's function a second rank tensor (see Section (2.4)). As we will see, the field due to a wavelet is the superposition of two fields originating from the same point: one field going as the Green's displacement tensor (simple), and the other as the third-rank Green's stress tensor (complex) (see equation (2.62)).

Unfortunately, this gain is bought at the price of added complexity, for not only does the method entail the inversion of a full matrix system, but certain BIE coefficients in that matrix are difficult to compute due to the singularity of the Green's function. To illustrate, imagine computing the wavelet superposition at a point directly on the surface where those wavelet sources are continuously distributed. Very close to the computation point the Green's function of the wavelets becomes infinitely large, but the boundary integral over the wavelets, defined in the Cauchy Principal Value (CPV) sense, remains bounded. The situation is further complicated in layered media because its Green's function must be expressed in terms of integral transforms that are computationally intensive; more so when evaluated close to the source than far away. Indeed, a good portion of this thesis is dedicated to computing the complete Green's function for layered media in both the near and far field of the source. In the final analysis, then, the BIE method is not a short cut around the FD and FE methods, but it ranks with them as an alternative numerical method that is especially suited to large three-dimensional domains, and this is important for geoacoustics.

To evaluate troublesome singular matrix coefficients in the BIE method, some modelers have extracted the singularity from the integral and integrated it analytically, leaving a regular component to be integrated numerically without difficulty [31] [33] [135], while others have perfected a direct numerical integration [52] [53], but similar methods have yet to be accomplished for three-dimensional elastic waves in layered elastic media due to its formidable Green's function. I follow a rather different course.

1.3.3 A new indirect BIE method

One of the principal innovations in this thesis is the indirect computation of troublesome BIE coefficients, by inferring their values from a family of known solutions to the integral equation. The method is similar to one proposed by Niku and Brebbia [94], in which particular solutions to the boundary integral equation are used to infer all boundary integral coefficients, whether numerically troublesome or not. Theirs was a general discussion, removed from the details of any given boundary value problem and without numerical examples, but they anticipated that the indirect computations may be numerically unstable. That is what I found when trying to infer all coefficients in early trials with strictly

fluid two-dimensional problems. I therefore modified the method to compute only the troublesome coefficients indirectly, while computing all straightforward coefficients numerically. This gave good results.¹¹

The indirect BIE method can be applied more generally, to compute any BIE coefficients that are numerically troublesome, not just those troubled by singularity. This makes it ideal for layered media, where convergence problems in the Green's function can lead to additional troublesome coefficients.

1.3.4 A flexible combined BIE method

The BIE method described here is very flexible. It permits several scattering objects at once, their boundaries being disconnected, in contact, or embedded one inside another. They can be penetrable fluids or solids, or impenetrable with linear boundary conditions, whether passive and actively vibrating (to model a hydrophone for example). They can have edges and corners. In layered media, they can pass through the interfaces between layers, and extend above or below its horizontal plane boundaries.

All of this may appear excessive, but almost all of these features are required for layered media, even in relatively simple problems. For in layered media, the scattering object may be embedded partly in solid layers, and partly in fluid, calling for different boundary conditions in each. And where the object passes through a solid-fluid interface, the boundary field may be discontinuous, calling for treatment much as if the boundary had an edge. If the object constitutes a deformation of an impenetrable plane boundary (a ridge in a floating ice plate, for example, or a mountain on otherwise level terrain), then it may extend outside the layered media, and its boundary may be penetrable in some places, but impenetrable in others. Actively vibrating boundaries should be included in all BIE models, if only to implement the comprehensive *free-field test* described in this thesis. Perhaps the only extravagant feature, then, is to permit more than one scattering object at a time. But as we will see, provision for several objects is only a minor extension of the provision for a single object that is penetrable.

¹¹Unfortunately, I did not come across Niku and Brebbia's work until after preliminary trials showed that instability was a problem when inferring all coefficients indirectly, and after I modified the indirect method for troublesome coefficients only.

A general BIE model is complicated by the fact that the integrand of the integral representation of the field generally involves the boundary values of both the field and its normal derivatives. Hence, changes to the boundary conditions may change the form of the integral equation being solved, which in turn may have drastic consequences for numerical stability. For example, if the normal derivatives of the represented field variable are prescribed on the boundary (the Neumann boundary conditions in scalar wave theory), then the integral representation yields an integral equation of the second kind, which ordinarily have excellent numerical stability [4].¹² But if the represented field is itself prescribed on the boundary (the Dirichlet boundary conditions in scalar wave theory), then an equation of the first kind results, which are notorious for being numerically unstable [4].¹³ Then again, for penetrable scattering objects, the integral representation remains as a mixed equation—of the second kind in the represented field variable, and of the first in its normal derivatives. The general properties of the mixed equation have apparently not been studied, at least not in the geoacoustic literature. It is not known, for instance, whether the occasional non-uniqueness that affects equations of the second kind, and the inherent instability of the first kind, may not both affect the solution of a mixed equation. All of this means that a general BIE model, though proven successful for one or another problem, may nevertheless become unstable and fail for others, possibly if only the boundary conditions are changed. Precautions against numerical instability are therefore an important part of a general BIE model.

In my own model, the threat of numerical instability is countered in the following way. First of all, it has several built-in numerical tests—consistency and comprehensive tests—that can verify different stages in the model for *every* application. These tests can be applied in any BIE method for scattering problems, but they have apparently received

¹²The integral representation for the elastic displacement field (Somigliana's identity (2.48)) reduces to an equation of the second kind in displacement when zero-traction boundary conditions are enforced from the outset, in scattering from a hollow trench or cavity in the earth, for example. In acoustic (scalar) wave scattering, the Helmholtz integral equation for the pressure similarly reduces to an equation of the second kind for impenetrable rigid objects [73] [22].

¹³Somigliana's identity (2.48) reduces to an equation of the first kind in traction when zero-displacement boundary conditions are enforced, in scattering from an impenetrable rigid body in welded contact with a solid, for example. In acoustic (scalar) models, a different integral representation of the field is ordinarily used for the Neumann and Dirichlet problems, to give an equation the second kind in each [22] [31].

little mention in the literature, probably because they are little known.

Secondly, in principle I follow the combined equation method developed by Schenck [106] for the Neumann problem for acoustic waves. The combined method exploits the fact that a boundary integral representation of the field also takes different forms according to the location of the point where the field is represented: whether inside, outside, or on the boundary of integration. Schenck began with the Helmholtz integral representation for the acoustic pressure, applied at points on the boundary (the *surface-field equation*), giving an equation of the second kind in the unknown pressure field. Using the theory of integral equations, he demonstrated that its solution is not unique at isolated critical frequencies, where ruinous numerical instability occurs. To force a unique solution, he over-determined the problem by combining the integral representation at points outside the boundary (the *null-field equation*, an equation of the first kind) with the surface-field equation in the numerical method. The extension now to elastic waves and penetrable objects pushes the combined method far beyond Schenck's original analysis: from the Helmholtz integral equation for acoustic (scalar) fields, to Somigliana's identity for elastic (vector) fields; from a surface-field equation strictly of the second kind for the Neumann problem, to one that is generally mixed for many different problems: and from one impenetrable object, which requires just one integral representation for the sole penetrable domain, to several penetrable objects, which calls for a different integral representation in each penetrable domain. It is impossible to predict the consequences of the extension. At the very least, we can expect to solve the equivalent Neumann problem for elastic waves (traction-free boundaries when Somigliana's identity is used) with much the same success Schenck had with acoustic waves. As I show in the examples in this thesis, however, the method works for a much wider range of problems, as intended from the outset.

The new model's broader success is due in part to its flexibility. The surface- and null-field equations can be combined in any proportion selected by the user, so that instabilities, if they occur, might be overcome by changing the proportions one way or another. To this end the user can choose any points on the boundary of the scattering object to apply the surface-field equation, rather than always using the element nodes as BIE methods ordinarily do. The number of points may actually exceed the number of

nodes on the boundary, over-determining the solution to the surface-field equation to a limited degree, even before it is combined with the null-field equation. (The freedom to choose boundary points also makes it possible to avoid nodes on edges of the boundary, or along the interface between fluid layers intersected by the boundary in layered media, where the surface-field equation has a more complicated specialized form.) In a similar way, the user can choose any points in the exterior domain to apply the null-field equation. In my experience, I have on occasion faced what at first appeared to be disastrous numerical instability, but I have yet to encounter a problem where it could not be overcome using this flexible combined equation method.

As with most models, the range of problems that can be solved is limited by the computer. As a rule, BIE methods are biased towards low and mid-frequency scattering, in which the dimensions of the object are not large compared to the wavelength. For as the frequency increases, smaller boundary elements are needed to sample the small-scale variations in the field, thereby increasing the number of boundary elements, as well as the computation time and memory demands. At this stage, the indirect coefficient computations appear limited by the number of troublesome boundary elements encountered at once. For not only does the computational effort increase with the number of troublesome elements, but the indirect computations become unstable. Ordinarily, however, less than six troublesome elements would be encountered at a time, which the indirect method now manages without difficulty.

1.4 A complete Green's function for layered media

The BIE method requires all nine components of the Green's function in both the near and far field of a point source. Numerical methods for computing the Green's function in layered media have developed independently, without reference to the BIE method.

1.4.1 History

Thomson (1950) [124] and Haskell (1953) [56] took the first steps towards computing the Green's function with their propagator matrix method for plane waves travelling

in layered media. Many improvements have been made since: Haskell (1964) [57] and Harkrider (1964) [55] added source excitation; Gilbert and Backus (1966) [49] formulated the fundamental theory behind the propagator matrix method; Hudson (1969) [60] extended the method to handle propagation in three dimensions; and Kennett (1979) [69], whose work features prominently here, recast the matrix problem using a numerically stable recursive scheme. There are many text-book treatments of the matrix method and its variations such as Ewing, Jardetsky and Press (1957) [44], Takeuchi and Saito (1972) [122], Aki and Richards (1980) [1], Brekhovskikh (1980) [16], and Kennett (1983) [71], and Jensen et al. (1994) [66].

Perhaps the most notable development in ocean acoustics has been the *global* matrix method due to Schmidt and Jensen (1985) [107], which is the basis of the SAFARI model for sound propagation [109]. SAFARI now ranks among the most widely-used models in ocean acoustics, but its wave propagation module is nevertheless incomplete for a three-dimensional BIE method, because it only computes part of the field (the normal stress, and vertical and horizontal displacement for P-SV waves excited by axially symmetric sources), and because it becomes inaccurate within a few wavelengths of a point source (due to asymptotic treatments of Bessel functions in its Fast Fourier Transform integration scheme). Dr. Schmidt has recently released an upgraded version of SAFARI called OASES [111], built in part on the work of Kim [74], that computes all field variables due to explosive point sources and point forces, with an option to use a full integration scheme that is accurate in the near field. To my knowledge, OASES is the first general purpose model adequate for a three-dimensional BIE method.

Both SAFARI and OASES are wavenumber (contour) integration models inasmuch as the field is represented as the superposition of cylindrical waves whose wavenumbers span the positive real axis. I follow a rather different approach, based on a normal mode model of wave propagation, in the hope that it will be more computationally efficient in the three-dimensional BIE method where the Green's function must be evaluated several million times. A normal mode method may prove more efficient since it represents the field as a series of distinct waves, the normal modes, rather than as an integral over a continuous spectrum of waves. The characteristic vibrations of each mode can be computed beforehand,

and saved, to speed up subsequent evaluations. Among the existing mode models for ocean acoustics is SNAP by Jensen and Ferla [65], KRAKEN by Porter [99], and more recently ORCA by Westwood [131]. Though proven successful for a wide range of ocean propagation models, none of these is adequate for the BIE method, mainly because they do not compute all components of the elastic field, and because they concentrate on only part of the mode series—the dominant P-SV modes vibrating in the water column—while omitting short-range, strongly evanescent modes and SH modes. A more complete normal mode model is therefore required.

1.4.2 A new normal mode program: SAMPLE

To compute the Green's function by modal summation, I develop a *scattering matrix* treatment of layers that in effect converts Kennett's recursive scheme to a global matrix method. At the same time, I introduce a schematic representation of vertical propagation through layered media, much like the diagrams an engineer might use to analyze a linear system. This aids the discussion because it helps us visualize how matrix methods for layered media work (or fail). There are many matrix methods for layered media, and they can all be illustrated using diagrams of this kind.

For simplicity, most normal mode programs search for a mode at a single depth, usually in the water column, with the effect of layers above and below being represented by an upper and lower reflection matrix. But as we will see, searching at a single depth is likely to miss modes whose vibrations do not extend through that depth. To ensure that all modes are detected, I test for singularity at many depths simultaneously by computing the singular values of the global matrix. The method has been implemented in a robust normal mode program called SAMPLE—an acronym for **Seismo-Acoustic Mode Program for Layered Environments**. The model is new inasmuch as it:

- undertakes to find all propagating modes, plus a significant portion of the long series of evanescent modes, needed for near-field propagation;
- computes all nine components of the three-dimensional elastic field due to a point source;

- supports a general class of seismic sources, including general point forces and couples with and without moment;¹⁴
- uses a mode search method based on singular value decomposition that can automatically identify and resolve uncommonly close mode pairs (double roots) that may occur when the layered media supports weakly coupled sound channels.¹⁵

SAMPLE has also been a valuable research tool, leading to a comprehensive understanding of mode behavior, such as

- upward energy flow in an infinitely deep basement layer;¹⁶
- well-behaved leaky modes on the proper Riemann sheet;¹⁷
- a Rayleigh mode “of the second kind” for a solid layer in welded contact with a rigid boundary;¹⁸
- the correspondence between a deep bounded waveguide and its unbounded counterpart.¹⁹

As we will see, a complete normal mode representation of the Green’s function is only possible when the layered media is bounded above and below by perfectly reflecting plane boundaries. Thus it will be assumed, as it often is [17], that the ocean-atmosphere interface is a traction-free plane boundary, and that the sea bed is terminated at depth by a reflecting interface.²⁰ A comprehensive normal mode approach for arbitrarily elastic media has apparently never been reported, so the technique developed here, and the properties of modes it has revealed, are of interest in their own right.

In the course of this work it became apparent that the mode sum very close to the source required so many (evanescent) modes that the preparatory mode computations

¹⁴Section (4.2.5).

¹⁵Section(5.3.3) and (6.5).

¹⁶Section (6.1.4).

¹⁷Section (6.2.1).

¹⁸Section(6.2.3).

¹⁹Section(6.4).

²⁰The correspondence between an infinitely deep and a corresponding deep bounded waveguide is the subject of Section (6.4).

became impractical. The new BIE method therefore reverts to an indirect coefficient computation scheme whenever the practical limits of the mode summation scheme are exceeded, in this way filling in where direct numerical integration could not manage.

1.5 Model verification

If a modeler's greatest obligation is to prove that his model works, then his crowning achievement is confirmation by experiment. But it is not unusual for a new model to make predictions in the absence of experimental data. In fact, the lack of data (or the resources to collect it) often motivates modeling in the first place, perhaps as a guide to setting up new experiments more effectively. In my own project, the collection of data was simply beyond its objectives and resources, and neither was data fortuitously discovered in the work of others, for the heroic task of measuring both the sound field and the environment to the level of detail needed to conclusively verify the model is rarely undertaken. So let us consider what alternative verification might be available.

Here we must distinguish between two levels of approximation made in every computer model. The first occurs when the physical is rendered mathematical: when a myriad presumably insignificant details are ignored to make the analysis of a physical phenomenon possible; and the second occurs when the mathematical is rendered numerical: when the equations of motion are approximated by the finite computations of a computer. Confirmation by experiment is most convincing because it verifies the combined effect of both levels of approximation at once. Without such proof, however, we must verify each level of approximation separately.

In geoaoustics, the first approximation occurs when the scattering problem is formulated as a boundary value problem (BVP) consisting of the equation of wave motion, plus boundary and continuity conditions. Here it is common practice to neglect the effects due to the forces of gravity, the earth's rotation, the ocean's currents, the anisotropy of solids, and so forth, in part to simplify matters, and in part because their status cannot be known with certainty [66] [127] [128] [1] [17] [28]. Verification at this level of approximation follows from direct measurement of the properties in question, together with demonstrations that

the omitted properties could not affect matters significantly under realistic circumstances. Verification of this kind is beyond the scope of my project.

In the second approximation, it is necessary to show that the numerical solution to the posed BVP is accurate, which usually amounts to showing that the model agrees with a solution computed by other means. Proof of this kind may at first appear scarce, for there are presently no analytic solution methods for the layered media problems posed here. Fortunately, the BIE method itself provides an unlimited number of analytic tests for each particular scattering problem, each made possible through trivial changes of the boundary and continuity conditions. In effect, the BIE method is asked to solve a problem for which it can already provide the solution by straightforward free-field propagation.²¹ There are, in addition, consistency tests that can verify each stage of the BIE computations as they progress and test the final solution to a given scattering problem.²² Though not new, these tests have been little used in the literature.²³

To provide still further verification of the new indirect BIE method, though in homogeneous domains rather than layered, the new model has been applied to the scatter of plane waves from spheres in homogeneous domains for which analytic solutions by separation of variables are available.²⁴

1.6 Summary

The balance of this thesis is divided into three main topics:

1. *The scattering of elastic waves in three dimensions by the indirect BIE method*
Chapters 2 and 3: Readers interested primarily in the indirect BIE method will find Chapters 2 and 3 give a complete description without the complication of layered domains.

²¹This is the *free-field test* described in Section (3.6).

²²These are the *consistency test* of Section(3.3), and the *null-field test* of Section(3.7).

²³Schenck [106] originally proposed the free-field test, and Wu [132] used it to test his BIE method for an elementary oceanic waveguide. The null-field test has been used by Seyert and Rengarajan [114].

²⁴These analytic tests are reported in Section (3.9).

2. *The elastic field due to a point source in layered media—Chapters 4, 5 and 6:* Readers interested primarily in the normal mode model for layered media (SAMPLE) could begin directly with Chapter 4, where the scattering matrix method for layered media is developed. The modal representation and the mode search using SVD are taken up in Chapter 5. Readers interested in the general properties of modes, but not the details of the mode search and computations, could go directly to Chapter 6, which is a catalogue of the many different kinds of modes encountered in layered media.
3. *The scattering by objects in layered media—Chapter 7:* Here the BIE and normal mode models are united into a new model of scattering in layered media.

Chapter 2

Waves in elastic media

The scattering of elastic waves must be formulated mathematically, as a boundary value problem whose solution we seek. To this end, we require the partial differential equations of motion, and the field continuity and boundary conditions that apply at the boundaries of an elastic domain, all of which are reviewed in this chapter. Of particular interest for ocean acoustics is the uniform treatment of waves in both fluid and solid media, which are so often treated separately, or parenthetically, one in favor of the other. As we will see, the fundamental difference between fluids and solids in the linear theory lies in their boundary conditions—a distinction that has apparently caused confusion in ocean acoustics. The equation of motion is then recast as an integral representation (Somigliana's identity) of the wave displacement field that can be interpreted physically using Huygens' principle and forms the basis of the BIE method.

2.1 Fundamental equations

An elastic wave is a travelling mechanical disturbance. It can be described by the displacement $\mathbf{u}(\mathbf{x}, t)$ of each point \mathbf{x} in the media from its initial rest position at some later time t .¹ When the disturbance is small, the local deformation of the media can be described

¹The fundamental equations of elastic wave motion reported in this section are derived in many excellent texts. See Graff (1975) [51], Hudson (1980) [61], and Aki and Richards (1980) [1] for example.

by the symmetric strain tensor whose Cartesian components are

$$\varepsilon_{ij} = \frac{1}{2}(u_{i,j} + u_{j,i}) . \quad (2.1)$$

Differentiation with respect to the j 'th Cartesian coordinate has been indicated by the subscript $,j$, and the time and position dependence of the field variables have been omitted for clarity. The internal restoring forces acting against the deformation are determined by the symmetric stress tensor, which, according to Hooke's law, is a linear transformation of the strain

$$\tau_{ij} = c_{ijkl}\varepsilon_{kl}, \quad (2.2)$$

where the coefficients c_{ijkl} depend on the properties of the elastic medium. (The Einstein convention of summing over repeated indices is implied throughout, unless stated otherwise.) The symmetry properties, $\varepsilon_{ij} = \varepsilon_{ji}$ and $\tau_{ij} = \tau_{ji}$, together with strain energy considerations [1, Sect. 2.2], imply that the number of independent coefficients in c_{ijkl} reduce from 81 to 21. In isotropic media the number reduces to just two coefficients, commonly denoted as λ and μ , known as the Lamé coefficients for the medium. In this case, Hooke's law reduces to

$$\tau_{ij} = \lambda\varepsilon_{kk}\delta_{ij} + 2\mu\varepsilon_{ij} , \quad (2.3)$$

in which δ_{ij} is the Kronecker delta. In reality, ocean sediments and ice are likely to be anisotropic due to small-scale structural biases established by prevailing sedimentation or freezing processes, but I will assume, as is often done, that the layered media representing the earth and ocean is isotropic [71][127][61][66]. The analysis can be applied to transversely isotropic media (isotropic in all horizontal directions, requiring five independent components in c_{ijkl}) using the method of Takeuchi and Saito [122]. The extension to general anisotropy is rarely undertaken, both because the orientation and degree of anisotropy is difficult to determine with certainty, and because anisotropy so complicates the analysis that it can be only included in the simplest models [1, Sect. 5.6].

The wave disturbance causes a small element of the media to push or pull upon the surrounding media, and the force between two adjacent elements depends on the way they are in contact. If we imagine two small volume elements in contact along a plane surface

ds , then the force on element 1 due to element 2 is given by

$$df_i = \tau_{ij} n_j ds, \quad (2.4)$$

where \mathbf{n} is normal to ds , pointing from element 1 to 2. Dividing both sides by ds gives the traction across the boundary

$$t_i = \frac{df_i}{ds} = \tau_{ij} n_j. \quad (2.5)$$

If the medium in one volume element is an inviscid fluid, then the shear components of the traction perpendicular to \mathbf{n} must always be zero, which implies that $\mu = 0$ for an inviscid fluid.² The stress tensor for fluids is therefore

$$\tau_{ij} = \lambda \varepsilon_{kk} \delta_{ij}, \quad (2.6)$$

and the traction vector is

$$t_i = \lambda \varepsilon_{kk} n_i. \quad (2.7)$$

The corresponding pressure disturbance is the negative of the normal component of the stress,

$$p = -n_i t_i = -\lambda \varepsilon_{kk} = -\lambda u_{k,k}. \quad (2.8)$$

Lighthill has shown [81, Sect. 2.7] that the effect of viscosity on compressional waves is confined to solid surfaces bounding the fluid, within a boundary layer whose thickness is directly proportional to $\sqrt{\mu/\omega\rho}$, where ω is the frequency of the wave motion. For waves at 10 Hz in water, the thickness of that layer is of the order of 1 mm [81, Fig. 26], which is insignificant compared with the geoacoustic length scale of one wavelength, roughly 150 m at 10 Hz. Water can therefore be treated as an inviscid fluid so far as ocean acoustics is concerned.

The equation of motion for elastic waves in both fluids and solids is the linearized Navier equation [61] [51],

$$\rho \ddot{u}_i = \tau_{ij,j} + \rho f_i, \quad (2.9)$$

where $\rho(\mathbf{x})$ is the mass density in the absence of wave motion, $f_i(\mathbf{x}, t)$ are the components of a body force in units of force per unit mass causing the wave motion, and second order

²Using (2.3) and (2.5), set $\mathbf{t} \times \mathbf{n} = \mathbf{0}$ and let \mathbf{n} point in each of the three Cartesian directions. Then $\mu \varepsilon_{ij} = 0$ for $i \neq j$; hence $\mu = 0$.

differentiation with respect to time t is indicated by double overhead dots. Combining (2.1), (2.3), and (2.3) for solid or (2.6) for fluid media, and (2.9) gives

$$\begin{aligned}\rho \ddot{u}_i &= (\lambda + \mu) u_{j,ij} + \mu u_{i,jj} + \rho f_i & \text{for solids,} \\ \rho \ddot{u}_i &= \lambda u_{j,ij} + \rho f_i = -p_{,i} + \rho f_i & \text{for fluids.}\end{aligned}\tag{2.10}$$

Here it has been assumed that the displacement field in a fluid is irrotational ($\nabla \times \mathbf{u} = \mathbf{0}$), as it will be if the fluid is initially at rest,³ and that the media is locally homogeneous ($\lambda_{,i} = \mu_{,i} = 0$). Inhomogeneous media will be modeled as an assembly homogeneous domains in Section 2.3. Then 2.10 applies within each domain, and the waves are coupled between adjacent domains through certain continuity and boundary conditions applied along their common boundaries.

The wave motion achieves a harmonic steady state if all of the sources of wave motion oscillate continuously with the same angular frequency ω , and if all transient disturbances created when the sources started oscillating have died away [61]. A common time dependence $e^{-i\omega t}$ can then be separated from the spatial dependence of all field variables

$$\begin{aligned}\mathbf{u}(\mathbf{x}, t) &\longrightarrow \mathbf{u}(\mathbf{x}) e^{-i\omega t}, \\ \varepsilon_{ij}(\mathbf{x}, t) &\longrightarrow \varepsilon_{ij}(\mathbf{x}) e^{-i\omega t}, \\ \tau_{ij}(\mathbf{x}, t) &\longrightarrow \tau_{ij}(\mathbf{x}) e^{-i\omega t}, \\ \mathbf{t}(\mathbf{x}, t) &\longrightarrow \mathbf{t}(\mathbf{x}) e^{-i\omega t}, \\ \mathbf{f}(\mathbf{x}, t) &\longrightarrow \mathbf{f}(\mathbf{x}) e^{-i\omega t},\end{aligned}\tag{2.12}$$

and differentiation with respect to time becomes multiplication by $-i\omega$. The equation of motion (2.9) then becomes

$$-\rho\omega^2 u_i = \tau_{ij,j} + \rho f_i,\tag{2.13}$$

where the common time dependence in all terms has been eliminated. Equation (2.10)

³We can assume that the velocity field is irrotational in an inviscid fluid away from all sources (taking $\mathbf{f} = \mathbf{0}$), for taking the curl of both sides of the equation of motion

$$\nabla \times \ddot{\mathbf{u}} = \frac{\partial}{\partial t} \left(\nabla \times \frac{\partial \mathbf{u}}{\partial t} \right) = \mathbf{0};\tag{2.11}$$

that is, the vorticity $\nabla \times \partial \mathbf{u} / \partial t$ is constant with time. Add to this is the assumption that all fluids are initially at rest and undeformed by wave motion, then $\nabla \times \mathbf{u} = \mathbf{0}$.

likewise becomes

$$\begin{aligned} -\rho\omega^2 u_i &= (\lambda + \mu) u_{j,ij} + \mu u_{i,jj} + \rho f_i && \text{for solids,} \\ -\rho\omega^2 u_i &= \lambda u_{j,ij} + \rho f_i = -p_{,i} + \rho f_i && \text{for fluids.} \end{aligned} \quad (2.14)$$

2.2 Plane waves and energy absorption

Let us introduce energy loss into the harmonic wave motion, whether due to viscosity, internal friction, or thermal conduction, simply by examining how gradual energy loss affects plane waves travelling in homogeneous unbounded media. More rigorous treatments of absorption that ultimately give the same results can be found in the references [1][12][13].

For a harmonic plane wave propagating in the x_1 direction in an unbounded homogeneous domain, the displacement field is independent of x_2 and x_3

$$\mathbf{u}(x) = \mathbf{U}e^{ikx_1}, \quad (2.15)$$

where $\mathbf{U} = [U_1, U_2, U_3]$ is a complex constant vector. Substituting this into (2.14) we find

$$\begin{aligned} (\rho\omega^2 - k^2(\lambda + 2\mu)) U_1 &= 0, \\ (\rho\omega^2 - k^2\mu) U_2 &= 0, \\ (\rho\omega^2 - k^2\mu) U_3 &= 0. \end{aligned} \quad (2.16)$$

Non-zero U_1 exists when

$$\rho\omega^2 - k^2(\lambda + 2\mu) = 0, \quad (2.17)$$

that is, when the wavenumber

$$k = k_\alpha = \omega/\alpha \quad (2.18)$$

with

$$\alpha = \sqrt{\frac{\lambda + 2\mu}{\rho}}; \quad (2.19)$$

and non-zero u_{02} and u_{03} exist when

$$\rho\omega^2 - k^2\mu = 0, \quad (2.20)$$

that is, when

$$k = k_\beta = \omega/\beta, \quad (2.21)$$

with

$$\beta = \sqrt{\frac{\mu}{\rho}}. \quad (2.22)$$

Thus a plane wave can be one of two types: either a *compressional wave* (P) with phase speed α , whose particle displacements are parallel to the direction of propagation; or a *shear wave* (S) with phase speed β , whose particle displacements are perpendicular to the direction of propagation.

Now consider a plane wave whose amplitude gradually decays as it propagates due to energy absorption by the medium. Approximate linear treatments of weak absorption show that a plane wave decays in direct proportion to its amplitude

$$\frac{\partial |U_i|}{\partial x_1} = -a |U_i|, \quad (2.23)$$

hence

$$|U_i(x_1)| = |U_i(x_1^0)| e^{-a(x_1 - x_1^0)}. \quad (2.24)$$

This exponential decay is equivalent to making the wavenumber in (2.15) complex, $k = k_r - ik_i$ with $k_i > 0$:

$$\mathbf{u}(x) = \mathbf{u}_0 e^{ik_r x_1} e^{-k_i x_1}, \quad (2.25)$$

where k_i is the absorption coefficient in nepers per unit length. Since ω is assumed real, complex k requires complex phase speed α or β

$$k = \frac{\omega}{c} = \frac{\omega}{c_r + ic_i} = \frac{\omega(c_r - ic_i)}{|c|^2}; \quad c = \alpha \text{ or } \beta. \quad (2.26)$$

Hence,

$$k_i = -\frac{\omega c_i}{|c|^2} \approx -\frac{\omega c_i}{c_r^2}, \quad (2.27)$$

provided $|c_i| \ll c_r$ and $c_i < 0$ to keep the absorption rate k_i small and positive.

Energy absorption can therefore be approximately modeled by giving the compressional and shear phase speeds of an elastic medium a small negative imaginary part

$$\begin{aligned} \alpha &= \alpha_r + i\alpha_i, \quad \text{where } \alpha_i \approx -k_{\alpha i} \alpha_r^2 / \omega, \\ \beta &= \beta_r + i\beta_i, \quad \text{where } \beta_i \approx -k_{\beta i} \beta_r^2 / \omega, \end{aligned} \quad (2.28)$$

The absorption rates $k_{\alpha i}$ and $k_{\beta i}$ are generally a function of frequency and must be determined experimentally. In geoacoustics it is usual to report the absorption rate in units

of dB per wavelength, from which the corresponding imaginary phase speed can be found using the conversion

$$1 \text{ Np} = 20 \log_{10} e \text{ dB}; \quad (2.29)$$

hence,

$$\alpha_i = -\frac{k_{\alpha i} \alpha_r^2}{2\pi f} = -\frac{k_{\alpha i} \lambda_\alpha \alpha_r}{2\pi} = -\frac{k'_{\alpha i} \alpha_r}{40\pi \log_{10} e}, \quad (2.30)$$

where $k'_{\alpha i}$ is in units of dB per wavelength, and in the same way,

$$\beta_i = -\frac{k'_{\beta i} \beta_r}{40\pi \log_{10} e}. \quad (2.31)$$

2.3 Field continuity and boundary conditions

The equation of motion (2.13) is too complicated to solve if we allow arbitrary variation of the elastic parameters. Instead we can approximate the continuously varying domain using an assembly of homogeneous domains whose elastic parameters approximately duplicate those of the original domain in a piecewise fashion. Then the equation of motion for homogeneous media can be used within each homogeneous domain, and the field can be coupled from one domain to another by applying field continuity conditions at their common interface. The stratified ocean will therefore be modeled as a stack of homogeneous fluid or solid layers, and the scattering object as an inclusion, which may itself be made up of several different homogeneous domains. The field continuity conditions at a penetrable interface, and the boundary conditions at an impenetrable, are reviewed below.

2.3.1 Solid-solid interface

At an interface between two solid media, the displacement \mathbf{u} must be continuous across the interface, or the media has ruptured, and the traction \mathbf{t} must be equal and opposite across the interface, or Newton's third law of motion has been violated. Thus,

$$\mathbf{u}(\mathbf{y}^+) = \mathbf{u}(\mathbf{y}^-) \quad (2.32)$$

$$\mathbf{t}(\mathbf{y}^+) = -\mathbf{t}(\mathbf{y}^-), \quad (2.33)$$

where \mathbf{y}^+ and \mathbf{y}^- are two points approaching in the limit a point \mathbf{y} on the interface from opposite sides of the interface, and the traction is defined using the normal to the interface: $\mathbf{n}(\mathbf{y}^+) = -\mathbf{n}(\mathbf{y}^-)$.

2.3.2 An interface with a fluid

At a fluid interface, the normal displacement is continuous (because cavitation is ignored), the normal traction is continuous (to satisfy Newton's third law), the tangential traction is zero (2.7), and the tangential displacement can be discontinuous (because fluids may undergo shear strain without dissociation); that is

$$\mathbf{u}(\mathbf{y}^+) \cdot \mathbf{n}(\mathbf{y}^+) = -\mathbf{u}(\mathbf{y}^-) \cdot \mathbf{n}(\mathbf{y}^-) , \quad (2.34)$$

$$\mathbf{t}(\mathbf{y}^+) \cdot \mathbf{n}(\mathbf{y}^+) = -p(\mathbf{y}^+) = \mathbf{t}(\mathbf{y}^-) \cdot \mathbf{n}(\mathbf{y}^-) = -p(\mathbf{y}^-) , \quad (2.35)$$

$$\mathbf{t}_{\parallel}(\mathbf{y}^+) = (\mathbf{n}(\mathbf{y}^+) \times \mathbf{t}(\mathbf{y}^+)) \times \mathbf{n}(\mathbf{y}^+) = \mathbf{0} , \quad (2.36)$$

$$\mathbf{t}_{\parallel}(\mathbf{y}^-) = (\mathbf{n}(\mathbf{y}^-) \times \mathbf{t}(\mathbf{y}^-)) \times \mathbf{n}(\mathbf{y}^-) = \mathbf{0} .$$

In a rotated Cartesian coordinate system, with axis \mathbf{e}'_1 directed along the normal vector and axes \mathbf{e}'_2 and \mathbf{e}'_3 directed tangentially to the surface, these boundary conditions reduce to

$$\begin{aligned} u'_1(\mathbf{y}^+) &= -u'_1(\mathbf{y}^-) , \\ t'_1(\mathbf{y}^+) &= t'_1(\mathbf{y}^-) , \\ t'_2(\mathbf{y}^{\pm}) &= 0 , \\ t'_3(\mathbf{y}^{\pm}) &= 0 , \end{aligned} \quad (2.37)$$

where $'$ denotes vector components in the rotated system, and $\mathbf{e}'_1(\mathbf{y}^+) = -\mathbf{e}'_1(\mathbf{y}^-)$ because the normal vector reverses across the boundary. This transformation will be used later in Section (3.2.4) to simplify the fluid boundary conditions when they are used in the BIE coefficient matrix.

These slip boundary conditions for fluids are due, of course, to our original assumption that they are inviscid. In reality, as fluid dynamics has shown, fluids obey a no-slip condition because viscosity acts to smooth out discontinuities in its particle motion [10]. A flowing fluid therefore forms a thin boundary layer in contact with a solid through which the fluid velocity parallel to the interface changes continuously to that of the solid.

So the question arises: if we are going to include viscosity by making the P wave speed complex, shouldn't we also enforce a corresponding no-slip condition at the boundary of a fluid? The answer is "No," because the stress-*velocity* relation for viscosity, which gives rise to the boundary layer, was omitted from the linear equation of motion from the outset, and it is impossible to restore it now, simply by enforcing the no-slip condition. Once omitted from the equation of motion, the only effect of viscosity we can include is the approximate way it makes the amplitude of harmonic waves decay.

2.5.3 Impenetrable boundaries

All linear boundary conditions for impenetrable surfaces can be represented as

$$\mathbf{A}(\mathbf{y})\mathbf{u}(\mathbf{y}) + \mathbf{B}(\mathbf{y})\mathbf{t}(\mathbf{y}) = \mathbf{C}(\mathbf{y}), \quad (2.38)$$

for \mathbf{y} on the boundary. \mathbf{A} and \mathbf{B} are complex matrices, and \mathbf{C} a complex vector, specified to suit the desired boundary conditions. Of the many possibilities, I will only consider the following cases:

1. a rigid boundary oscillating with displacement $\mathbf{C}(\mathbf{y})$ in welded contact with a solid

$$\mathbf{u}(\mathbf{y}) = \mathbf{C}(\mathbf{y}); \quad (2.39)$$

2. a rigid boundary oscillating with normal displacement $C(\mathbf{y})$ in frictionless contact with a fluid or solid

$$\begin{bmatrix} \mathbf{n}(\mathbf{y}) \cdot \mathbf{u}(\mathbf{y}) \\ \mathbf{v}^1(\mathbf{y}) \cdot \mathbf{t}(\mathbf{y}) \\ \mathbf{v}^2(\mathbf{y}) \cdot \mathbf{t}(\mathbf{y}) \end{bmatrix} = \begin{bmatrix} n_1 & n_2 & n_3 \\ 0 & 0 & 0 \\ 0 & 0 & 0 \end{bmatrix} \mathbf{u}(\mathbf{y}) + \begin{bmatrix} 0 & 0 & 0 \\ v_1^1 & v_2^1 & v_3^1 \\ v_1^2 & v_2^2 & v_3^2 \end{bmatrix} \mathbf{t}(\mathbf{y}) = \begin{bmatrix} C(\mathbf{y}) \\ 0 \\ 0 \end{bmatrix}, \quad (2.40)$$

where \mathbf{n} , \mathbf{v}^1 and \mathbf{v}^2 are mutually perpendicular unit vectors at the interface;

3. a free boundary in contact with fluid or solid

$$\mathbf{t}(\mathbf{y}) = \mathbf{C}(\mathbf{y}) = \mathbf{0}. \quad (2.41)$$

Actively radiating boundaries would not ordinarily be used in geoaoustics because the source is often small enough to be treated as a point, but active boundaries are needed to model the performance of an acoustic driver, to predict its radiation pattern or the effect of mechanical supports for example. As we will see in Chapter 3, active boundaries also permit excellent numerical tests of the BIE method.

2.3.4 Infinite domains

The final class of boundary conditions to be considered are the radiation conditions for infinite domains. In effect the radiation condition says that no waves come from infinitely far away when all sources are confined within an finite diameter. Its mathematical formulation varies according to wave type, whether compressional or shear, or body waves or normal modes in layered media. The radiation conditions for compressional and shear waves in an unbounded homogeneous domain are reported by Pao [96]. These body waves decay at least as fast as $1/r$ at large distances r away from all sources and scattering inclusions. Somewhat different conditions are required for modes propagating in a layered waveguide because modes can decay more slowly, at least as fast as $1/\sqrt{r}$. In any case, the radiation conditions follow from taking the limit as the outer boundary recedes to infinity, when the field is represented using Somigliana's identity (which is derived in the next section). This is similar to the way the Sommerfeld radiation conditions can be derived for scalar fields using the Helmholtz integral equation [118]. I will not derive the conditions here, but rely instead on the intuition that waves radiating to infinity should not affect matters near the origin.

2.4 Somigliana's Identity

Somigliana's integral equation, the basis of the BIE method, can be derived from Betti's (1872) reciprocity equation [1]. Consider two different displacement fields, \mathbf{u} and \mathbf{v} , that satisfy the equation of motion with associated forcing terms $\rho\mathbf{f}^u$ and $\rho\mathbf{f}^v$, so that

$$\begin{aligned}\rho\omega^2 u_i + \tau_{ik,k}^u &= -\rho f_i^u, \\ \rho\omega^2 v_i + \tau_{ik,k}^v &= -\rho f_i^v.\end{aligned}\tag{2.42}$$

The fields satisfy the same constituent equation (2.2) and boundary conditions in a common domain \mathcal{V} . Now separate \mathcal{V} into interior and exterior domains V and V' , by constructing a simply connected closed surface S in \mathcal{V} , with its surface normal vector directed from V to V' as shown in Fig. (2.1). Betti's reciprocity relation for the two wave fields is

$$\int_V \rho (u_k f_k^v - v_k f_k^u) d\tau = \int_S (v_k t_k^u - u_k t_k^v) ds, \quad (2.43)$$

where \mathbf{t}^u and \mathbf{t}^v are the surface tractions associated with \mathbf{u} and \mathbf{v} , respectively, $d\tau$ is a differential volume element in V , and ds is a differential area element on S . If we make \mathbf{v} the displacement field due to a unit point force in the direction $\hat{\mathbf{m}}$, acting at the point \mathbf{x} , then

$$\rho \mathbf{f}^v(\mathbf{y}) = \delta(\mathbf{y} - \mathbf{x}) \hat{\mathbf{m}}, \quad (2.44)$$

and the component of \mathbf{u} in the direction $\hat{\mathbf{m}}$ at the point \mathbf{x} , will be "sifted" from the volume integral by the properties of the delta function,

$$\zeta(\mathbf{x}) u_k(\mathbf{x}) m_k = \int_S (v_k(\mathbf{y}) t_k^u(\mathbf{y}) - u_k(\mathbf{y}) t_k^v(\mathbf{y})) ds(\mathbf{y}) + \int_V \rho(\mathbf{y}) v_k(\mathbf{y}) f_k^u(\mathbf{y}) d\tau(\mathbf{y}). \quad (2.45)$$

Here it is helpful to include the position dependence of the field variables: \mathbf{x} is the location of the point force $\rho \mathbf{f}^v$, and \mathbf{y} is the integration variable ranging over the surface S .

The way in which $\mathbf{u}(\mathbf{x})$ is sifted has been indicated by the factor $\zeta(\mathbf{x})$. In particular,

$$\zeta(\mathbf{x}) = \begin{cases} 1, & \mathbf{x} \in V; \\ 0, & \mathbf{x} \in V'. \end{cases} \quad (2.46)$$

When \mathbf{x} is directly on the surface S , $\zeta(\mathbf{x})$ depends on the shape of S —whether it is smooth or has an edge—as well as on the properties of the media in the portion of the neighborhood of \mathbf{x} lying inside V . In general, $\zeta(\mathbf{x})$ is a tensor, and the left hand side of (2.45) is more complicated than shown. But when S is smooth (i.e., has a unique tangent plane at \mathbf{x}), and the medium in the neighborhood of \mathbf{x} inside V is homogeneous and isotropic, then $\zeta(\mathbf{x})$ is an isotropic tensor whose operation is equivalent to a simple scalar $1/2$,

$$\zeta(\mathbf{x}) = \frac{1}{2} \quad \text{for } \mathbf{x} \in S. \quad (2.47)$$

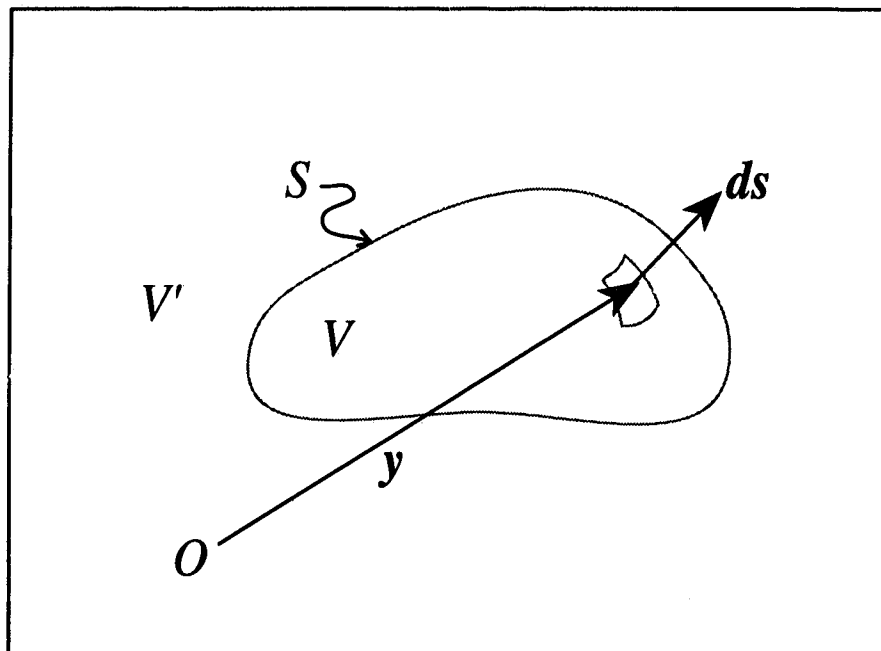


Figure 2.1: The volume and surface of integration in Betti's reciprocity relation. The volume integration variable $d\tau$ ranges throughout the interior domain V , and the surface integration variable \mathbf{y} over the surface S . The integration vector $d\mathbf{s}$, taken parallel to the boundary normal vector \mathbf{n} , points outwards from interior to exterior.

A derivation of ζ will not be undertaken here. Suffice it to say that ζ is the result of a limiting process in which the delta-function singularity of the Green's function is excluded from the domain V by a vanishingly small sphere centered at \mathbf{x} .⁴

To get an integral representation for all three components of \mathbf{u} , we must consider three separate cases of (2.45), with $\widehat{\mathbf{m}}$ directed along each of the three Cartesian component directions. Grouping the three resultant displacement and stress fields into tensors, we have

$$\zeta(\mathbf{x})u_i(\mathbf{x}) = \int_S (G_{ik}(\mathbf{y}, \mathbf{x}) t_k(\mathbf{y}) - T_{ik}(\mathbf{y}, \mathbf{x}) u_k(\mathbf{y})) ds(\mathbf{y}) + \int_V \rho(\mathbf{y}) G_{ik}(\mathbf{y}, \mathbf{x}) f_k(\mathbf{y}) d\tau(\mathbf{y}), \quad (2.48)$$

where the superscript u has been dropped without confusion. \mathbf{G} is the Green's displacement tensor holding the components of \mathbf{v} for each force; $G_{ij}(\mathbf{y}, \mathbf{x})$ being the j 'th component of displacement at the point \mathbf{y} due to a unit point force in the i 'th direction acting at the point \mathbf{x} . It can be partitioned into three rows made up of the components of each displacement field

$$\mathbf{G}(\mathbf{y}, \mathbf{x}) = \begin{bmatrix} v_{11}(\mathbf{y}) & v_{12}(\mathbf{y}) & v_{13}(\mathbf{y}) \\ v_{21}(\mathbf{y}) & v_{22}(\mathbf{y}) & v_{23}(\mathbf{y}) \\ v_{31}(\mathbf{y}) & v_{32}(\mathbf{y}) & v_{33}(\mathbf{y}) \end{bmatrix} \quad \text{for point source at } \mathbf{x}. \quad (2.49)$$

\mathbf{G} satisfies the equation of motion⁵

$$\rho\omega^2 G_{ij}(\mathbf{y}, \mathbf{x}) + \Sigma_{ijk,k}(\mathbf{y}, \mathbf{x}) = -\delta_{ij} \delta(\mathbf{y} - \mathbf{x}), \quad (2.50)$$

in which $\Sigma_{ijk}(\mathbf{y}, \mathbf{x})$ is the third rank Greens stress tensor; $\Sigma_{ijk}(\mathbf{y}, \mathbf{x})$ being the jk 'th element in the stress tensor at the point \mathbf{y} due to a unit point source in the i 'th direction at the point \mathbf{x} ,

$$\Sigma_{ijk} = \lambda G_{il,l} \delta_{jk} + \mu(G_{ij,k} + G_{ik,j}); \quad (2.51)$$

and it satisfies all of the boundary and continuity conditions for the total domain $\mathcal{V} = V + V'$.

Using Betti's relation (2.43), it can also be shown that \mathbf{G} satisfies the reciprocity relation

⁴Derivations are given in [101] and [78]. To my knowledge the tensor ζ when \mathbf{x} is both on an edge of S and on an interface between homogeneous layers has not been solved. Presumably this situation can be avoided by displacing \mathbf{x} a very small distance away from an interface, provided, of course, that it is not precisely the combined edge-interface effect being investigated.

⁵The partial derivatives in the equation of motion and stress-strain relation are taken with respect to the field point \mathbf{y} , the first variable in the argument of the Green's function.

[61]

$$G_{ij}(\mathbf{y}, \mathbf{x}) = G_{ji}(\mathbf{x}, \mathbf{y}). \quad (2.52)$$

\mathbf{T} in (2.48) is the traction tensor holding the components of \mathbf{t}^v ; $T_{ij}(\mathbf{y}, \mathbf{x})$ being the j 'th component of traction vector at the point \mathbf{y} due to a unit point force in the i 'th direction acting at the point \mathbf{x} :

$$T_{ij}(\mathbf{y}, \mathbf{x}) = \Sigma_{ijk}(\mathbf{y}, \mathbf{x}) \hat{n}_k(\mathbf{y}). \quad (2.53)$$

\mathbf{T} can also be partitioned into rows

$$\mathbf{T}(\mathbf{y}, \mathbf{x}) = \begin{bmatrix} \frac{\mathbf{t}^{v1}(\mathbf{y})}{\text{-----}} \\ \frac{\mathbf{t}^{v2}(\mathbf{y})}{\text{-----}} \\ \mathbf{t}^{v3}(\mathbf{y}) \end{bmatrix} = \begin{bmatrix} t_{11}^v(\mathbf{y}) & t_{12}^v(\mathbf{y}) & t_{13}^v(\mathbf{y}) \\ t_{21}^v(\mathbf{y}) & t_{22}^v(\mathbf{y}) & t_{23}^v(\mathbf{y}) \\ t_{31}^v(\mathbf{y}) & t_{32}^v(\mathbf{y}) & t_{33}^v(\mathbf{y}) \end{bmatrix} \quad (\text{point source at } \mathbf{x}). \quad (2.54)$$

\mathbf{G} and \mathbf{T} for an unbounded homogeneous solid medium are sometimes called [101] the Stoke's displacement and traction tensors. The Stoke's displacement tensor evaluated at \mathbf{y} due to orthogonal point sources at \mathbf{x} can be written as [96] [78] [61]

$$G_{mn}(\mathbf{y}, \mathbf{x}) = \left[\delta_{mn} k_{\beta} e^{ik_{\beta} r} / r - \partial_m \partial_n \left(e^{ik_{\alpha} r} / r - e^{ik_{\beta} r} / r \right) \right] / (4\pi \rho \omega^2) \quad (2.55)$$

where

$$r = |\mathbf{y} - \mathbf{x}|. \quad (2.56)$$

Its explicit form, and that of the corresponding traction tensor are rather complicated, but both can be derived straightforwardly from (2.55) using an algebraic manipulator program.

With \mathbf{G} and \mathbf{T} partitioned by rows, (2.48) can be written in matrix form with \mathbf{u} , \mathbf{t} and \mathbf{f} as column vectors

$$\zeta(\mathbf{x}) \mathbf{u}(\mathbf{x}) = \int_S [\mathbf{G}(\mathbf{y}, \mathbf{x}) \mathbf{t}(\mathbf{y}) - \mathbf{T}(\mathbf{y}, \mathbf{x}) \mathbf{u}(\mathbf{y})] ds(\mathbf{y}) + \int_V \rho(\mathbf{y}) \mathbf{G}(\mathbf{y}, \mathbf{x}) \mathbf{f}(\mathbf{y}) d\tau(\mathbf{y}). \quad (2.57)$$

Finally, using the reciprocity relation (2.52), the volume integral on the right can be written as the incident displacement field for a point force distribution $\rho \mathbf{f}$ in V ,

$$\int_V \rho(\mathbf{y}) \mathbf{G}(\mathbf{y}, \mathbf{x}) \mathbf{f}(\mathbf{y}) d\tau(\mathbf{y}) = \int_V \rho(\mathbf{y}) \mathbf{G}^T(\mathbf{x}, \mathbf{y}) \mathbf{f}(\mathbf{y}) d\tau(\mathbf{y}) = \mathbf{u}^{inc}(\mathbf{x}), \quad (2.58)$$

giving Somigliana's identity for the displacement field

$$\zeta(\mathbf{x}) \mathbf{u}(\mathbf{x}) = \int_S [\mathbf{G}(\mathbf{y}, \mathbf{x}) \mathbf{t}(\mathbf{y}) - \mathbf{T}(\mathbf{y}, \mathbf{x}) \mathbf{u}(\mathbf{y})] ds(\mathbf{y}) + \mathbf{u}^{inc}(\mathbf{x}). \quad (2.59)$$

For convenience, we can rewrite it as

$$\mathcal{G}\mathbf{t}(\mathbf{x}) - \mathcal{T}\mathbf{u}(\mathbf{x}) + \mathbf{u}^{inc}(\mathbf{x}) = \begin{cases} \mathbf{0}, & \mathbf{x} \in V' \text{ (exterior)} \quad \dots \text{null field,} \\ \zeta(\mathbf{x}) \mathbf{u}(\mathbf{x}), & \mathbf{x} \in S \quad \dots \text{surface field,} \\ \mathbf{u}(\mathbf{x}), & \mathbf{x} \in V \text{ (interior)} \quad \dots \text{whole field.} \end{cases} \quad (2.60)$$

using the integral operators

$$\begin{aligned} \mathcal{G}\mathbf{t}(\mathbf{x}) &= \int_S \mathbf{G}(\mathbf{y}, \mathbf{x}) \mathbf{t}(\mathbf{y}) ds(\mathbf{y}), \\ \mathcal{T}\mathbf{u}(\mathbf{x}) &= \int_S \mathbf{T}(\mathbf{y}, \mathbf{x}) \mathbf{u}(\mathbf{y}) ds(\mathbf{y}); \end{aligned} \quad (2.61)$$

the three different forms of the integral equation being due to the discontinuous behavior of $\zeta(\mathbf{x})$.

V has so far been a bounded domain, but infinite domains can be treated as a limiting case of bounded by taking the limit as a distant boundary recedes to infinity. The radiation conditions on the field imply that a boundary infinitely far away does not contribute to the field $\mathbf{u}(\mathbf{x})$, making the integral over boundaries infinitely far away equal to zero.⁶

2.5 Huygens' principle

At first glance, Somigliana's identity (2.60) may not offer insight into the physical behavior of elastic waves. Its physical interpretation was actually given many years earlier when Huygens (1678) formulated his well-known principle of wave front construction [96] [28],⁷ when he speculated that light consists of vibrations in an elastic ether. The principle is a rule for geometrically constructing a wave front by summing the fields due to secondary point sources distributed on the surface of the wave front at an earlier instant as shown in Fig.(2.2). The waves emitted from each secondary source is called a *wavelet*.

⁶The extension to infinite homogeneous domains is treated at length by Pao [96].

⁷The Helmholtz integral equation for scalar fields was interpreted as a mathematical formulation of Huygens' principle by Baker and Copson [7]. Skudrzyk [118] goes so far as to call the Helmholtz integral equation, the Helmholtz-Huygens integral equation.

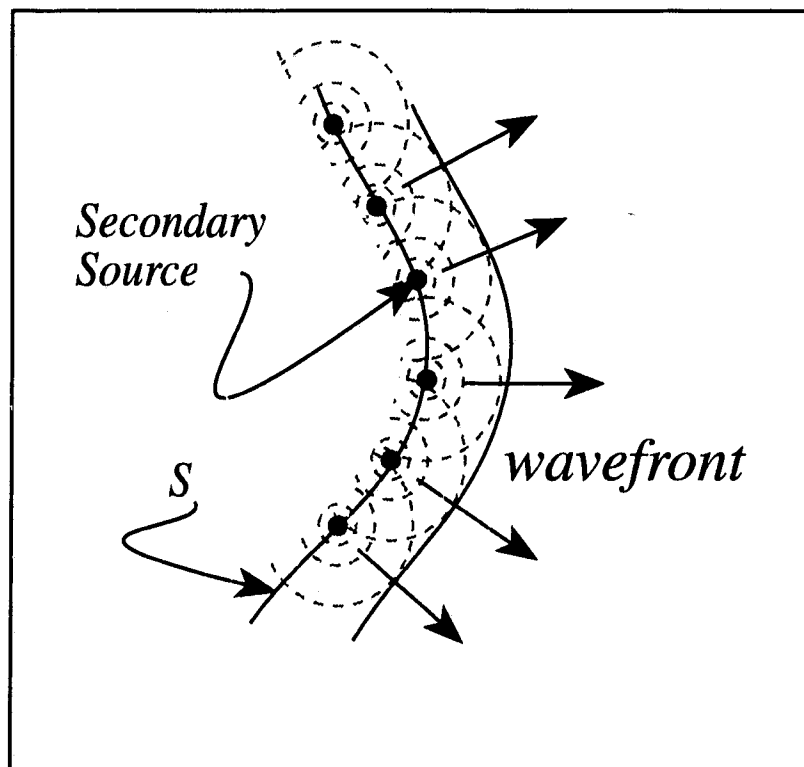


Figure 2.2: Huygens' principle for wavefront reconstruction. The wavefront is the superposition of wavelets due to secondary sources on a surface.

Huygens' principle involves two conjectures implicit in (2.60). The first is that the displacement field is the superposition of wavelets originating from a distribution of secondary sources on a surface, plus any direct waves emitted from actual sources. This becomes evident when we view the integrands of the operators (2.61) as two different wavelets, where the field variables \mathbf{u} and \mathbf{t} play the role of secondary source strengths on the surface S , and the boundary integral is their superposition taken in the limit of a continuous source distribution:

$$\begin{aligned}
 \text{simple wavelet} & \Rightarrow \mathbf{G}(\mathbf{y}, \mathbf{x}) \mathbf{t}(\mathbf{y}) ds(\mathbf{y}), \\
 \text{complex wavelet} & \Rightarrow -\mathbf{T}(\mathbf{y}, \mathbf{x}) \mathbf{u}(\mathbf{y}) ds(\mathbf{y}), \\
 \text{direct waves from source} & \Rightarrow \mathbf{u}^{inc}(\mathbf{x}).
 \end{aligned} \tag{2.62}$$

The surface source distributions are often called potential layers [78]. They are an extension of the monopole and dipole potential layers of a scalar wave theory [68].

The second conjecture is that the behavior of the wavelet propagation is not affected by what lies in the domain excluded by the boundary S . This is evident because the Green's tensors, \mathbf{G} and \mathbf{T} , governing the wavelet propagation are determined without reference to the boundary S . Hence the wavelets always radiate as if into the entire domain \mathcal{V} , regardless of what may lie in the exterior domain \mathcal{V}' .

We can make full use of Huygens' principle when solving scattering problems. Applying the first conjecture, we can subdivide the domain of our scattering problem into any number of subdomains in which the displacement field can be expressed as the superposition of wavelets from secondary sources on its boundary. A subdomain can have any size because the wavelet integral (2.60) is exact. Applying the second, we see that a subdomain only interacts with its neighbors through the wavelet source strengths \mathbf{u} and \mathbf{t} along a common boundary, so we can treat it as a volume element embedded in one scattering problem or another, but whose integral operators in the boundary integral equation remain the same for all problems. This modular interchangeability of subdomains is central to the new indirect BIE method and to numerical tests. It also implies that we have some freedom in choosing the Green's function for the wavelets in a subdomain: it must satisfy the equation of motion and boundary conditions everywhere inside, but it can satisfy any conditions at points outside the boundaries. In a subdomain consisting of a homogeneous medium, for

instance, we can use the Green's function for the corresponding unbounded homogeneous domain because it satisfies the equation of motion everywhere inside the subdomain.⁸

In summary, Huygens' principle, formulated mathematically using Somigliana's identity, allows us to subdivide a complicated domain for which the Green's function is intractable, into simpler domains in each of which the Green's function is tractable. Within each subdomain, the displacement field is represented by the superposition of the wavelet fields, and adjacent subdomains are coupled together through field continuity conditions applied at their common boundaries. In terms of Huygens' principle, the BIE method proceeds in two steps: 1) to compute the wavelet source strengths \mathbf{u} and \mathbf{t} on the boundary of each subdomain in the scattering problem; and 2) to compute the displacement field at any point within a subdomain by wavelet superposition.

2.6 The boundary integral perspective

When a domain is subdivided, we quickly run into confusion between *interior* and *exterior*, for the interior of one subdomain lies in the exterior of another. The problem is compounded by the three possibilities in (2.60) that depend on the location of \mathbf{x} relative to the boundary of the subdomain under consideration. We must be clear about which enclosing surface we are integrating over, which Green's tensors are to be used in the integrand, and which side of the boundary is to be interior and which the exterior domain. I call this the *perspective* of the integral equation. Switching the perspective changes the integral equation completely.

Suppose, for instance, that we have a single homogeneous scattering object embedded in an oceanic waveguide. One obvious way—no doubt the best way—of subdividing the domain is to use the surface of the scattering object itself as the integration boundary separating the infinitely large layered domain from the finite scattering object. From the perspective of the host waveguide, then, the interior domain is the infinite region outside the scattering object, whereas, from the perspective of the scattering object, the interior domain is the homogeneous region within it. And from the perspective of the host waveguide,

⁸The Green's functions for an unbounded homogeneous fluid and solid domains can be found in the literature [96] [78] [61] [91] [101].

the simplest Green's function is that of the undeformed waveguide (the scattering object being entirely excluded by the integration boundary), whereas, from the perspective of the embedded inclusion, the simplest Green's function is that of an unbounded homogeneous medium having the same elastic parameters as the scattering object (the host waveguide being entirely excluded by the integration boundary). The boundary integral is "told" which is the interior for each perspective by the direction of the normal vector on the boundary. Following the convention used in Betti's reciprocity theorem, the normal vector always points outwards from the interior domain.

2.7 Determining the boundary fields

Having subdivided the scattering problem into domains for which we can compute suitable Green's functions, it remains to decide which of the three integral formulations in Somigliana's identity—the null-, surface-, or whole-field equation—can be used together with the continuity and boundary conditions to determine the elastic field on the boundaries.

Consider first the null-field equation in (2.60). The unknown field variables, \mathbf{u} and \mathbf{t} , only appear within the integrands making it an integral equation of the first kind, which as a rule are disastrously unstable.⁹ Nevertheless equations of the first-kind have been used with some success [123], so let us include it as a possible candidate for determining the boundary field and use it with caution.

Next consider the surface-field equation in (2.60). The unknown boundary displacement \mathbf{u} appears both inside and outside the integral, whereas the traction \mathbf{t} only appears inside the integral. Thus, we might say the surface-field equation is of the second kind in \mathbf{u} , but of the first kind in \mathbf{t} . If we consider a traction-free boundary, for exam-

⁹Arfken [4] explains the instability this way: In an equation of the first kind

$$\varphi(x) = \int K(x, y) f(y) dy \equiv Kf(x),$$

φ is insensitive to small variations in K and f because integration is a "smoothing" operator, whereas f is very sensitive to variations in φ . When K and φ are approximated numerically, the solution

$$f(x) = K^{-1}\varphi(x),$$

will therefore be sensitive to small numerical errors in φ , which means that K^{-1} must be unstable—small numerical errors are magnified and accuracy is lost.

ple, which is typically used in seismology for scattering from surface topology [67] [92], then $\mathbf{t} = \mathbf{0}$ from the outset, giving an equation strictly of the second kind in \mathbf{u} . But at a rigid-welded boundary, $\mathbf{u} = \mathbf{0}$ from the outset, giving an equation of the first kind in \mathbf{t} .

As a rule, equations of the second kind have excellent numerical stability,¹⁰ though on occasion their solution may become nonunique, as shown by the Fredholm theory of integral equations.¹¹ The problem is well known in scalar wave theory, for it occurs at isolated critical frequencies in the Neumann and Dirichlet boundary value problems, and a variety of remedial measures have been developed [29] [106] [22]. In our case, however, the mixed nature of the surface-field equation—part first and second kind—raises doubts about its overall stability. Perhaps both the numerical instability which plagues the solution of equations of the first kind, and the occasional nonuniqueness problem of the equations of the second kind, may trouble the numerical solution. The question has apparently not been raised in the literature, and I am not in a position to resolve it here, but until it is resolved, we must proceed cautiously; careful testing is needed for the solution to any scattering problem.

Another numerical difficulty with the surface-field equation invariably arises when computing the Cauchy Principal Value (CPV) because the integrand is singular at the computation point $\mathbf{x} \in S$ due to the singularity in the Green's function. This can be a difficult task, especially for layered waveguides whose Green's function cannot be written in simple closed form and is also slowly convergent in the very near field. I will use an indirect integration method to avoid both problems at once.

It should be noted that Somigliana's identity could be converted to an equation of the second kind in \mathbf{t} by first differentiating it to construct an integral representation for the strain tensor (2.1), then using Hooke's law (2.2) to get the corresponding stress tensor. The

¹⁰In equations of the second kind

$$\varphi(x) = \int K(x, y) f(y) dy + \lambda f(x) \equiv Kf(x) + \lambda f(x),$$

the $\lambda f(x)$ term generally leads to diagonal dominance, hence stability, in the numerical system of equations that determine $f(x)$.

¹¹The Fredholm theory for integral equations establishes the existence and uniqueness of the solution to an integral equation of the second kind [129]. The Riesz theory for compact operators is the extension to integral equations having weakly singular kernels [105][29].

equivalent has been done more simply in scalar wave theory to solve (Dirichlet) problems with zero-pressure boundary conditions, converting the Helmholtz integral equation from the second kind in pressure, to the second kind in normal velocity [22]. Where the original equation is weakly singular [29], however, the modified is hypersingular, which presents still greater numerical complications for the BIE method, except when used with the zero-pressure boundary conditions. In the vector theory, the ensuing hypersingular integrals would ordinarily be encountered in all problems except scattering from impenetrable rigid inclusions. It may be possible to avoid troublesome hypersingularities using the indirect integration method I propose, though I do not explore the possibility here.¹²

Finally, consider the whole field equation in (2.60) as a means for deriving the unknown boundary field. As it stands, the equation cannot be used because it introduces yet another unknown function, the displacement field in the interior domain, $\mathbf{u}(\mathbf{x})$ for $\mathbf{x} \in V$. The interior displacement field must somehow be eliminated first, possibly by relating the field at \mathbf{x} to the field on the boundary in an approximate way.¹³

2.7.1 A combined equation method

To overcome occasional nonuniqueness problems in equations of the second kind in the Neumann problem in acoustics, Schenck [106] used both the surface- and null-field equations together in his combined equation method. In effect, the null-field equation overdetermines the numerical solution, forcing a unique best-fit result when the solution to the surface-field equation on its own is nonunique. Going one step further, the combined method can be viewed as a generalization of BIE methods that are so often based exclusively on either one equation or the other. One could, for example, attempt a solution based strictly on either the surface- or null-field equation, or combine them in varying degrees

¹²I have not come across any references to the modified integral representation for the stress tensor in the literature.

¹³While at the SACLANT Center in La Spezia Italy, I developed a simple finite-difference scheme to do just that for scalar fields in two-dimensional fluid media. By placing the computation point \mathbf{x} very close to the boundary, a single finite difference step could accurately connect the field at \mathbf{x} to the field on the boundary in its immediate vicinity; a complete finite-difference treatment of the interior volume was not required. The modified equation has the stable properties of the surface-field equation with the singularity in the integrand favorably weakened since \mathbf{x} is no longer on the boundary. Unfortunately, I have not been able to extend the method to vector fields.

to overdetermine, and possibly stabilize, an otherwise unstable solution. The freedom to experiment with combinations this way would be an advantage, especially as numerical stability is not assured. In the next chapter I develop a flexible combined method that can use any combination of the surface- and null-field equations.

Chapter 3

The indirect BIE method

We have seen how the domain of a scattering problem can be subdivided into subdomains (volume elements), each with its own perspective for the boundary integral equation. The BIE method continues in two steps: 1) by computing the field on the boundaries of the subdomains (the Huygens' wavelet strengths); and 2) by computing the displacement field at any point off the boundary, again using Somigliana's identity (the superposition of wavelets). In this chapter I take up the numerical details. The method is demonstrated for scattering by spheres, for which benchmark analytic solutions can be computed by separation of variables methods. Examples involving layered waveguides must wait until Chapter 7, after the requisite Green's function is developed in Chapters 4, 5 and 6.

3.1 Numerical approximation of the boundary integral

The number of points on the boundary where \mathbf{u} and \mathbf{t} must be computed is infinite, so the first numerical approximation is to reduce the continuous domain to a finite number of points, called nodes, by dividing the boundary into small elements on which the field can be interpolated from its values at the nodes. The elements cannot be too large or the interpolation becomes inaccurate, nor too small or the demands upon computer memory become excessive.

A boundary element can be mapped to a square in a two-dimensional coordinate system $\boldsymbol{\xi} = [\xi_1, \xi_2]^T$; $-1 \leq \xi_{1,2} \leq +1$. When interpolated from its nodes using shape

functions $N_m(\boldsymbol{\xi})$, the field at a point $\mathbf{x}(\boldsymbol{\xi})$ on the n 'th boundary element is [8]

$$\begin{aligned} u_i(\mathbf{x}) &= N_m(\boldsymbol{\xi}) u_{im}^n, \\ t_i(\mathbf{x}) &= N_m(\boldsymbol{\xi}) t_{im}^n. \end{aligned} \quad (3.1)$$

$\mathbf{u}_m^n = [u_{1m}^n, u_{2m}^n, u_{3m}^n]^T$ and $\mathbf{t}_m^n = [t_{1m}^n, t_{2m}^n, t_{3m}^n]^T$ are the displacement and normal traction at the m 'th node on the n 'th boundary element, and summation over m is implied. Many different shape functions for boundary elements can be used. In my own BIE program I use quadrilateral boundary elements as shown in Fig. (3.1), with triangular elements treated as degenerate quadrilaterals. Quadratic shape functions accurate to second order can be constructed using a nine-node interpolation scheme [132] [79]

$$\begin{aligned} N_1(\boldsymbol{\xi}) &= \frac{1}{2}\xi_1(\xi_1 - 1) \cdot \frac{1}{2}\xi_2(\xi_2 - 1), \\ N_2(\boldsymbol{\xi}) &= (1 - \xi_1^2) \cdot \frac{1}{2}\xi_2(\xi_2 - 1), \\ N_3(\boldsymbol{\xi}) &= \frac{1}{2}\xi_1(\xi_1 + 1) \cdot \frac{1}{2}\xi_2(\xi_2 - 1), \\ N_4(\boldsymbol{\xi}) &= \frac{1}{2}\xi_1(\xi_1 + 1) \cdot (1 - \xi_2^2), \\ N_5(\boldsymbol{\xi}) &= \frac{1}{2}\xi_1(\xi_1 + 1) \cdot \frac{1}{2}\xi_2(\xi_2 + 1), \\ N_6(\boldsymbol{\xi}) &= (1 - \xi_1^2) \cdot \frac{1}{2}\xi_2(\xi_2 + 1), \\ N_7(\boldsymbol{\xi}) &= \frac{1}{2}\xi_1(\xi_1 - 1) \cdot \frac{1}{2}\xi_2(\xi_2 + 1), \\ N_8(\boldsymbol{\xi}) &= \frac{1}{2}\xi_1(\xi_1 - 1) \cdot (1 - \xi_2^2), \\ N_9(\boldsymbol{\xi}) &= (1 - \xi_1^2) \cdot (1 - \xi_2^2). \end{aligned} \quad (3.2)$$

In general, the numerical approximation for the integral operators (2.61) can be written as

$$\begin{aligned} \mathcal{G}t_i(\mathbf{x}) &\approx \mathcal{G}_{ijm}^n(\mathbf{x}) t_{jm}^n, \\ \mathcal{T}u_i(\mathbf{x}) &\approx \mathcal{T}_{ijm}^n(\mathbf{x}) u_{jm}^n, \end{aligned} \quad (3.3)$$

where

$$\begin{aligned} \mathcal{G}_{ijm}^n(\mathbf{x}) &= \int_{S^n} G_{ij}[\mathbf{y}(\boldsymbol{\xi}), \mathbf{x}] N_m(\boldsymbol{\xi}) J(\boldsymbol{\xi}) d\xi_1 d\xi_2, \\ \mathcal{T}_{ijm}^n(\mathbf{x}) &= \int_{S^n} T_{ij}[\mathbf{y}(\boldsymbol{\xi}), \mathbf{x}] N_m(\boldsymbol{\xi}) J(\boldsymbol{\xi}) d\xi_1 d\xi_2. \end{aligned} \quad (3.4)$$

Here $J(\boldsymbol{\xi})$ is the Jacobian for the transformation from $\boldsymbol{\xi}$ to the local coordinates of the element [8], and S^n is the surface of the n 'th boundary element. \mathcal{G}_{ijm}^n and \mathcal{T}_{ijm}^n are boundary integral coefficients that depend on 1) the Green's function for the perspective of the

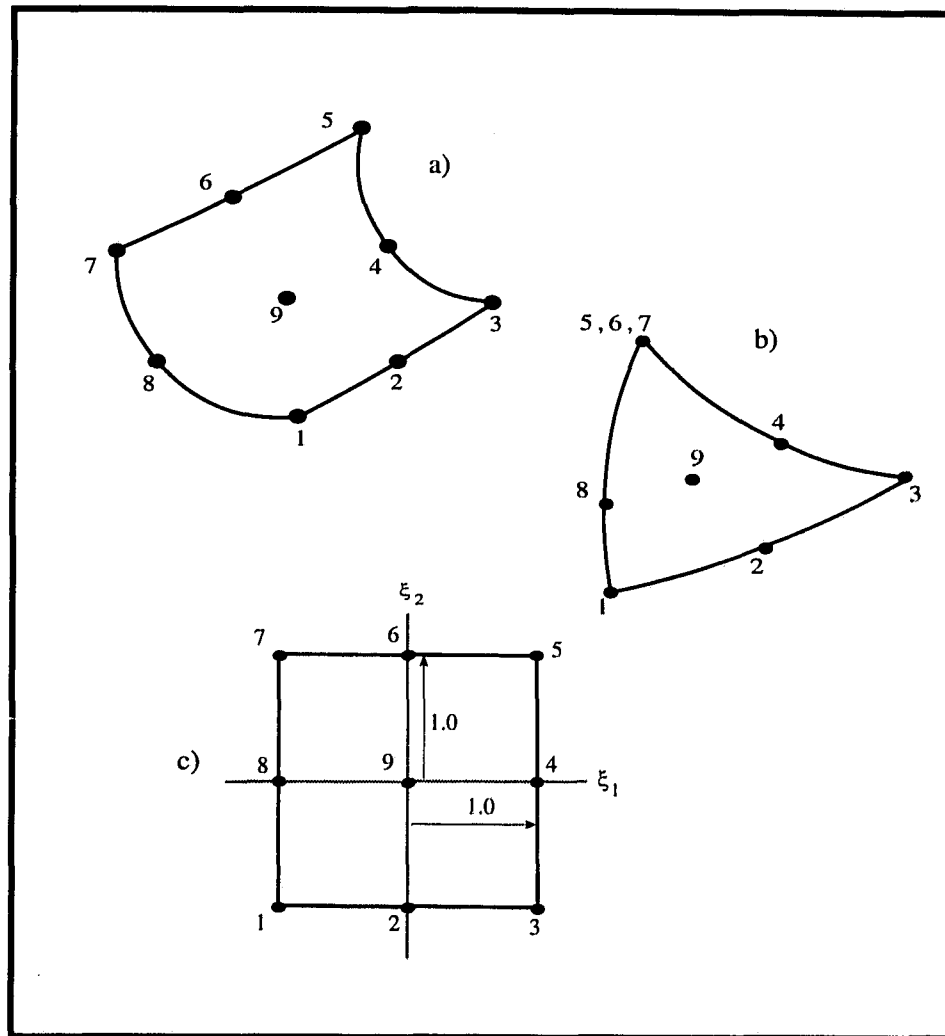


Figure 3.1: Quadrilateral boundary element and nodes. a) A quadrilateral boundary element with nine nodes. b) Triangular elements are degenerate quadrilaterals. c) Each element has a two-dimensional parametric representation.

equation, 2) the shape of the boundary element, and 3) the computation point \mathbf{x} ; but they do not depend on the boundary or continuity conditions applied to the field. Substituting the approximate operators into (2.60) gives

$$\mathcal{G}_{ijm}^n(\mathbf{x}) t_{jm}^n - \mathcal{T}_{ijm}^n(\mathbf{x}) u_{jm}^n + u_i^{inc}(\mathbf{x}) \approx \begin{cases} 0 & \dots \text{ null-field,} \\ \zeta(\mathbf{x}) N_{m'}(\mathbf{x}) u_{im'}^n & \dots \text{ surface-field,} \\ u_i(\mathbf{x}) & \dots \text{ whole-field.} \end{cases} \quad (3.5)$$

In the surface-field equation, n' is the boundary element containing \mathbf{x} , and the summation over m' is over the nodes on just that element.

Nodes often touch several boundary elements because they lie on the perimeter of an element. The double indices $\frac{n}{m}$ can therefore be replaced by a single index m ranging over all the nodes by switching to a global numbering scheme for all distinct nodes

$$\mathcal{G}_{ijm}(\mathbf{x}) = \sum_{n=1}^{n(m)} \mathcal{G}_{ijm}^n(\mathbf{x}), \quad (3.6)$$

$$\mathcal{T}_{ijm}(\mathbf{x}) = \sum_{n=1}^{n(m)} \mathcal{T}_{ijm}^n(\mathbf{x}).$$

$n(m)$ is the number of boundary elements in contact with the m 'th node. Equation (3.5) therefore becomes

$$\mathcal{G}_{ijm}(\mathbf{x}) t_{jm} - \mathcal{T}_{ijm}(\mathbf{x}) u_{jm} + u_i^{inc}(\mathbf{x}) \approx \begin{cases} 0 & \dots \text{ null-field,} \\ \zeta(\mathbf{x}) N_{m'}(\mathbf{x}) u_{im'} & \dots \text{ surface-field,} \\ u_i(\mathbf{x}) & \dots \text{ whole-field.} \end{cases} \quad (3.7)$$

This numerical approximation to the whole-field equation is perhaps the way we usually think of Huygens' principle: the field $\mathbf{u}(\mathbf{x})$ is the superposition of m boundary wavelet sources distributed on a boundary plus the incident field \mathbf{u}^{inc} due to sources in the interior domain.

3.2 A flexible combined equation method

As mentioned in Section (2.7), the unknown boundary field u_{jm} and t_{jm} can be computed using both the surface-field equation and the null-field equation. Here I describe

a flexible numerical method that permits any combination of the two.

3.2.1 Surface-field equations

If \mathbf{x} is placed at the m 'th node, then $u_j(\mathbf{x}) = u_j(\mathbf{x}_m) = u_{jm}$, which occurs on both sides of the surface-field equation (3.7). By placing \mathbf{x} successively at each of the nodes, we can in principle construct a full system of equations in terms of u_{jm} and t_{jm} ; one vector equation arising from each node on the boundary; hence twice as many unknowns as equations. More generally, computation points can be placed anywhere on the boundary using interpolation as shown on the right side of (3.7). Thus, any number of computation points can be placed on the boundary giving any number of equations, though additional points beyond the number of nodes do not help to determine the solution because the additional equations approximate linear combinations of the others. The freedom to place surface nodes anywhere on the boundary—especially away from the perimeter of the boundary elements—is an advantage because we can avoid computing a complicated sifting factor ζ for nodes on edges. It is also helpful in the new indirect BIE method as we will see.

3.2.2 Null-field equations

Null-field equations have the same form as surface-field equations, except the right-hand side of (3.7) is identically zero. Here again, we can construct any number of equations by choosing any number of computation points \mathbf{x} in the exterior domain of the perspective.

As mentioned in Section(2.7), the null-field equation is likely to suffer from instability because it is an equation of the first kind. Instability sets in as the boundary elements are made smaller for improved accuracy. Increasing the node density eventually makes the matrix coefficients for a node roughly equal to a scalar multiple of the same coefficients for a nearby node, which in turn makes the columns in the matrix linearly dependent. Attempts to improve accuracy may therefore make it worse.¹ Null-field equations have been used successfully nonetheless [123]. Notice that a greater degree of error due to instability can

¹The same problem does not occur in equations of the second kind because its distinctive term—the unknown variable appearing outside the integral—is independent of the element size, ensuring diagonal dominance as the element size is reduced since the magnitude of the matrix coefficients G_{ijm} and T_{ijm} decrease roughly in proportion to the element area.

be tolerated in scattering than if the boundary field were itself the final objective, for the boundary field is only an intermediate step towards the field at points off the boundary, for which the whole-field equation will tend to smooth out irregularities due to instability provided they are not too large.² Moreover, there may be an optimal boundary element size that is at once small enough to adequately sample the boundary field by their node spacing, and large enough to avoid disastrous instability. At any rate, it is clear that null-field equations must be used with caution and careful testing.

3.2.3 Combined equation method

To fully determine the boundary field, additional equations must come from the boundary conditions (2.38) and the continuity equations (2.32 to 2.36) applied to the field at each node. Clearly these play an important role because they assemble the subdomains of the scattering problem together; the continuity conditions connecting domains across their penetrable boundaries, and boundary conditions prescribing the behavior at impenetrable boundaries. Unlike the integral equations, the boundary and continuity equations are sparse because each pertains to just one or two nodes rather than to many nodes at once.

A general algorithm to manage the continuity and boundary conditions is difficult to write, especially in layered media where an inclusion may be in contact with fluids in some places and solids in others, or when a scattering problem includes several objects in contact with the host medium as well as with each other, perhaps with one object completely embedded within another. Boundary conditions are also needed whenever a scattering inclusion is in contact with a free surface or rigid bottom, or if it is a source actively radiating energy. Perhaps the simplest approach is to include each boundary and continuity equation as additional equations in the overall BIE coefficient matrix. The final matrix equation that determines the field on all of the boundaries simultaneously might look something like this when there are just two inclusions, perspectives 1 and 2. embedded

²Equations of the first kind are particularly worrisome when the boundary field is of primary interest, in the study of dynamic stress concentrations that lead to fractures at a boundary for example.

in a host medium, perspective 0:

$$\begin{bmatrix}
 \mathcal{BIE}^{(0)} & \mathbf{0} & \mathbf{0} \\
 \mathbf{0} & \mathcal{BIE}^{(1)} & \mathbf{0} \\
 \mathbf{0} & \mathbf{0} & \mathcal{BIE}^{(2)} \\
 \mathcal{BC}^{(0)} & \mathbf{0} & \mathbf{0} \\
 \mathbf{0} & \mathcal{BC}^{(1)} & \mathbf{0} \\
 \mathbf{0} & \mathbf{0} & \mathcal{BC}^{(2)} \\
 \mathcal{C}^{(0,1)} & \mathcal{C}^{(1,0)} & \mathbf{0} \\
 \mathbf{0} & \mathcal{C}^{(1,2)} & \mathcal{C}^{(2,1)} \\
 \mathcal{C}^{(0,2)} & \mathbf{0} & \mathcal{C}^{(2,0)}
 \end{bmatrix}
 \begin{bmatrix}
 \mathbf{b}^{(0)} \\
 \mathbf{b}^{(1)} \\
 \mathbf{b}^{(2)}
 \end{bmatrix}
 =
 \begin{bmatrix}
 \mathcal{U}^{inc(0)} \\
 \mathcal{U}^{inc(1)} \\
 \mathcal{U}^{inc(2)} \\
 \mathbf{C}^{(0)} \\
 \mathbf{C}^{(1)} \\
 \mathbf{C}^{(2)} \\
 \mathbf{0} \\
 \mathbf{0} \\
 \mathbf{0}
 \end{bmatrix}. \quad (3.8)$$

The matrix partitions are

$$\begin{aligned}
 \mathcal{BIE}^{(i)} &= \text{surface- and null-field equations for } i\text{'th perspective,} \\
 \mathcal{BC}^{(i)} &= \text{boundary condition equations for } i\text{'th perspective,} \\
 \mathcal{C}^{(i,j)} &= \text{continuity equations for coupling perspective } i \text{ to } j, \\
 \mathbf{b}^{(i)} &= \text{unknown surface field at nodes in } i\text{'th perspective,} \\
 \mathcal{U}^{inc(i)} &= \text{incident fields for } i\text{'th perspective,} \\
 \mathbf{C}^{(i)} &= \text{active boundary condition term for } i\text{'th perspective.}
 \end{aligned} \quad (3.9)$$

Changes to accommodate more or less scattering objects are obvious.

In the combined equation method, the system of equations is likely to be overdetermined (more equations than unknowns) because the number of surface and null-field equations in the $\mathcal{BIE}^{(i)}$ partitions would ordinarily be more than strictly required. Therefore, the system must be solved using a least squares method, possibly using singular value decomposition. A least squares solution minimizes the error of all equations simultaneously, whereas the individual equations are each satisfied to varying degrees of accuracy, so the solution will only be accurate for all equations if the equations are consistent with each other, as they should be because each equation is derived from the same boundary value problem. Thus, a simple test of a solution is to check how well it satisfies each of the original equations: a large error for just one equation suggests an error in that equation alone; a large error for many equations suggests something is terribly wrong possibly the size of the boundary elements is too large.

3.2.4 Compressing the BIE coefficient matrix

The form of the BIE coefficient matrix (3.8) is straightforward in construction, even for rather complicated problems having fluid and solid media, multiple penetrable inclusions with impenetrable boundaries, and so forth; but it is terribly inefficient because the matrix is very large (six unknowns, \mathbf{u} and \mathbf{t} , for every node in every perspective of the scattering problem), while containing many sparse partitions (all of the $\mathcal{BC}^{(i)}$ and $\mathcal{C}^{(i,j)}$). Before the matrix equation is solved, the simplest boundary and continuity equations—those that merely assign a value to a field variable or couple two variables across a boundary—should therefore be eliminated using a simple algorithm that 1) checks for rows in the BIE coefficient matrix with just one or two non-zero elements, and then 2) eliminates one column for each accordingly. The algorithm is simple because it acts without reference to the particular scattering problem. All of the welded continuity equations between a two solid media can be eliminated this way, reducing the number of unknowns by a factor of two for strictly solid domains in contact. To do the same for fluid media, however, we must first remove the role of the normal vector from the boundary and continuity equations for nodes inside a fluid, by rotating the boundary displacement and traction vectors to a local coordinate system having one axis along the boundary normal vector, as mentioned earlier with regards to equation (2.37). The reduced system of equations can be solved much faster than the unreduced.

Another reason for compressing the matrix is to ensure that the boundary and continuity equations are strictly enforced in the solution. Recall that the solution of an overdetermined system of equations satisfies the system of equations in a least squares sense, but not every equation considered individually. The boundary and continuity equations will therefore “drift” when left in the BIE coefficient matrix: zero traction on a free boundary will become a “small” traction condition, and welded contact between solids will be slightly broken for example. The drift will be negligible if the numerical approximation of the boundary value problem is accurate, but noticeable upon careful inspection nonetheless.

BIE programs intended for strictly solid media often enforce continuity of displacement and traction across a boundary in the way the $\mathcal{BTE}^{(i)}$ partitions are assembled, rather

than by including separate continuity equations as in (3.8). From the outset, then, the displacement field on the boundary of one perspective is taken as the displacement field of another in contact, and the traction field of one taken as the negative traction field of the other. In effect, the continuity equations in (3.8) are eliminated before constructing the matrix, thereby reducing the number of unknowns immediately by a factor of two, much as I propose doing with a matrix compression algorithm. But it is wrong to equate the displacement on both sides of an interface with an inviscid fluid, for that enforces no-slip (welded) continuity at a fluid boundary, rather than the slip condition (See Section (2.3.2)), which necessarily involves the boundary normal vector.³

3.2.5 A modular approach to the combined equation method

I follow a modular approach to the BIE method. One program computes and saves the equation coefficients \mathcal{G}_{ijm} and \mathcal{T}_{ijm} for each point \mathbf{x} in a list of computation points read from a data file. Another constructs and saves the non-zero partitions of the sparse boundary condition equations for all the impenetrable elements in a perspective. A third constructs the total coefficient matrix by packing the previously saved boundary integral and boundary condition partitions into the matrix, while also computing the incident fields on the left side of (3.8). It then constructs the coupling equation partitions at the bottom of the matrix, compresses the matrix, solves for the remaining unknowns using least squares, decompresses the solution to get the boundary field at every node in every perspective of the problem, and finally saves the boundary fields. A fourth program computes and saves the displacement vector at points off the boundaries using the whole-field equation, and a fifth plots the field in a number of ways, using polar plots, grey scale diagrams, and so forth.

The modular approach has the advantage that many computations do not have to be repeated every time certain aspects of the problem are changed. If the incident field is changed, by relocating a source for example, only the incident field on the left side of (3.8) needs to be recomputed. If additional surface- or null-field equations are added later for

³In a scalar theory the boundary normal vector is intrinsic to the field variables, the acoustic pressure and normal velocity, making it correct (and most efficient) to equate and eliminate the unknown field variables between penetrable domains in contact directly in the $BIE^{(1)}$ partitions, as Seybert and Casey [115], and Colton and Kress [29] do for example. But in a vector theory, the normal vector must be included explicitly to relate only the normal components of the field while leaving the tangential displacement undetermined.

numerical stability, only the equations for the new computation points need to be computed.

Any combination of surface- and null-field equations is possible using the modular approach because the computations are driven by an arbitrary list of computation points in a data file. The user might specify points for surface field equations that coincide with the boundary nodes, or points that are displaced from the perimeter of the elements to avoid edges. Points for null-field equations might be distributed randomly or on a rectangular grid in the exterior domain, or they might be omitted altogether. A utility program automatically picks points in a variety of ways and writes the corresponding computation point file.⁴ The user can modify this file or create a new one as desired.

The stress tensor could be computed at points off the boundary, either by approximating the strain tensor (2.1) from the displacement field using finite differences, then using Hooke's law (2.2), or by modifying Somigliana's identity to an integral representation for the stress as described in Section (2.7). The hypersingular integral equations resulting in the later method do not pose particular numerical difficulty when computing the stress at points that are not close to the integration boundary. Computation of the stress has not been implemented in my own program at the time of writing.

3.2.6 Specifying the scattering problem in a flexible way

In my own BIE program, each boundary integral perspective is defined by a boundary specification file that lists all the boundary element specifications for one object element by element. Included for each element is

1. its surface element type, whether spherical, cylindrical, plane, etc., plus any defining geometric parameters, such as the radius for a spherical or cylindrical element;

⁴It is often necessary for the point picking program to check if a point lies inside or outside a closed boundary. This is easy to do since the solid angle Ω subtended by the boundary viewed from a point can be computed using a boundary integral like the integrals in the BIE method

$$\Omega(\mathbf{x}) = \int_S \frac{(\mathbf{x} - \mathbf{y}) \cdot \hat{\mathbf{n}}(\mathbf{y})}{|\mathbf{x} - \mathbf{y}|^3} ds(\mathbf{y}) = \begin{cases} 4\pi, & \mathbf{x} \in \text{interior;} \\ 2\pi, & \mathbf{x} \in \text{boundary } S; \\ 0, & \mathbf{x} \in \text{exterior.} \end{cases}$$

In fact, by substituting the solid angle kernel for the Green's function kernel in the BIE method, we have an excellent first test for the integration algorithm for null- and whole-field equations.

2. the limits of the parametric representation for the element, ξ_1 and ξ_2 in (3.1), which fix the perimeter of the element;
3. the sign (\pm) of the normal vector, such that it points outwards from the perspective of the scattering object;
4. the shift and rotation needed to orient the element with respect to a global coordinate system used for the entire scattering problem.

The elements can be specified in any order. The program scans the elements for common nodes and sets up a global node numbering system of all unique nodes for each BIE perspective. It also compares the boundary elements on different perspectives, looking for identical matches (aside from the direction of the normal vector, which are reversed) for which coupling equations are required. The nature of the coupling is determined by checking the type of media on both sides of the element, whether it is solid, fluid or impenetrable. All unmatched elements are assumed to be impenetrable, and the linear boundary conditions (2.38) for their nodes, whether rigid or free, passive or actively vibrating, are read from a data file set up under the direction of the user.

3.3 A consistency test using Huygens' principle

Before continuing, it will be helpful to see how Huygens' principle can be used to test how well the boundary integral is approximated numerically. Let us embed the interior domain of a particular BIE perspective in a domain contrived so that the inclusion does not produce a scattered field. There is always one such domain: the domain whose Green's function is being used for the perspective in the original scattering problem. A homogeneous solid scattering object, for example, could be embedded into an unbounded homogeneous domain of the same material. The inclusion cannot scatter waves because it does not alter the entire domain in any way; it is simply an arbitrary division of the host domain into interior and exterior regions.

Now place a point source, for which we know the Green's function, anywhere in this contrived problem, and we can compute the total elastic field (displacement vector and

stress tensor) at any point using only the Green's function because there is no scattered field. In fact, we can compute all of the field variables appearing in (3.7), $\mathbf{u}_m = \mathbf{u}(\mathbf{x}_m)$ and $\mathbf{t}_m = \mathbf{t}(\mathbf{x}_m)$ at the element nodes \mathbf{x}_m , and $\mathbf{u}^{inc}(\mathbf{x}) = \mathbf{u}(\mathbf{x})$ at any point \mathbf{x} , and this is just what we need to test the coefficients in the integral equation (3.7), for we have two ways of computing the displacement field $\mathbf{u}(\mathbf{x})$, the results of which should be identical: 1) using the Green's function without regard for the boundary of the "false" inclusion, and 2) using the numerical BIE equation (3.7) as if the boundary were a genuine separation between two domains. Assuming the Green's function is correct, any difference between the two methods must be due to inaccuracies or errors in the numerical computations; from inadequate sampling of the field by nodes for the interpolation scheme, inaccurate computation of \mathcal{G}_{ijm} or \mathcal{T}_{ijm} (especially when \mathbf{x} is close to the boundary), or some other more serious error. In effect, we are checking how consistent the numerical integration scheme is with Huygens' principle.

The consistency test can be applied in many different ways since we can choose any configuration of point sources to generate test fields in the test domain, and any computation point for which the integral equation is to be computed. In fact, all of the integral coefficients needed for many consistency tests are already available in the boundary integral partitions $\mathcal{BIE}^{(i)}$ of (3.8); we need only choose the same computation points for the consistency test as we used to generate the surface- and null-field integral equations. The coefficients are the same for the test and the actual scattering problem because the perspective for the integral equation is identical for both. Each integral equation can therefore be tested for consistency as they are computed with little additional effort, immediately detecting errors and saving considerable effort that would be wasted by continuing with bad integral coefficients.

3.4 Troublesome integral coefficients

\mathcal{G}_{ijm}^n and \mathcal{T}_{ijm}^n in (3.5) can usually be computed without difficulty. I use a simple two-dimensional Gaussian quadrature scheme [100, sect. 4.5] in the local coordinates $[\xi_1, \xi_2]$ of each element. But each surface-field equation has at least one set of troublesome coefficients when a simple integration scheme will not work: the coefficients for elements touching

the computation point \mathbf{x} , due to the Green's function singularity at \mathbf{x} . The integral over the element containing \mathbf{x} is only defined in the Cauchy Principal Value sense - in the limit that \mathbf{x} comes in contact with the boundary, or as a small hemispherical deformation of the surface around the point \mathbf{x} becomes vanishingly small. Any integration scheme that does not first regularize the singularity cannot compute the limit accurately. The null-field and whole-field equations may also require special attention if the point \mathbf{x} is close to the boundary for the same reasons.

Another problem occurs in layered media. As we will see, at small horizontal ranges the modal representation of the Green's function can suffer from poor convergence to such a degree that it becomes impractical to compute. In a normal mode representation of the Green's function, this occurs whenever the computation point \mathbf{x} lies directly above or below the boundary element being integrated; \mathbf{x} need not be particularly close to the element. This poor convergence occurs equally for the null-, surface-, and whole-field equations. In the next section I present an indirect BIE method for troublesome integral coefficients of any kind.

3.5 Using Huygens' principle to evaluate troublesome integral coefficients indirectly

We have seen how Huygens' principle can test the numerical integral equation in a specially contrived problem. If most of the integral coefficients can be evaluated with certainty, leaving only a few troublesome coefficients unknown, perhaps we could reverse the test, using the known free-field solution to infer what the unknown troublesome coefficients should be. Proceeding as in Section (3.3), then, let us again insert the volume element for a perspective into the domain whose Green's function is that of the perspective. Once again there is no scattered field from the boundary, and we can compute the field at any point, for any number of sources, using only their Green's functions. Let the field at the m nodes of the n 'th boundary element due to a particular source configuration labelled f be $\mathbf{u}_m^{n,f}$ and $\mathbf{t}_m^{n,f}$ (a return from the global node numbering scheme in (3.6) to that used earlier in (3.5)); and let \mathbf{x} be a computation point for which the integral coefficients for the

\tilde{n} 'th boundary element cannot be straightforwardly computed due to singularity or poor convergence. Then the surface-field equation (3.5) gives three equations in the troublesome coefficients,

$$\mathcal{G}_{ij\tilde{m}}^{\tilde{n}}(\mathbf{x}) t_{j\tilde{m}}^{\tilde{n}f} - \mathcal{T}_{ij\tilde{m}}^{\tilde{n}}(\mathbf{x}) u_{j\tilde{m}}^{\tilde{n}f} = \mathbf{R}_i^f(\mathbf{x}), \quad i = 1..3, \quad (3.10)$$

where $\mathbf{R}_i^f(\mathbf{x})$ is expressed in terms of the boundary field and integral coefficients for all of the tractable boundary elements

$$\mathbf{R}_i^f(\mathbf{x}) = -u_i^{incf}(\mathbf{x}) - \mathcal{G}_{ijm}^n(\mathbf{x}) t_{jm}^{nf} + \mathcal{T}_{ijm}^n(\mathbf{x}) u_{jm}^{nf} + \zeta_{ij}(\mathbf{x}) N_{\tilde{m}}^n(\mathbf{x}) u_{j\tilde{m}}^{\tilde{n}f}. \quad (3.11)$$

$\mathbf{R}_i^f(\mathbf{x})$ is known because all of the terms on the right in can be computed without difficulty. The summation n ranges over all boundary elements excluding \tilde{n} , and $m = m(n)$ over the nodes on the each element. For the moment let us assume there is only one troublesome boundary element; hence, no summation over \tilde{n} in (3.10), with the summation \tilde{m} ranging over all nodes on just that element.

Equation (3.10) represents an inverse problem: given a particular solution to the boundary integral equation (u_{jm}^{nf} and t_{jm}^{nf}) plus the integral coefficients for tractable boundary elements $\mathcal{G}_{ijm}^n(\mathbf{x})$ and $\mathcal{T}_{ijm}^n(\mathbf{x})$, determine the integral coefficients $\mathcal{G}_{ij\tilde{m}}^{\tilde{n}}(\mathbf{x})$ and $\mathcal{T}_{ij\tilde{m}}^{\tilde{n}}(\mathbf{x})$ for the intractable boundary element. Choosing F different source configurations, we can construct a system of equations to solve this inverse problem; each source configuration giving three vector equations ($i=1..3$) in $2 \cdot i \cdot j \cdot \tilde{m} = 18\tilde{m}$ unknowns,

$$\begin{bmatrix} -u_{11}^{\tilde{n}1} & -u_{21}^{\tilde{n}1} & -u_{31}^{\tilde{n}1} & t_{11}^{\tilde{n}1} & t_{21}^{\tilde{n}1} & t_{31}^{\tilde{n}1} & -u_{12}^{\tilde{n}1} & -u_{22}^{\tilde{n}1} & -u_{32}^{\tilde{n}1} & t_{12}^{\tilde{n}1} & t_{22}^{\tilde{n}1} & t_{32}^{\tilde{n}1} & \cdots & t_{3\tilde{m}}^{\tilde{n}1} \\ -u_{11}^{\tilde{n}2} & -u_{21}^{\tilde{n}2} & -u_{31}^{\tilde{n}2} & t_{11}^{\tilde{n}2} & t_{21}^{\tilde{n}2} & t_{31}^{\tilde{n}2} & -u_{11}^{\tilde{n}2} & -u_{21}^{\tilde{n}2} & -u_{31}^{\tilde{n}2} & t_{11}^{\tilde{n}2} & t_{21}^{\tilde{n}2} & t_{13}^{\tilde{n}2} & \cdots & t_{3\tilde{m}}^{\tilde{n}2} \\ \vdots & \vdots & \vdots & \vdots & \vdots & \vdots & \vdots & \vdots & \vdots & \vdots & \vdots & \vdots & \ddots & \vdots \\ -u_{11}^{\tilde{n}F} & -u_{21}^{\tilde{n}F} & -u_{31}^{\tilde{n}F} & t_{11}^{\tilde{n}F} & t_{21}^{\tilde{n}F} & t_{31}^{\tilde{n}F} & -u_{11}^{\tilde{n}F} & -u_{21}^{\tilde{n}F} & -u_{31}^{\tilde{n}F} & t_{11}^{\tilde{n}F} & t_{21}^{\tilde{n}F} & t_{31}^{\tilde{n}F} & \cdots & t_{3\tilde{m}}^{\tilde{n}F} \end{bmatrix} \times \begin{bmatrix} \mathcal{T}_{i11}^{\tilde{n}} & \mathcal{T}_{i21}^{\tilde{n}} & \mathcal{T}_{i31}^{\tilde{n}} & \mathcal{G}_{i11}^{\tilde{n}} & \mathcal{G}_{i21}^{\tilde{n}} & \mathcal{G}_{i31}^{\tilde{n}} & \cdots & \mathcal{G}_{i3\tilde{m}}^{\tilde{n}} \end{bmatrix}^T = \begin{bmatrix} \mathbf{R}_i^1 \\ \mathbf{R}_i^2 \\ \vdots \\ \mathbf{R}_i^F \end{bmatrix} \quad (3.12)$$

At least $6\tilde{m}$ different source configurations are required to determine the integral coefficients for one boundary element. My own BIE program, which uses a nine-node boundary element scheme, needs at least $6\tilde{m} = 6 \times 9 = 54$ different source configurations for each troublesome boundary element. Notice that the free-field matrix has $6\tilde{m}$ columns rather than $18\tilde{m}$, because there are three different vectors for the right-hand side $i=1..3$ giving three corresponding solution vectors. The *free-field matrix* on the left in (3.12) must only be decomposed once to compute all three sets of unknown vectors.

3.5.1 Several troublesome elements

When several boundary elements are troublesome for the same computation point, the system of unknowns and equations can be extended to include a set of unknown coefficients for each of them: simply let the repeated index \tilde{n} imply summation over all troublesome elements in (3.10), and add a proportional number of source configurations to determine all of the intractable coefficients simultaneously. It may look as though we could carry on this way to indirectly compute all of the integral coefficients for a boundary integral equation without ever integrating numerically. I tried this using scalar integral equations for fluid media, but found that the likelihood of an unstable free-field matrix increases as the number of troublesome elements increases, so much so that it was irreparably unstable whenever an inversion for all coefficients was attempted. As mentioned in Chapter 1, Niku and Brebbia [94] proposed a total inversion scheme for a generic BIE method, and they suspected that instability would be a problem, much as I found. The indirect method apparently works best when only a few troublesome boundary elements are encountered.

In elastic wave scattering I find that as many as six troublesome elements can be handled in one equation with confidence, but there is no well-defined limit. To minimize the number of troublesome elements due to singularities, it is best to choose surface-field computation points away from the perimeter of the boundary elements so they are in contact with just one element. This is why I included the flexibility to locate computation points anywhere on the surface in Section (3.2.1), rather than always using the element nodes as routinely done in the BIE method.

3.5.2 The particular solutions

Following Niku and Brebbia [94], let us call the free fields \mathbf{u}_m^{nf} , \mathbf{t}_m^{nf} and u_i^{incf} for $f = 1..F$ the *particular solutions*. It is evident that many particular solutions will be required to compute troublesome integral coefficients—at least six configurations for each node on each troublesome boundary element. In my own program, each particular solution is due to a single point source having a different location and excitation. There is no rule for source placement, but I have achieved best results when the sources are evenly distributed in both the interior and exterior domains when possible. There is also no explicit rule regarding source excitation. For homogeneous perspectives I have had the best results using a point forces having random orientation and complex excitation. More will be said about the location and excitation of the particular solutions for layered media in Chapter 7.

It is advisable to use more particular solutions than strictly required, for it is possible to unknowingly specify particular solutions that leave the free-field matrix ill-conditioned. Once again the over determined matrix system can be solved using least-squares. The troublesome coefficients should always be verified using the consistency test in Section (3.3), before they are used in the BIE method to identify any problems.

3.5.3 The importance of the residue term

It may appear that the coefficient ζ_{ij} for the surface field equation, whose operation has so far been treated as simple scalar multiplication⁵, could also be included as part of the unknown integral coefficients in (3.10), by rolling it in with the unknown $T_{ijm}^{\tilde{\sim}}$ rather than with R_i^f as in (3.11). This would be an advantage when the computation point \mathbf{x} is located at an edge or corner of the inclusion boundary where $\zeta_{ij}(\mathbf{x})$ is not known. But consistency tests with coefficients computed with $\zeta_{ij}(\mathbf{x})$ rolled into $T_{ijm}^{\tilde{\sim}}$ failed when \mathbf{x} lay in a solid. The reason for failure is not known. I would venture that important information is provided by explicitly setting $\zeta_{ij}(\mathbf{x}) = \delta_{ij}/2$ in (3.11), for it informs the inversion method that \mathbf{x} lies on the boundary and that the boundary is smooth there, whereas rolling it into

⁵See Section (2.4).

\tilde{T}_{ijm}^n reduces (3.10) for \mathbf{x} on the boundary to the same form as that for \mathbf{x} in the interior, thereby erasing all distinction between the surface- and null-field equations so far as the inversion is concerned.

3.5.4 Nonunique indirect coefficients

Inverse problems are notorious for having nonunique solutions [24], so it is no surprise that the free-field matrix determining the troublesome coefficients may be ill conditioned. In that case, a practicable solution can still be computed using singular value decomposition, which allows us to suppress the non-unique unstable part of the solution (the null-field of the free-field matrix) by zeroing the smallest singular values in the decomposition [100].

Nonuniqueness is easily demonstrated in the case of fluid media. Recall from (2.8) that the stress in fluid media is directly proportional to the pressure times the boundary normal vector, $t_{jm}^{nf} = -p_m^{nf} n_j$. This makes three consecutive traction columns in the free-field matrix linearly dependent for each node immersed in a fluid, which in turn makes the free-field matrix singular and the solution vector nonunique. Indeed, the troublesome coefficients cannot be computed by matrix inversion unless all groups of three offending columns are grouped into one, or unless singular value decomposition (SVD) is used.

The inferred coefficients are nonunique in another way. Imagine deforming the shape of a troublesome element slightly by stretching it outwards from the original inclusion while keeping its perimeter and the rest of the boundary unchanged. (If the element has a surface-field computation point on it, then the deformed element must still pass smoothly through it.) The indirect method takes no account of such a deformation, neither in the free-field matrix (3.12) or the tractable integration term (3.11), so the same coefficients would be inferred despite the deformation. In a direct integration scheme, however, the deformation would alter the coefficients for the element since they depend explicitly on its shape.

The solution may be nonunique in other ways, but the question will not be pursued further here. In practice we need coefficients that work in the boundary integral equation. Whether the method yields the same coefficients as direct integration, when that is possible,

is a secondary question.

3.6 Using Huygens' principle to test the entire BIE method: the free-field test

An ingenious comprehensive test of the BIE method was proposed by Schenck for the Neumann problem for acoustics [106] [73]. We can apply it to elastic scattering as well in the following way.

In the consistency test of Section (3.3), a subdomain of the original scattering problem was embedded into a test problem in which it produced no scattered field so the field at the boundary nodes for a given source configuration could be computed using only the Green's function for the sources. Rather than assigning the complete field to each node on the boundary to test the equation, let us now assign only part of the boundary field to each node using the boundary condition equations—either the displacement or traction—and ask the BIE method to compute the unassigned part. How well the BIE method reproduces the unassigned part of the field shows how well the method can be expected to perform in a particular application. The total coefficient matrix for the free-field test for one perspective would be

$$\begin{bmatrix} BIE \\ BC \end{bmatrix} \begin{bmatrix} \mathbf{b} \end{bmatrix} = \begin{bmatrix} \mathcal{U}^{inc} \\ \mathbf{C} \end{bmatrix}, \quad (3.13)$$

with matrix partitions defined as in (3.9), and \mathbf{C} holding the assigned free-field variables. The *BIE* partition is the same as the one used for that perspective in the final scattering problem, so the test includes the boundary element configuration, frequency and media of the scattering problem at hand. It also exercises all of the routines needed to numerically compute the boundary field. Active boundary conditions are rarely used in geoacoustics, but it is always advisable to make provisions for them, if only to perform this conclusive test.

We can also test the next step in the BIE method, by computing the displacement at any point \mathbf{x} in the interior domain to verify the accuracy of the whole field equation (3.7). Usually the results of the second step are more accurate than the first because the

whole-field equation tends to average over numerical errors in the boundary field.

3.7 Testing the boundary field: the null-field test

Once the boundary field for an actual scattering problem has been computed, it can be tested using the null-field equation, simply by checking that the newly computed boundary field gives the null result at points \mathbf{x} in the exterior domain of the perspective [114][73]. A boundary field that does not satisfy the null-field equation this way must be in error, possibly because some integral equation coefficients were inaccurately computed, the field was inadequately sampled by nodes on the boundaries, or the total coefficient matrix suffered from instability. Exact zero is unlikely because numerical computations are always subject to some degree of error, so we need a measure against which the integral must appear negligibly small. One measure could be taken from the incident field, $|\mathbf{u}^{inc}(\mathbf{x})|$,⁶ provided \mathbf{x} was not close to a null in the incident displacement field. A better measure is to use the maximum displacement on the boundary $\max |\mathbf{u}_m|$, which is independent of \mathbf{x} .

3.8 Measuring error in numerical tests

When verifying the BIE method in a test, whether in the free-field test or a benchmark scattering problem solved by different means, it is difficult to measure the error in the field using a single quantity. We could measure error in the displacement field relatively as

$$\text{err}_1(\mathbf{x}) = 100\% \times \frac{|\mathbf{u}_{\text{numerical}}(\mathbf{x}) - \mathbf{u}_{\text{exact}}(\mathbf{x})|}{\max |\mathbf{u}_{\text{exact}}|}, \quad (3.14)$$

doing the same for traction, but this can make the error look deceptively small when there are large $|\mathbf{u}_{\text{exact}}|$ at just relatively few points. Nevertheless, it often works well for low frequency scattering problems, when the wavelength is larger than the dimensions of the scattering object, because the magnitude of the exact field is not likely to vary dramatically over its boundary. One alternative is to use a weighted average in place of the maximum norm

$$\text{err}_2(\mathbf{x}) = 100\% \times \frac{|\mathbf{u}_{\text{numerical}}(\mathbf{x}) - \mathbf{u}_{\text{exact}}(\mathbf{x})|}{\text{avg} |\mathbf{u}_{\text{exact}}|}, \quad (3.15)$$

⁶ $|\mathbf{u}| = \sqrt{u_k u_k^*}$, where $*$ denotes complex conjugate.

but this can make the error look deceptively large when the field over part of the boundary is identically zero due to the boundary conditions. If part of the boundary to a solid inclusion is impenetrably rigid, for example, the average of $|\mathbf{u}_{\text{exact}}|$ over the rigid part will be zero, reducing the overall average considerably, amplifying err_2 . A third method is to use the exact field at the point itself for the norm

$$\text{err}_3(\mathbf{x}) = 100\% \times \frac{|\mathbf{u}_{\text{numerical}}(\mathbf{x}) - \mathbf{u}_{\text{exact}}(\mathbf{x})|}{|\mathbf{u}_{\text{exact}}(\mathbf{x})|}, \quad (3.16)$$

but this obviously suffers when the field at \mathbf{x} is very small, for it ranks the errors over parts of the boundary that contribute very little to the boundary integral equal (where \mathbf{u} is small) with those that contribute significantly.

As I will only be considering low to mid frequency scattering problems, I will report errors in the boundary field using (3.14), and include the ratio

$$\text{err}_2(\mathbf{x}) / \text{err}_1(\mathbf{x}) = \max |\mathbf{u}_{\text{exact}}| / \text{avg} |\mathbf{u}_{\text{exact}}|, \quad (3.17)$$

which converts err_1 to err_2 . For points off all boundaries, however, I will use $\text{err}_3(\mathbf{x})$ because $|\mathbf{u}_{\text{exact}}(\mathbf{x})|$ removes the effect of decay with distance.

3.9 Example: Plane wave scattering by spheres

To demonstrate the indirect BIE method, I will apply it to the scattering of plane waves by rigid, fluid and solid spheres embedded in unbounded homogeneous domains for which analytic solutions, by separation of variables, are available.⁷ The following variables

⁷The analytic solutions are of course evaluated numerically, and this is no easy task. Their numerical representations often cannot be computed for all ranges, directly on the boundary of the scattering sphere for instance, because terms in their series representation or the series itself becomes intractable. I was unable to compute the field on the boundary of the scattering spheres, for example, so the comparisons of the boundary field could not be made.

are used throughout this section:

- a = radius of spherical boundary,
- $\alpha_0, \beta_0, \rho_0$ = elastic parameters outside sphere,
- $\alpha_1, \beta_1, \rho_1$ = elastic parameters inside sphere,
- $k_{\alpha 0}$ = P wavenumber outside sphere = $2\pi f/\alpha_0$,
- $\lambda_{\alpha 0}$ = P wavelength outside sphere = $2\pi/k_{\alpha 0}$,
- ka = $k_{\alpha 0} a$,
- ϵ = close neighborhood of computation point
within which a boundary element is deemed troublesome,
- \mathbf{n} = boundary unit normal vector,
- $\mathbf{v}_1, \mathbf{v}_2, \mathbf{n}$ = three mutually perpendicular unit vectors.

There are at most two perspectives for the boundary integral equations: perspective 0 is the unbounded homogeneous domain outside the scattering sphere, and perspective 1 the finite domain inside, when the sphere is penetrable.

3.9.1 Plane wave scattering from a rigid sphere in a fluid

The BIE method will be verified in two ways for an unbounded fluid domain; using 1) the free-field test, and 2) the analytic solution to the scattering of a plane wave by a rigid sphere immersed in a fluid [91]. The boundary elements and nodes comprising the sphere are shown in Fig. (3.2). A total of 366 particular solutions were used to determine troublesome integral coefficients (150 randomly distributed inside, 216 on rectangular grid length $6a$ on a side, with no source closer than $\epsilon = 0.2a$ to the boundary), each being generated by a point force with a randomly assigned direction. One set of troublesome coefficients arose for each boundary element in contact with the computation point generating each surface-field equation due to singularity. Details of the BIE set up are tabulated in Table (3.1).

Free-field test

Recall that the spherical inclusion is not rigid in the free-field test, but it is filled with the same medium as the host domain to preclude scattering. Nevertheless, the same

Rigid Sphere

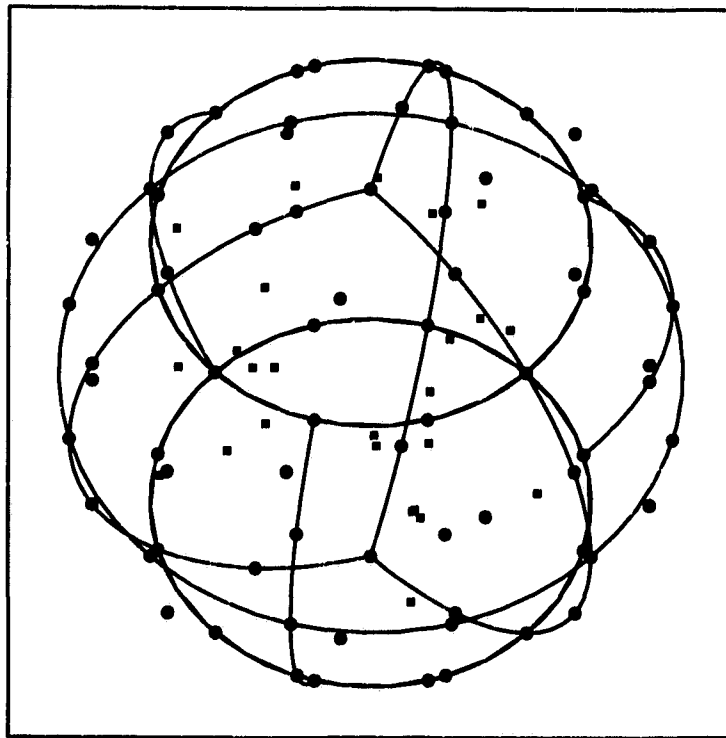
| | |
|------------------------|----------|
| No. boundary elements: | 18 |
| No. boundary nodes: | 74 |
| Avg. node spacing: | $0.412a$ |
| Symmetry assumed: | None |

Equations for Fluid domain: Perspective 0

| | |
|----------------------------------|--|
| No. surface computation points: | 74 at boundary element nodes |
| No. interior computation points: | 25 scattered randomly inside sphere |
| Straightforward integration: | 7 by 7 Gaussian quadrature scheme for each boundary element |
| Close neighborhood of elements: | $\epsilon = 0.20a$ |
| No. particular solutions: | 366 |
| Boundary Conditions: | $\mathbf{u} \cdot \mathbf{n} = 0; \quad \mathbf{t}_{ } = (\mathbf{n} \times \mathbf{t}) \times \mathbf{n} = \mathbf{0}$ |

Table 3.1: Setup for scattering from a rigid sphere. There is only one penetrable domain the unbounded homogeneous fluid region outside the sphere and therefore only one perspective for the boundary integral equations perspective 0.

Boundary Element Plot



Oblique projection

Figure 3.2: The boundary elements for the rigid sphere. There are 18 spherical boundary elements requiring 74 nodes, which are marked as circular dots. The nodes were also used as surface field computation points. 25 randomly placed interior points for null-field equations are shown as small squares.

| ka | Avg. | Max. | err_2 / err_1 |
|------|-----------------------|-----------------------|-----------------|
| | Error in \mathbf{t} | Error in \mathbf{t} | |
| | err_1 % | err_1 % | |
| 1.0 | 0.80 | 2.10 | 1.29 |
| 2.0 | 0.74 | 2.45 | 1.29 |
| 4.0 | 1.06 | 4.10 | 1.29 |

Table 3.2: Free-field test summary for rigid sphere boundary. The errors are between the free-field (exact) traction and the BIE computed traction at the boundary element nodes in the free-field test.

boundary integral coefficients are used for both the test and the final scattering problem because the perspective of the BIE equations are the same. In these free-field tests, the incident displacement was assigned to the boundary nodes using the boundary condition equation (2.38), and the BIE method was used to compute the unassigned boundary traction field \mathbf{t}_m , which should be the same as the incident traction field \mathbf{t}^{inc} . The free-field for the test is that of an explosive point source inside the sphere at $(x, y, z) = (0.1a, 0.1a, 0.2a)$, hence no symmetry was assumed. The error in the boundary traction vector at the nodes on the boundary is reported for three different values of ka in Table (3.2). The error increases with ka , as the wavelength becomes smaller relative to the boundary element size, as we would expect.

Plane wave scattering from rigid sphere

Scattering from a rigid sphere can be solved using the same boundary integral equations used in the free-field test, but the boundary conditions are now $\mathbf{u} \cdot \mathbf{n} = 0$, and the incident field is a plane P wave with direction $\hat{\mathbf{k}} = (0, 0, 1)$. Fig. (3.3) shows good agreement at lower frequencies ($kr = 1.0$ and 2.0) between the analytic and BIE scattered fields on a circle of points in the xz -plane, far from the center of the sphere. The results agree well with those of Stenzel (1938) [28, fig. 6.2.6] The BIE method errs at higher frequencies when the wavelength $\lambda_{\alpha 0}$ becomes comparable to the dimensions Δl of the elements; $\lambda_{\alpha 0} = 1.88 \Delta l_{avg}$ for $kr = 4.0$. More boundary elements are required as the frequency increases.

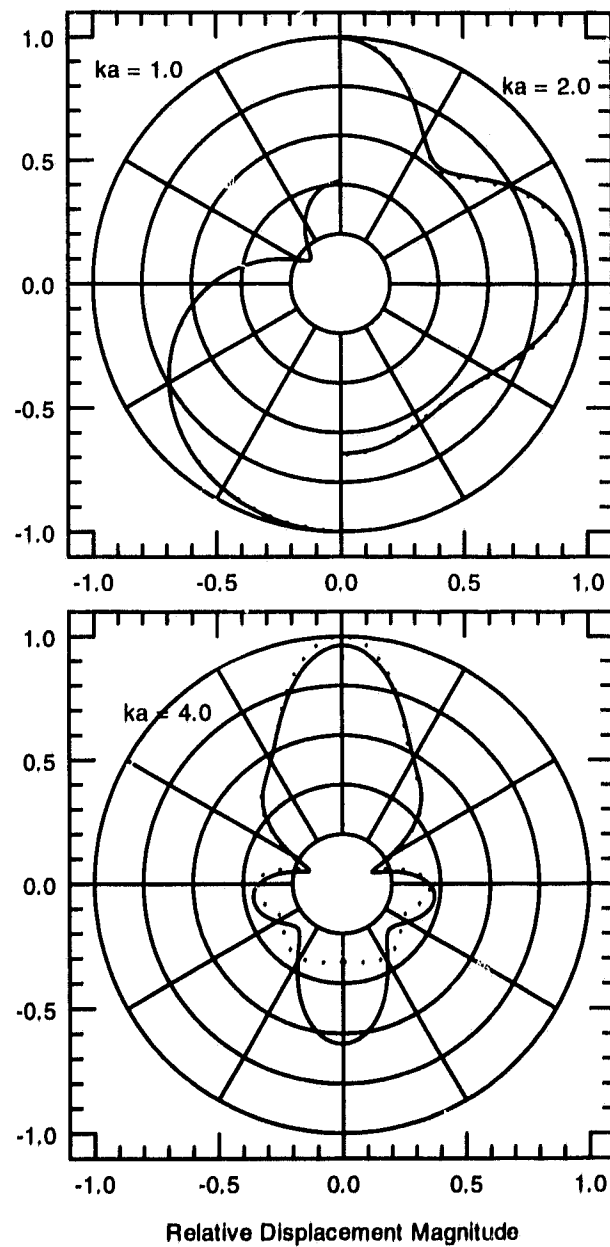


Figure 3.3: Farfield polar plot of the scattered displacement field for a plane wave striking a rigid sphere, computed using the BIE method (solid line), and the analytic separation of variables (dotted line). The incident plane wave is travelling upwards from below. The large errors in $ka = 4.0$ are due to an inadequate number of boundary elements at the smaller wavelength.

3.9.2 Fluid sphere in a fluid

Here the BIE method is verified for the scattering of a plane waves by a penetrable fluid sphere immersed in an unbounded homogeneous fluid domain. The fluid has an unrealistic phase speed ($\alpha = 6000$ m/s) to correspond as much as possible to the solid sphere considered later. The boundary elements and nodes comprising the sphere are shown in Fig.(3.4), and the numerical parameters are tabulated in Table (3.3). In this case bilateral symmetry about the plane $y = 0$ was used to reduce the number of unknowns by roughly one half. The boundary and continuity conditions are the slip conditions for penetrable fluid boundaries from Section (2.3.2). Fig. (3.5) shows good agreement in the far-field polar plot of the scattered field using an analytic separation of variables method and the BIE method.⁸ $\lambda = 2.17\Delta l_{\text{avg}}$ and $1.63 \Delta l_{\text{avg}}$ for perspectives 0 and 1, respectively, when $kr = 4.0$.

3.9.3 Solid sphere in a solid

Here the BIE method is applied to scattering of a plane waves by a penetrable solid sphere immersed in an unbounded homogeneous solid domain. The boundary elements and nodes comprising the sphere are the same as in Fig.(3.4); the particulars are tabulated in Table (3.4). Bilateral symmetry about the plane $y = 0$ was used again to reduce the number of unknowns. The boundary and continuity conditions are those for penetrable solid boundaries in welded contact from Section (2.3.1). Fig. (3.6) shows good agreement in the far-field polar plot of the scattered field using an analytic separation of variables method and the BIE method. These results duplicate those of Korneev and Johnson [75]. Fig. (3.7) shows a grey-scale plot of the total field in the exterior domain. The field is dark in the interior of the sphere because the exterior perspective was used at every point in plot; points inside the sphere being null-field points where the boundary integral must give zero. The boundary field therefore passes the null-field test of Section (3.7). To view the field inside the sphere we must reverse the perspective as shown in Fig. (3.8).

⁸I am indebted to Dr. Trevor Dawson who provided the main subroutines for evaluating the scattered field using a separation of variables method [75] for the penetrable fluid and solid spheres.

Fluid Sphere

| | |
|------------------------|----------------------------------|
| No. boundary elements: | 24 |
| No. boundary nodes: | 98 |
| Avg. node spacing: | $0.358a$ |
| Symmetry assumed: | Bilateral Symm. in $y = 0$ plane |

Unbounded fluid domain: Perspective 0

| | |
|----------------------------------|---|
| α_0 | 6000.0 m/s |
| ρ_0 | 2700.0 kg/m ³ |
| No. surface computation points: | 60; 5 points on 12 elements with $y > 0$ |
| No. interior computation points: | 0 |
| Straightforward integration: | 7 by 7 Gaussian quadrature scheme for each boundary element |
| Close neighborhood of elements | $\epsilon = 0.0625a$ |
| No. particular solutions: | 204 interior; 150 exterior |
| Boundary Conditions: | $\mathbf{t}_{ } = (\mathbf{n} \times \mathbf{t}) \times \mathbf{n} = \mathbf{0}$ |

Spherical fluid domain: Perspective 1

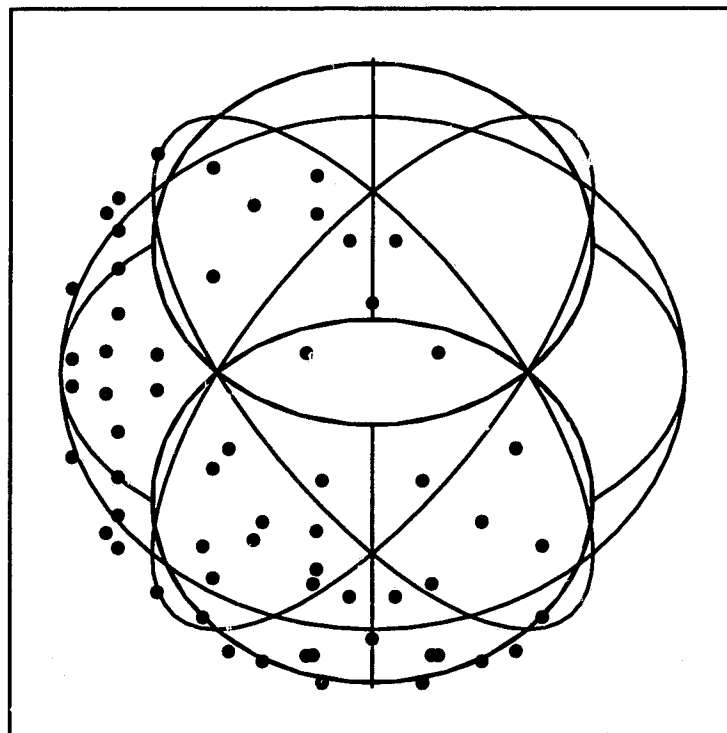
| | |
|----------------------------------|---|
| α_1 | 4500.0 m/s |
| ρ_1 | 2300.0 kg/m ³ |
| No. surface computation points: | 60; 5 points on 12 elements with $y > 0$ |
| No. interior computation points: | 0 |
| Straightforward integration: | 7 by 7 Gaussian quadrature scheme for each boundary element |
| Close neighborhood of elements: | $\epsilon = 0.0625a$ |
| No. particular solutions: | 150 interior; 204 exterior |
| Boundary Conditions: | $\mathbf{t}_{ } = (\mathbf{n} \times \mathbf{t}) \times \mathbf{n} = \mathbf{0}$ |

Coupling Perspective 0 and 1

| | |
|----------------------|---|
| Coupling Conditions: | $\mathbf{u}^0 \cdot \mathbf{n}^0 = -\mathbf{u}^1 \cdot \mathbf{n}^1; \mathbf{t}^0 \cdot \mathbf{n}^0 = \mathbf{t}^1 \cdot \mathbf{n}^1$ |
|----------------------|---|

Table 3.3: Setup for scattering from a fluid sphere. There are two penetrable domains the exterior and interior of the fluid sphere and therefore two perspectives for the boundary integral equations perspective 0 and 1 respectively.

Boundary Element Plot



Oblique projection

Figure 3.4: The boundary elements for the penetrable fluid and solid spheres. There are 24 spherical boundary elements requiring 98 nodes (not shown). A total of 64 surface-field computation points were used for each perspective; 5 points for each element on just one half of the sphere as shown by the dots. Full coverage of the surface was unnecessary because bilateral symmetry was assumed. No null-field points were used.

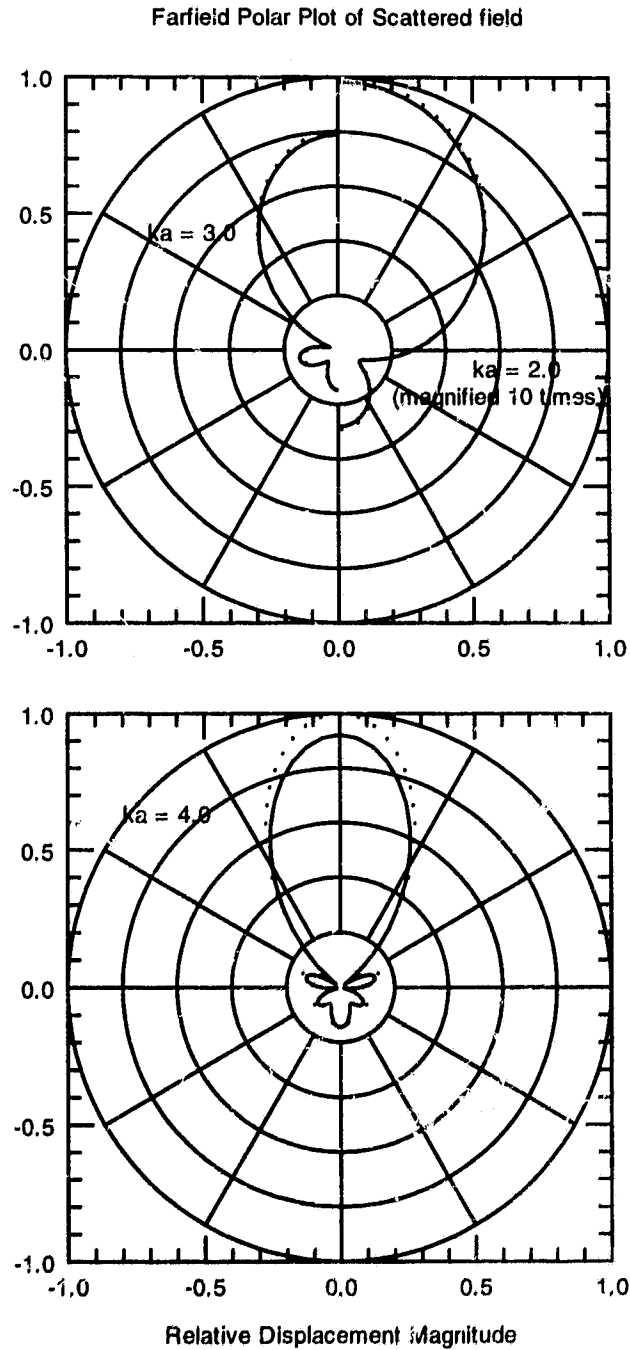


Figure 3.5: Farfield polar plot of the scattered displacement field for a plane wave striking a penetrable fluid sphere, computed using the BIE method (solid line) and the analytic separation of variables (dotted line). The incident plane wave is travelling upwards from below. The errors in $ka = 4.0$ are due to an inadequate number of boundary elements at the smaller wavelength.

Solid Sphere

| | |
|------------------------|----------------------------------|
| No. boundary elements: | 24 |
| No. boundary nodes: | 98 |
| Avg. node spacing: | $0.358a$ |
| Symmetry assumed: | Bilateral Symm. in $y = 0$ plane |

Unbounded solid domain: Perspective 0

| | |
|----------------------------------|--|
| α_0 | 6000.0 m/s |
| β_0 | 3500.0 m/s |
| ρ_0 | 2700.0 kg/m ³ |
| No. surface computation points: | 60; b points on 12 elements with $y > 0$ |
| No. interior computation points: | 0 |
| Straightforward integration: | 7 by 7 Gaussian quadrature scheme for each boundary element |
| Close neighborhood of elements | $\epsilon = 0.0625a$ |
| No. particular solutions: | 204 interior; 150 exterior |
| Boundary Conditions: | None |

Spherical solid domain: Perspective 1

| | |
|----------------------------------|--|
| α_1 | 4500.0 m/s |
| β_1 | 2600.0 m/s |
| ρ_1 | 2300.0 kg/m ³ |
| No. surface computation points: | 60; 5 points on 12 elements with $y > 0$ |
| No. interior computation points: | 0 |
| Straightforward integration: | 7 by 7 Gaussian quadrature scheme for each boundary element |
| Close neighborhood of elements: | $\epsilon = 0.0625a$ |
| No. particular solutions: | 150 interior; 204 exterior |
| Boundary Conditions: | None |

Coupling Perspective 0 and 1

| | |
|----------------------|--|
| Coupling Conditions: | $\mathbf{u}^0 = \mathbf{u}^1; \mathbf{t}^0 = \mathbf{t}^1$ |
|----------------------|--|

Table 3.4: Setup for plane wave scattering from a solid sphere. There are two penetrable domains, the exterior and interior of the solid sphere, and therefore two perspectives for the boundary integral equations, perspective 0 and 1 respectively.

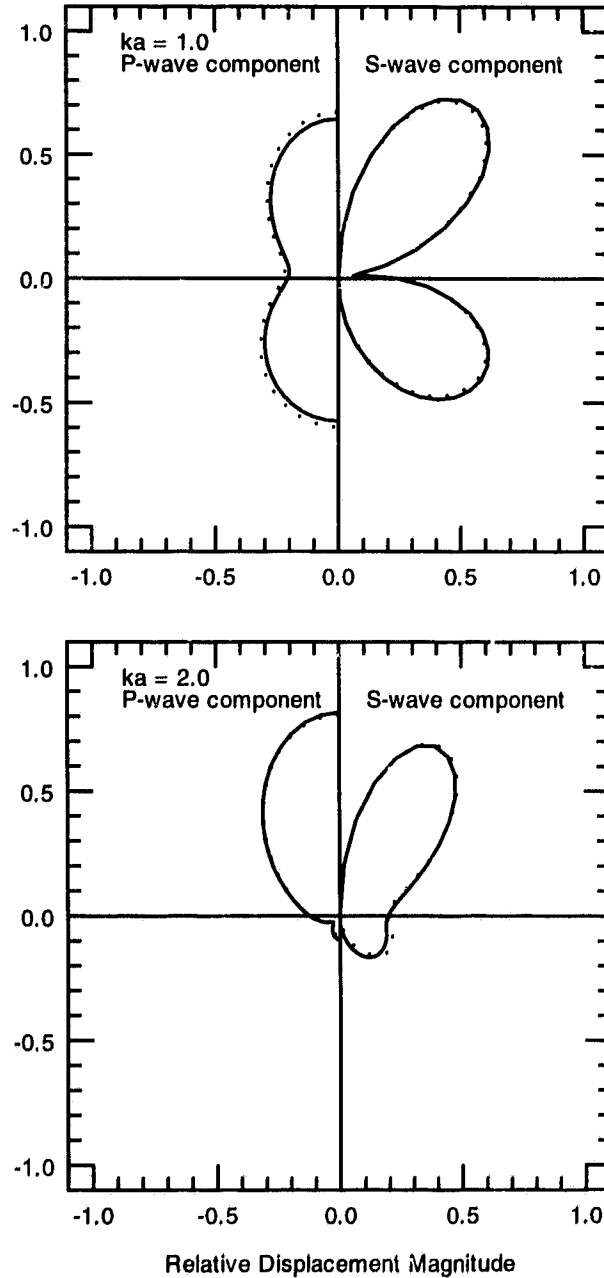


Figure 3.6: Farfield polar plot of the scattered displacement field for a plane wave striking a penetrable solid sphere, computed using the BIE method (solid line) and the analytic separation of variables (dotted line). The field has been separated into its radial u_r and angular u_θ components, which separates the field into its compressional (P) and shear (S) components, respectively. The incident plane wave is travelling upwards from below.

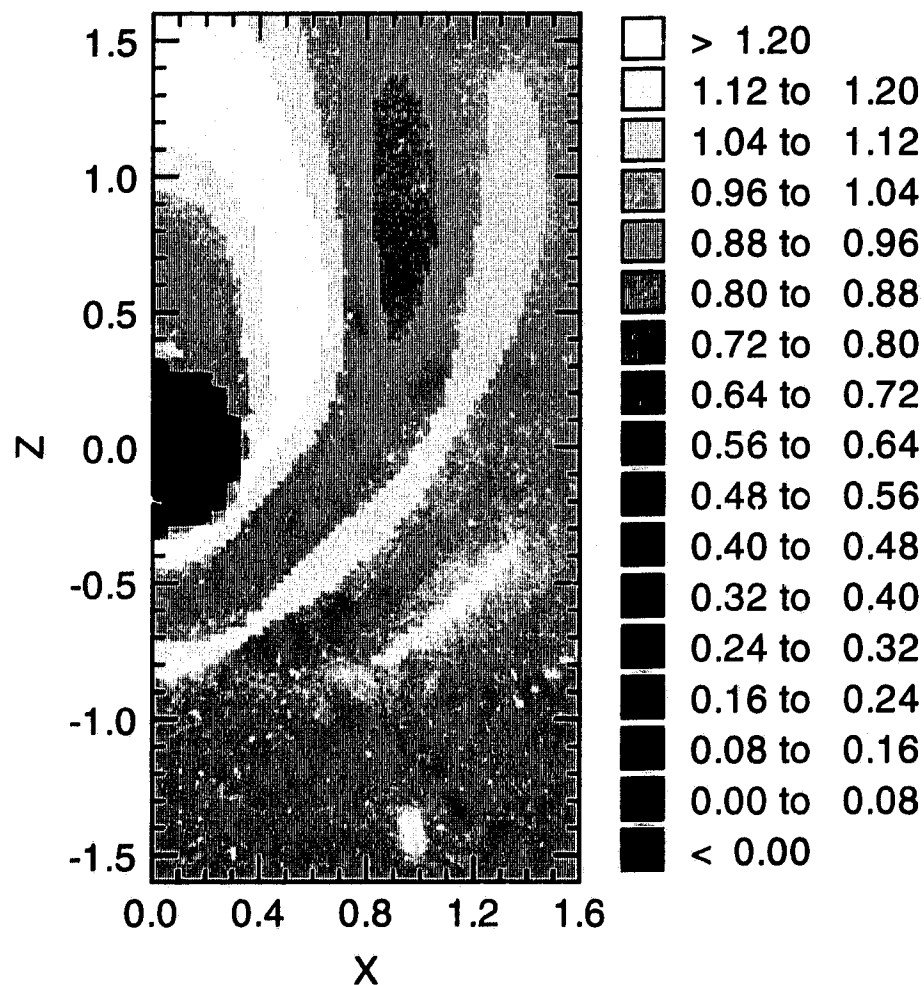


Figure 3.7: Plane wave scattering from a penetrable solid sphere. Shown is the magnitude of the total displacement field (incident plus scattered) when $ka = 2.0$. The incident plane wave is travelling upwards from below, with unit displacement amplitude. The interior of the sphere is dark because exterior perspective 0 was used at all points, giving the whole-field result at points outside the sphere, but the null-field result inside. The length scales are in units of wavelength.

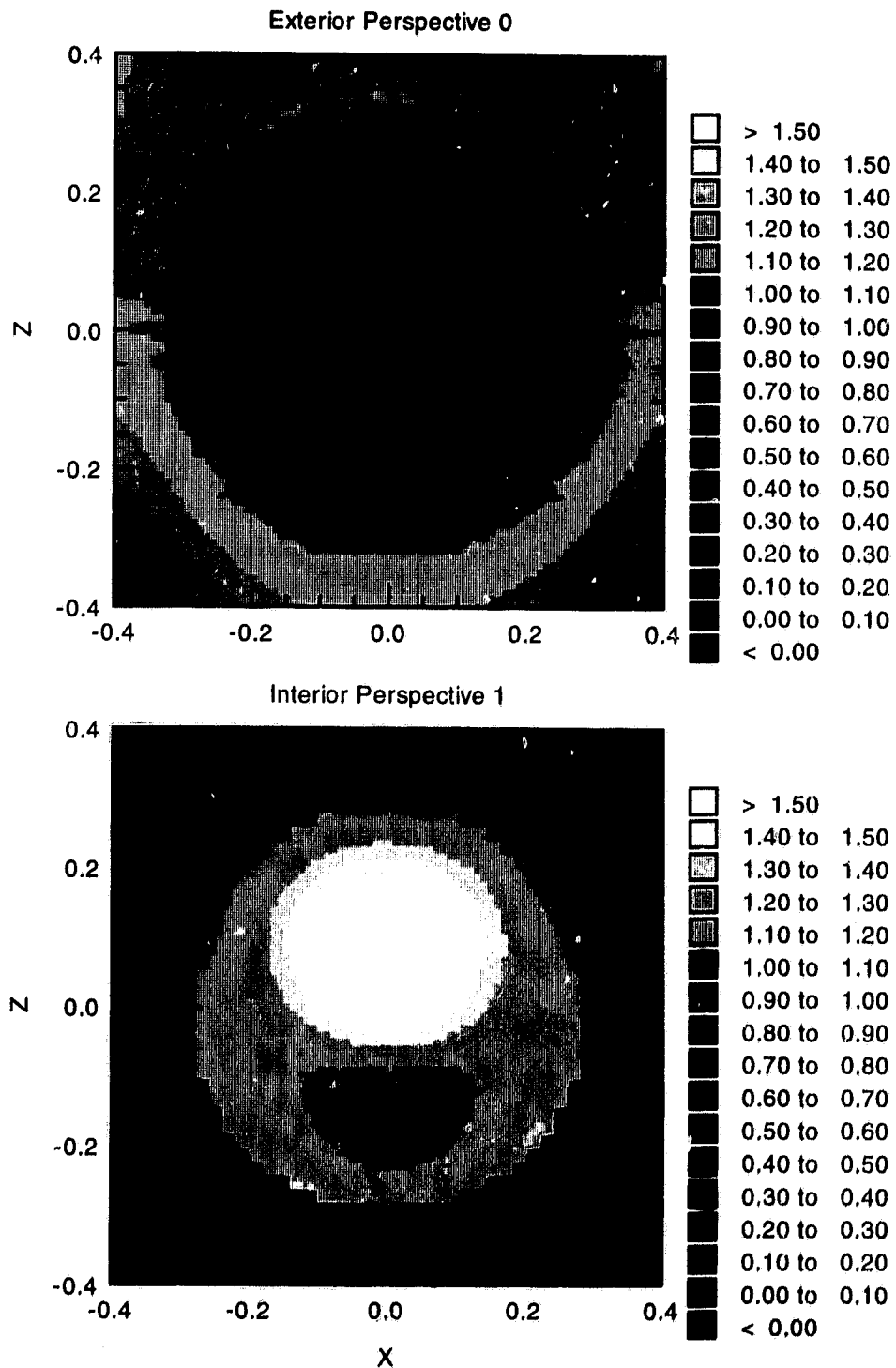


Figure 3.8: To view the field inside the penetrable solid sphere requires a change to the interior perspective 1 for the whole-field equation. The magnitude of the total displacement field is plotted here for both perspectives. The incident plane wave is travelling upwards from below with unit displacement amplitude. The length scales are in units of wavelength.

Chapter 4

The field from a point source in layered media

The BIE method requires a Green's function for each perspective in the scattering problem. The Green's function for an unbounded homogeneous medium can be written in closed form and is easily computed, whereas the Green's function for layered media must be written in terms of integral transforms that are much more difficult to evaluate. The numerical methods for layered media have improved considerably since Thomson [124] and Haskell [56] first formulated their propagator matrix approach, but the essentials remain the same: Fourier-Bessel integral transforms separate the vertical and horizontal dependence of the field reducing the problem to two independent boundary value problems in the vertical dimension alone; one for coupled shear and compressional wave motion (P-SV) and another for strictly shear (SH). These are solved numerically using matrix methods.

In this chapter I review the matrix method for layered media and make a few contributions of my own. In particular, using a numerically stable *scattering matrix* method, I show how the wave field can be illustrated using a schematic "ladder" diagram like the diagrams engineers might use to analyze linear systems, which is helpful for illustrating the operation of matrix methods for layered media. I rely heavily on Kennett's monograph on seismic waves [71] throughout this chapter, following his method and notation as much as possible, and adding results for fluid layers as required. The extension from an integral

transform to a normal mode representation of the Green's function is taken up in the next chapter. It should be emphasized that here we are concerned with computing the Green's function in the absence of scattering objects. We shall return to scattering in layered media using the BIE method in Chapter 7.

4.1 The two-point boundary value problem

Using a cylindrical polar coordinate system (r, ϕ, z) , in which the z -axis points vertically downwards, the displacement field, the equation of motion (2.14), and Hooke's law (2.2) become

$$\mathbf{u}(r, \phi, z, t) = u_r(r, \phi, z, t) \hat{\mathbf{e}}_r + u_\phi(r, \phi, z, t) \hat{\mathbf{e}}_\phi + u_z(r, \phi, z, t) \hat{\mathbf{e}}_z, \quad (4.1)$$

$$\begin{aligned} \rho \partial_{tt} u_r &= \partial_z \tau_{rz} + \partial_r \tau_{rr} + r^{-1} \partial_\phi \tau_{r\phi} + r^{-1} (\tau_{rr} - \tau_{\phi\phi}) + \rho f_r \\ \rho \partial_{tt} u_\phi &= \partial_z \tau_{\phi z} + \partial_r \tau_{r\phi} + r^{-1} \partial_\phi \tau_{\phi\phi} + 2r^{-1} \tau_{r\phi} + \rho f_\phi \\ \rho \partial_{tt} u_z &= \partial_z \tau_{zz} + \partial_r \tau_{rz} + r^{-1} \partial_\phi \tau_{\phi z} + r^{-1} \tau_{rz} + \rho f_z \end{aligned} \quad (4.2)$$

$$\begin{aligned} \tau_{rr} &= (\lambda + 2\mu) \partial_r u_r + \lambda \{ \partial_z u_z + r^{-1} (\partial_\phi u_\phi + u_r) \}, \\ \tau_{\phi\phi} &= (\lambda + 2\mu) r^{-1} (\partial_\phi u_\phi + u_r) + \lambda (\partial_z u_z + \partial_r u_r), \\ \tau_{zz} &= (\lambda + 2\mu) \partial_z u_z + \lambda \{ \partial_r u_r + r^{-1} (\partial_\phi u_\phi + u_r) \}, \\ \tau_{rz} &= \mu (\partial_z u_r + \partial_r u_z), \\ \tau_{\phi z} &= \mu (r^{-1} \partial_\phi u_z + \partial_z u_\phi), \\ \tau_{r\phi} &= \mu (\partial_r u_\phi + r^{-1} \partial_\phi u_r - r^{-1} u_\phi). \end{aligned} \quad (4.3)$$

$\hat{\mathbf{e}}_r, \hat{\mathbf{e}}_\phi$ and $\hat{\mathbf{e}}_z$ are the unit vectors of the coordinate system, and $\mathbf{f} = [f_r, f_\phi, f_z]^T$ is the body force. Since the displacement and the traction must be continuous across an interface between layers, we might expect that \mathbf{u} , and traction vector acting on a horizontal surface element

$$\mathbf{t}(r, \phi, z, t) = \tau_{rz}(r, \phi, z, t) \hat{\mathbf{e}}_r + \tau_{\phi z}(r, \phi, z, t) \hat{\mathbf{e}}_\phi + \tau_{zz}(r, \phi, z, t) \hat{\mathbf{e}}_z, \quad (4.4)$$

should play an important role, whereas the remaining three elements of stress, $\tau_{rr}, \tau_{\phi\phi}$ and $\tau_{r\phi}$ might be eliminated. In fact, it can be shown [35] that (4.2) and (4.3) reduce to two

independent sets of equations

$$\partial_z \begin{bmatrix} u_z \\ u_V \\ \tau_{zz} \\ \tau_{Vz} \end{bmatrix} = \begin{bmatrix} 0 & -\lambda/\lambda_* & 1/\lambda_* & 0 \\ -\Delta_h & 0 & 0 & 1/\mu \\ \rho\partial_{tt} & 0 & 0 & -1 \\ 0 & \rho(\partial_{tt} - \nu^2\Delta_h) & -(\lambda/\lambda_*)\Delta_h & 0 \end{bmatrix} \begin{bmatrix} u_z \\ u_V \\ \tau_{zz} \\ \tau_{Vz} \end{bmatrix} - \rho \begin{bmatrix} 0 \\ 0 \\ f_z \\ f_V \end{bmatrix}, \quad (4.5)$$

and

$$\partial_z \begin{bmatrix} u_H \\ \tau_{Hz} \end{bmatrix} = \begin{bmatrix} 0 & 1/\mu \\ \rho(\partial_{tt} - \mu\Delta_h) & 0 \end{bmatrix} \begin{bmatrix} u_H \\ \tau_{Hz} \end{bmatrix} - \rho \begin{bmatrix} 0 \\ f_H \end{bmatrix}, \quad (4.6)$$

where

$$\begin{aligned} u_V &= r^{-1} [\partial_r (r u_r) + \partial_\phi u_\phi], \\ \tau_{Vz} &= r^{-1} [\partial_r (r \tau_{rz}) + \partial_\phi \tau_{\phi z}], \\ u_H &= r^{-1} [\partial_r (r u_\phi) - \partial_\phi u_r], \\ \tau_{Hz} &= r^{-1} [\partial_r (r \tau_{\phi z}) - \partial_\phi \tau_{rz}], \\ f_V &= r^{-1} [\partial_r (r f_r) + \partial_\phi f_\phi], \\ f_H &= r^{-1} [\partial_r (r f_\phi) - \partial_\phi f_r], \end{aligned} \quad (4.7)$$

$$\begin{aligned} \lambda_* &= \lambda + 2\mu, \\ \nu^2 &= 4\lambda(\lambda + \mu) / \rho\lambda_*, \end{aligned} \quad (4.8)$$

and where

$$\Delta_h \equiv r^{-1}\partial_r(r\partial_r) + r^{-2}\partial_{\phi\phi} \quad (4.9)$$

is the horizontal Laplacian.

Notice that (4.6) does not involve the vertical displacement u_z , the normal stress τ_{zz} , or the Lamé coefficient λ . It therefore describes horizontally polarized shear waves called SH waves. Equation (4.5) describes coupled compressional and shear waves called P-SV waves.¹

¹The name P-SV is apparently borrowed from the simpler two-dimensional treatment of waves in which the shear displacement of these waves is confined to the vertical plane. But in three dimensions, cylindrical P-SV waves also have horizontal displacements due to both compressional and shear wave components. The vector nature of P-SV and SH waves to the total displacement field will become evident when the displacement field is written in terms of cylindrical harmonics, in equation (4.78), where U and V are P-SV, and W is an SH field variable.

4.1.1 Transformation to stress-displacement vectors

The operators ∂_{tt} and Δ_h can be converted to multiplication in the frequency ω and horizontal wavenumber k domains by applying the Fourier-Bessel transform

$$\hat{\psi}(k, m, z, \omega) \equiv \frac{1}{2\pi} \int_{-\infty}^{+\infty} dt e^{i\omega t} \int_0^{+\infty} dr r J_m(kr) \int_{-\pi}^{+\pi} d\phi e^{-im\phi} \psi(r, \phi, z, t); \quad (4.10)$$

∂_{tt} becoming multiplication by $-\omega^2$, and Δ_h by $-k^2$. The inverse transform is

$$\psi(r, \phi, z, t) \equiv \int_{-\infty}^{+\infty} d\omega e^{-i\omega t} \int_0^{+\infty} dk k J_m(kr) \sum_{m=-\infty}^{+\infty} e^{im\phi} \hat{\psi}(k, m, z, \omega). \quad (4.11)$$

For convenience, Kennett introduces scaled variables in the transform domain

$$\begin{aligned} U &= \hat{u}_z, & P &= \omega^{-1} \hat{\tau}_{zz}, & F'_z &= \omega^{-1} \rho \hat{f}'_z, \\ V &= -k^{-1} \hat{u}_V, & S &= -(\omega k)^{-1} \hat{\tau}_{Vz}, & F'_V &= -(\omega k)^{-1} \rho \hat{f}'_V, \\ W &= -k^{-1} \hat{u}_H, & T &= -(\omega k)^{-1} \hat{\tau}_{Hz}, & F'_H &= -(\omega k)^{-1} \rho \hat{f}'_H. \end{aligned} \quad (4.12)$$

He also works with horizontal slowness

$$p = k/\omega, \quad (4.13)$$

rather than wavenumber k , and with phase speeds α and β (given by (2.19) and (2.22), respectively) rather than the Lamé coefficients λ and μ . Following Kennett then, the transformation of (4.5) becomes

$$\partial_z \begin{bmatrix} U \\ V \\ P \\ S \end{bmatrix} = \omega \begin{bmatrix} 0 & p(1 - 2\beta^2/\alpha^2) & (\rho\alpha^2)^{-1} & 0 \\ -p & 0 & 0 & (\rho\beta^2)^{-1} \\ -\rho & 0 & 0 & p \\ 0 & \rho(rp^2 - 1) & -p(1 - 2\beta^2/\alpha^2) & 0 \end{bmatrix} \begin{bmatrix} U \\ V \\ P \\ S \end{bmatrix} - \begin{bmatrix} 0 \\ 0 \\ F'_z \\ F'_V \end{bmatrix}, \quad (4.14)$$

with

$$v = 4\beta^2(1 - \beta^2/\alpha^2), \quad (4.15)$$

and the transformation of (4.6) becomes

$$\partial_z \begin{bmatrix} W \\ T \end{bmatrix} = \omega \begin{bmatrix} 0 & (\rho\beta^2)^{-1} \\ \rho(\beta^2 p^2 - 1) & 0 \end{bmatrix} \begin{bmatrix} W \\ T \end{bmatrix} - \begin{bmatrix} 0 \\ F'_H \end{bmatrix}. \quad (4.16)$$

These results must be modified for fluid layers because $\beta \rightarrow 0$. An ideal inviscid fluid cannot support shear stress, and its displacement field is assumed to be irrotational.²

²See the note regarding irrotational motion on page 24.

Setting $\tau_{rz} = \tau_{\phi z} = 0$ in (4.7) we find $\tau_{Vz} = \tau_{Hz} = 0$, and setting $\nabla \times \mathbf{u} = \mathbf{0}$ we find $(\nabla \times \mathbf{u})_z = u_H = 0$, making all shear components $S, T, W = 0$, making (4.16) of no use, and simplifying (4.14) to

$$\partial_z \begin{bmatrix} U \\ V \\ P \\ 0 \end{bmatrix} = \omega \begin{bmatrix} 0 & p & (\rho\alpha^2)^{-1} \\ -p & 0 & 0 \\ -\rho & 0 & 0 \\ 0 & -\rho & -p \end{bmatrix} \begin{bmatrix} U \\ V \\ P \end{bmatrix} - \begin{bmatrix} 0 \\ 0 \\ F_z \\ F_V \end{bmatrix}. \quad (4.17)$$

P and V are no longer independent. In fact,

$$\omega\rho V = -\omega pP - F_V, \quad (4.18)$$

and (4.17) can be reduced to just two equations

$$\partial_z \begin{bmatrix} U \\ P \end{bmatrix} = \omega \begin{bmatrix} 0 & (\alpha^{-2} - p^2)/\rho \\ -\rho & 0 \end{bmatrix} \begin{bmatrix} U \\ P \end{bmatrix} - \begin{bmatrix} pF_V/\rho \\ F_z \end{bmatrix}. \quad (4.19)$$

which I call the P wave case.³

Summarizing the results so far, the Fourier-Bessel transform represents the elastic field as the superposition of an infinite number of P-SV and SH cylindrical waves, with a different system of cylindrical waves resulting for each ω and p in the transform. The range r dependence of the waves is given by the Bessel function $J_m(\omega pr)$, and the vertical dependence by a *stress-displacement* vector $\mathbf{b}(z)$,

$$\mathbf{b}(z) = \begin{cases} [U, P]^T & \dots \text{P waves,} \\ [U, V, P, S]^T & \dots \text{P-SV waves,} \\ [W, T]^T & \dots \text{SH waves,} \end{cases} \quad (4.20)$$

which takes account of reverberation of the cylindrical waves between the layers in the waveguide. $\mathbf{b}(z)$ satisfies a first-order equation

$$[\partial_z - \omega A(p, z)] \mathbf{b}(z) = \mathbf{F}(\omega, p, m, z), \quad (4.21)$$

where A is the square matrix in either (4.14), (4.16) or (4.19), depending on the wave type. Taken together with boundary conditions applied at the top and bottom of the waveguide, (4.21) must be solved for each value of ω , m and $k = \omega p$ required to invert the Fourier-Bessel transform (4.11) and recover the elastic wave field in time and space.

³This result for fluids agrees with Kennett [69, app. B] when $F_V = F_z = 0$.

4.1.2 Transformation to wave vectors

Equation (4.21) would be easier to solve if A were a diagonal matrix. We can diagonalize A by constructing a matrix D whose columns are the eigenvectors of A ⁴

$$D^{-1}AD = \Lambda. \quad (4.22)$$

Λ is a diagonal matrix holding the eigenvalues of A . Applying this diagonalization to (4.21) gives

$$\left[\partial_z - \omega D^{-1}A D \right] D^{-1} \mathbf{b} = \left[\partial_z - \omega \Lambda \right] D^{-1} \mathbf{b} = D^{-1} \mathbf{F}, \quad (4.23)$$

in a homogeneous layer, using the fact that $D^{-1}\partial_z D = \partial_z$ because A , and therefore D , is independent of z . If we write \mathbf{b} as a linear combination of eigenvectors

$$\mathbf{b} = D\mathbf{v}, \quad (4.24)$$

then (4.23) is reduced to independent, first order differential equations

$$\left[\partial_z - \omega \Lambda \right] \mathbf{v} = D^{-1} \mathbf{F}. \quad (4.25)$$

In this way, the wave field has been transformed once again: from the *stress-displacement* vector $\mathbf{b}(z)$ to the *wave vector* $\mathbf{v}(z)$ through the linear transformation D .

Using the matrix A for each wave type, it can be shown that the eigenvalues are

$$\begin{aligned} \Lambda_{11} = +iq_\alpha, \quad \Lambda_{22} = -iq_\alpha, & \quad \text{for P waves,} \\ \Lambda_{11} = +iq_\alpha, \quad \Lambda_{22} = +iq_\beta, \quad \Lambda_{33} = -iq_\alpha, \quad \Lambda_{44} = -iq_\beta, & \quad \text{for P-SV waves,} \\ \Lambda_{11} = +iq_\beta, \quad \Lambda_{22} = -iq_\beta, & \quad \text{for SH waves,} \end{aligned} \quad (4.26)$$

where

$$\begin{aligned} q_\alpha &= \sqrt{\alpha^{-2} - p^2} \\ q_\beta &= \sqrt{\beta^{-2} - p^2} \end{aligned} \quad (4.27)$$

are the vertical slownesses for P and S cylindrical waves with horizontal slowness p . Moreover, the eigenvector matrices D for each are

$$D = \begin{bmatrix} M^+ & M^- \\ N^+ & N^- \end{bmatrix} \quad (4.28)$$

⁴We require only that the eigenvalues of A be distinct. Then the eigenvectors are linearly independent and D^{-1} exists.

with partitions

$$\begin{aligned}
 & \left. \begin{aligned} M^\pm &= \pm i q_\alpha \epsilon_\alpha \\ N^\pm &= -\rho \epsilon_\alpha \end{aligned} \right\} \text{for P waves,} \\
 & \left. \begin{aligned} M^\pm &= \begin{bmatrix} \pm i q_\alpha \epsilon_\alpha & p \epsilon_\beta \\ p \epsilon_\alpha & \pm i q_\beta \epsilon_\beta \end{bmatrix} \\ N^\pm &= \begin{bmatrix} \rho (2\beta^2 p^2 - 1) \epsilon_\alpha & \pm 2i \rho \beta^2 p q_\beta \epsilon_\beta \\ \pm 2i \rho \beta^2 p q_\alpha \epsilon_\alpha & \rho (2\beta^2 p^2 - 1) \epsilon_\beta \end{bmatrix} \end{aligned} \right\} \text{for P-SV waves} \\
 & \left. \begin{aligned} M^\pm &= \epsilon_\beta / \beta \\ N^\pm &= \pm i \rho \beta q_\beta \epsilon_\beta \end{aligned} \right\} \text{for SH waves.}
 \end{aligned} \tag{4.29}$$

ϵ_α and ϵ_β are normalization factors ($\neq 0$) applied to the columns of D . Any such normalization can be used (because the columns of D , being eigenvectors of A , can be arbitrarily scaled), but Kennett's choice

$$\begin{aligned}
 \epsilon_\alpha &= (2\rho q_\alpha)^{-1/2}, \\
 \epsilon_\beta &= (2\rho q_\beta)^{-1/2},
 \end{aligned} \tag{4.30}$$

derived from vertical energy flow considerations,⁵ has the advantage that D^{-1} has the simple form

$$D^{-1} = i \begin{bmatrix} (N^-)^T & -(M^-)^T \\ -(N^+)^T & (M^+)^T \end{bmatrix}. \tag{4.31}$$

D^{-1} is required later when considering the excitation due to a point source in Section (4.2.5).

It is convenient to partition \mathbf{b} into displacement \mathbf{w} and stress \mathbf{t} components, $\mathbf{b} = [\mathbf{w}, \mathbf{t}]^T$, such that (4.24) becomes

$$\begin{bmatrix} \mathbf{w} \\ \mathbf{t} \end{bmatrix} = \begin{bmatrix} M^+ & M^- \\ N^+ & N^- \end{bmatrix} \begin{bmatrix} \mathbf{v}^+ \\ \mathbf{v}^- \end{bmatrix} \tag{4.32}$$

⁵Vertical energy flow in cylindrical waves is considered later in Section (5.6).

EJP branch cuts for vertical slowness

Suitable branch cuts must be chosen when computing the vertical slowness in (4.27). In their classic work, Ewing, Jardetsky, and Press [44] used the line along which the imaginary vertical slowness is zero for a branch cut—called the EJP cut in geoaoustics [66], but the Sommerfeld cut elsewhere [24].⁶ The line $\text{Im}\{q\} = q_i = 0$ follows a hyperbolic curve in the complex p plane

$$p_r p_i = -\frac{c_r c_i}{(c_r^2 + c_i^2)^2} \approx -\frac{c_i}{c_r^3}, \tag{4.33}$$

as shown in Fig. (4.1), where $c = c_r + ic_i$ is the complex phase speed α or β . It is assumed that $|c_i| \ll c_r$ as in Section (2.2). In the limit $c_i \rightarrow 0$, which applies in ideal lossless media, the branch cut follows the real and imaginary p axes, making an “L” shape as shown in the figure. Every solid layer requires two branch cuts (for P and S waves), and every fluid layer requires one (for P waves only). We will consider the role of the branch cuts further as required, but for the moment notice that, so far as the transformation from stress-displacement to wave vectors (4.24) is concerned, flipping the sign option of q_α and q_β by switching p from one Riemann sheet to another, simply switches M^+ and M^- , and N^+ and N^- . The down and up going partitions of the D matrix transformation therefore switch roles according to the Riemann sheet.

4.1.3 The solution to the homogeneous equation

The homogeneous form of (4.25) applies at depths other than the source depth

$$\partial_z v_i(z) - \omega \lambda_i v_i(z) = 0. \tag{4.34}$$

The form of its solution is easily guessed

$$v_j(z) = V_j e^{\omega \lambda_j z}, \tag{4.35}$$

where V_j is a constant within a layer, though it may jump discontinuously across an interface between layers because D depends on the discontinuous elastic parameters α, β and ρ .

⁶Another branch cut commonly used in geoaoustics is the Pekeris branch cut extending vertically upwards from the branch point in a straight line, named after Pekeris who first used them for propagation in a two-layered fluid waveguide [97].

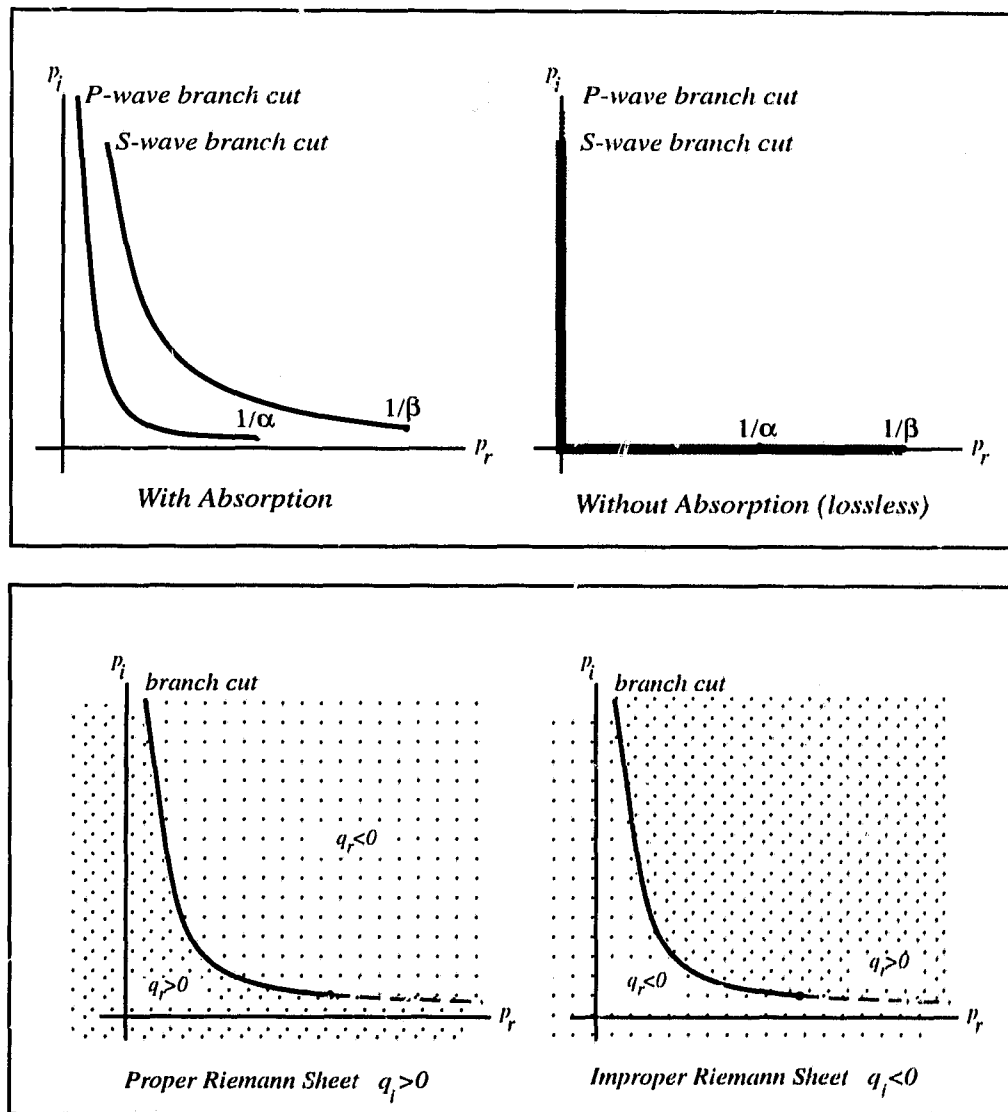


Figure 4.1: The Ewing-Jardetsky-Press (EJP) branch cut for the vertical slowness q follows a hyperbolic curve in the complex horizontal slowness p plane. The branch point is $1/c$, where c is the phase speed. **Upper:** EJP cuts for a solid layer with and without absorption. **Lower:** The hyperbolic curve followed by a cut separates the p plane according to the sign of the corresponding real vertical slowness q_r .

Substituting the eigenvalues (4.26) into (4.35) gives

$$v_j(z) = V_j \exp(\pm i \omega q_{\alpha,\beta} z), \quad (4.36)$$

which is the vertical dependence of P and S cylindrical or plane waves in a homogeneous medium. The vertical two-point boundary value problem would be solved if the complex wave vector amplitudes were known at each interface in the waveguide. To compute them numerically we cast the vertical boundary value problem in matrix form.

4.2 The scattering matrix method

A *scattering* matrix is a transformation from input variables to output variables for a linear network. If the inputs and outputs are accessed through two ports *A* and *B* as shown in Fig. (4.2), the transformation can be partitioned in this way

$$\begin{bmatrix} \text{output vector at port A} \\ \text{output vector at port B} \end{bmatrix} = \begin{bmatrix} \mathbf{R}^{AB} & \mathbf{T}^{AB} \\ \mathbf{T}^{BA} & \mathbf{R}^{BA} \end{bmatrix} \begin{bmatrix} \text{input vector at port A} \\ \text{input vector at port B} \end{bmatrix}, \quad (4.37)$$

where

$$\begin{aligned} \mathbf{R}^{AB} &= \text{reflection matrix seen at port A,} \\ \mathbf{R}^{BA} &= \text{reflection matrix seen at port B,} \\ \mathbf{T}^{AB} &= \text{transmission matrix from port B to A,} \\ \mathbf{T}^{BA} &= \text{transmission matrix from port A to B.} \end{aligned} \quad (4.38)$$

The matrix partitions, represented using triangular symbols, act as multiplication operators (or amplifiers) on the signals.

4.2.1 Scattering matrix for a homogeneous layer

Let us formulate the scattering matrix for a homogeneous layer spanning the depth z_A to z_B ; $z_B > z_A$. The inputs to the layer are the incoming wave vector elements, $\mathbf{v}^+(z_A)$ and $\mathbf{v}^-(z_B)$, and the outputs are the outgoing wave vector elements, $\mathbf{v}^-(z_A)$ and $\mathbf{v}^+(z_B)$, as shown in Fig.(4.3). The scattering matrix for a homogeneous layer is particularly simple because transmission through the homogeneous media is the same in both directions, and

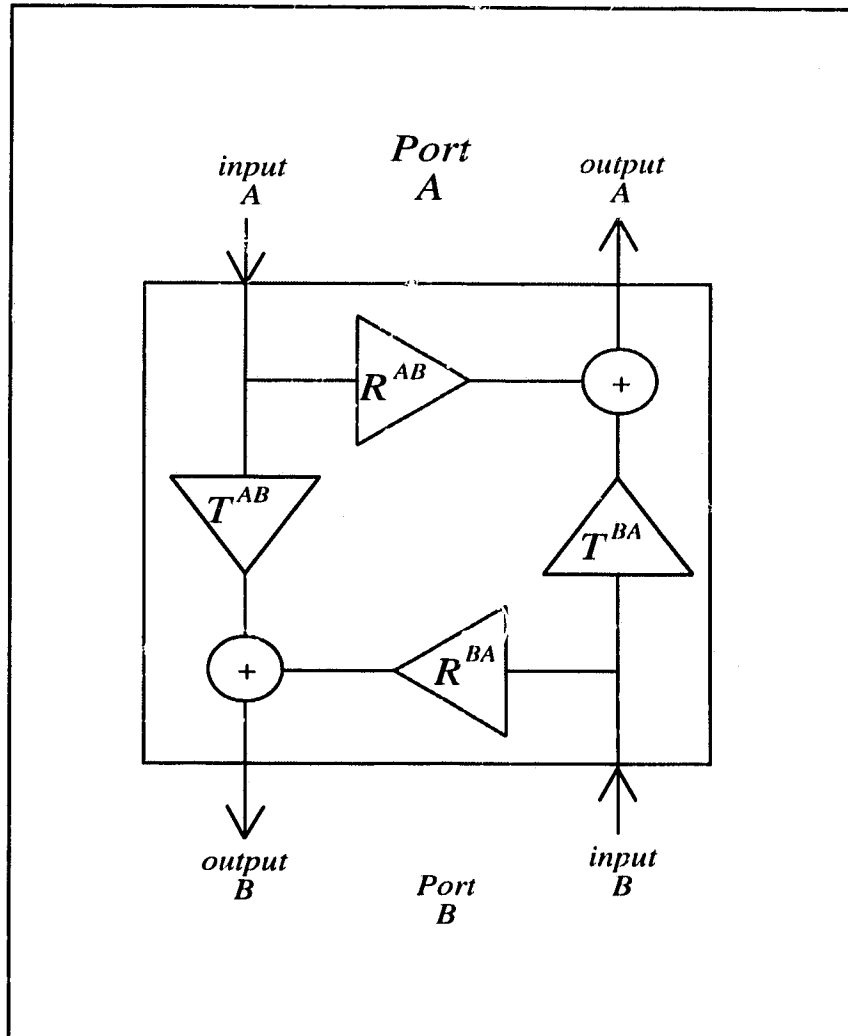


Figure 4.2: A two-port scattering matrix network. Reflection from and transmission through the network are represented by triangular multiplication operators. The outputs are the sum of the reflected and transmitted inputs.

reflection from within the layer is zero. The relation between inputs and outputs can be written directly from (4.36) in matrix form

$$\begin{bmatrix} \mathbf{v}^-(z_A) \\ \mathbf{v}^+(z_B) \end{bmatrix} = \begin{bmatrix} \mathbf{0} & \mathbf{T}_L(z_B - z_A) \\ \mathbf{T}_L(z_B - z_A) & \mathbf{0} \end{bmatrix} \begin{bmatrix} \mathbf{v}^+(z_A) \\ \mathbf{v}^-(z_B) \end{bmatrix} = \mathbf{S} \begin{bmatrix} \mathbf{v}^+(z_A) \\ \mathbf{v}^-(z_B) \end{bmatrix}, \quad (4.39)$$

where \mathbf{T}_L is the transmission matrix for the layer

$$\begin{aligned} \mathbf{T}_L(z_B - z_A) &= e^{i\omega q_\alpha(z_B - z_A)} && \dots \text{for P waves,} \\ \mathbf{T}_L(z_B - z_A) &= \begin{bmatrix} e^{i\omega q_\alpha(z_B - z_A)} & 0 \\ 0 & e^{i\omega q_\beta(z_B - z_A)} \end{bmatrix} && \dots \text{for P-SV waves,} \\ \mathbf{T}_L(z_B - z_A) &= e^{i\omega q_\beta(z_B - z_A)} && \dots \text{for SH waves.} \end{aligned} \quad (4.40)$$

Vertical evanescence

In general the vertical slowness is complex, $q = q_r + iq_i$, giving inhomogeneous cylindrical wave behavior. The sign of q_i determines the vertical decay (or growth) of the wave amplitude. When it is positive, the wave decays as it propagates, and we say that the wave is vertically *evanescent*. When it is sufficiently large, the wave cannot traverse the entire layer since $|e^{i\omega q h}| = e^{-\omega q_i h} \rightarrow 0$, cutting off vertical transmission through a layer, in effect separating the waveguide in two independent layer structures so far as that system of cylindrical waves is concerned. Similar decoupling occurs through the accumulated effect of many thin consecutive evanescent layers.

4.2.2 Scattering matrix for an interface between layers

The coefficient matrix A in (4.21) does not depend on the derivatives of the elastic properties ρ , α and β , so the stress-displacement vector \mathbf{b} for each wave type is continuous at an interface between layers on which there is no source ($\mathbf{F} = \mathbf{0}$); that is,

$$\mathbf{b}(z_I^+) = \mathbf{b}(z_I^-), \quad (4.41)$$

at interface z_I , where $z_I^\pm = z_I \pm \epsilon$, in the limit $\epsilon \rightarrow 0^+$. This implies

$$D_A \mathbf{v}(z_I^-) = D_B \mathbf{v}(z_I^+), \quad (4.42)$$

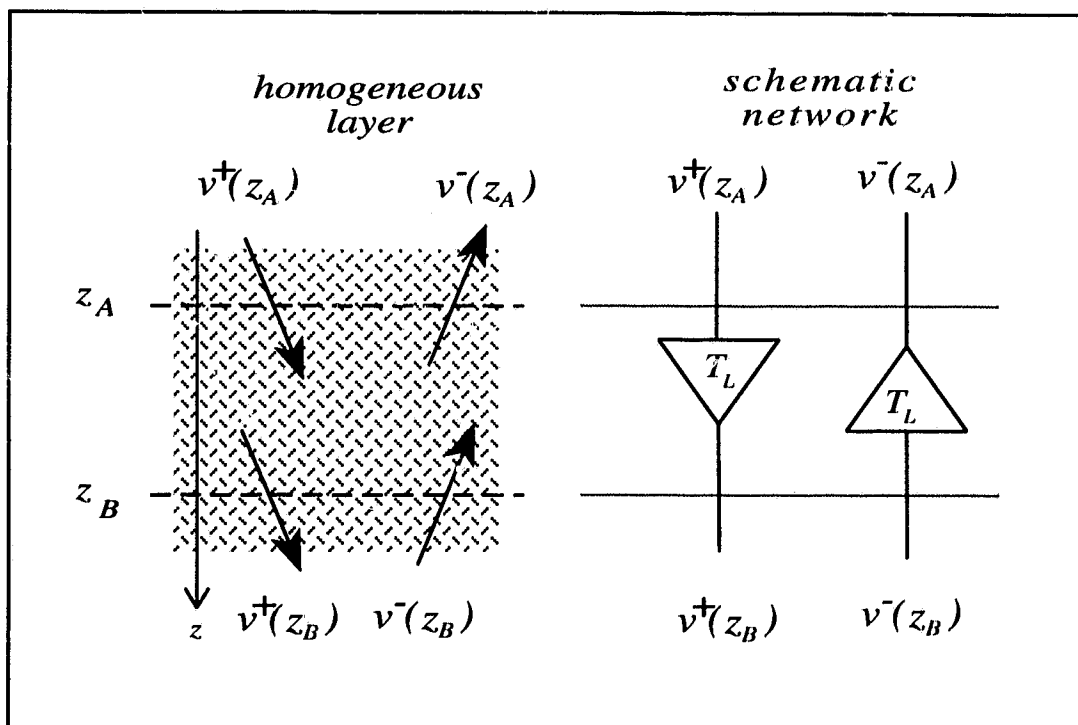


Figure 4.3: Scattering matrix network for a homogeneous layer. The interface between one layer and another are not included here, so there is no reflection within the network. The up and down going transmission operators are the same but point in opposite directions.

where D_A and D_B are for the upper and lower media, respectively.⁷ The scattering matrix \mathbf{S} follows by solving for the out-going wave vector components in terms of the incoming,

$$\begin{aligned} \begin{bmatrix} \mathbf{v}^-(z_I^-) \\ \mathbf{v}^+(z_I^+) \end{bmatrix} &= \left(\begin{bmatrix} -M^{A-} & M^{B+} \\ -N^{A-} & N^{B+} \end{bmatrix}^{-1} \begin{bmatrix} M^{A+} & -M^{B-} \\ N^{A+} & -N^{B-} \end{bmatrix} \right) \begin{bmatrix} \mathbf{v}^+(z_I^-) \\ \mathbf{v}^-(z_I^+) \end{bmatrix} \\ &= \mathbf{S} \begin{bmatrix} \mathbf{v}^+(z_I^-) \\ \mathbf{v}^-(z_I^+) \end{bmatrix}, \end{aligned} \quad (4.43)$$

where the matrices D_A and D_B have been reduced to their partitions (4.28). The elements in the scattering matrix are rather complicated when written out explicitly, especially for P-SV waves, but they can easily be computed numerically using (4.43). The scattering matrix for an interface is shown schematically in Fig.(4.4).

At an interface between a solid and fluid layer, the boundary conditions in (2.34) to (2.36) impose the conditions 1) that the normal field components U and P must be continuous, 2) that the tangential components V and W are discontinuous, and 3) that the shear stress components T and S must vanish in both the solid and the fluid. If the fluid lies on top of the solid, for example, we must have

$$\begin{aligned} U(z_I^+) &= U(z_I^-), \\ P(z_I^+) &= P(z_I^-), \\ S(z_I^+) &= S(z_I^-) = 0, \\ T(z_I^+) &= T(z_I^-) = 0, \end{aligned} \quad (4.44)$$

where z_I is the depth of the plane of contact. Converting the first three conditions for P-SV wave vectors into conditions for wave vectors, then solving for the out-going components

⁷Note that the horizontal displacement variable V in a fluid, which has been eliminated from the P-wave stress-displacement vector, is not generally continuous across an interface. At a fluid-fluid interface, for example, continuous normal stress P in (4.18), in the absence of forcing, implies a jump in V whenever there is a jump in density ρ .

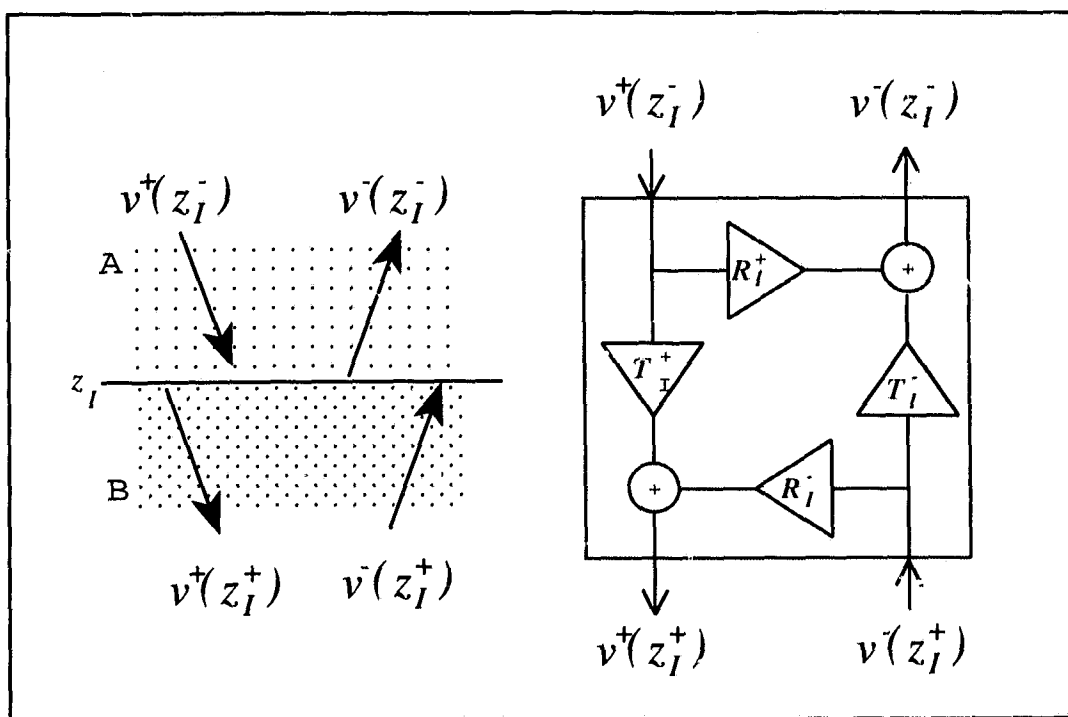


Figure 4.4: The scattering matrix network for an interface between layers. The transmission and reflection operators are the plane wave transmission and reflection matrices for the interface.

gives the scattering matrix

$$\begin{aligned} \begin{bmatrix} v_P^-(z_I^-) \\ v_P^+(z_I^+) \\ v_S^+(z_I^+) \end{bmatrix} &= \left(\begin{bmatrix} -M^{f-} & M_{11}^{s+} & M_{12}^{s+} \\ -N^{f-} & N_{11}^{s+} & N_{12}^{s+} \\ 0 & N_{21}^{s+} & N_{22}^{s+} \end{bmatrix}^{-1} \begin{bmatrix} M^{f+} & -M_{11}^{s-} & -M_{12}^{s-} \\ N^{f+} & -N_{11}^{s-} & -N_{12}^{s-} \\ 0 & -N_{21}^{s-} & -N_{22}^{s-} \end{bmatrix} \right) \begin{bmatrix} v_P^+(z_I^+) \\ v_P^-(z_I^-) \\ v_S^-(z_I^-) \end{bmatrix} \\ &= \mathbf{S} \begin{bmatrix} v_P^+(z_I^+) \\ v_P^-(z_I^-) \\ v_S^-(z_I^-) \end{bmatrix}, \end{aligned} \quad (4.45)$$

where $M^{f\pm}$ and $N^{f\pm}$ are elements of the two-by-two D matrix for the fluid, and $M_{ij}^{s\pm}$ and $N_{ij}^{s\pm}$ are elements of the four-by-four for the solid. The partitioning of \mathbf{S} into reflection and transmission matrices (4.37) still applies, but now the partitions do not have the same matrix dimensions because the wave vectors v^\pm have length 1 in fluids and 2 in solids. When a fluid layer lies below the solid, the scattering matrix is the inverse of \mathbf{S} shown.

SH waves in a solid do not couple with P waves in a fluid. Rather, the vanishing shear stress condition of the fluid makes the interface behave as a traction free boundary for SH waves which is considered below.

It is well-known that a plane interface between differing media may support a P-SV mode of vibration travelling along the interface [127]. For example, the interface between two solid homogeneous half-spaces can support a Stonely wave, and the interface between a fluid and solid half-space always supports a Scholte mode.⁸ Although the effect of other layers make it unlikely that the interface mode for joined homogeneous halfspaces is a mode in the actual waveguide, we cannot construct the scattering matrix close to the interface mode because the matrices to be inverted in (4.43) or (4.45) are singular there. To avoid the singularity, we can use the equivalent forms (4.42) or (4.44) for numerical work.

4.2.3 Scattering matrix for impenetrable boundaries

An impenetrable boundary is a plane interface that does not transmit waves. It can be modeled as a single-port network with one input and output, the incident and reflected

⁸These interface modes are considered further in Section(6.2.3).

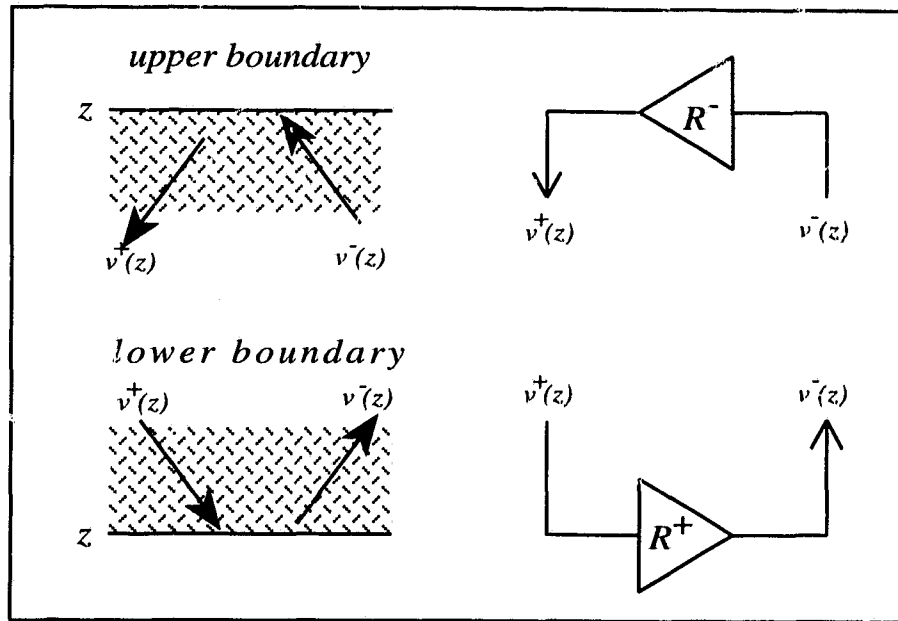


Figure 4.5: The scattering network for an impenetrable plane boundary is a reflection operator, which is the plane wave reflection matrix.

waves, and a single reflection matrix as shown in Fig.(4.5)

Traction free boundary

The upper interface of an oceanic or seismic waveguide in contact with the atmosphere is usually modeled by a traction free boundary where $P, S, T = 0$. Setting the traction portion $\mathbf{t} = \mathbf{0}$ in (4.32) we find

$$0 = N^+ \mathbf{v}^+(z) + N^- \mathbf{v}^-(z) \quad (4.46)$$

where z is the depth of the boundary. The reflection matrix for a lower (+) and upper (-) free interface are therefore

$$\mathbf{R}^+ = -(N^-)^{-1} N^+ = (\mathbf{R}^-)^{-1}. \quad (4.47)$$

Using the expressions for N^\pm in (4.29), we can simplify $\mathbf{R}^\pm = -1$ for P waves in a fluid, and $\mathbf{R}^\pm = 1$ for SH waves in a solid.

It is well-known that a free boundary on a homogeneous solid half space supports a P-SV interface wave, the Rayleigh mode [127].⁹ Here again, the effect of other layers on the wave motion make it unlikely that the Rayleigh mode of the homogeneous half space is a mode of vibration in the waveguide, but we cannot construct the reflection matrix (4.47) close to the Rayleigh mode because N^\pm are singular there, and then it is best to use (4.46) in the numerical computations.

Rigid-welded boundary

The waveguide may be bounded below by a rigid, displacement free boundary at depth z . For a solid layer in welded contact $U, V, W = 0$. Setting the displacement partition $\mathbf{u} = \mathbf{0}$ in (4.32) we find

$$\mathbf{0} = M^+ \mathbf{v}^+(z) + M^- \mathbf{v}^-(z). \quad (4.48)$$

The plane wave reflection matrices for a lower (+) and upper (-) rigid interface are therefore

$$\mathbf{R}^+ = -(M^-)^{-1} M^+ = (\mathbf{R}^-)^{-1}. \quad (4.49)$$

Using the expressions for M^\pm in (4.29) we can simplify $\mathbf{R}^\pm = -1$ for SH waves in a solid. The rigid boundary on an infinite solid half space supports a P-SV interface mode, a lesser known leaky (improper) counterpart of the Rayleigh mode,¹⁰ at which M^\pm for P-SV waves are singular.

Rigid-lubricated boundary

A rigid boundary makes frictionless contact with an inviscid fluid layer, and the vertical (normal) displacement $U = 0$, while the horizontal (tangential) displacement V for P waves remains unconstrained. For P waves in fluids we find

$$\mathbf{R}^+ = -(M^-)^{-1} M^+ = (\mathbf{R}^-)^{-1} = 1. \quad (4.50)$$

⁹The Rayleigh wave is considered further in Section(6.2.3).

¹⁰I have not come across these modes in the literature. For lack of a better name, I call this the Rayleigh mode of the second kind in Section(6.2.3).

Though rarely used with solid media, it is also possible for a rigid boundary to be in frictionless (lubricated) rather than welded contact. This condition is of interest because the P and SV components of P-SV waves are not coupled at the boundary, and the boundary cannot support an interface wave as do the free and rigid-welded boundaries.¹¹ The rigid-lubricated case requires $U, S = 0$ for P-SV waves. Thus, (4.24) gives two equations

$$\begin{bmatrix} U \\ S \end{bmatrix} = \begin{bmatrix} M_{11}^+ & M_{12}^+ & M_{11}^- & M_{12}^- \\ N_{21}^+ & N_{22}^+ & N_{21}^- & N_{22}^- \end{bmatrix} \begin{bmatrix} \mathbf{v}^+ \\ \mathbf{v}^- \end{bmatrix} = \begin{bmatrix} 0 \\ 0 \end{bmatrix}, \quad (4.51)$$

which give the reflection matrix

$$\mathbf{R}^+ = - \begin{bmatrix} M_{11}^- & M_{12}^- \\ N_{21}^- & N_{22}^- \end{bmatrix}^{-1} \begin{bmatrix} M_{11}^+ & M_{12}^+ \\ N_{21}^+ & N_{22}^+ \end{bmatrix} = \begin{bmatrix} 1 & 0 \\ 0 & -1 \end{bmatrix} = (\mathbf{R}^-)^{-1} = \mathbf{R}^-. \quad (4.52)$$

Zero off-diagonals indicate that the P and SV components are not coupled.

For SH waves, the rigid-lubricated boundary behaves as the traction-free boundary because SH waves have no vertical displacement.

4.2.4 Scattering matrix for an infinite half space and the importance of Riemann sheets

I will only consider scattering in waveguides that are bounded above and below by perfectly reflecting interfaces, but infinitely thick layers cannot be ignored because of their importance to normal modes in layered media. We have seen that the vertical slownesses q_α or q_β in (4.27) evoke two branch cuts in the complex p -plane for every solid layer, and one for every fluid layer. The choice of Riemann sheet is inconsequential for all of the waveguide components we have considered so far, because a change in sign in q_α or q_β simply reverses the role of up going (-) and down going (-+) quantities for that layer: the up going wave vector \mathbf{v}^- and partitions M^- and N^- switch roles with their down going counterparts \mathbf{v}^+ , M^+ and N^+ . The exception to this rule is the infinitely thick layer, or half space.

In an infinitely deep basement layer, at a depth below all sources, the waves must be down going for there are no reflecting interfaces or boundaries to direct waves upwards.

¹¹Miklowitz [90], for example, begins his treatment of the solid plate by assuming rigid-lubricated boundary conditions to indicate what may be expected when free boundary conditions are used.

In a lower half space starting at depth z_L , for example, we have the wave vector

$$\mathbf{v}(z) = \begin{bmatrix} \mathbf{v}^+(z) \\ \mathbf{v}^-(z) \end{bmatrix} = \begin{bmatrix} \mathbf{T}(z - z_L) \mathbf{v}^+(z_L) \\ 0 \end{bmatrix} \quad (4.53)$$

The exclusion of up-going waves breaks the symmetry between up and down going waves found in the other elements in the scattering diagram. The same is true for the exclusion of down-going waves in an upper half space. For when the EJP branch cut (4.33) is used, $q_i > 0$ on the proper Riemann sheet, making the waves in a lower or upper half space decay exponentially as $z \rightarrow \pm\infty$, whereas $q_i < 0$ on the improper sheet, making the waves grow exponentially without bound. Thus, there is more than one system of cylindrical waves having the same horizontal slowness p , depending on the choice of Riemann sheet for the vertical slowness q in an infinite half space.

The situation becomes rather complicated for a solid half space because it requires two branch cuts, for P and S waves, giving four Riemann sheets, hence four different cylindrical wave systems for the same slowness p : one proper, and three improper. If there are both upper and lower solid half spaces, then there are four branch cuts, eight Riemann sheets, and sixteen different cylindrical wave systems having the same slowness p : one proper, fifteen improper. Ordinarily, the proper sheet is used, because all waves are well-behaved at $z = \pm\infty$ on the proper sheet. But in the analysis of normal modes, there may be improper modes that contribute significantly to the wave field.¹²

4.2.5 Point Sources

It remains to show how a point source excites the wave vectors in the schematic diagram. To this end we must 1) decide what point sources to allow, 2) derive their equivalent forcing $\mathbf{f}(\mathbf{x})$ for use in the original equation of motion, and 3) transform $\mathbf{f}(\mathbf{x})$ to the horizontal slowness domain of the stress-displacement vectors $\mathbf{b}(z)$. This considerable task has been reported in detail by notable authors such as Takeuchi and Saito [122], Hudson [60], and Kennett [71]. I will briefly outline Kennett's approach, reporting only the final results while omitting the details.

¹²Improper modes are often called leaky modes, but not all leaky mode are improper when energy absorption is included in the layers. See Section (6.2.1).

The equivalent forcing for a variety of seismic sources, such as “explosive” sources, opening cracks, and a shear fault, can be derived from Somigliana’s identity [21]. This forcing can be expressed generally using the form

$$f_j(\mathbf{x}) = \epsilon_j \delta(\mathbf{x} - \mathbf{x}_s) - \partial_k [M_{jk} \delta(\mathbf{x} - \mathbf{x}_s)], \quad (4.54)$$

where ϵ_j are the components of a point force, and M_{jk} are components of a moment tensor. A simple point force, for example, requires simply $f_i = \epsilon_i$, with all M_{jk} set to zero, whereas an explosive (dilatational) point source requires ϵ_j set to zero, and $M_{jk} = \alpha^2 V \delta_{jk}$ where V is the volume displacement of the source.

The field variables f_V and f_H for this family of sources must be constructed by taking the horizontal divergence and curl of f_j as given by (4.7), and together with f_z they must be transformed by the Fourier-Bessel transform (4.10) to get \hat{f}_V , \hat{f}_H , and \hat{f}_z , which in turn give the stress-displacement vector forcing terms F_V , F_H , and F_z in (4.12). It is found that the forcing term in the stress-displacement field (4.21) can be written as

$$[\partial_z - \omega A] \mathbf{b}(z) = \mathbf{F} = \mathbf{F}_1 \delta(z - z_S) + \mathbf{F}_2 \partial_z \delta(z - z_S). \quad (4.55)$$

\mathbf{F}_1 and \mathbf{F}_2 are different for P, P-SV, and SH waves, and they depend on ϵ_j and M_{jk} for the source, and on the variables p , ω , and m of the Fourier-Bessel transform (4.11), with m limited to the range -2 to +2.

Integrating both sides of (4.55) across the source depth, and using the propagator matrix method, Kennett shows that the forcing causes a jump in the stress-displacement vector at the source depth

$$\mathfrak{J}(z_S) = \begin{bmatrix} S_W \\ S_T \end{bmatrix} = \mathbf{b}(z_S^+) - \mathbf{b}(z_S^-) = \mathbf{F}_1 + \omega A \mathbf{F}_2, \quad (4.56)$$

where A is the matrix in (4.21). When all of the components of \mathbf{F}_1 and \mathbf{F}_2 are worked out,

the non-zero elements in $S(z_S)$ for P-SV waves are

$$\begin{aligned}
S_1(z_S) &= \frac{M_{33}}{\rho\alpha^2}, & m &= 0, \\
S_2(z_S) &= \frac{1}{2\rho\beta^2} (\pm M_{13} - iM_{23}), & m &= \pm 1, \\
S_3(z_S) &= -\frac{\epsilon_3}{\omega}, & m &= 0, \\
&= \frac{\nu}{2} [i(M_{32} - M_{23}) \pm (M_{13} - M_{31})], & m &= \pm 1, \\
S_4(z_S) &= \frac{\nu}{2} (M_{11} + M_{22}) - \rho M_{33} \left(1 - \frac{2\beta^2}{\alpha^2}\right), & m &= 0, \\
&= \frac{1}{2\omega} (\mp \epsilon_1 + i\epsilon_2), & m &= \pm 1, \\
&= \frac{\nu}{4} [(M_{22} - M_{11}) \pm i(M_{12} + M_{21})], & m &= \pm 2;
\end{aligned} \tag{4.57}$$

for P waves in fluid media

$$\begin{aligned}
S_1(z_S) &= \frac{M_{33}}{\rho\alpha^2} + \frac{\nu^2}{\rho} \left(\frac{1}{2}(M_{11} + M_{22}) - M_{33}\right), & m &= 0, \\
&= \frac{\nu}{2\rho\omega} (\mp \epsilon_1 + i\epsilon_2), & m &= \pm 1, \\
&= \frac{\nu^2}{4\rho} ((M_{22} - M_{11}) \pm i(M_{12} + M_{21})), & m &= \pm 2, \\
S_2(z_S) &= -\frac{\epsilon_3}{\omega}, & m &= 0, \\
&= \frac{\nu}{2} [\mp (M_{13} + M_{31}) + i(M_{32} + M_{23})], & m &= \pm 1;
\end{aligned} \tag{4.58}$$

and for SH waves

$$\begin{aligned}
S_1(z_S) &= \frac{1}{2\rho\beta^2} (\mp M_{23} - iM_{13}), & m &= \pm 1, \\
S_2(z_S) &= \frac{\nu}{2} (M_{12} - M_{21}), & m &= 0, \\
&= \frac{1}{2\omega} (i\epsilon_1 \pm \epsilon_2), & m &= \pm 1, \\
&= \frac{\nu}{4} [\pm i(M_{11} - M_{22}) + (M_{12} + M_{21})], & m &= \pm 2.
\end{aligned} \tag{4.59}$$

The stress-displacement jump $S(z_S)$ can be converted to a corresponding jump in the wave vector \mathbf{v}

$$\mathbf{v}(z_S^+) - \mathbf{v}(z_S^-) = D^{-1}(\mathbf{F}_1 + \omega A\mathbf{F}_2) = D^{-1}S(z_S) = \begin{bmatrix} \Sigma^+(z_S) \\ -\Sigma^-(z_S) \end{bmatrix}, \tag{4.60}$$

where D^{-1} is given in (4.31). A point source can therefore be represented by a pair of summation operators in the schematic diagram, as shown in Fig.(4.6), which introduces a jump in the wave vector at the source depth.

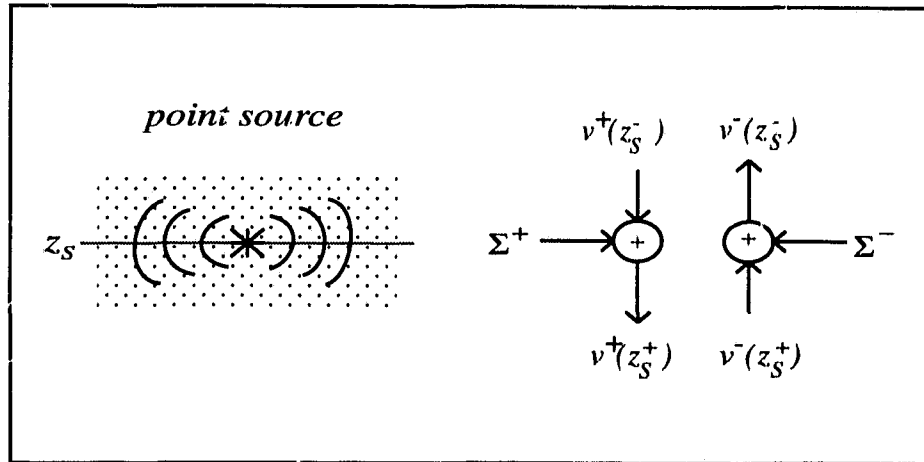


Figure 4.6: The summation operator for a point source, represented schematically by “+” within a circle, introduces a discontinuous jump Σ^\pm in the wave vector.

4.3 Ladder diagram for the global matrix method

All parts of the waveguide have now been rendered schematically. A stack of layers becomes a series of schematic networks representing the layers and their interfaces, connected port to port in series, giving a “ladder” diagram as shown in Fig.(4.7). The interfaces between layers have been drawn as irreducible two-port networks for simplicity. The wave vector components \mathbf{v}^\pm are signals that flow around the ladder in the direction of the arrows. A single source has been shown; the extension to multiple sources is obvious.

We can formulate a matrix solution for the unknown wave vectors \mathbf{v}_i^\pm directly from the ladder diagram. Working from top to bottom, we simply pack the equations represented by each network element into a matrix as shown in Fig.(4.8). Solving the matrix system gives the unknown wave vectors above and below each interface in the waveguide. This is called a *global* matrix approach because it gives the wave vectors at many depths throughout the entire waveguide simultaneously.

It is possible to speed up the matrix solution by combining adjacent components

into larger networks before the global matrix is constructed, thereby eliminating many unknowns and equations from the outset. We might, for example, eliminate roughly half the unknowns by combining every instance of transmission through a layer with the continuity condition at its lower interface, as indicated by the loops in Fig.(4.9). The equations representing the combined components can be derived using (4.39) for a layer and (4.42) for an interface

$$D_n \begin{bmatrix} \mathbf{T}_n \mathbf{v}_{2(n-1)}^+ \\ \mathbf{T}_n^{-1} \mathbf{v}_{2(n-1)}^- \end{bmatrix} = D_{n+1} \begin{bmatrix} \mathbf{v}_{2n}^+ \\ \mathbf{v}_{2n}^- \end{bmatrix}, \quad (4.61)$$

or more explicitly as

$$\begin{bmatrix} M_n^+ \mathbf{T}_n & M_n^- \mathbf{T}_n^{-1} \\ N_n^+ \mathbf{T}_n & N_n^- \mathbf{T}_n^{-1} \end{bmatrix} \begin{bmatrix} \mathbf{v}_{2(n-1)}^+ \\ \mathbf{v}_{2(n-1)}^- \end{bmatrix} = \begin{bmatrix} M_{n+1}^+ & M_{n+1}^- \\ N_{n+1}^+ & N_{n+1}^- \end{bmatrix} \begin{bmatrix} \mathbf{v}_{2n}^+ \\ \mathbf{v}_{2n}^- \end{bmatrix} \quad (4.62)$$

This combined component was used in the global matrix method of Chin, et. al., [25]. It is also representative of the element used in most *propagator matrix* methods [124] [16].

A numerical difficulty is immediately apparent in (4.62). The transmission matrix $\mathbf{T} \rightarrow \mathbf{0}$ for a vertically evanescent layer, making the elements of its inverse \mathbf{T}_n^{-1} extremely large for a strongly evanescent layer. If they do not cause immediate overflow errors, they can make the matrix computations numerically unstable [66, p. 218-222]. In effect, a wave vector that is numerically zero at one depth due to evanescence is pulled backwards against its direction of propagation, being exponentially amplified in the process, from negligible error to significance. Many variations of the propagator method have been developed to resolve this numerical instability. Most notable for ocean acoustics is the global matrix method used in the SAFARI program [109] due to Schmidt and Jensen [107]. In their method, the global matrix is constructed using "finite wave elements" similar to the propagator elements (4.61) and the matrix is solved in a stable way using Gaussian elimination with partial pivoting.

The instability in the propagator method suggests that components should be combined in such a way that transmission terms are never inverted. A scattering matrix approach to combining network components does just that, for a scattering matrix always advances the wave vectors in the direction of their flow around the schematic diagram. This is evident from the rules for combining two scattering networks in series, which can be

derived by eliminating the shared inputs and outputs between two series connected two-port networks, with scattering matrices \mathbf{S}_{AB} and \mathbf{S}_{BC} say, as shown in Fig.(4.10). Considered independently, the two networks require

$$\begin{bmatrix} \mathbf{v}_A^- \\ \mathbf{v}_B^+ \end{bmatrix} = \mathbf{S}_{AB} \begin{bmatrix} \mathbf{v}_A^+ \\ \mathbf{v}_B^- \end{bmatrix} = \begin{bmatrix} \mathbf{R}_{AB}^+ & \mathbf{T}_{AB}^- \\ \mathbf{T}_{AB}^+ & \mathbf{R}_{AB}^- \end{bmatrix} \begin{bmatrix} \mathbf{v}_A^+ \\ \mathbf{v}_B^- \end{bmatrix}, \quad (4.63)$$

$$\begin{bmatrix} \mathbf{v}_B^- \\ \mathbf{v}_C^+ \end{bmatrix} = \mathbf{S}_{BC} \begin{bmatrix} \mathbf{v}_B^+ \\ \mathbf{v}_C^- \end{bmatrix} = \begin{bmatrix} \mathbf{R}_{BC}^+ & \mathbf{T}_{BC}^- \\ \mathbf{T}_{BC}^+ & \mathbf{R}_{BC}^- \end{bmatrix} \begin{bmatrix} \mathbf{v}_B^+ \\ \mathbf{v}_C^- \end{bmatrix}.$$

Eliminating the shared variables \mathbf{v}_B^+ and \mathbf{v}_B^- , we find

$$\begin{bmatrix} \mathbf{v}_A^- \\ \mathbf{v}_C^+ \end{bmatrix} = \mathbf{S}_{AC} \begin{bmatrix} \mathbf{v}_A^+ \\ \mathbf{v}_C^- \end{bmatrix} = \begin{bmatrix} \mathbf{R}_{AC}^+ & \mathbf{T}_{AC}^- \\ \mathbf{T}_{AC}^+ & \mathbf{R}_{AC}^- \end{bmatrix} \begin{bmatrix} \mathbf{v}_A^+ \\ \mathbf{v}_C^- \end{bmatrix}, \quad (4.64)$$

where \mathbf{S}_{AC} is the resultant scattering matrix with partitions

$$\begin{aligned} \mathbf{R}_{AC}^+ &= \mathbf{R}_{AB}^+ + \mathbf{T}_{AB}^- (\mathbf{I} - \mathbf{R}_{BC}^+ \mathbf{R}_{AB}^-)^{-1} \mathbf{R}_{BC}^+ \mathbf{T}_{AB}^+ \\ &= \mathbf{R}_{AB}^+ + \mathbf{T}_{AB}^- \mathbf{R}_{BC}^+ (\mathbf{I} - \mathbf{R}_{AB}^- \mathbf{R}_{BC}^+)^{-1} \mathbf{T}_{AB}^+, \\ \mathbf{T}_{AC}^+ &= \mathbf{T}_{BC}^+ (\mathbf{I} - \mathbf{R}_{AB}^- \mathbf{R}_{BC}^+)^{-1} \mathbf{T}_{AB}^+, \\ \mathbf{R}_{AC}^- &= \mathbf{R}_{BC}^- + \mathbf{T}_{BC}^+ (\mathbf{I} - \mathbf{R}_{AB}^- \mathbf{R}_{BC}^+)^{-1} \mathbf{R}_{AB}^- \mathbf{T}_{BC}^- \\ &= \mathbf{R}_{BC}^- + \mathbf{T}_{BC}^+ \mathbf{R}_{AB}^- (\mathbf{I} - \mathbf{R}_{BC}^+ \mathbf{R}_{AB}^-)^{-1} \mathbf{T}_{BC}^-, \\ \mathbf{T}_{AC}^- &= \mathbf{T}_{AB}^- (\mathbf{I} - \mathbf{R}_{BC}^+ \mathbf{R}_{AB}^-)^{-1} \mathbf{T}_{BC}^-. \end{aligned} \quad (4.65)$$

These combination rules are just Kennett's recursion relations [71, sect. 6.1] for combining reflection and transmission matrices, and if they are applied repeatedly to combine many layers together into a single scattering matrix, we are in fact performing Kennett's recursive method. Notice that the transmission matrix partitions \mathbf{T} are never inverted because the wave vectors are always advanced in their direction of propagation. This is why Kennett's method and the scattering matrix method do not suffer from numerical instability due to evanescent layers.

In field computations we will need to compute the wave vector at a depth within a combined element. The scattering matrix for the combined element must then be split into two scattering matrices at the desired depth. Hence, the wave vectors at z_A and z_C in Fig.(4.10) are now known, and we must solve (4.63) for the intermediate wave vector \mathbf{v}_B

$$\begin{bmatrix} \mathbf{v}_B^+ \\ \mathbf{v}_B^- \end{bmatrix} = \begin{bmatrix} (\mathbf{I} - \mathbf{R}_{AB}^- \mathbf{R}_{BC}^+)^{-1} \mathbf{T}_{AB}^+ & (\mathbf{I} - \mathbf{R}_{AB}^- \mathbf{R}_{BC}^+)^{-1} \mathbf{R}_{AB}^- \mathbf{T}_{BC}^- \\ (\mathbf{I} - \mathbf{R}_{BC}^+ \mathbf{R}_{AB}^-)^{-1} \mathbf{R}_{BC}^+ \mathbf{T}_{AB}^+ & (\mathbf{I} - \mathbf{R}_{BC}^+ \mathbf{R}_{AB}^-)^{-1} \mathbf{T}_{BC}^- \end{bmatrix} \begin{bmatrix} \mathbf{v}_A^+ \\ \mathbf{v}_C^- \end{bmatrix} \quad (4.66)$$

Here again, terms like \mathbf{T}^{-1} do not occur, so evanescent layers do not cause numerical instability.

4.4 A single source and receiver

Using a scattering matrix approach, or equivalently, Kennett's recursive scheme, the ladder diagram for any waveguide can be reduced to its simplest form consisting of the source and an upper and lower reflection matrix as shown in Fig. (4.11). A matrix equation for the waveguide can then be written directly from the diagram

$$\begin{bmatrix} \mathbf{I} & -\mathbf{R}_{0S}^- \\ -\mathbf{R}_{SL}^+ & \mathbf{I} \end{bmatrix} \begin{bmatrix} \mathbf{v}^+(z_S^+) \\ \mathbf{v}^-(z_S^-) \end{bmatrix} = \begin{bmatrix} \Sigma^+ \\ \Sigma^- \end{bmatrix}. \quad (4.67)$$

The solution is

$$\begin{aligned} \mathbf{v}^+(z_S^+) &= (\mathbf{I} - \mathbf{R}_{0S}^- \mathbf{R}_{SL}^+)^{-1} [\Sigma^+ + \mathbf{R}_{0S}^- \Sigma^-], \\ \mathbf{v}^-(z_S^-) &= (\mathbf{I} - \mathbf{R}_{SL}^+ \mathbf{R}_{0S}^-)^{-1} [\mathbf{R}_{SL}^+ \Sigma^+ + \Sigma^-], \end{aligned} \quad (4.68)$$

which can be interpreted physically using "rays" [71] if the left hand side is expanded in the series

$$\begin{aligned} \mathbf{v}^+(z_S^+) &= \left(\mathbf{I} + \mathbf{R}_{0S}^- \mathbf{R}_{SL}^+ + (\mathbf{R}_{0S}^- \mathbf{R}_{SL}^+)^2 + \dots \right) [\Sigma^+ + \mathbf{R}_{0S}^- \Sigma^-], \\ \mathbf{v}^-(z_S^-) &= \left(\mathbf{I} + \mathbf{R}_{SL}^+ \mathbf{R}_{0S}^- + (\mathbf{R}_{SL}^+ \mathbf{R}_{0S}^-)^2 + \dots \right) [\mathbf{R}_{SL}^+ \Sigma^+ + \Sigma^-]. \end{aligned} \quad (4.69)$$

The terms in the series give first a direct source contribution, then a pair of reflections, then reflections of those reflections, and so on. In this way, $(\mathbf{I} - \mathbf{R}_{0S}^- \mathbf{R}_{SL}^+)^{-1}$ and $(\mathbf{I} - \mathbf{R}_{SL}^+ \mathbf{R}_{0S}^-)^{-1}$ account for the reverberation in the waveguide at the source depth, and they are often called

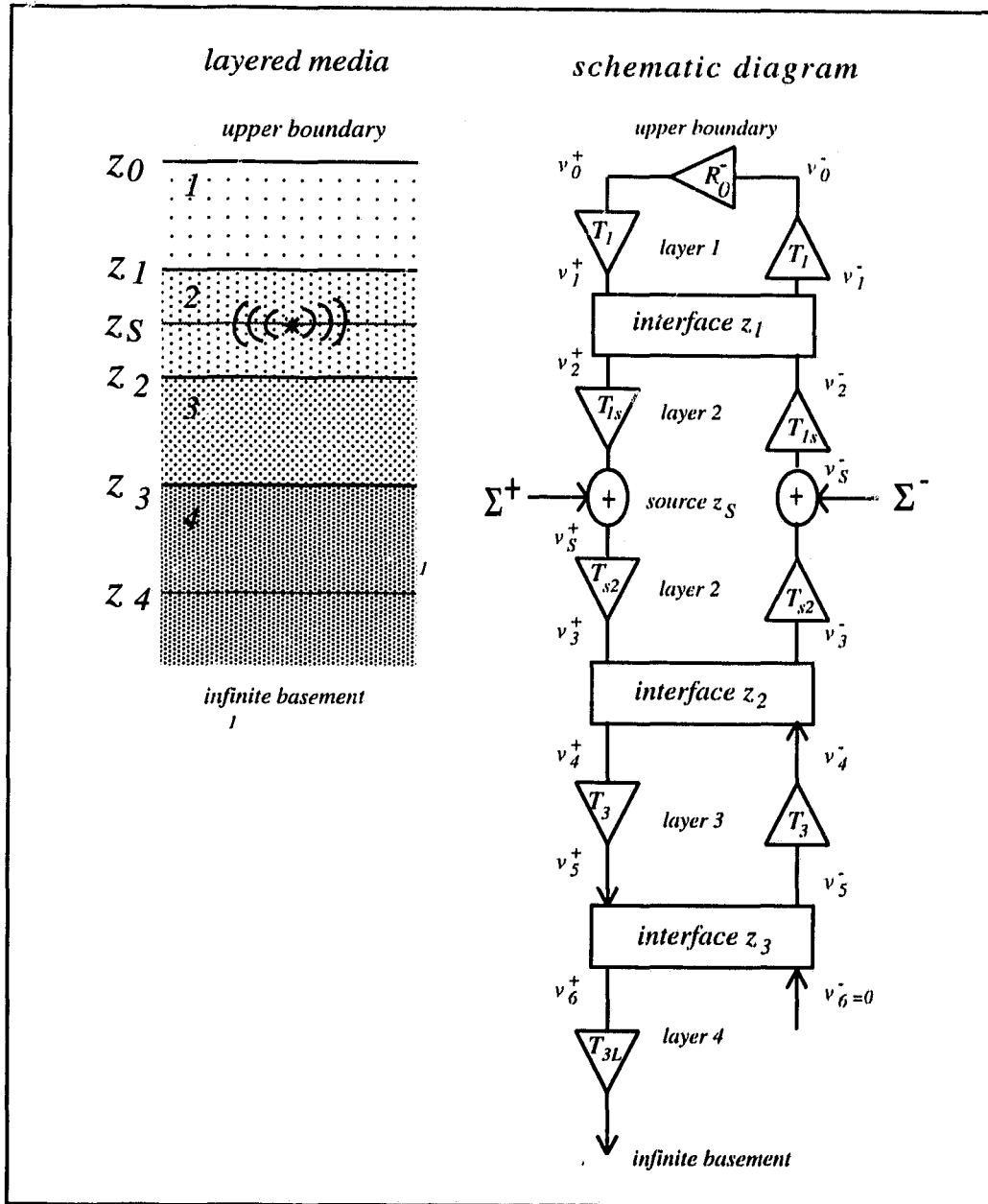


Figure 4.7: The schematic ladder diagram is constructed by connecting the scattering networks for each layer and interface in the waveguide together in series. The total network emulates vertical propagation of cylindrical and plane waves through the waveguide.

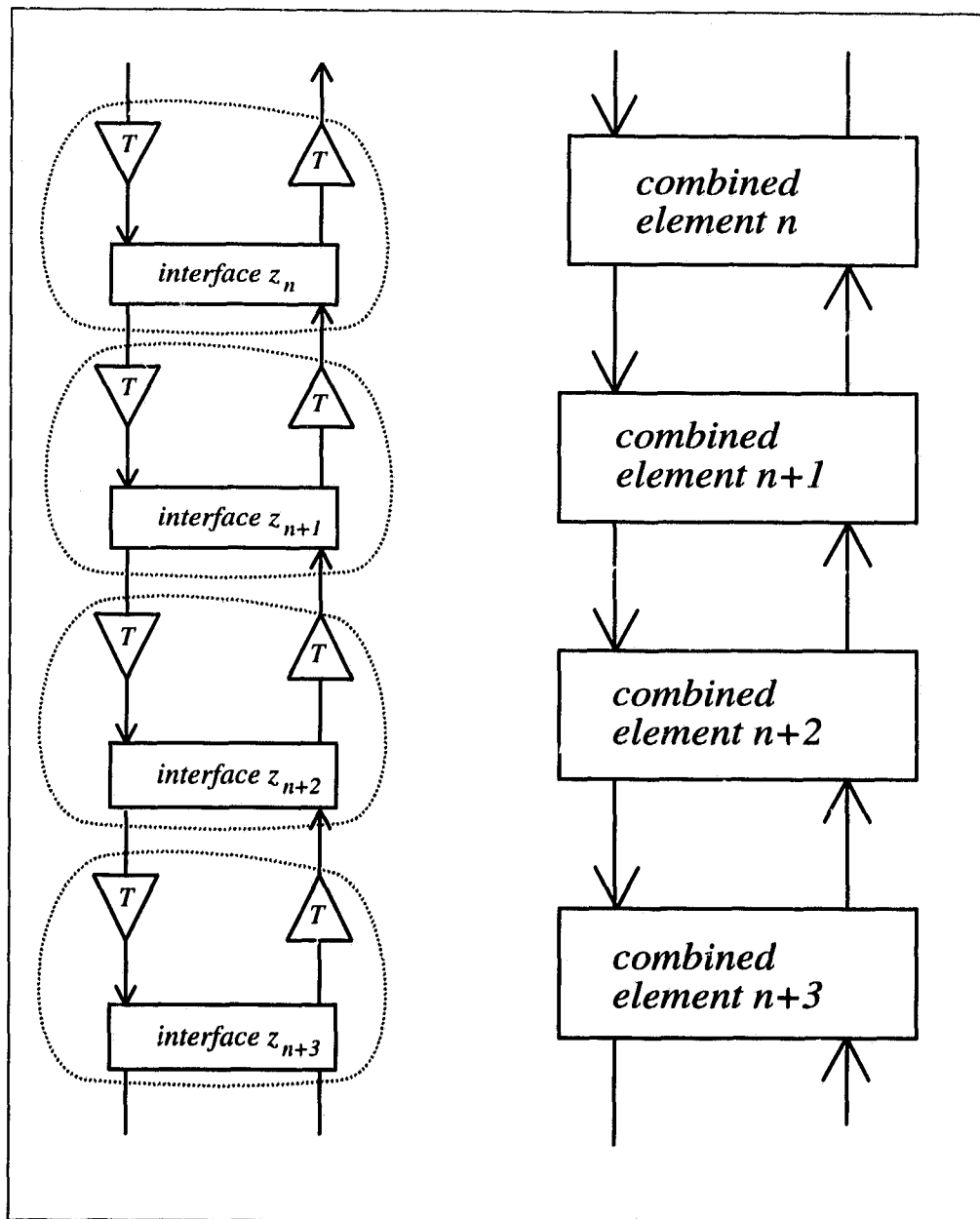


Figure 4.9: Components in the schematic diagram can be combined in different ways to eliminate unknown variables and compress the size of the global matrix.

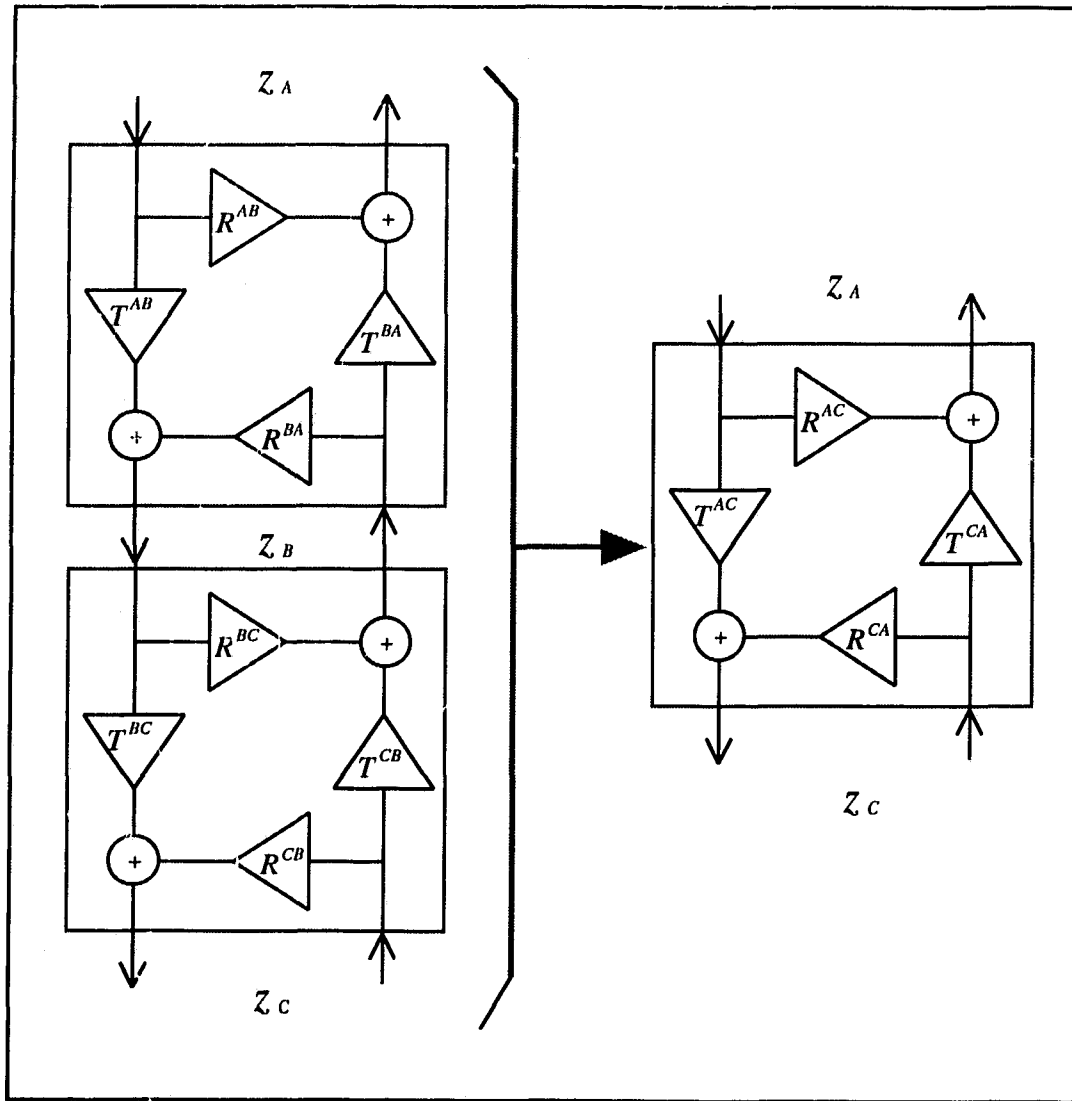


Figure 4.10: Two scattering networks, S_{AB} and S_{BC} , connected together. These can be combined into a single representative scattering network S_{AC} in a numerically stable way using the scattering matrix combination rules.

the *reverberation operators*. Notice that reverberation operators also appear in the recursion relations (4.65) due to the reverberation between the connected networks.

To derive the wave vector at some receiver depth z_R , we must split the waveguide at z_R and combine all of the components between z_R and z_S into a single scattering matrix \mathbf{S}_{RS} . All layers above and below both the source and receiver can again be combined into single reflection matrices. Fig.(4.12) shows the schematic diagram when $z_R < z_S$. By inspection we can write

$$\mathbf{v}^-(z_R) = \mathbf{T}_{RS}^- \mathbf{v}^-(z_S^-) + \mathbf{R}_{RS}^+ \mathbf{v}^+(z_R). \quad (4.70)$$

Solving for $\mathbf{v}^-(z_R)$ and using $\mathbf{v}^+(z_R) = \mathbf{R}_{0R}^- \mathbf{v}^-(z_R)$ gives

$$\begin{aligned} \mathbf{v}(z_R) &= \left\{ \left[\begin{array}{c} \mathbf{R}_{0R}^- \\ \mathbf{I} \end{array} \right] (\mathbf{I} - \mathbf{R}_{RS}^+ \mathbf{R}_{0R}^-)^{-1} \mathbf{T}_{RS}^- \right\} \mathbf{v}^-(z_S^-) \\ &= \left\{ \left[\begin{array}{c} \mathbf{R}_{0R}^- \\ \mathbf{I} \end{array} \right] (\mathbf{I} - \mathbf{R}_{RS}^+ \mathbf{R}_{0R}^-)^{-1} \mathbf{T}_{RS}^- \right\} (\mathbf{I} - \mathbf{R}_{SL}^+ \mathbf{R}_{0S}^-)^{-1} [\mathbf{R}_{SL}^+ \Sigma^+ + \Sigma^-] \end{aligned} \quad (4.71)$$

Fig. (4.12) also shows the situation when $z_R > z_S$, in which case

$$\begin{aligned} \mathbf{v}(z_R) &= \left\{ \left[\begin{array}{c} \mathbf{I} \\ \mathbf{R}_{RL}^+ \end{array} \right] (\mathbf{I} - \mathbf{R}_{SR}^- \mathbf{R}_{RL}^+)^{-1} \mathbf{T}_{SR}^+ \right\} \mathbf{v}^+(z_S^+) \\ &= \left\{ \left[\begin{array}{c} \mathbf{I} \\ \mathbf{R}_{RL}^+ \end{array} \right] (\mathbf{I} - \mathbf{R}_{SR}^- \mathbf{R}_{RL}^+)^{-1} \mathbf{T}_{SR}^+ \right\} (\mathbf{I} - \mathbf{R}_{0S}^- \mathbf{R}_{SL}^+)^{-1} [\Sigma^+ + \mathbf{R}_{0S}^- \Sigma^-]. \end{aligned} \quad (4.72)$$

Here again the expressions can be interpreted physically using rays.

4.5 Recovery of the total elastic field

We must invert the Fourier-Bessel transforms (4.11) to recover the elastic wave field from the stress displacement vector. This inversion determines the range of values for ω , p and m for which the stress displacement vector $\mathbf{b}(z_R)$ —and hence, the wave vector

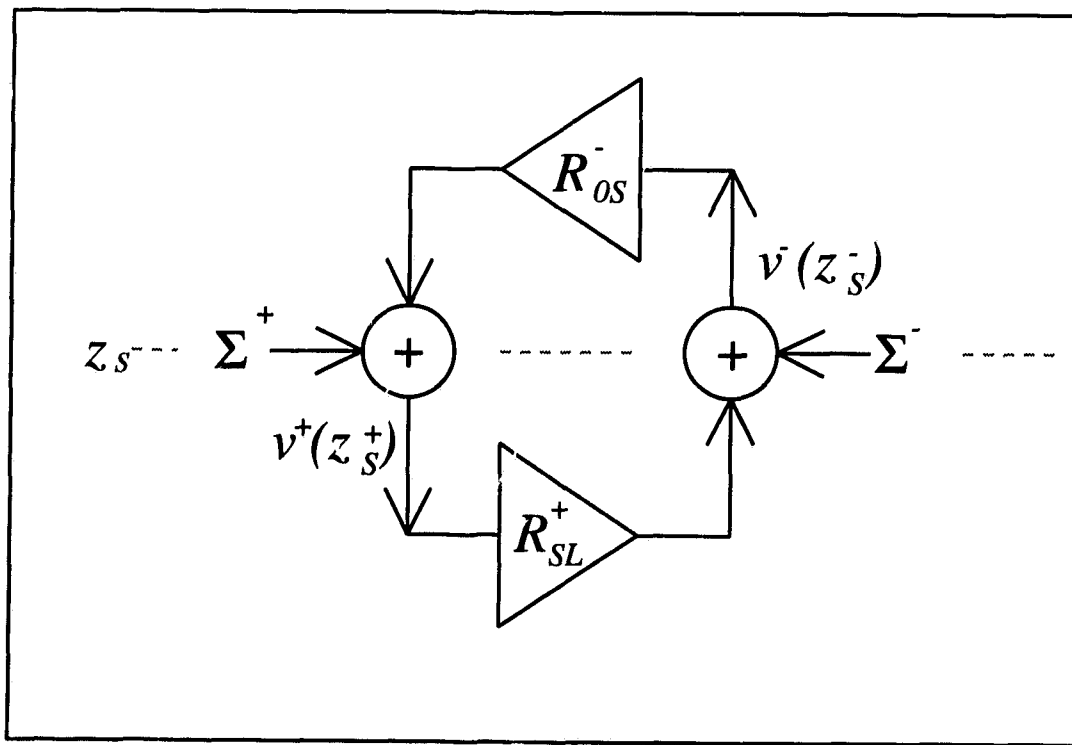


Figure 4.11: The waveguide can be reduced to its simplest form by repeatedly combining the scattering networks in the ladder diagram.

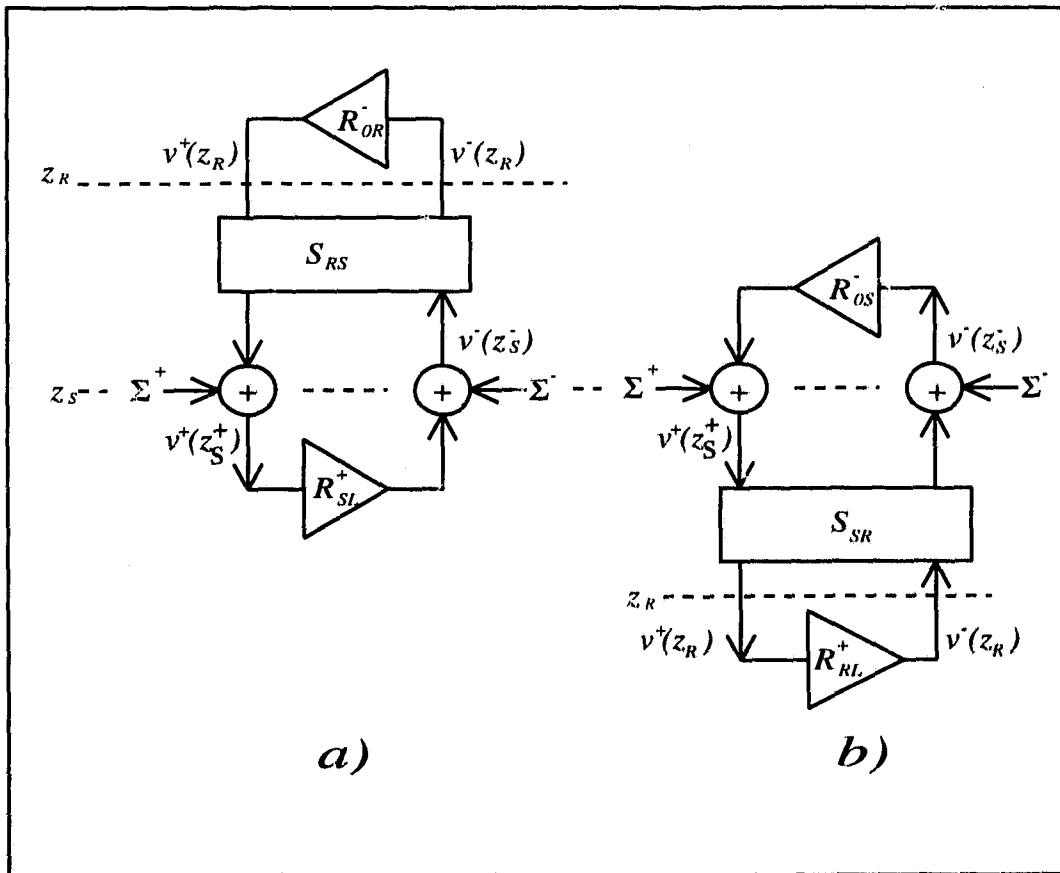


Figure 4.12: A single source and receiver. The waveguide must be split at the receiver depth z_R to compute the field there. The reduced schematic diagram takes a different form when the receiver is above or below the source.

$\mathbf{v}(z_R)$ —must be computed.¹³ The inverse transforms for the vector fields are most simply cast in terms of surface vector harmonics [71] [122]

$$\begin{aligned}\mathbf{R}_k^m(r, \phi) &= \hat{\mathbf{e}}_z Y_k^m(r, \phi), \\ \mathbf{S}_k^m(r, \phi) &= k^{-1} \nabla_h Y_k^m(r, \phi), \\ \mathbf{T}_k^m(r, \phi) &= -\hat{\mathbf{e}}_z \times \nabla_h Y_k^m(r, \phi),\end{aligned}\quad (4.73)$$

where

$$\begin{aligned}Y_k^m(r, \phi) &= J_m(kr) e^{im\phi}, \\ \nabla_h &\equiv \hat{\mathbf{e}}_r \partial_r + \hat{\mathbf{e}}_\phi r^{-1} \partial_\phi, \\ k &= \omega p\end{aligned}\quad (4.74)$$

These harmonics are orthogonal under the inner product [71, sect. 2.1.2] [122]

$$\langle \mathbf{X}, \mathbf{Y} \rangle = \int_0^\infty dr r \int_{-\pi}^{+\pi} d\phi \mathbf{X}(r, \phi) \cdot \mathbf{Y}^*(r, \phi), \quad (4.75)$$

so that

$$\langle \mathbf{R}_k^m, \mathbf{S}_k^m \rangle = \langle \mathbf{R}_k^m, \mathbf{T}_k^m \rangle = \langle \mathbf{S}_k^m, \mathbf{T}_k^m \rangle = 0 \quad (4.76)$$

and

$$\langle \mathbf{R}_k^m, \mathbf{R}_\kappa^\mu \rangle = \langle \mathbf{S}_k^m, \mathbf{S}_\kappa^\mu \rangle = \langle \mathbf{T}_k^m, \mathbf{T}_\kappa^\mu \rangle = \frac{2\pi \delta_{m\mu} \delta(k - \kappa)}{\sqrt{k\kappa}}. \quad (4.77)$$

Writing the displacement and traction vertical fields as a linear combination of these harmonics, it can be shown [71] that

$$\mathbf{u}(r, \phi, z, \omega) = \frac{1}{2\pi} \int_0^\infty dk k \sum_{m=-\infty}^{+\infty} (U\mathbf{R}_k^m + V\mathbf{S}_k^m + W\mathbf{T}_k^m) \quad (4.78)$$

and

$$\mathbf{t}(r, \phi, z, \omega) = \frac{\omega}{2\pi} \int_0^\infty dk k \sum_{m=-\infty}^{+\infty} (P\mathbf{R}_k^m + S\mathbf{S}_k^m + T\mathbf{T}_k^m). \quad (4.79)$$

Here U, V, P, S, W and T are the components of the stress-displacement vector computed via wave vectors using the matrix method. Recall that these components are all zero for $|m| > 2$ for the class of sources considered here.¹⁴

¹³The inversion from frequency to time domain will not be considered here since I am only considering the harmonic steady state.

¹⁴See Section(4.2.5).

The traction vector holds only three elements of the stress tensor $\mathbf{t} = [\tau_{rz}, \tau_{\phi z}, \tau_{zz}]$, whereas a complete stress field requires three more elements of the symmetric stress tensor, τ_{rr} , $\tau_{\phi\phi}$, and $\tau_{r\phi}$. All six unique components of the stress tensor can be derived from (4.78) using Hooke's law (2.2). The total field for each wave type is

$$\mathbf{u}(r, \phi, z, \omega) = \frac{\omega^2}{2\pi} \int_0^\infty dp p \sum_{m=-\infty}^{+\infty} e^{im\phi} \mathcal{L}(m, \omega, p, r, z) \cdot \begin{bmatrix} J_m(\omega pr) \\ J_{m+1}(\omega pr) \end{bmatrix}, \quad (4.80)$$

$$\boldsymbol{\tau}(r, \phi, z, \omega) = \frac{\omega^2}{2\pi} \int_0^\infty dp p \sum_{m=-\infty}^{+\infty} e^{im\phi} \mathcal{M}(m, \omega, p, r, z) \cdot \begin{bmatrix} J_{1..}(\omega pr) \\ J_{m+1}(\omega pr) \end{bmatrix},$$

where $\boldsymbol{\tau} = [\tau_{rr}, \tau_{r\phi}, \tau_{rz}, \tau_{\phi\phi}, \tau_{\phi z}, \tau_{zz}]^T$, and \mathcal{L} and \mathcal{M} are matrices for P-SV waves are¹⁵

$$\mathcal{L}(m, k, r, z) = \begin{bmatrix} \frac{m}{kr} V & -V \\ \frac{im}{kr} V & 0 \\ U & 0 \end{bmatrix}, \quad (4.81)$$

$$\mathcal{M}(m, k, r, z) = \begin{bmatrix} \left\{ \frac{2\mu}{kr^2(\lambda+2\mu)} [\eta_m - 2k^2 r^2 (\lambda + \mu)] V + \frac{\omega\lambda}{(\lambda+2\mu)} P \right\} & \frac{2\mu}{r} V \\ \frac{2im(m-1)\mu}{kr^2} V & -\frac{2im\mu}{r} V \\ \frac{m\omega}{kr} S & -\omega S \\ \left\{ \frac{-2\mu}{kr^2(\lambda+2\mu)} [\eta_m + k^2 r^2 \lambda] V + \frac{\omega\lambda}{(\lambda+2\mu)} P \right\} & \frac{-2\mu}{r} V \\ \frac{im\omega}{kr} S & 0 \\ \omega P & 0 \end{bmatrix}, \quad (4.82)$$

where

$$\eta_m = m(m-1)(\lambda + 2\mu). \quad (4.83)$$

¹⁵ \mathcal{M}_{11} and \mathcal{M}_{41} for P-SV waves, written in terms of the phase speeds rather than the Lamé coefficients, are

$$\mathcal{M}_{11} = \frac{2\rho\beta^2 k [2(\beta^2/\alpha^2 - 1) + m(m-1)/k^2 r^2] V + \omega\rho(1 - 2\beta^2/\alpha^2) P}{}$$

and

$$\mathcal{M}_{41} = \frac{2\rho\beta^2 k [2\beta^2/\alpha^2 - 1 - m(m-1)/k^2 r^2] V + \omega\rho(1 - 2\beta^2/\alpha^2) P}{}$$

For P waves, \mathcal{L} is the same as for P-SV waves with $V = -kP/(\omega\rho)$ (not at the source depth) and

$$\mathcal{M}(m, k, r, z) = \omega P \begin{bmatrix} 1 & 0 \\ 0 & 0 \\ 0 & 0 \\ 1 & 0 \\ 0 & 0 \\ 1 & 0 \end{bmatrix}; \quad (4.84)$$

for SH waves

$$\mathcal{L}(m, k, r, z) = W \begin{bmatrix} \frac{im}{kr} & 0 \\ -\frac{m}{kr} & 1 \\ 0 & 0 \end{bmatrix}, \quad (4.85)$$

$$\mathcal{M}(m, k, r, z) = \begin{bmatrix} \frac{2i\mu m(m-1)}{kr^2} W & -\frac{2i\mu m}{r} W \\ \frac{\mu}{k} \left[k^2 + \frac{2m}{r^2} (1-m) \right] W & -\frac{2\mu}{r} W \\ \frac{i\omega m}{kr} T & 0 \\ \frac{2i\mu m(1-m)}{kr^2} W & \frac{2i\mu m}{r} W \\ -\frac{\omega m}{kr} T & \omega T \\ 0 & 0 \end{bmatrix}. \quad (4.86)$$

Chapter 5

Modes in layered media

We have seen that the field due to a harmonic point source can be computed by evaluating the Fourier-Bessel transforms (4.80). Perhaps the most powerful analytic method for evaluating such integrals is the residue theorem, which reduces the integral to a sum over the residues of poles in the complex plane, offering an alternative to direct numerical integration. In this chapter it is shown that the poles of the Fourier-Bessel transforms are the *normal modes* of the waveguide, and the sum of the residues is the sum of the contribution of each normal mode to the field. The motivation for the switch is the prospect of greater computation speed, since the bulk of the mode computations can be carried out beforehand and saved for ready access during the BIE method. The normal mode approach is particularly efficient when the receiver is far from a source, when relatively few (*propagating*) modes contribute significantly.¹ Close to the source, however, all advantage may be lost because many short range (*evanescent*) modes are needed.

The modal representation of the field begins with a search for poles in the complex slowness plane, or, what amounts to the same thing, a search for the roots of the denominator of the Fourier-Bessel integrand. A computer search for the complex roots of any complicated function is difficult and uncertain; difficult because we must by analysis deduce roughly where and how close the roots are likely to be to direct the computer search

¹When describing a mode search, it is impossible to avoid distinguishing between modes such as *propagating*, *evanescent* and *leaky modes*, but it would detract to define them here. All mode names printed in italics are defined later in Chapter 6.

with confidence; and uncertain because we cannot, in general, verify conclusively that all of the roots have been found.² The problem is worse in the search for modes because different characteristic equations for roots result in different layers in the waveguide; all modes cannot be detected at a single depth. In an exhaustive mode search, we must therefore scan many different characteristic equations for roots simultaneously. Existing normal mode programs simplify matters by aiming to find just the *propagating* modes whose vibrations dominate the total field far from a source, and in ocean acoustics they are often limited to modes whose vibrations extend significantly into the water column. This partial approach is efficient and accurate when the source and receiver are positioned accordingly,³ but in the BIE method, the receiver is the boundary integration variable and the source the computation point, and they come very close together—actually touching in the limit in the surface-field equation—making short-acting *evanescent* modes indispensable. The receiver may also lie within the sea floor or an ice plate, where modes confined within those solid media dominate the field, making it necessary to include modes vibrating outside the water column. A new exhaustive search method was therefore required.

A robust *channel matrix* method for the mode search is described here. It builds upon the *scattering matrix* method of the last chapter, and it forms the basis for a new normal mode computer program called SAMPLE—an acronym for Seismo-Acoustic Mode Program for Layered Environments—, written specially for the extreme demands of the BIE method.

5.1 The discrete and continuous spectrum

Let us apply the residue theorem to the Fourier-Bessel transforms (4.80) by first closing the contour of integration, then writing the integral as a sum over the residues of

²In their practical treatment of root finding, Press et al., [100, chapt 9] stress, “It cannot be overemphasized, however, how crucially success depends on having a good first-guess for the solution, especially for multidimensional problems. This crucial beginning usually depends on analysis rather than numerics. Carefully crafted initial estimates reward you not only with reduced computational effort, but also with increased self-esteem.” This is especially true in the search for modes.

³A rare exception occurs when a resonant bottom mode is weakly coupled with a mode in the water column, for the accumulated effect of weak coupling over long ranges causes energy to alternate between the water column sediments as demonstrated in Section (6.5).

the encircled poles, plus contour integrals around any branch cuts. To this end, it can be shown that $p\mathcal{L}_{i1}$ and $p\mathcal{M}_{i1}$ are even functions of p when m is odd, but odd functions of p when m is even; and that $p\mathcal{L}_{i2}$ and $p\mathcal{M}_{i2}$ are even functions of p when m is even, but odd functions of p when m is odd.⁴ This permits integration along the entire real p axis, for writing the Bessel functions in terms of Hankel functions of the first kind we find

$$\begin{aligned} J_m(\omega pr) &= \frac{1}{2} \left[H_m^{(1)}(\omega pr) + H_m^{(2)}(\omega pr) \right], \\ &= \frac{1}{2} \left[H_m^{(1)}(\omega pr) - e^{im\pi} H_m^{(1)}(e^{i\pi}\omega pr) \right], \\ &= \begin{cases} \frac{1}{2} \left[H_m^{(1)}(\omega pr) - H_m^{(1)}(e^{i\pi}\omega pr) \right] & \text{for } m \text{ even,} \\ \frac{1}{2} \left[H_m^{(1)}(\omega pr) + H_m^{(1)}(e^{i\pi}\omega pr) \right] & \text{for } m \text{ odd,} \end{cases} \end{aligned} \quad (5.1)$$

which, together with the source jump terms, has just the symmetry properties to let us write (4.80) as⁵

$$\begin{bmatrix} \mathbf{u}(r, \phi, z, \omega) \\ \boldsymbol{\tau}(r, \phi, z, \omega) \end{bmatrix} = \frac{\omega^2}{4\pi} \int_{-\infty}^{\infty} dp p \sum_{m=-2}^{+2} e^{im\phi} \begin{bmatrix} \mathcal{L}(m, \omega, p, r, z) \\ \mathcal{M}(m, \omega, p, r, z) \end{bmatrix} \cdot \begin{bmatrix} H_m^{(1)}(\omega pr) \\ H_{m+1}^{(1)}(\omega pr) \end{bmatrix} \quad (5.2)$$

(Recall that \mathbf{u} has three rows and $\boldsymbol{\tau}$ six, and \mathcal{L} is a 3×2 matrix and \mathcal{M} a 6×2 .) The Hankel function has a branch point at the origin, and its branch cut will be taken along the negative real axis [4]. The contour integral over the negative axis lies above that cut as shown in Fig. (5.1).

Recall from Section (4.2.4) that the vertical slowness for each wave type in each layer requires a branch cut, but the wave vectors are nevertheless continuous across the branch cuts for layers of finite thickness. The contour of integration for a bounded waveguide can therefore be closed by a simple semicircular path of infinite radius as shown in the diagram. For an unbounded waveguide, however, the stress-displacement vector in \mathcal{L} and \mathcal{M} is discontinuous across the branch cuts for the vertical slowness in each infinite half

⁴It is a simple matter to check this numerically for any particular waveguide, by computing the terms for trial $\pm p$ and all orders of $m = -2 \dots 2$. An analytic proof is given in [35].

⁵The contour integral identity

$$\int_0^{\infty} f(k) J_m(kr) dk = \frac{1}{2} \int_{-\infty}^{\infty} f(k) H_m^{(1)}(kr) dk$$

generally holds provided $f(k)$ is an even function of k when m is odd, or $f(k)$ is an odd function of k when m is even.

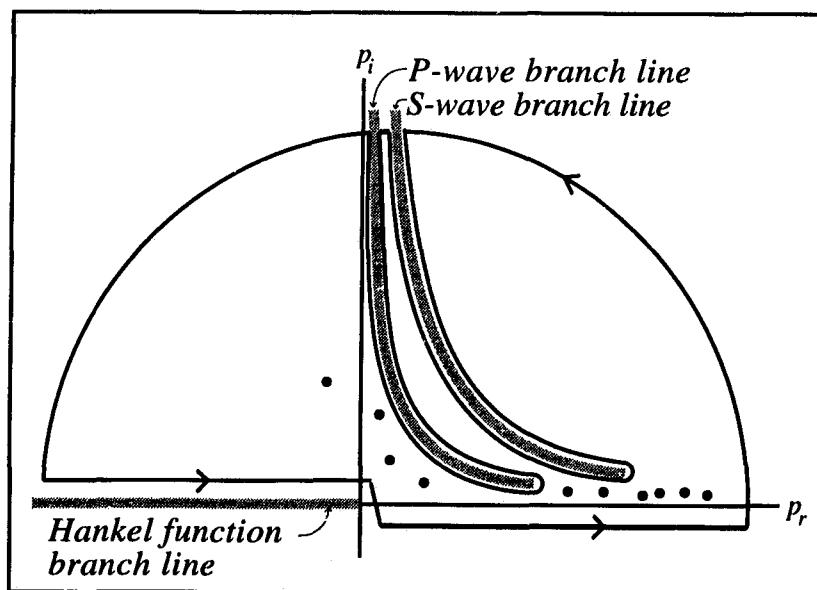


Figure 5.1: The slowness integral in the Fourier-Bessel transform can be extended to the entire real axis. It lies just above the branch cut for the Hankel function along the negative real axis, and just below the positive real axis to avoid hitting poles (circular dots) due to resonant modes of the waveguide.

space, and the contour must be deformed to exclude the cuts or venture on to improper Riemann sheets to keep the integrands continuous. In any case, the infinite semicircular contour integral vanishes because the Hankel function decays exponentially [2, eq. 9.2.3]

$$\left| H_m^{(1)}(\omega pr) \right| \rightarrow \left| \sqrt{\frac{2}{\pi \omega pr}} e^{i(\nu pr - \frac{1}{2} m \pi - \frac{1}{4} \pi)} \right| = \sqrt{\frac{2}{\pi \omega pr}} e^{-\omega \text{Im}\{p\}r} \rightarrow 0. \quad (5.3)$$

Applying the residue theorem to the closed contour, the original Fourier-Bessel transform (5.2) can therefore be written as a sum over the residues of encircled poles p_j , minus any branch line integrals

$$\begin{aligned} \begin{bmatrix} \mathbf{u}(r, \phi, z, \omega) \\ \boldsymbol{\tau}(r, \phi, z, \omega) \end{bmatrix} &= \frac{i\omega^2}{2} \sum_{m, p=p_j} \text{Res} \left\{ p e^{im\phi} \begin{bmatrix} \mathcal{L} \\ \mathcal{M} \end{bmatrix} \cdot \begin{bmatrix} H_m^{(1)}(\omega pr) \\ H_{m+1}^{(1)}(\omega pr) \end{bmatrix} \right\} \\ &\quad - \frac{\omega^2}{4\pi} \sum_m \int_{\text{branch lines}} dp \quad p e^{im\phi} \begin{bmatrix} \mathcal{L} \\ \mathcal{M} \end{bmatrix} \cdot \begin{bmatrix} H_m^{(1)}(\omega pr) \\ H_{m+1}^{(1)}(\omega pr) \end{bmatrix} \end{aligned} \quad (5.4)$$

The sum over the residues is called the discrete spectrum because it consists of distinct cylindrical waves of complex slownesses p_j —the modes of the waveguide. The residue term is evaluated in Section (5.5.4) below. The branch line integrals are called the continuous spectrum because they represent a continuum of cylindrical waves. Their contributions exhibit spherical spreading $e^{-\omega \text{Im}\{p\}r}/r$ or faster far from the source,⁶ so they become insignificant compared to modes which retain the $e^{-\omega \text{Im}\{p\}r}/\sqrt{r}$ behavior characteristic of

⁶Detailed asymptotic treatments of the branch line integrals for reflection of spherical waves from a plane interface can be found in [36], [16].

Spherical spreading of the branch line contribution in the bottom can be demonstrated using the method of stationary phase. The farfield range dependence of $H_m^{(1)}(\omega pr)$ together with the vertical dependence of $\mathbf{b}(z)$ give a combined range and phase dependence for terms within the integrals

$$e^{i\omega(pr+qz)}/\sqrt{r}$$

when z is in a homogeneous half space. q is real on the EJP branch line and, assuming a lossless medium, p is pure real along the horizontal portion of the branch line. The integral along the real p axis dominates in the farfield because the part of the integral along the imaginary axis decays exponentially with range. The integration in p can be converted to integration in vertical slowness q since $dp = -(q/p) dq$ with limits of integration $q = -\infty$ to ∞ . Stationary points are points q on the branch line where $d(pr+qz)/dq = (-qr/p+z) = 0$, and the method of stationary phase applied when $r \rightarrow \infty$ gives a $1/\sqrt{r}$ dependence to the branch line integral [113], which multiplied by the $1/\sqrt{r}$ dependence for the Hankel functions gives a total range dependence $1/r$.

Notice that the condition for a stationary point is that for a direct ray from source to receiver $q/p = z/r$. Other stationary points corresponding to multiply reflected rays also exist.

cylindrical waves in the far field. The field consists entirely of the discrete spectrum in bounded waveguides because they require no branch cuts so far as the residue theorem is concerned.

5.2 The condition for modes

The poles in the integrand of (5.2) enter \mathcal{L} and \mathcal{M} through the reverberation operators, for \mathcal{L} and \mathcal{M} depend on the elements of the stress-displacement vector $\mathbf{b}(\mathbf{z})$, which in turn depend on the wave vector $\mathbf{v}(\mathbf{z})$, which in turn depend on $\mathbf{v}(z_S)$ at the source depth according to (4.24), which finally depend on the reverberation operators $(\mathbf{I} - \mathbf{R}_{0S}^- \mathbf{R}_{SL}^+)^{-1}$ and $(\mathbf{I} - \mathbf{R}_{SL}^+ \mathbf{R}_{0S}^-)^{-1}$ according to (4.68). From Cramer's rule for matrix inversion, the elements of the reverberation operators depend inversely on the determinant

$$\Delta = |\mathbf{I} - \mathbf{R}_{0S}^- \mathbf{R}_{SL}^+| = |\mathbf{I} - \mathbf{R}_{SL}^+ \mathbf{R}_{0S}^-| = 0, \quad (5.5)$$

which must be zero to create a pole. Returning to (4.68), then, we must have

$$\begin{aligned} (\mathbf{I} - \mathbf{R}_{0S}^- \mathbf{R}_{SL}^+) \mathbf{v}^+(z_S) &= \mathbf{0}, \\ (\mathbf{I} - \mathbf{R}_{SL}^+ \mathbf{R}_{0S}^-) \mathbf{v}^-(z_S) &= \mathbf{0}, \end{aligned} \quad (5.6)$$

at a mode. In strictly theoretical terms, a mode of vibration in a waveguide is a non-trivial solution $\mathbf{v}^\pm(z_S)$ to (4.68) in the absence of sources.

Since the depth z_S loses particular status for modes, $\mathbf{v}^\pm(z_S)$ actually represents the mode's characteristic vibrations at all depths $z_S = z$, and is called the *mode function*. Just as a mode cannot be detected by a receiver placed at depths where its vibrations are zero, the characteristic equation cannot detect a mode whose vertical mode function is zero at the depth where (5.5) is tested for roots. This is because the condition $\mathbf{v}^\pm(z_S) = \mathbf{0}$ implies that the determinants cannot be zero. Thus, it is necessary to test for a mode at a depth where its mode function is significantly large. Most mode search programs for ocean acoustics test for modes in the water column only (see [98][126][80] for example), in which case modes trapped in sediment layers may go undetected. To perform an exhaustive mode search, however, we must test the characteristic equation at many depths at once—in solid layers as well as fluid.

Notice that it is impossible to detect modes using (5.5) at depths where either \mathbf{R}_{SL}^+ or \mathbf{R}_{0S}^- are numerically zero, in which case $\Delta = 0$ reduces to the impossible condition $1 = 0$. This happens if z_S lies within an infinitely deep basement layer, because the down going reflection matrix \mathbf{R}_{SL}^+ is identically zero for all p ; or if z_S lies in a strongly evanescent layer, because vertical decay prevents waves from reaching interfaces where reflection might occur.

The unreduced global matrix G for a waveguide must be singular at the roots of the characteristic equation (5.5) because the reduced waveguide represents the same two-point boundary value problem. A non-trivial solution $\mathbf{v}^\pm(z_S)$ to (5.6) is just part of a larger null-field vector \mathbf{v} of the global matrix,

$$G\mathbf{v} = \mathbf{0}. \quad (5.7)$$

Thus, one way of testing for modes at many depths simultaneously, is by constructing the global matrix G for the waveguide, and searching for those slownesses p where G is singular. Following a suggestion by Dr. Trevor Dawson, I have used singular value decomposition (SVD) to test for singularity with excellent results.

5.2.1 Singular value decomposition (SVD)

SVD factors the (square) global matrix G into two complex orthogonal matrices, U and V , and a real diagonal matrix W

$$G = UWV^*, \quad (5.8)$$

where $*$ denotes the conjugate transpose [100, sect. 2.9]. The diagonal of W holds the singular values $w_i \geq 0$. The magnitude of the determinant of G is equal to the product of all the singular values since U and V are orthogonal; hence G is singular when one or more of its singular values w_i are zero. Moreover, assuming that the n 'th singular value w_n is zero, and post multiplying both sides of (5.8) by V , we find that $G_{nk}V_{kn} = 0$. That is to say, the columns of V whose same numbered singular values equal zero are vectors lying in the null-space of G . Together they form an orthonormal basis for the null-space because V is orthogonal.

Using SVD, we can 1) search for modes at all depths simultaneously by searching for zeros in the smallest singular value where the global matrix is singular; 2) identify and resolve uncommonly close (double) modes by monitoring the second smallest singular value; and 3) extract the vertical mode function (aside from a normalization factor) directly from the columns of V . The first two tasks are described further below—the mode search in Section (5.3.2), and double modes in Section (5.3.3). About the third, it should be noted that the vertical mode function, when extracted from V , gives the wave vector comprising the mode function at isolated depths (the layer interfaces) of the waveguide. From these, the wave vector $\mathbf{v}(z)$ can be computed at any depth using the scattering matrix method (4.66). The corresponding stress-displacement vector $\mathbf{b}(z)$ can be computed from $\mathbf{v}(z)$ using (4.24).⁷ The normalization that scales the mode function for use in the modal representation of the Green's function is derived later in Section (5.5).

5.2.2 The channel matrix method

In Section (4.3) we saw that the global matrix is a sparse banded matrix. This suggests that the singular values might be computed more efficiently using a SVD routine specially designed for banded matrices. I am not aware of such a routine, and neither did I write one. Another way to speed up the decomposition, possibly just as effective, is to reduce the size of the global matrix before it is decomposed, by grouping many layers into a single component in the schematic diagram using the scattering matrix method of the previous chapter.

In the process of grouping layers, it is important to ensure that the reduced matrix remains sensitive to modes trapped at any depth in the waveguide. This can be done by splitting the waveguide at a depth where the mode function is expected to be significantly large, which is the condition for sensitivity noted earlier; then grouping the interposing layers into single two-port networks in the schematic ladder diagram. I call this the *channel matrix* method. A sound *channel* usually refers to a band of layers bounding a minimum in

⁷When plotting a mode function as a function of depth, I prefer plotting \mathbf{b} because it shows all of the continuity and boundary conditions in an obvious way, whereas \mathbf{v} jumps discontinuously at every interface with a solid layer to satisfy the continuity and boundary conditions on \mathbf{b} . The question of which variables should be plotted also arises when potentials are used rather than wave vectors [44] [1]; potentials are likewise discontinuous at each solid interface.

the phase speed α in the water column, where sound resonates due to repeated reflections from the bounding high speed layers, as in the deep sound channel in ocean acoustics for example [17]. But let us use the term *channel* more generally for any band of layers in which the vibrations of a mode are significantly large. Then every mode in an elastic waveguide has a channel associated with it, regardless of the physical mechanism causing resonance.

Although an oceanic waveguide may have many thin layers approximating continuous variation in the sound speed profile, it typically has only a few channels at any given slowness p , and the computer time spent grouping many layers into just a few channels is considerably less than the time spent decomposing the unreduced global matrix. The channel matrix method therefore speeds up the search for modes using SVD, while ensuring that the search is sensitive to all modes in the waveguide. Before we can identify the channels in a waveguide, we must understand the mechanisms that trap modes, and that is the subject of Chapter 6. For the moment, let us proceed with the mode search, assuming that either the global or channel matrix method is in use, together with SVD to test for a mode.

5.3 The search for modes

5.3.1 Restricting the search area

We can estimate where modes must lie in the complex slowness plane in the following way. If the vibrations of a mode span a layer, and the thickness of that layer is greater than the P and S wave lengths, then its horizontal slowness p must lie close to the EJP branch cuts for the vertical slowness $q_{\alpha,\beta}$ for that layer, where the imaginary part of $q_{\alpha,\beta}$ is small, otherwise the vibrations will be vertically evanescent and not traverse the layer. The modes traversing a very thick layer must therefore be very close to its branch lines. The same reasoning applies to a stack of thin similar layers, for the accumulated effect of a number of thin evanescent layers is much the same as one thick representative layer spanning the same depths. Since all of the EJP branch lines for all of the layers in the waveguide lie fairly close together—within an “L”-shaped region along the real p axis, and up along the imaginary p axis, as shown in Fig. (5.2)—any mode whose vibrations span a significant depth in the waveguide must lie close to that “L”-shaped region; and this is

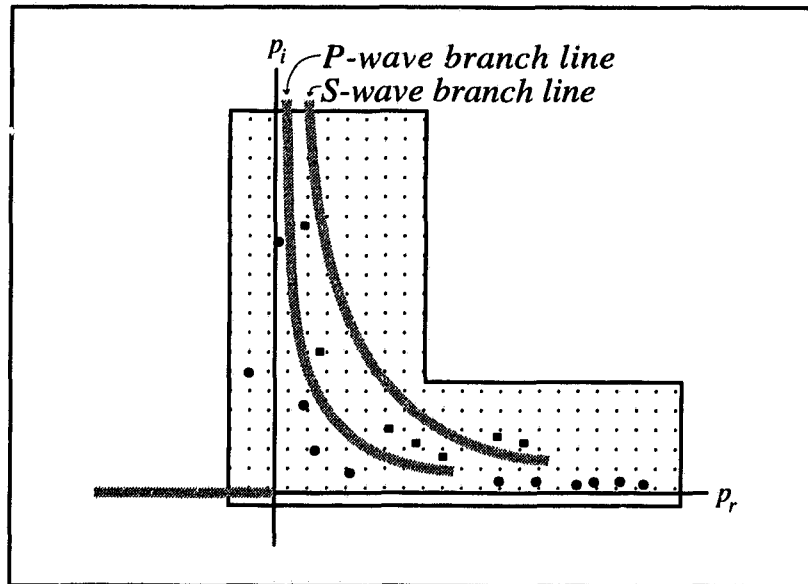


Figure 5.2: Any mode whose vibrations span a significant depth in the waveguide must lie close to the “L”-shaped region covering the EJP branch cuts for all layers in the waveguide because modes far from the branch lines decay during vertical transmission due to vertical evanescence. The locations of proper modes have been suggested by circular dots, and improper by square.

what we find in practice. Typically there is a finite number of modes along the base of the “L” ranging from the branch point furthest from the origin (corresponding to the smallest phase speed in the waveguide) to the corner of the “L” at the origin, and there is an infinite series of modes trailing upwards along the back of the “L”, along the imaginary p axis.

But there are two kinds of modes that may lie far outside that region because their vibrations span only a thin part of the waveguide. The first are *interface modes* confined close to an interface, which usually lie close to the real p axis, but beyond the branch point furthest from the origin. The second are *plate modes* confined within a thin contrasting layer, such as a floating ice plate. Because they are thin, the mode’s vibrations traverse the

layer, even when the vertical slowness q has a significantly large imaginary part, so plate modes can lie far from the branch lines and can prove most troublesome to find. To get us started on a mode search, however, it is enough to begin within the “L”-shaped branch line zone, for this keeps us from searching aimlessly where modes do not exist.

5.3.2 Using SVD to search for modes

As in a computer search for roots, the search for modes proceeds iteratively. Under the direction of the user, the location of a mode is first roughly located or “bracketed”, and then iteratively refined. In SAMPLE, a rough search scans the complex plane for minima in the smallest singular value w_1 , by computing it at evenly spaced points along a line—or series of parallel lines—in a region of the complex p plane selected by the user. For efficiency, the full decomposition need not be computed since only the singular values are required. It is important to plot the search function to visually verify that the rough search adequately samples the search function.

Taking up each minimum in turn, SAMPLE then executes a step-by-step refinement search by repeatedly computing the gradient of the w_1 surface using a finite difference scheme, then stepping in the direction of maximal decrease towards still smaller w_1 . Close to a zero in w_1 , however, the gradient search method must be abandoned because search surface resembles a conical hole with its apex reaching down to the complex plane, as shown in Fig. (5.3), where the finite difference scheme fails. SAMPLE then executes a final trial-and-error search in which w_1 is computed at a number of points distributed on a small circle centered at the latest point in the search; the radius of the circle being somewhat larger than the finite difference step last used in the gradient search. The search either steps to the minimum value found on the circle, or, if the center of the circle is the smallest value, the search remains where it is and the radius of the circle is decreased for a new set of trial points on a smaller circle. The procedure is repeated until the ratio of the trial radius to the magnitude of p at the deepest minimum is less than some preset tolerance. In practice, of course, minute numerical errors keep the smallest singular value from being identically zero at a mode, so a threshold must be set below which a minimum is considered a mode.

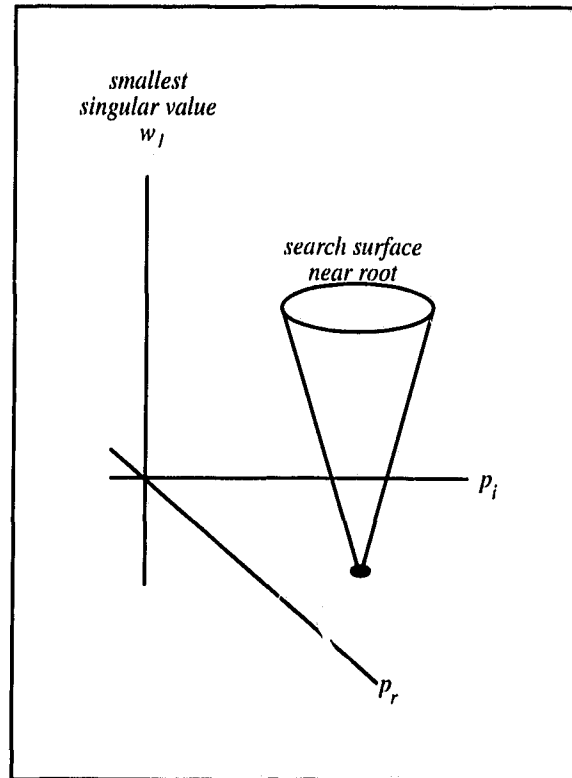


Figure 5.3: The search surface resembles a conical hole close to a zero in w_1 . The gradient method must be eventually be abandoned because the finite difference estimate of the gradient fails near the apex of the cone, and a final trial and error refinement is used locate the mode precisely.

5.3.3 Weakly coupled channels

One difficulty in the search for roots is the double root or pair of roots uncommonly close together. These can occur when the waveguide supports two weakly coupled channels separated by a band of vertically evanescent layers, each having a mode at almost the same slowness p . The theory behind these *close mode pairs* is the subject of Section (6.5), but for the moment let us consider how to identify and resolve them.

Kennett and Kerry [69] propose splitting the waveguide at a depth between the weakly coupled channels where their mode functions are numerically zero. The modes in each channel are then found using two searches, one for each channel separated from the other, thereby eliminating one mode or the other from each search. Although this channel separation method works very well as they show, it is difficult to implement in a generally applicable way, especially for oceanic waveguides where many different channels must be considered. Moreover, separating the channels disturbs the close mode locations slightly when their weak coupling is eliminated, and at times it may be their weak interaction that is of particular interest.

When using a global or channel matrix method together with SVD in the mode search, we can identify and resolve a double mode or close mode pair using both the smallest and second smallest singular values, w_1 and w_2 . Two perfectly coincident modes are easily identified since $w_1 = w_2 = 0$, in which case the SVD also computes two null-space vectors, one for each vertical mode function. For a close mode pair, the w_1 and w_2 surfaces viewed on a magnified scale look like two inverted cones with their points slightly displaced as shown in Fig. (5.4). Having refined the location of one mode in the pair using the iterative method described above, the location of the second can be found by

1. refining the location of a nearby minimum in w_2 where $w_1 = w_2$, point B, starting from the location of the known mode, point A;
2. estimating where $w_1 = 0$ by projecting a line through w_2 (A) and B to intersect the complex plane at point C;
3. refining the second mode location in w_1 , starting from C with a search resolution

somewhat less than the distance from B to C in the complex plane.

If step 1 fails to locate a nearby minimum in w_2 , there is no close mode and the procedure is abandoned. The search program therefore determines when, where, and at what resolution to search for a nearby mode. An example of a close mode pair is given in Section (6.5).

The question arises whether the method could be used more generally to direct the search from mode to mode in the complex plane. Unfortunately, the method is unreliable for widely spaced modes because it relies on linear interpolation. Furthermore, the behavior of w_1 and w_2 does not generally follow that shown in Fig. (5.4) except for close mode pairs in weakly coupled channels; there may not always be a minimum in w_2 between two modes trapped within the same channel for instance.

5.3.4 Searching for SH modes

Fluid layers sandwiched between solid layers totally decouple the SH waves propagating in the solids. This can be viewed as an extreme form of layer decoupling peculiar to SH waves. Using the first and second singular values, each band of consecutive solid layers can be searched simultaneously for modes, with the fluid layers treated as impenetrable vacuum layers that decouple the solid portions of the waveguide while also providing traction-free boundary conditions for SH waves. In SAMPLE, the user can switch from P-SV to SH mode computations using a simple software flag.

5.4 Verifying the mode search

At the end of a search we must always ask if any significant modes have been overlooked, or if any found are amiss.⁸ Several ways to check for missing modes and test for genuine modes are reviewed below.

⁸Sometimes a questionable mode may be found, whose minimum in the search function appears like that of a mode, though it does not reach down to the numerical zero of other modes. I find these sometimes occur at slownesses $p = 1/\alpha$ or $1/\beta$ (the branch points) for a layer in the waveguide. Why they occur is not known. It is interesting that Xie [134] reports similar "false" modes for a floating ice plate found using a different mode search method. But they are not always false. $p = 1/\beta$ is indeed a mode for SH waves in a free plate for example.

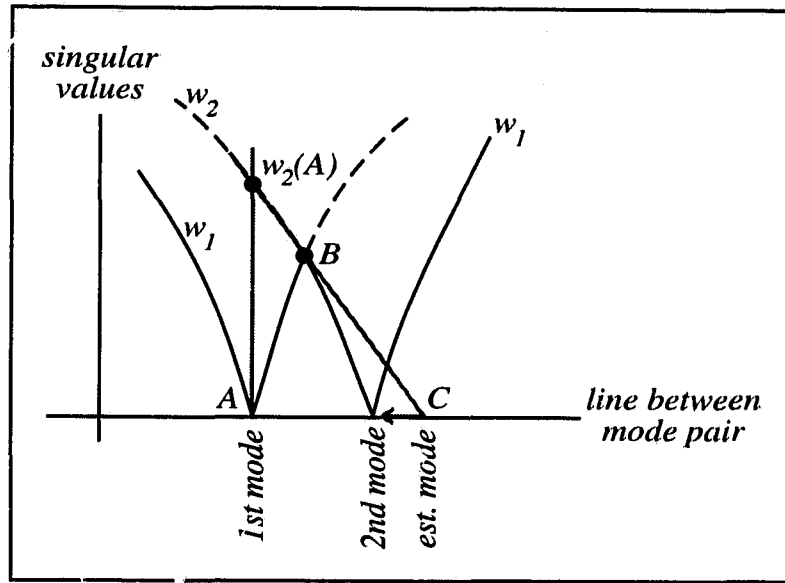


Figure 5.4: Once the position A of a mode has been found, a nearby mode pair can be found by 1) refining the location of a nearby minimum in w_2 where $w_1 = w_2$, point B; 2) estimating where $w_1 = 0$ by projecting a line through A and B to intersect the complex plane at point C; 3) refining the second mode location in w_1 , starting from C.

5.4.1 Node counting

In the elementary oceanic waveguide,⁹ the number of nodes (zero crossings) in the normal stress of each vertical mode function is a way of ordering the modes in a series. A missing mode can be identified simply by counting the nodes in the mode functions [66]. Unfortunately, the mode functions for P-SV modes in elastic media usually do not follow this simple ordering scheme because they are made up of a linear combination of waves having two vertical slownesses (q_α and q_β) rather than one (q_α). Furthermore, the mode functions—especially for *leaky modes*—are not real functions of depth as in the elementary waveguide, but complex functions produced by inhomogeneous waves, which ruins a direct relation between the nodes in a mode function and the mode ordering. Nevertheless, node counting can sometimes be used to detect missing modes in one or another portion of the mode series. It works best for *propagating duct modes* trapped in the water column, and for high order *evanescent modes* where the regular spacing of modes in the complex plane makes it easy to spot missing modes without node counting.

5.4.2 Contour Integration

The residue theorem shows that the contribution of a single mode to the elastic field—that is, the residue of its pole in the complex plane—must be equivalent to a contour integral encircling just that mode, and the contribution of many modes must be equivalent to a contour integral encircling just those modes. Thus, it is possible to test part of the mode series by comparing the resulting field to that computed by an encircling contour integral. The two will be different when a mode is missing or amiss. Unfortunately, a single test is inconclusive because the contribution of a missing mode might be negligibly small for the source and receiver used to conduct the test, making it impossible to detect its absence. The test should therefore be repeated using several source and receiver positions.

SAMPLE includes contour integration routines to test modes this way. Space does not permit elaboration, except to say that an arbitrary contour is specified by the user using any number of straight line segments in the complex plane, and that many

⁹See footnote on page 8.

of the subroutines for contour integration are already available among mode computation routines. When I added the contour integration routines to SAMPLE, I was not aware of any other contour integration program that computes all components of the elastic field due to seismic sources in layered elastic media. Dr. Henrik Schmidt has since pointed out to me that Kim [74] wrote such a program in 1989, and that it has been included in Dr. Schmidt's general purpose seismo-acoustic modeling package called OASES [111]. The main difference between the contour integration routines of SAMPLE and those of OASES is that SAMPLE evaluates Hankel integrals of the form (5.2), while OASES evaluates the Bessel integrals of the form (4.80). The contour of integration in SAMPLE may therefore follow any path in the complex slowness plane, to verify modes by applying the residue theorem in a flexible way, while the contour in OASES (and SAFARI) always runs parallel to the real slowness axis, to compute the field due to a point source.

5.4.3 Continuity and boundary conditions

If we are uncertain about a mode, its mode function should be checked to see if it satisfies all of the boundary and continuity conditions in the waveguide, simply by plotting the elements of its stress-displacement vector as a function of depth. Only a genuine mode satisfies all conditions in the waveguide simultaneously.

5.4.4 Rayleigh's Principle

Takeuchi and Saito [122] recommend verifying a mode using Rayleigh's Principle, which states that the average kinetic and potential energies are equal for the vertical mode function. Rayleigh's Principle is derived in the next section. Using the kinetic and potential energy terms, $\omega^2 I_1$ and I_2 from (5.14) in that section, the principle requires that $\omega^2 I_1 = I_2$. When the deviation

$$\epsilon = I_2 / (\omega^2 I_1) - 1 \quad (5.9)$$

is significantly large it indicates an erroneous mode or mode function. The test has proven most valuable, and it has been included in SAMPLE.

5.5 Five properties of modes

Rayleigh's principle, mode orthogonality, group velocity, mode excitation by a source, and mode normalization, can all be derived from the following integral identity. Consider any two modes a and b of the same wave type, P-SV or SH, having horizontal wavenumbers $k_a = p_a \omega_a$ and $k_b = p_b \omega_b$, respectively. P waves can be viewed as a special instance of P-SV. Using the partitioned forms of each mode's stress-displacement vector $\mathbf{b}(z) = [\mathbf{w}(z), \mathbf{t}(z)]^T$ from (4.32), we can construct the integral identity

$$\omega_b [\mathbf{w}_a(z_B) \cdot \mathbf{t}_b(z_B) - \mathbf{w}_a(z_A) \cdot \mathbf{t}_b(z_A)] = \omega_b \int_{z_A}^{z_B} \frac{\partial}{\partial z} (\mathbf{w}_a(z) \cdot \mathbf{t}_b(z)) dz. \quad (5.10)$$

Expanded, with the vertical derivatives eliminated using the original differential equations (4.5) or (4.6), the right side becomes

$$\omega_b \int_{z_A}^{z_B} \frac{\partial}{\partial z} (\mathbf{w}_a(z) \cdot \mathbf{t}_b(z)) dz = -\omega_b^2 I_1 + I_2, \quad (5.11)$$

where

$$I_1 = \begin{cases} \int_{z_A}^{z_B} \rho (U_a U_b + V_a V_b) dz & \text{for P-SV waves,} \\ \int_{z_A}^{z_B} \rho W_a W_b dz & \text{for SH waves.} \end{cases} \quad (5.12)$$

$$I_2 = \begin{cases} \int_{z_A}^{z_B} \left[\omega_a \omega_b \left(\frac{P_a P_b}{\rho \alpha^2} + \frac{S_a S_b}{\rho \beta^2} \right) + \rho k_b^2 v V_a V_b + \omega_b (k_a - k_b) \left[\left(1 - 2 \frac{\beta^2}{\alpha^2} \right) P_b V_a - U_a S_b \right] \right] dz & \text{for P-SV waves,} \\ \int_{z_A}^{z_B} \left(\omega_a \omega_b \frac{T_a T_b}{\rho \beta^2} + k_b^2 \rho \beta^2 W_a W_b \right) dz & \text{for SH waves,} \end{cases}$$

and $v = 4\beta^2 (1 - \beta^2/\alpha^2)$.

Taking z_A and z_B at the top and bottom of a bounded waveguide, the left side of (5.10) must be zero due to the conditions imposed on the stress-displacement vectors at an impenetrable boundary.¹⁰ In an infinitely deep waveguide, we must take the limit

¹⁰The impenetrable boundary conditions for the stress-displacement vector were reviewed in Section(4.2.3).

$z_B \rightarrow \infty$, and the left is again zero provided the modes lie on the proper Riemann sheet where the vertical mode functions decay exponentially with depth. If both modes lie on an improper Riemann sheet, however, $\mathbf{w}_a(z_B) \cdot \mathbf{t}_b(z_B)$, I_1 , and I_2 will be infinitely large because improper modes grow exponentially with depth. If just one mode is improper, the integrals may or may not blow up depending on the relative rates of exponential growth and decay in the improper and proper modes. In what follows, let us assume both are proper modes so that the integration spans the entire waveguide without difficulty.

5.5.1 Rayleigh's principle

Taking mode a and b as the same mode, (5.10) becomes

$$\omega^2 I_1 = I_2 \quad (5.13)$$

with

$$I_1 = \begin{cases} \int_{z_A}^{z_B} \rho (U^2 + V^2) dz & \text{for P-SV waves,} \\ \int_{z_A}^{z_B} \rho W^2 dz & \text{for SH waves.} \end{cases} \quad (5.14)$$

$$I_2 = \begin{cases} \int_{z_A}^{z_B} \left[\omega^2 \left(\frac{P^2}{\rho\alpha^2} + \frac{S^2}{\rho\beta^2} \right) + \rho k^2 v V^2 \right] dz & \text{for P-SV waves,} \\ \int_{z_A}^{z_B} \left(\omega^2 \frac{T^2}{\rho\beta^2} + k^2 \rho \beta^2 W^2 \right) dz & \text{for SH waves,} \end{cases}$$

This is Rayleigh's principle, which states that the kinetic energy $\omega^2 I_1$ in a vertical mode function is equal to the potential energy I_2 [71, sec. 11.4.4]. It was used in Section (5.4.4) to verify the modes found in the mode search.

5.5.2 Mode orthogonality

The identity (5.10) can be evaluated in two different ways for a pair of modes by switching their roles. An orthogonality relation derived by Takeuchi and Saito [122, sect.

III] follows from the difference of the two,

$$\begin{aligned}
 (\omega_a^2 - \omega_b^2) I_1 &= (k_a^2 - k_b^2) \int_{z_A}^{z_B} \rho v V_a V_b dz && \text{for P-SV waves,} \\
 &+ (k_a - k_b) \left(\omega_b \int_{z_A}^{z_B} \xi_{ab} dz + \omega_a \int_{z_A}^{z_B} \xi_{ba} dz \right) && (5.15)
 \end{aligned}$$

$$(\omega_a^2 - \omega_b^2) I_1 = (k_a^2 - k_b^2) \int_{z_A}^{z_B} \rho \beta^2 W_a W_b dz \quad \text{for SH waves,}$$

where

$$\xi_{ab} = S_b U_a - \left(1 - 2 \frac{\beta^2}{\alpha^2} \right) P_b V_a, \quad (5.16)$$

and I_1 is that of (5.12) for the corresponding wave type. This is an orthogonality relation inasmuch as the right side is zero for any two modes having the same frequency, and the left is zero for any two modes having the wavenumber.

5.5.3 Group velocity

Group velocity is an important property for the interpretation of data from distant impulsive sources, for no matter what shape the initial disturbance has in time, it becomes spread out far from the source in a wave train of varying horizontal slowness in which waves with horizontal wavenumber $k = \omega p$ move at a velocity roughly equal to the group velocity $c_g(k) = \partial\omega(k)/\partial k$ [113, sect. 9.3]. The group velocity for a mode can be approximately evaluated by changing its frequency slightly $\delta\omega$ while tracking the mode along its dispersion curve.¹¹ Proceeding this way, we can again apply (5.10) in two different ways, first with $\omega_a = \omega$, $\omega_b = \omega + \delta\omega$, $k_a = k = \omega p$, and $k_b = k + \delta k$, and then with $\omega_b = \omega$, $\omega_a = \omega + \delta\omega$, $k_b = k$, and $k_a = k + \delta k$. Taking the difference between the identities, retaining terms to first order, gives

$$0 = -2\omega (I_1 \delta\omega - p I_3 \delta k), \quad (5.17)$$

¹¹A dispersion curve is a plot of the horizontal slowness, wavenumber, phase speed, or group velocity of a mode as frequency ω is varied continuously. A mode whose phase speed is independent of ω is non-dispersive.

where I_1 is that of (5.12) with a denoting the original mode (ω, k) , and b the displaced $(\omega + \delta\omega, k + \delta k)$; and where

$$I_3 = \begin{cases} \int_{z_A}^{z_B} \frac{1}{2p} [U_a S_b + U_b S_a - (1 - 2\frac{\beta^2}{\alpha^2})(V_a P_b + V_b P_a) + 2p\rho v V_a V_b] dz & \text{for P-SV waves,} \\ \int_{z_A}^{z_B} \rho\beta^2 W_a W_b dz & \text{for SH waves.} \end{cases} \quad (5.18)$$

The exact group velocity is

$$c_g = \lim_{\delta k \rightarrow 0} \frac{\delta\omega}{\delta k} = \frac{pI_3}{I_1}, \quad (5.19)$$

with I_1 and I_3 evaluated when mode b is the same as a , in which case I_1 becomes (5.14) and

$$I_3 = \begin{cases} \int_{z_A}^{z_B} \left[\frac{1}{p} US - \frac{1}{p} \left(1 - 2\frac{\beta^2}{\alpha^2}\right) VP + \rho v V^2 \right] dz & \text{for P-SV waves,} \\ \int_{z_A}^{z_B} \rho\beta^2 W^2 dz & \text{for SH waves.} \end{cases} \quad (5.20)$$

5.5.4 Mode excitation

In Section (5.2.1) we saw that SVD computes a mode function to within a scale factor. It remains to determine that factor for a given source excitation, and this amounts to evaluating the residue term in (5.4). As noted earlier in Section (5.2), the poles of the integrand are found in the depth-dependent matrices \mathcal{L} and \mathcal{M} , and they are due to the determinants of the reverberation operators. In fact, elements of \mathcal{L} and \mathcal{M} share a common factor

$$\Delta^{-1} = \left| \mathbf{I} - \mathbf{R}_{0S}^- \mathbf{R}_{SL}^+ \right|^{-1} = \left| \mathbf{I} - \mathbf{R}_{SL}^+ \mathbf{R}_{0S}^- \right|^{-1}, \quad (5.21)$$

and we can isolate its role by factoring it out. The contribution of a single mode (pole) in (5.4) is then

$$\begin{bmatrix} \mathbf{u}(r, \phi, z, \omega) \\ \boldsymbol{\tau}(r, \phi, z, \omega) \end{bmatrix} = \frac{i\omega^2}{2} \sum_m \text{Res} \left(\frac{1}{\Delta} \right) p e^{im\phi} \begin{bmatrix} \tilde{\mathcal{L}} \\ \tilde{\mathcal{M}} \end{bmatrix} \cdot \begin{bmatrix} H_m^{(1)}(\omega pr) \\ H_{m+1}^{(1)}(\omega pr) \end{bmatrix}, \quad (5.22)$$

where $\tilde{\mathcal{L}} = \Delta \mathcal{L}$ and $\tilde{\mathcal{M}} = \Delta \mathcal{M}$ are regular at the mode.

To evaluate the residue, let us proceed as for group velocity, but this time let \mathbf{b}_b be the stress-displacement vector for cylindrical waves as they would be encountered in the original contour integral (4.80) for a given point source excitation, and let \mathbf{b}_a be that of a mode. Now the integral in (5.10) must be split at the source depth z_S because the cylindrical waves \mathbf{b}_b have a different representation for z above and below the source, through the wave vectors in (4.71) and (4.72); hence, the left side of (5.10) is not zero but

$$\begin{aligned} \omega_b \left[\mathbf{w}_a(z_S) \cdot \mathbf{t}_b(z_S^-) - \mathbf{w}_a(z_S) \cdot \mathbf{t}_b(z_S^+) \right] &= \omega_b \mathbf{w}_a(z_S) \cdot \left[\mathbf{t}_b(z_S^-) - \mathbf{t}_b(z_S^+) \right] \\ &= -\omega_b \mathbf{w}_a(z_S) \cdot \mathbf{S}_T. \end{aligned} \quad (5.23)$$

Here I have used the fact that $\mathbf{w}_a(z_A) \cdot \mathbf{t}_b(z_A) = \mathbf{w}_a(z_B) \cdot \mathbf{t}_b(z_B) = 0$, and the source jump $\mathbf{S} = [\mathbf{S}_W, \mathbf{S}_T]$ in \mathbf{b}_b at the source depth given by (4.56). A similar identity follows by reversing the roles of a and b , in which case the left side becomes

$$\begin{aligned} \omega_a \left[\mathbf{w}_b(z_S^-) \cdot \mathbf{t}_a(z_S) - \mathbf{w}_b(z_S^+) \cdot \mathbf{t}_a(z_S) \right] &= \omega_a \mathbf{t}_a(z_S) \cdot \left[\mathbf{w}_b(z_S^-) - \mathbf{w}_b(z_S^+) \right] \\ &= -\omega_a \mathbf{t}_a(z_S) \cdot \mathbf{S}_W. \end{aligned} \quad (5.24)$$

Taking the cylindrical waves very close to the mode, $k_b = k_a + \delta k$, and $\omega_a = \omega_b$, and taking the difference of the modified identities we get

$$\omega_a \mathbf{t}_a(z_S) \cdot \mathbf{S}_W - \omega_a \mathbf{w}_a(z_S) \cdot \mathbf{S}_T = 2k_a I_3 \delta k = 2\omega_a^2 p_a \tilde{I}_3 \delta p / \Delta. \quad (5.25)$$

where $\tilde{I}_3 = \Delta I_3$ and I_3 is given by (5.18). In the limit $k_b \rightarrow k_a$, the determinant

$$\Delta = \Delta(p_b) = \Delta(p_a + \delta p) \rightarrow \Delta(p_a) + (\partial \Delta / \partial p) \delta p = (\partial \Delta / \partial p) \delta p \quad (5.26)$$

because $\Delta(p_a) = 0$; hence

$$\mathbf{t}_a(z_S) \cdot \mathbf{S}_W - \mathbf{w}_a(z_S) \cdot \mathbf{S}_T = 2\omega_a p_a \tilde{I}_3 (\partial \Delta / \partial p)^{-1}, \quad (5.27)$$

and the residue in (5.22) is

$$\text{Res} \left(\frac{1}{\Delta} \right) = (\partial \Delta / \partial p)^{-1} = \frac{\mathbf{t}_a(z_S) \cdot \mathbf{S}_W - \mathbf{w}_a(z_S) \cdot \mathbf{S}_T}{2\omega_a p_a \tilde{I}_3}. \quad (5.28)$$

Here I have equated \mathbf{b}_a and \mathbf{b}_b when evaluating \tilde{I}_3 , simplifying it to I_3 in (5.20) for just the mode \mathbf{b}_a because the scaling of \mathbf{b}_a is arbitrary, and because $\tilde{\mathbf{b}}_b$ is directly proportional

to \mathbf{b}_a in the limit $k_b \rightarrow k_a$.¹² The field due to a mode is finally

$$\begin{bmatrix} \mathbf{u}(r, \phi, z, \omega) \\ \boldsymbol{\tau}(r, \phi, z, \omega) \end{bmatrix} = \frac{i\omega}{4} \sum_m \frac{\mathbf{t}(z_S) \cdot \mathbf{S}_W - \mathbf{w}(z_S) \cdot \mathbf{S}_T}{I_3} e^{im\phi} \begin{bmatrix} \mathcal{L} \\ \mathcal{M} \end{bmatrix} \cdot \begin{bmatrix} H_m^{(1)}(\omega pr) \\ H_{m+1}^{(1)}(\omega pr) \end{bmatrix}, \quad (5.29)$$

where I_3 , \mathcal{L} , and \mathcal{M} are all expressed in terms of the arbitrarily scaled vertical mode function $\mathbf{b}_a = \mathbf{b} = [\mathbf{w}, \mathbf{t}]^T$. The excitation of a mode by a source therefore depends both on the vertical mode function at the source depth, and on the jump in the stress-displacement vector caused by the source.¹³

5.5.5 Mode normalization

Since a mode can be scaled arbitrarily, a proper mode can always be scaled to make $I_3 = 1$. The field due to a mode (5.29) then simplifies to

$$\begin{bmatrix} \mathbf{u}(r, \phi, z, \omega) \\ \boldsymbol{\tau}(r, \phi, z, \omega) \end{bmatrix} = \frac{i\omega}{4} \sum_m \left(\hat{\mathbf{t}}(z_S) \cdot \mathbf{S}_W - \hat{\mathbf{w}}(z_S) \cdot \mathbf{S}_T \right) e^{im\phi} \begin{bmatrix} \mathcal{L} \\ \mathcal{M} \end{bmatrix} \cdot \begin{bmatrix} H_m^{(1)}(\omega pr) \\ H_{m+1}^{(1)}(\omega pr) \end{bmatrix}; \quad (5.30)$$

the $\hat{\mathbf{t}}$ denoting that $\hat{\mathbf{t}}$ and $\hat{\mathbf{w}}$ have been normalized.

5.6 Vertical energy flow in a mode

Increasing the viscoelastic absorption in layers where the vertical mode function is significantly large obviously makes a mode decay more quickly with range. Less obvious

¹²The fact that $\tilde{\mathbf{b}}_b$ is directly proportional to \mathbf{b}_a follows from the general result, that the solution to a nearly singular matrix equation multiplied by its vanishing determinant ($\tilde{\mathbf{b}}_b$) is directly proportional to the null-space vector (\mathbf{b}_a). In a global matrix formulation for the wave vector, for example,

$$G\mathbf{v} = \boldsymbol{\Sigma},$$

for which the solution is

$$\mathbf{v} = V W^{-1} U^* \boldsymbol{\Sigma}$$

using singular value decomposition (5.8). The determinant $|G| = |U||V| \cdot w_1 \cdot w_2 \cdot w_3 \cdots$, where the magnitude of $|U|$ and $|V|$ are unity, and w_i are singular values in the diagonal matrix W . As the smallest singular value $w_1 \rightarrow 0$ near a mode,

$$|G| v_j \rightarrow |U||V| \cdot w_2 \cdot w_3 \cdots V_{j1} U_{1k} \Sigma_k \propto V_{j1}.$$

That is, $|G| \mathbf{v}$ is directly proportional to the first column of V , which is the null-space vector of G and therefore the vertical mode function. It follows that the stress-displacement vector $\tilde{\mathbf{b}}_b = \Delta \mathbf{b}_b \propto \mathbf{b}_a$ in the limit $k_b \rightarrow k_a$ when k_a is a mode.

¹³The source jump terms $\mathbf{S} = [\mathbf{S}_W, \mathbf{S}_T]^T$ were derived in Section (4.2.5).

perhaps is the fact that decay due to absorption affects a mode uniformly at all depths, rather than causing more rapid decay in lossy layers than in lossless, because the vertical function cannot change its relative shape as it propagates in a range independent waveguide. Vertical energy flow in a mode preserves the shape of a mode function by transferring energy vertically from lossless to lossy layers at precisely the rate needed to keep the relative strengths of the vibrations in each layer constant, and this makes vertical energy flow of interest in viscoelastic media.

The energy flow through an element of surface is given by [61, p. 28]

$$df = \partial_t \mathbf{u} \cdot \mathbf{t} \, ds = \underset{\sim}{\mathcal{F}} \cdot \hat{\mathbf{n}} \, ds, \quad (5.31)$$

where \mathbf{u} and \mathbf{t} are the displacement and traction on the surface, $\underset{\sim}{\mathcal{F}}$ is the energy flux density ($\mathcal{F}_i = -\tau_{ki} \partial_t u_k$), and $\hat{\mathbf{n}} \, ds$ is the surface element vector. The vertical flux density is therefore

$$\mathcal{F}_z = \underset{\sim}{\mathcal{F}} \cdot \hat{\mathbf{e}}_z = \partial_t \mathbf{u} \cdot \mathbf{t}, \quad (5.32)$$

where $\mathbf{t} = (\tau_{rz}, \tau_{\phi z}, \tau_{zz})$. Averaging the oscillatory flux over a single period $T = 2\pi/\omega$ gives [61, p. 57]

$$\langle \mathcal{F}_z \rangle = \frac{1}{T} \int_0^T \mathcal{F}_z \, dt = \frac{1}{2} \partial_t \mathbf{u} \cdot \mathbf{t}^* = -i\omega \mathbf{u} \cdot \mathbf{t}^*, \quad (5.33)$$

in which the asterisk denotes the complex conjugate. The real and imaginary parts of $\langle \mathcal{F}_z \rangle$ are the real and reactive vertical energy flux density.

Now let us consider the axially symmetric ($m = 0$) contribution from the j 'th mode alone,¹⁴ when normalized to the strength of its excitation. Then (5.30) becomes

$$\begin{bmatrix} \mathbf{u}(r, \phi, z, \omega) \\ \boldsymbol{\tau}(r, \phi, z, \omega) \end{bmatrix} = \frac{i\omega^2}{2} p_j \begin{bmatrix} \mathcal{L}(p_j) \\ \mathcal{M}(p_j) \end{bmatrix} \cdot \begin{bmatrix} H_0^{(1)}(\omega p_j r) \\ H_1^{(1)}(\omega p_j r) \end{bmatrix}, \quad (5.34)$$

¹⁴It should be noted that the energy flux density for an elastic field consisting of several modes is not simply the sum of the energy flux for each mode considered independently, because energy is of second order in the field variables. Nevertheless, it is the energy of a single mode that is of interest here.

and substituting \mathbf{u} and \mathbf{t} from this into the vertical flux (5.33) we find

$$\langle \mathcal{F}_z \rangle = -i\omega \left(\frac{\omega^4 |p_j|^2}{4} \right) \left([\mathcal{L}] \begin{bmatrix} H_0^{(1)} \\ H_1^{(1)} \end{bmatrix} \right) \cdot \left(\begin{bmatrix} \mathcal{M}_{31} & \mathcal{M}_{32} \\ \mathcal{M}_{51} & \mathcal{M}_{52} \\ \mathcal{M}_{61} & \mathcal{M}_{62} \end{bmatrix}^* \begin{bmatrix} H_0^{(1)} \\ H_1^{(1)} \end{bmatrix} \right)^*, \quad (5.35)$$

which can be simplified using \mathcal{L} and \mathcal{M} in (4.81) through (4.86), giving

$$\begin{aligned} \langle \mathcal{F}_z \rangle &= \frac{-i\omega^6 |p_j|^2}{4} \left(UP^* |H_0^{(1)}|^2 + VS^* |H_1^{(1)}|^2 \right) \quad \text{for a P-SV mode;} \\ \langle \mathcal{F}_z \rangle &= \frac{-i\omega^6 |p_j|^2}{4} \left(WT^* |H_1^{(1)}|^2 \right) \quad \text{for an SH mode.} \end{aligned} \quad (5.36)$$

At long ranges from the source, the asymptotic form of the Hankel function (5.3) gives

$$|H_0^{(1)}| \approx |H_1^{(1)}| \rightarrow \left| \sqrt{\frac{2}{\pi\omega p_j r}} \right| \exp[-\omega \operatorname{Im}(p_j) r]; \quad (5.37)$$

hence

$$\begin{aligned} \langle \mathcal{F}_z \rangle &= \frac{-i\omega^5 |p_j|}{2\pi r} (UP^* + VS^*) \exp[-2\omega \operatorname{Im}(p_j) r] \quad \text{for a P-SV mode;} \\ \langle \mathcal{F}_z \rangle &= \frac{-i\omega^5 |p_j|}{2\pi r} WT^* \exp[-2\omega \operatorname{Im}(p_j) r] \quad \text{for an SH mode.} \end{aligned} \quad (5.38)$$

Separating the vertical dependence gives a measure of the real vertical energy transport in a mode

$$\begin{aligned} \mathcal{Y}(z) &\equiv \operatorname{Re}[-i(UP^* + VS^*)] \quad \text{for a P-SV mode;} \\ \mathcal{Y}(z) &\equiv \operatorname{Re}[-i(WT^*)] \quad \text{for an SH mode.} \end{aligned} \quad (5.39)$$

A mode transports energy downwards at depths where $\mathcal{Y}(z)$ is positive, but upwards where negative.

Now let us separate the vertical flux into up and down going P and S wave components for *propagating* P-SV mode in lossless media (p, α, β all real). Then replacing the stress-displacement elements with their corresponding wave vector elements using (4.24), we find

$$\mathcal{Y} = \mathcal{Y}^P + \mathcal{Y}^S, \quad (5.40)$$

where \mathcal{Y}^P and \mathcal{Y}^S are independent P and S wave energy terms

$$\begin{aligned}\mathcal{Y}^P &= \frac{q_{\alpha r}}{2|q_{\alpha}|} (|P^+|^2 - |P^-|^2), \\ \mathcal{Y}^S &= \frac{q_{\beta r}}{2|q_{\beta}|} (|S^+|^2 - |S^-|^2).\end{aligned}\tag{5.41}$$

$q_{\alpha r}$ and $q_{\beta r}$ are the real parts of the vertical slowness, and P^{\pm} and S^{\pm} are the down and up going P and S wave components of the wave vectors. When $q_{\alpha r}$ and $q_{\beta r}$ are positive, the energy flows in the assumed directions: superscript “+” for down going energy and “—” for up; but if either is negative, then the corresponding vertical flux is reversed from the assumed directions. Thus it is the sign of the real vertical slowness that determines the direction of vertical energy flow.

More generally, when α , β , p and the wave vectors are all complex, the expression for \mathcal{Y} is much more complicated. But absorption is by assumption slight, so it only perturbs the propagating modes slightly, leaving the direction of vertical energy flow under the control of the sign of the real vertical slowness. In any case, the precise value of \mathcal{Y} can be evaluated numerically using the stress-displacement vector in (5.39), as I do later in Section (6.1.4), where, in apparent defiance of the radiation condition, I demonstrate the possibility upward energy flow from an infinitely deep basement layer.

5.7 The Green’s function for bounded waveguides by modal summation

5.7.1 The mode series

Evaluation of the Green’s function requires all modes that contribute significantly for the given source and receiver positions. To determine whether or not a given mode is important, we must look at its vertical mode function and horizontal range dependence. The vertical dependence in (5.30) shows that a mode will be insignificant if all components of the vertical mode function $\mathbf{b}(z)$ are zero at the source or receiver depths. A man-made source and receiver are often restricted to a band of layers, usually within the water column in ocean acoustics, or near the surface of the earth in geophysics; hence the modes whose vertical mode functions are zero at those depths can be omitted. But in the indirect BIE method, the

source and receiver locations vary freely, including nodes on the boundary of the inclusion, the location of sources generating the particular solutions, and the computation points for the whole-, surface-, and null-field equations; so more modes are generally required. The range dependence of a mode shows that a mode will be insignificant if the Hankel function becomes very small. With physical sources, we must specify a lower limit on the distance between the source and receiver r_{\min} because a real source is not point-like in its near-field. In the BIE method, we also must specify a minimum range r_{\min} for the ideal point source for numerical reasons. The Hankel functions in each mode are singular at $r = 0$, which makes the terms in the mode series very large terms, and the sum becomes lost in extreme cancellation.

The lower bound r_{\min} fixes an upper bound in the complex slowness plane above which modes cannot contribute significantly. As p in a mode series moves upwards term by term in the complex slowness plane, the argument of the Hankel function eventually satisfies $\omega p_i r \gg 1$, and the exponential asymptotic form of the Hankel function (5.3) can be used, which decays exponentially with further increases in the imaginary slowness p_i . Hence, we can safely assume that the significant modes lie below the value of p_i at which the exponential envelope of the Hankel functions reaches some small value ϵ ,

$$\epsilon > \left| e^{i\omega p r} \right| = \left| e^{-\omega p_i r} \right| \quad \text{with } 0 < \epsilon \ll 1, \quad (5.42)$$

which implies

$$p_i(r) < \frac{-\ln \epsilon}{\omega r} \leq \frac{-\ln \epsilon}{\omega r_{\min}}. \quad (5.43)$$

This fixes an upper bound on the “L”-shaped region of Fig. (5.2) for any range. When r_{\min} for a particular application is large, as it is for long range propagation modeling, all of the important modes must lie close to the real p axis. But when r_{\min} is small, the mode series, and therefore the mode search, must venture far from the real p axis. In the indirect BIE method, r_{\min} should be slightly smaller than the radius of the close neighborhood of a computation point, within which a boundary element is automatically designated as troublesome, to ensure that all of the significant modes are available.

5.7.2 Series convergence

The sum of a long series of complicated terms can be computed more quickly if the terms are first ordered from largest to smallest, for then we can test convergence as the summation progresses, possibly by checking if the latest terms added are negligibly small compared with the latest partial sum, to halt the series without adding all of its insignificant terms. A good way of ordering modes is to sort them from smallest to largest imaginary slowness p_i ; because, in a long series of *evanescent* modes, the magnitude of the terms eventually follows the exponential decay of the asymptotic Hankel function, making it likely that successive terms will on the whole be steadily decreasing. It is best to decide when a mode series has converged by testing only the exponential decay envelope of the Hankel function using (5.43), rather than testing the relative size of the latest term in the series. There are two reasons for this. When computing the entire Green's displacement and stress tensors due to a point source, there are a total of 27 unique field variables (three displacement and six stress for each of three Cartesian axes) that must be tested to assure convergence, making the convergence test itself a weighty burden, against which (5.42) appears trivial. More importantly, the vertical dependence of modes can make the contributions of a few sequential modes negligibly small, thereby fooling the convergence test to stop the series prematurely. False convergence tests can be reduced by requiring that a number of successive convergence tests have passed successfully, but the scheme would not be foolproof.

5.7.3 The Green's function singularity

For the Green's function to satisfy the equation of motion (2.50), it must have a singularity in order that its spatial gradient produces a δ -function behavior. In a bounded waveguide, this singularity arises from the infinite mode series, in part because of the singularity in the Hankel function range dependence of each series

$$\begin{aligned} \lim_{r \rightarrow 0} H_0^{(1)}(\omega pr) &= \frac{2i}{\pi} \lim_{r \rightarrow 0} \ln(\omega pr) = -\infty; \\ \lim_{r \rightarrow 0} H_m^{(1)}(\omega pr) &= -\frac{i}{\pi} \Gamma(m) \lim_{r \rightarrow 0} \left(\frac{1}{2}\omega pr\right)^{-m} = -\infty, \quad m > 0, \end{aligned} \tag{5.44}$$

(the $H_1^{(1)}$ singularity contributing a delta-function behavior $\delta(r)/r$), and in part because of lack of convergence in the infinite series of evanescent modes trailing upwards along the imaginary p axis (contributing $\delta(z - z_s)$). The infinite series of modes work to cancel out the Hankel function singularities of all modes along the vertical line through the source, while also shaping the delta-function singularity at the source depth. At very short ranges, then, the mode series for a point source becomes one of infinitely large terms whose mutual cancellation lose the finite sum in numerical error. The problem occurs at small horizontal ranges, regardless of the vertical separation of source and receiver, because the terms in the mode series are infinitely large. This is why we must place a lower bound r_{\min} on the range between source and receiver in (5.43), and why we encounter convergence problems in the BIE method for layered media whenever the computation point lies directly above or below the scattering inclusion.

Convergence problems of one sort or another always seem to plague near-field Green's function evaluations for layered media no matter what method is used. In unbounded waveguides, the branch line integrals face similar convergence problems because their integrands behave roughly like the evanescent mode series. Alternatively, the contour integrals (4.80) along the positive real p axis could be evaluated directly, with the range dependence in the integrands kept in terms of Bessel functions $J_m(\omega pr)$, which are well-behaved as $r \rightarrow 0$. No doubt avoiding the Hankel function singularities this way helps in the near field, but convergence problems still occur close to the source point due to oscillatory integrands, much as Gerstoft and Schmidt [50] report in their two-dimensional BIE method.¹⁵ It may be advantageous to switch from a modal to such a contour integral representation, depending on the proximity to the source and receiver, as Lu and Felson do in their hybrid ray-mode model [84] [85]. I do not explore the possibility here, but rely instead on the indirect BIE method to avoid the very near field altogether.

¹⁵To accelerate convergence of the slowly decaying oscillatory integrand for points the near field, Gerstoft and Schmidt force the integrands to zero artificially by multiplying them by a gradual monotonically decreasing function of $k = \omega p$.

5.8 Model verification

I have charted a rather long course to develop the channel matrix method for normal modes to compute the field due to a point source in layered media. To demonstrate that it is practicable, I will compare the SAMPLE program based upon it with the well-known and well-established SAFARI program (version 4.0) [109]. An exhaustive verification this way is not possible because SAFARI only supports axially symmetric sources (uniform explosive and vertical point source), only computes τ_{zz} , u_r , u_z ; and is not accurate at small ranges $r < \lambda_\alpha$. SAMPLE is equipped with Fast Fourier Transform (FFT) contour integration routines like those of SAFARI, but they are based upon the channel matrix method rather than the global matrix method of SAFARI. These will also be reported.¹⁶

5.8.1 Arctic ocean model

A shallow Arctic ocean sound speed profile is given in Table (5.1). The waveguide has a 3 m ice layer at the surface, a 200 m water column typical of the Arctic ocean [66] [130], two 2 m sediment layers at the sea floor, and 2000 m deep rock basement layer bounded below by an impenetrable rigid boundary. The field due a 20 Hz dilatational point source at a depth of 10 m and a vertical point source at the ice surface will be computed.

Let us begin with the search for modes closest to the real horizontal slowness axis. Fig. (5.5) shows the smallest and second smallest singular values, w_1 and w_2 , along the axis. w_1 is the search function whose minima suggest the presence of modes close to the axis. Mode locations were refined from these, and from other minima detected in the same way in searches along the P and S wave branch lines for the deep basement layer.¹⁷ Fig. (5.6) shows the modes in the complex slowness plane on a scale so expanded that the lowest order plate mode (mode 1) has been forced off the diagram. Fig. (5.7) shows the vertical mode functions for the first 5 modes ordered by descending p_r . There are other modes, such as evanescent modes needed in the very near field, and modes trapped in the two

¹⁶More extensive testing of all components in the elastic field could be done using the OASES model[111], which is much more complete than SAFARI (see page 15). I did not use OASES here because it is a very recent program, and I was unaware of its capabilities until very late in my project.

¹⁷The reason for searching along the branch lines for the basement layer in a bounded waveguide is that radiation modes are found nearby; see Section (6.4).

sediment layers, that have not been included in the search because they will not contribute significantly in these tests.

Now let us consider the SAMPLE and SAFARI contour integration models. When using a contour integration routine, it is recommended to plot the integrand for the desired field variable to ensure adequate sampling. Fig. (5.8) shows the magnitude of the vertical dependence in the integrand for τ_{zz} computed by SAFARI (dotted) and SAMPLE (dashed) at a depth of 10 m for the dilatational point source at depth 10 m. In both cases the contour was displaced slightly below the positive real slowness axis to avoid crossing directly over the poles due to modes. As it is, the sharp peaks indicate where the contour passes over the shoulder of a nearby pole due to a mode. The models differ by a constant scaling factor because SAFARI normalizes the field to its strength at one meter from the source, whereas SAMPLE uses the absolute strengths given to the source. The factor has been removed by normalizing each curve to its maximum value. Close agreement between the two curves makes them indistinguishable. Imposed upon Fig. (5.8) are the relative contributions of the dominant modes at a distant receiver. There is one mode at the horizontal slowness of every sharp peak in the contour due to the connection between modes and peaks. Perfect agreement between the peak heights and mode strengths should not be expected because multiplication by Hankel-function range dependence and integration over slowness transform the contour peaks into mode contributions. Fig. (5.9) shows the normal stress field plotted as a function of horizontal distance from the source. The three results are indistinguishable in the figure.

Fig. (5.10) shows the vertical displacement due to a vertical point force acting at the surface of the ice computed by all three models.

| layer no. | z upper (m) | z lower (m) | α (m/s) | β (m/s) | ρ (kg/m ³) |
|--------------|---------------------|---------------------|-----------------------|-----------------------|--------------------------------|
| 1 | 0.0 | 3.0 | 3300.0-33.00 <i>i</i> | 1730.0-20.00 <i>i</i> | 900.0 |
| 2 | 3.0 | 16.0 | 1436.3 | 0.0 | 1024.5 |
| 3 | 16.0 | 38.2 | 1436.3 | 0.0 | 1024.5 |
| 4 | 38.2 | 55.9 | 1436.7 | 0.0 | 1025.0 |
| 5 | 55.9 | 75.1 | 1438.3 | 0.0 | 1025.6 |
| 6 | 75.1 | 92.1 | 1439.9 | 0.0 | 1026.3 |
| 7 | 92.1 | 135.2 | 1440.6 | 0.0 | 1026.6 |
| 8 | 135.2 | 161.8 | 1441.5 | 0.0 | 1027.1 |
| 9 | 161.8 | 180.5 | 1443.2 | 0.0 | 1027.7 |
| 10 | 180.5 | 203.0 | 1444.3 | 0.0 | 1028.0 |
| 11 | 203.0 | 205.0 | 1446.0 | 0.0 | 1028.2 |
| 12 | 205.0 | 207.0 | 1575.0-28.86 <i>i</i> | 80.0-2.20 <i>i</i> | 1700.0 |
| 13 | 207.0 | 209.0 | 1650.0-24.18 <i>i</i> | 110.0 - 5.04 <i>i</i> | 1900.0 |
| 14 | 209.0 | 2209 | 5250.0-19.00 <i>i</i> | 2500.0-18.00 <i>i</i> | 2700.0 |

Table 5.1: Arctic profile with floating ice layer. The upper surface at $z = 0$ m is a traction-free boundary, and the deep bottom boundary at $z = 2209.0$ m is rigid and in welded contact with the basement solid.

SAMPLE: Plot of Singular Values Along Search Line

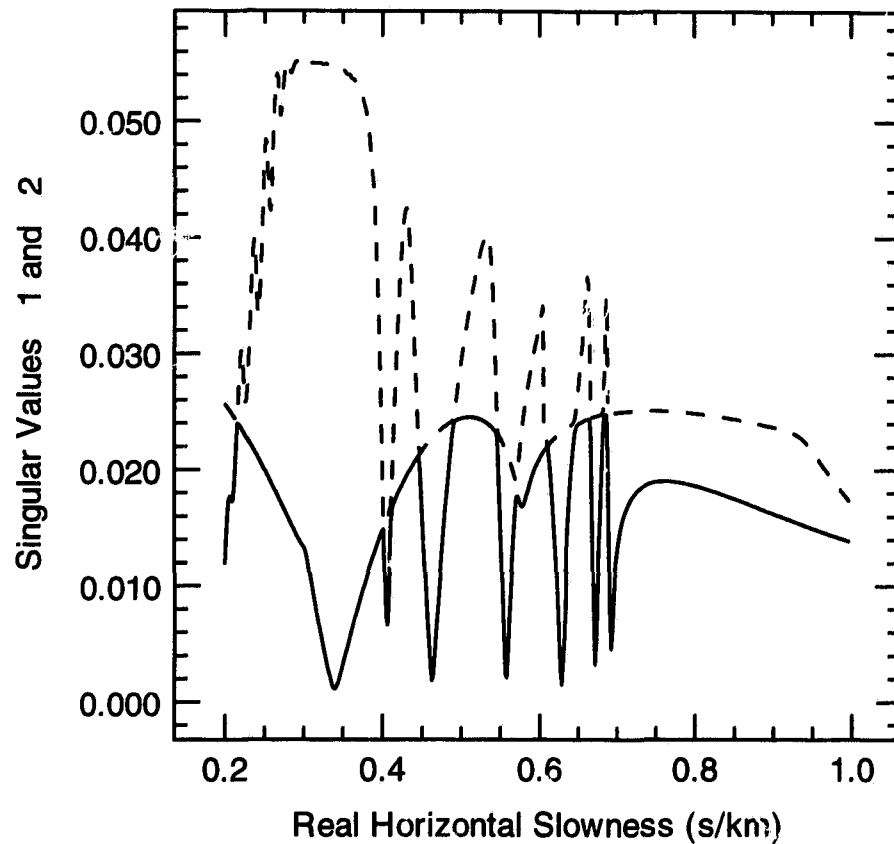


Figure 5.5: The search function for modes in the Arctic waveguide at 20 Hz. The smallest singular value w_1 (solid line) was scanned for minima along a horizontal line slightly above the real p axis. Each minima was later refined to locate the nearby zero which is a mode; numerical zero at a mode being of the order $w_1 \approx 10^{-13}$. Also shown is the second smallest singular value w_2 (dashed line) whose deep minima suggest double roots, though none are found here.

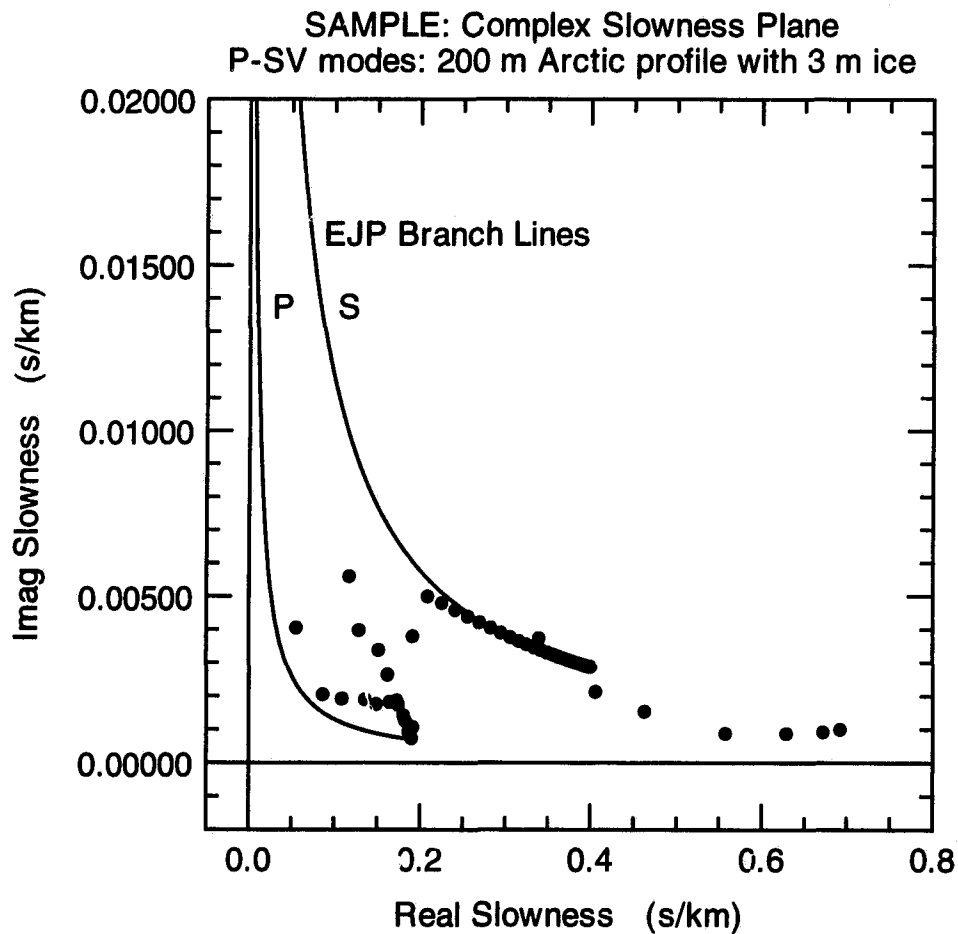


Figure 5.6: P-SV mode locations (circular dots) for the Arctic waveguide at 20 Hz. All of the modes are proper because the waveguide is bounded above and below. Not all modes are shown here: the fundamental plate mode (mode 1) is off scale to the right, and evanescent modes trailing upward along the imaginary axis and modes confined to the low-shear sediment layers are not shown because they were not needed for this test.

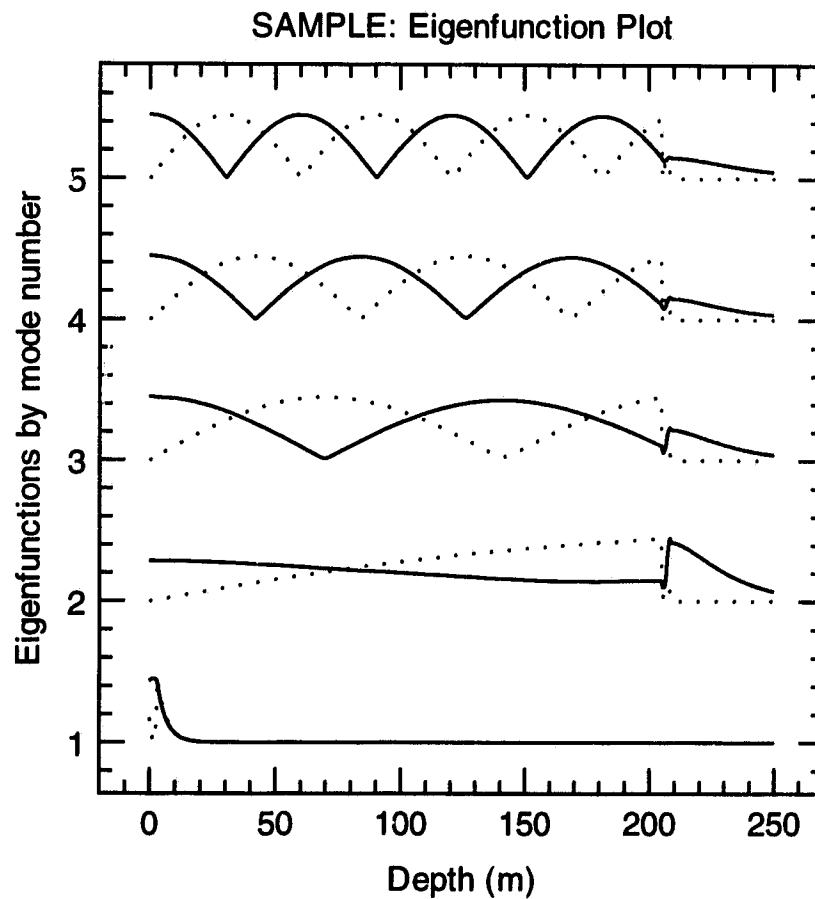


Figure 5.7: The shape of the vertical mode functions for the first five P-SV modes in the Arctic waveguide at 20 Hz. The relative magnitudes of the vertical U (solid) and horizontal V (dashed) displacements of the characteristic vibrations are shown. The top of the sediment layers is evident from the discontinuity in V between the fluid and solid layers. Mode 1 is the fundamental plate mode; the only propagating plate mode at this frequency.

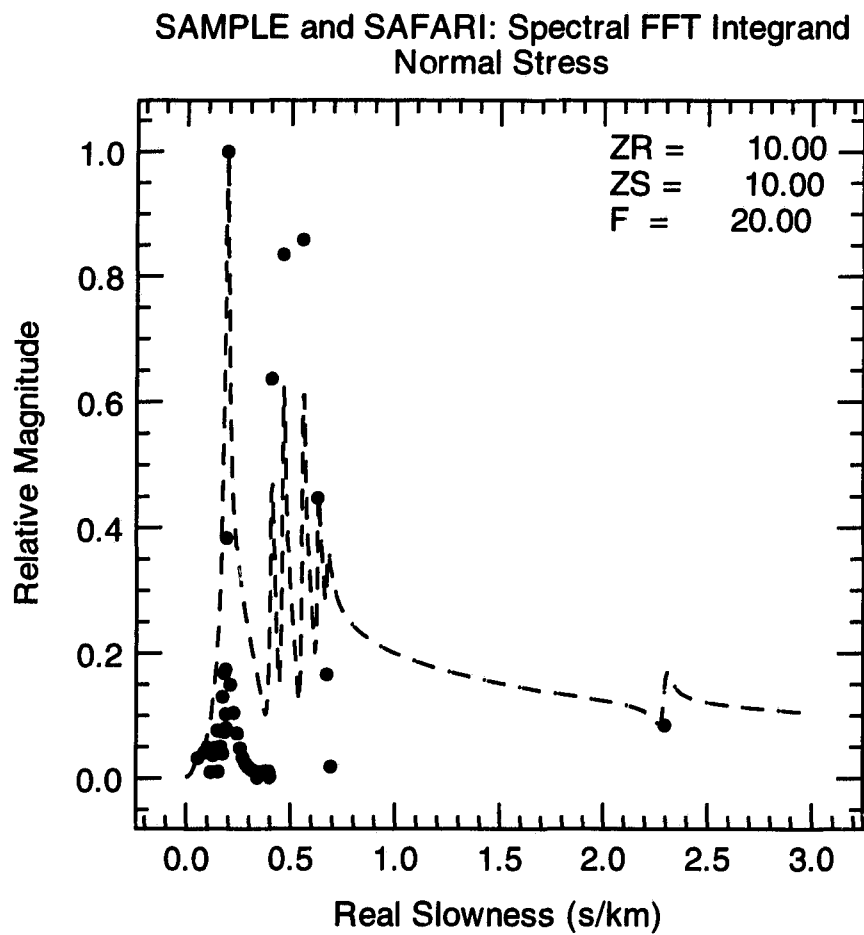


Figure 5.8: The vertical dependence of the integrand in the contour integral representation of τ_{zz} for source and receiver at depth $z = 10$ m. SAMPLE (dashed) and SAFARI (dotted) integrands are virtually coincident. The circular points mark the mode locations along the real axis and their relative excitation by the source at a distant receiver, computed using SAMPLE's normal mode routines.

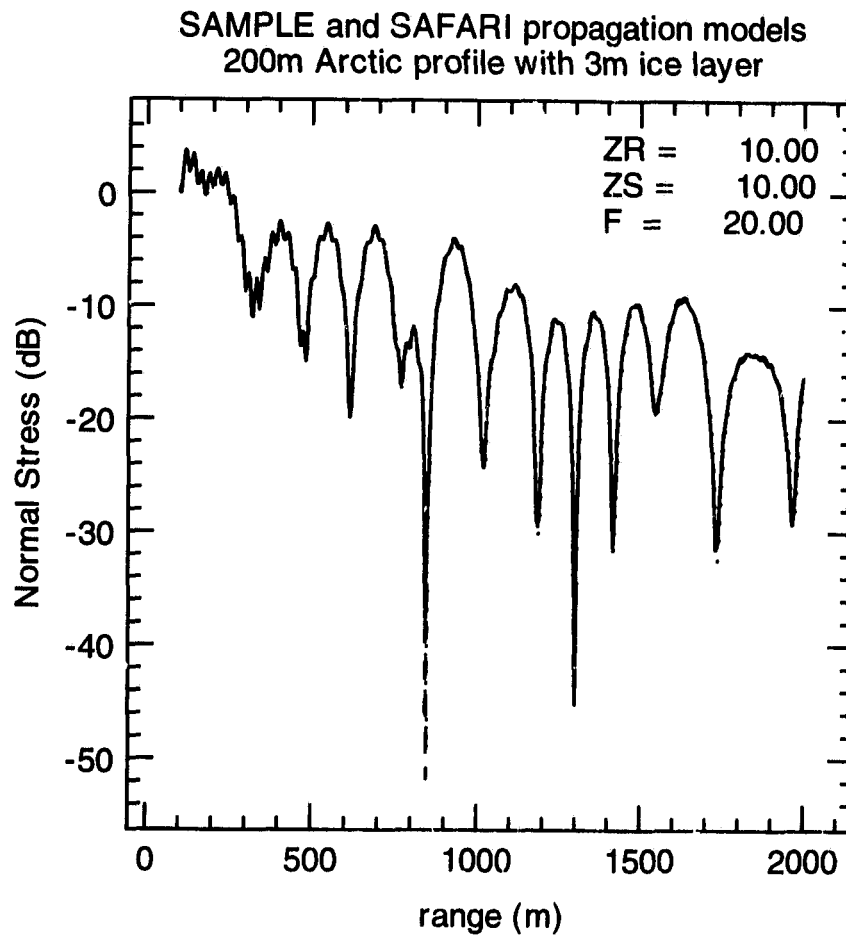


Figure 5.9: The normal stress τ_{zz} as a function of range for source and receiver in the water column, at depth $z = 10$ m. The source is an explosive point source vibrating at 20 Hz. SAMPLE's normal mode computations (solid) agree very well with SAFARI (dotted) and SAMPLE's (dashed) contour integral (FFT) models.

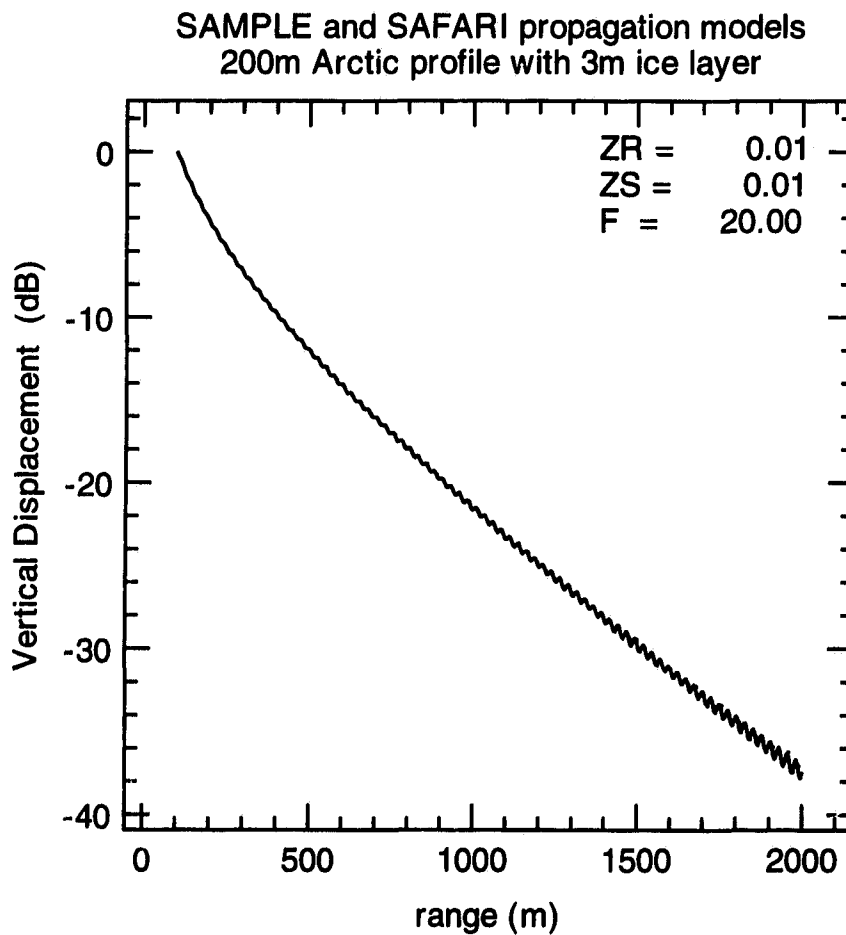


Figure 5.10: The vertical displacement u_z as a function of range for source and receiver at the surface of the ice, at depth $z = 0.01$ m. The source is a vertical point force operating at 20 Hz. SAMPLE's normal mode computations (solid) agree very well with SAFARI (dotted) and SAMPLE's (dashed) contour integral (FFT) models. The lack of interference suggests a single dominant mode, in this case the fundamental plate mode.

5.8.2 Gutenberg earth model

Similar tests were made using the layered model of continental structure in the earth in Table (5.2) and Fig. (5.11) proposed by Gutenberg [1]. Slight artificial absorption was added to the layers to displace the modes and EJP branch lines for the basement layer off the real slowness axis. This time the vertical displacement at the surface due to a point source at depth lying between the two low-velocity channels at $z = 50$ km, and pulsating at 0.05 Hz—a frequency typical of deep penetrating seismic waves.

Fig. (5.12) shows the mode search function w_1 along the real slowness axis. The mode refinement process located 16 *proper modes* and 7 *improper S-leaky modes*, as shown in Fig. (5.13). The vertical mode functions for the first five proper modes are shown in Fig. (5.14); mode 1 being the *Rayleigh mode*, and the others being *duct modes* trapped in the deeper low-velocity channel. At this low frequency the upper channel is too thin to trap propagating *duct modes* of its own.

Fig. (5.15) shows the magnitude of the integrand of the integral for the vertical displacement u_z computed by SAFARI (dotted) and SAMPLE (dashed), again over a contour displaced slightly below the positive real slowness axis. The relative contribution of the *proper modes* at a distant receiver on the surface have been included, showing good correspondence between the modes and integrand peaks, and a rough correspondence between the relative strength of the mode and the height of the peak. The dominant mode at the surface is of course the Rayleigh mode. The leaky modes were not included because SAMPLE could not normalize their vertical mode functions which grow exponentially with depth.

The vertical displacement at the surface of the earth is plotted as a function of range in Fig. (5.16). Only the first 11 proper modes were included in the mode series and the contour integrands were forced smoothly to zero (windowed) below $p = 0.15$ s/km to exclude the contribution from the improper leaky modes. Slight discrepancies between the models may be due to several approximations, such as displacement of the contour from the real axis, windowing of the integrand, and weak contributions from modes omitted in the mode series. Fig. (5.17) shows the real phase and group velocity for the Rayleigh mode,

| layer no. | z upper (km) | z lower (km) | α (m/s) | β (m/s) | ρ (kg/m ³) |
|--------------|----------------------|----------------------|-------------------|------------------|--------------------------------|
| 1 | 0. | 19. | 6140.-2.0i | 3550.-2.0i | 2740. |
| 2 | 19. | 38. | 6580.-2.0i | 3800.-2.0i | 3000. |
| 3 | 38. | 50. | 8200.-2.0i | 4650.-2.0i | 3320. |
| 4 | 50. | 60. | 8170.-2.0i | 4620.-2.0i | 3340. |
| 5 | 60. | 70. | 8140.-2.0i | 4570.-2.0i | 3350. |
| 6 | 70. | 80. | 8100.-2.0i | 4510.-2.0i | 3360. |
| 7 | 80. | 90. | 8070.-2.0i | 4460.-2.0i | 3370. |
| 8 | 90. | 100. | 8020.-2.0i | 4410.-2.0i | 3380. |
| 9 | 100. | 125. | 7930.-2.0i | 4370.-2.0i | 3390. |
| 10 | 125. | 150. | 7850.-2.0i | 4350.-2.0i | 3410. |
| 11 | 150. | 175. | 7890.-2.0i | 4360.-2.0i | 3430. |
| 12 | 175. | 200. | 7980.-2.0i | 4380.-2.0i | 3460. |
| 13 | 200. | 225. | 8100.-2.0i | 4420.-2.0i | 3480. |
| 14 | 225. | 250. | 8210.-2.0i | 4460.-2.0i | 3500. |
| 15 | 250. | 300. | 8380.-2.0i | 4540.-2.0i | 3530. |
| 16 | 300. | 350. | 8620.-2.0i | 4680.-2.0i | 3580. |
| 17 | 350. | 400. | 8870.-2.0i | 4850.-2.0i | 3620. |
| 18 | 400. | 450. | 9150.-2.0i | 5040.-2.0i | 3690. |
| 19 | 450. | 500. | 9450.-2.0i | 5210.-2.0i | 3820. |
| 20 | 500. | 600. | 9880.-2.0i | 5450.-2.0i | 4010. |
| 21 | 600. | 700. | 10300.-2.0i | 5760.-2.0i | 4210. |
| 22 | 700. | 800. | 10710.-2.0i | 6030.-2.0i | 4400. |
| 23 | 800. | 900. | 11100.-2.0i | 6230.-2.0i | 4560. |
| 24 | 900. | 901. | 11350.-2.0i | 6320.-2.0i | 4630. |

Table 5.2: The Gutenberg earth model.

computed using SAMPLE's dispersion and group velocity routines. The figure duplicates a similar figure reported by Aki and Richards [1, box 7.5].

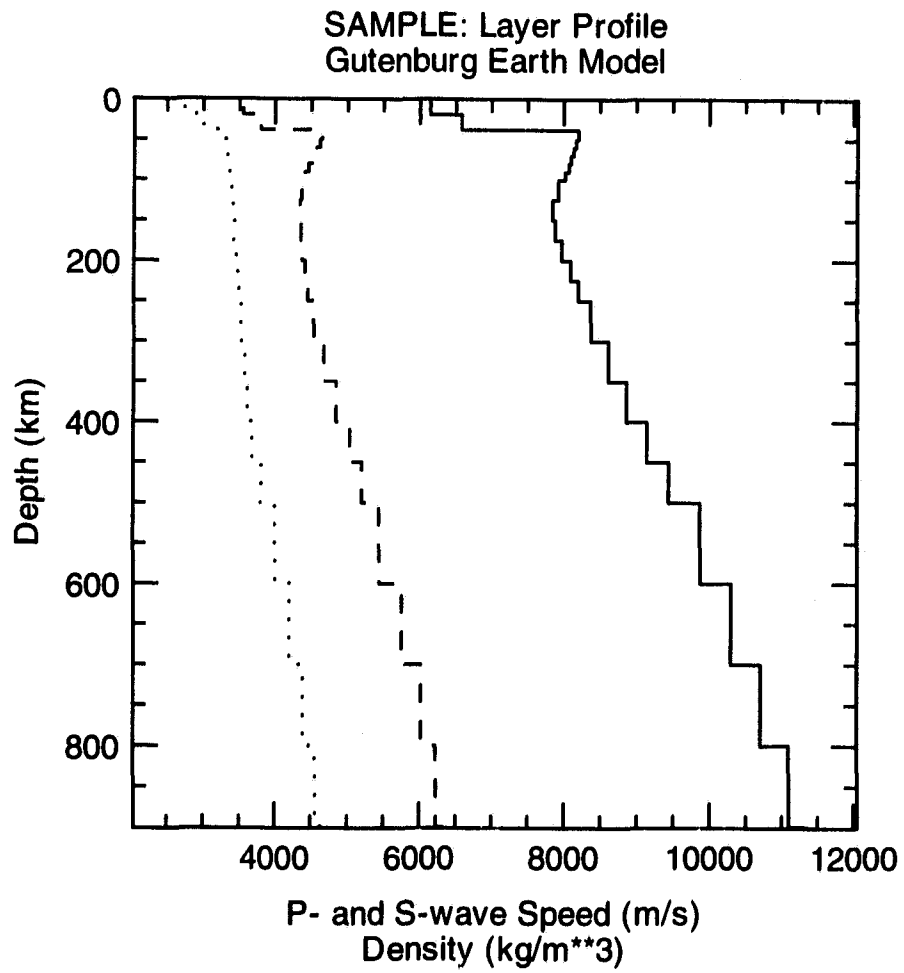


Figure 5.11: Wave speed and density profile in the Gutenberg earth model: P-wave speed is the solid line, S-wave speed the dashed, and density the dotted.

SAMPLE: Plot of Singular Values Along Search Line

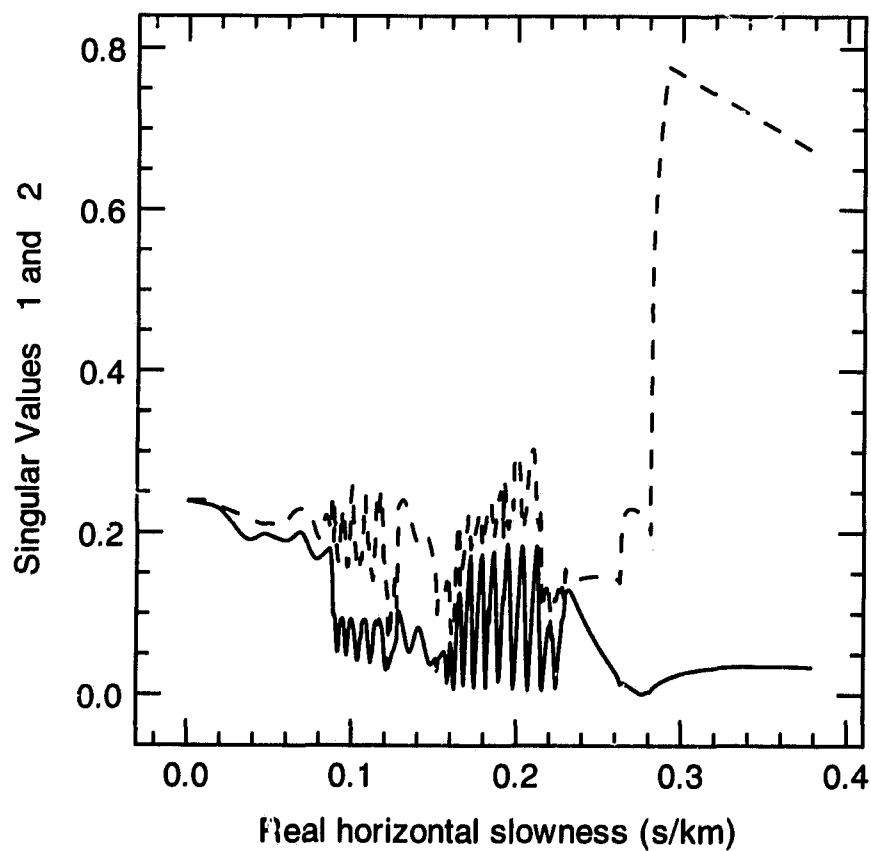


Figure 5.12: In the search for modes for the Gutenberg earth model, the smallest singular value w_1 (solid line) was scanned for minima along a path displaced slightly above the real p axis. Each minimum was then refined to locate the nearby zero which is the mode; the numerical zero at a mode being of the order $w_1 \approx 10^{-13}$. Also shown is the second smallest singular value w_2 (dashed line), whose deep minima suggest double roots, though none are found here.

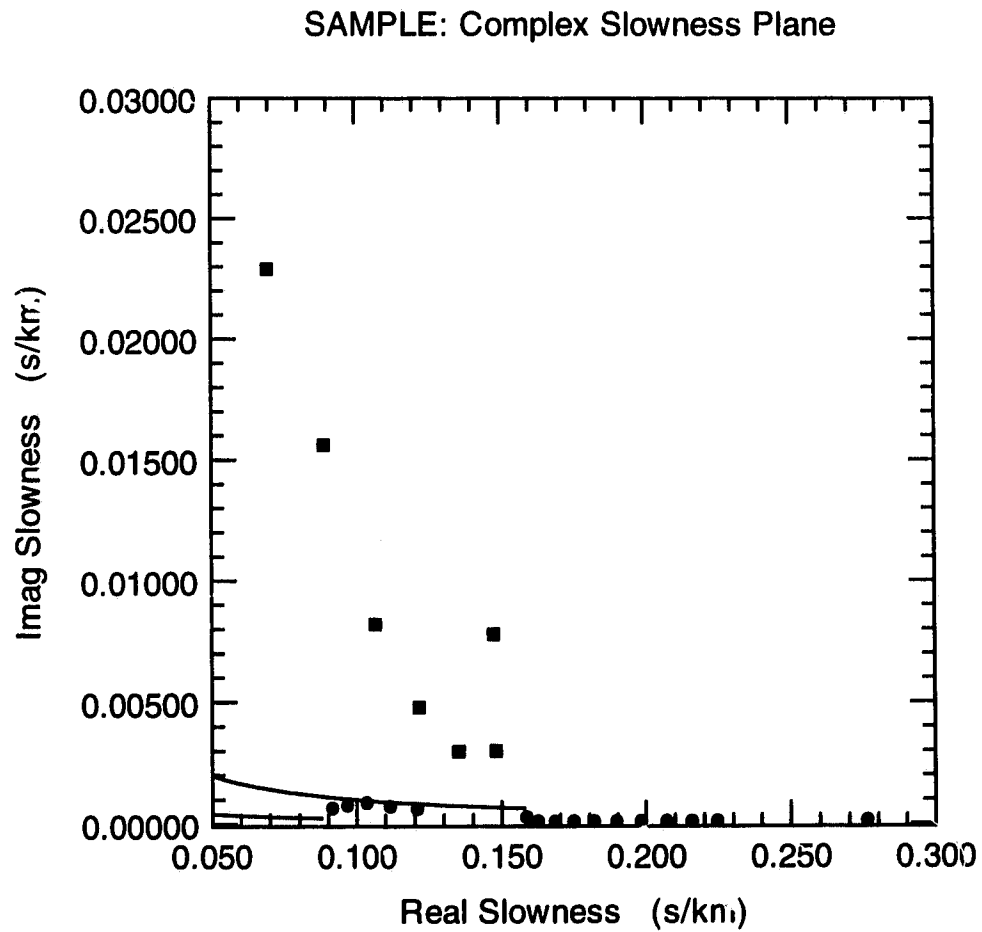


Figure 5.13: P-SV mode locations for the Gutenberg earth model at 0.05 Hz. Proper modes are indicated by circular dots, and improper by square. The solid lines are the P and S branch lines. Proper modes to the left of the S-wave branch point ($p_r = 0.1582$ s/km) are well behaved S-leaky modes.

SAMPLE: Eigenfunction Plot

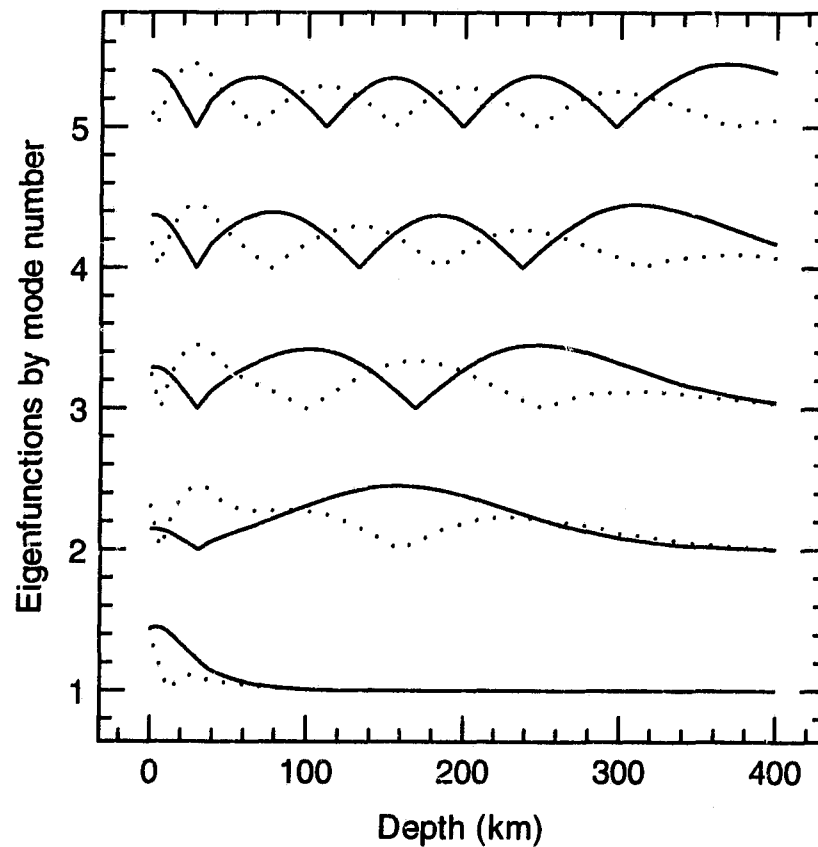


Figure 5.14: The vertical mode functions for the first five P-SV modes in the Gutenberg earth model at 0.05 Hz. The magnitude of the vertical displacement U (solid line) and horizontal displacement V (dashed line) for the characteristic vibrations of each mode are shown. Mode 1 is the Rayleigh interface mode.

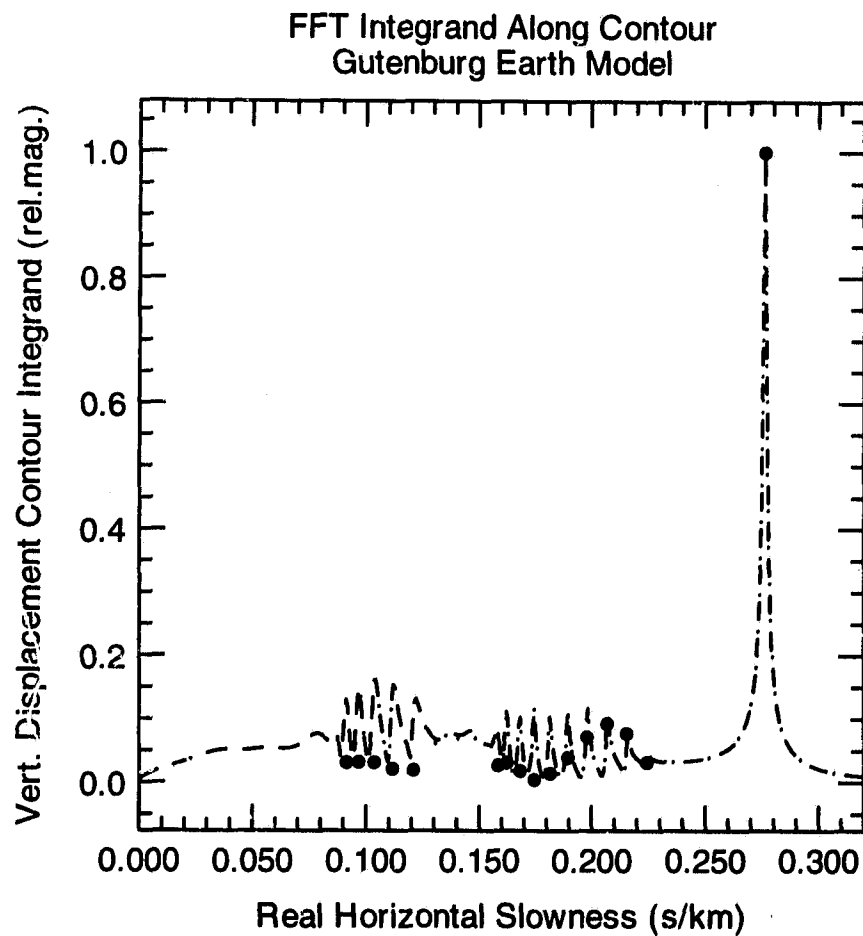


Figure 5.15: The vertical dependence of the integrand in the contour integral representation of u_z for a source at depth $z = 50.0$ km and receiver at the surface $z = 0.0$ km. The normalized integrands for SAMPLE (solid line) and SAFARI (dotted) are virtually coincident. The points mark the location of proper modes and their relative excitation by the source at a distant receiver, computed using SAMPLE's normal mode routines. The dominance of the Rayleigh mode at the surface is clearly evident.

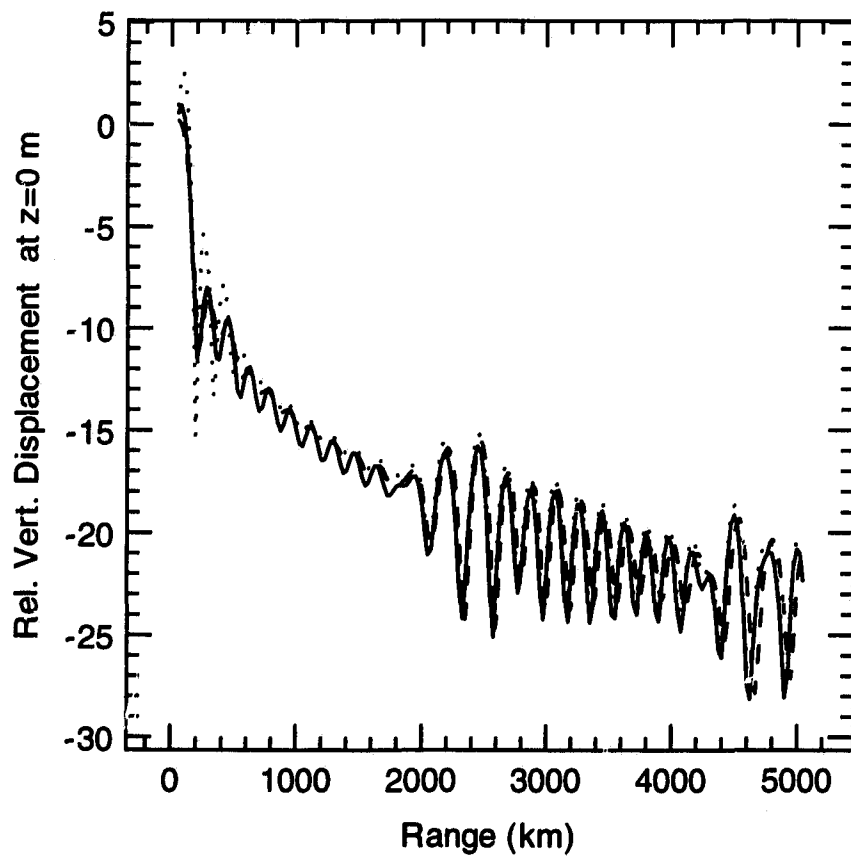


Figure 5.16: The displacement u_z at the surface $z = 0.0$ km as a function of range from an explosive point source at 0.05 Hz, and depth $z = 50.0$ km. SAMPLE normal mode computations are shown by the solid line, SAFARI's contour integral by the dotted, and SAMPLE's contour integral by the dashed.

SAMPLE: Dispersion Curves

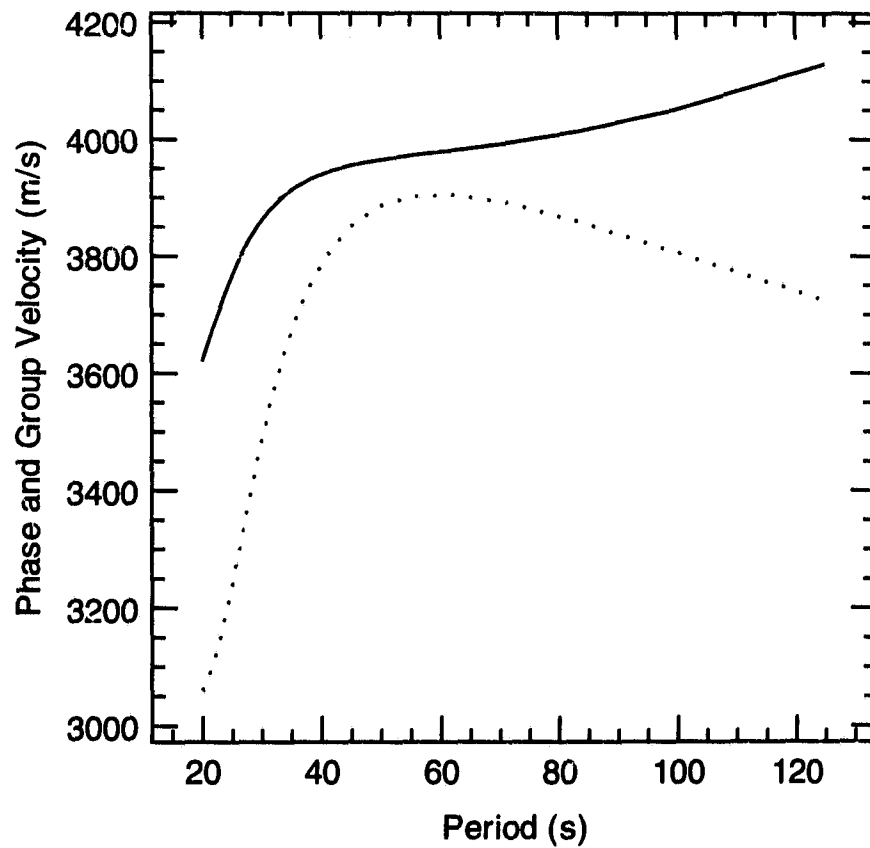


Figure 5.17: The dispersion of the Rayleigh interface wave (mode 1) in the Gutenberg earth model was computed using SAMPLE's mode tracking routines as frequency was steadily decreased. The phase speed of the mode is indicated by the solid line, and group velocity by the dotted.

Chapter 6

Catalogue of normal modes

If our goal is to understand the physics of wave propagation using modes, or if we hope to exploit the advantages of modes in numerical models, the analysis must be brought to a practical level where, by inspection, we are able to quickly estimate 1) what modes are likely to exist, 2) which of those will be important for a given application, and 3) where the modes are likely to be in the complex slowness plane. To be conversant this way, we must first name and classify modes according to their important properties, relating them to the properties of the waveguide using general rules of thumb. I have tried to condense this vast topic into a single chapter, to give an indication of the wide variety of modes that can exist in layered media, to predict where they are to be found in the complex plane, and to present properties about modes that I have not found in the literature. The examples I include have been chosen to demonstrate lesser-known properties of normal modes.

Textbook treatments of modes in oceanic waveguides usually develop their subject starting with the elementary oceanic waveguide consisting of a single homogeneous fluid layer, and build up to the two layer (Pekeris) model, thereby demonstrating many aspects of normal modes in their simplest context. The approach provides an excellent introduction, but the jump to many-layered waveguides having solid media with absorption is a big one, requiring a more general approach that treats modes simply as reverberant cylindrical waves, and that is how I proceed here.

6.1 Modes as cylindrical waves

We have seen that a mode is a cylindrical wave that reverberates constructively within the waveguide. Hence, there are P-SV and SH modes that propagate independently of the other in the absence of scattering inclusions, layer roughness, or variation in the layer structure. Both wave types are generally required to model propagation due to a point source in solid layers.

Many important properties of modes can be deduced from the general representation of cylindrical waves

$$e^{\pm i\omega qz} H_m^{(1)}(\omega pr), \quad (6.1)$$

where the “+” option is for down-going waves, and “—” for up, z being positive downwards; $p = p_r + ip_i$ is the horizontal slowness, a complex root of the characteristic equation for modes (5.5); and q is the complex P or S wave vertical slowness

$$q = q_r + iq_i = \sqrt{\frac{1}{c^2} - p^2}, \quad c = \alpha \text{ or } \beta, \quad (6.2)$$

which changes from layer to layer according to the wave speeds. Complex vertical and horizontal slowness make the representative cylindrical waves inhomogeneous waves.

Far from the source the asymptotic form of the Hankel function give the range dependence¹

$$\frac{e^{i\omega p_r r} e^{-\omega p_i r}}{\sqrt{\omega p r}}. \quad (6.3)$$

The $1/\sqrt{r}$ reduction with range is due to cylindrical spreading of the wave as it diverges from its vertical axis at $r = 0$. There is no net energy loss associated with this decrease. When energy loss does occur, whether due to viscosity or friction in the media, or to downward radiation of energy into an infinite basement layer, it shows up as the exponential decay with range due to p_i . Clearly $p_i \geq 0$ or the wave grows without bound as it diverges from the source. All modes therefore lie in quadrants one and two in the complex p -plane.²

¹See Abramowitz and Stegun [2, equation 9.2.3].

²This is due to the time harmonic dependence $e^{-i\omega t}$ chosen at the outset. $e^{i\omega t}$ could have been used, in which case the outgoing cylindrical waves require Hankel functions of the second kind, and the modes would lie in quadrant three and four.

6.1.1 Propagating modes

In Section (5.3.1) we saw that modes tend to lie along either the real or imaginary p -axes, in the “L”-shaped region bounding the EJP branch cuts. Modes located close to the real p axis ($p_i \approx 0$) are called *propagating modes* because they lose energy at the slowest rate and therefore dominate the total wave field far from the source. Often there are only a few propagating modes that model long range propagation accurately and efficiently. Propagating modes are sometimes called trapped modes or bound modes because their energy is efficiently confined vertically within the waveguide.

6.1.2 Evanescent modes

Modes close to the imaginary p axis, with significantly large p_i , are called *evanescent modes* because their horizontal slowness is mostly imaginary in the manner of evanescent waves. These modes have received little attention in the literature because they decay quickly with range, making them ineffectual in long range propagation. But they cannot be ignored in the BIE method, or in coupled mode methods for that matter [24][45], where close range effects are important.

Most familiar perhaps are the evanescent P modes found in the elementary oceanic waveguide.³ They are an infinite series of evenly spaced modes tailing upwards in the complex plane, along the EJP branch line for vertical slowness in the solitary fluid layer [17]. The mode locations can be derived analytically in this simple case, and it is not difficult to show that the spacing between consecutive evanescent modes in the series approaches

$$\Delta p \approx i/2fH, \quad (6.4)$$

where f is frequency, and H is the thickness of the homogeneous fluid.⁴ As we will see, this estimate can be applied more generally to the evanescent mode series for arbitrarily layered elastic media. It is helpful because the mode spacing determines the resolution needed during a computer search for modes, and it indicates how many modes may be expected.

³See footnote on page 8.

⁴An equivalent spacing estimate is derived later (6.23) for deep bounded waveguides in general. The same analysis can be applied to the elementary oceanic waveguide, to derive the mode locations exactly.

Less familiar perhaps, are the evanescent P-SV modes found in a homogeneous solid plate with free boundaries. These modes occur in two infinite series on both sides of the imaginary slowness axis [90] [6] [51] as shown in Fig. (6.1) for a 3 m ice plate. In a lossless homogeneous plate, these evanescent modes occur in symmetric pairs—each mode in the first quadrant having a symmetric counterpart in the second quadrant—but absorption or additional layers disturbs this symmetry. At greater frequencies the evanescent P-SV modes lie closer to the imaginary axis. The mode locations cannot be derived analytically in this case, but the spacing estimate (6.4) for evanescent modes still applies. In the 3 m ice plate at 750 Hz or example, $\Delta p \approx i / (2 \times 750 \times 3) = 0.222i$ s/km, which compares well with the actual spacing in the two symmetric mode series in Fig. (6.1). Evanescent plate modes occur very often in geoacoustics, for it would appear that all plate-like structures—bands of undivided solid layers spanning a finite thickness, but not touching a solid half space—behave like plates to some degree.

To illustrate, Fig.(6.2) shows part of the evanescent mode series for the Arctic profile of Table (5.1) considered earlier. The higher order evanescent modes (larger p_i) separate into three distinct series: 1) water-borne modes along the imaginary axis, 2) closely spaced bottom-borne modes on both sides of the imaginary axis that appear to swirl around the axis, and 3) widely spaced ice-borne modes on both sides of the imaginary axis, only two of which are shown in the figure. This thick bottom layer and the thin ice layer plate structures giving rise to evanescent modes on both sides of the imaginary axis. The swirling pattern of the bottom-borne mode locations is due to interactions between the bottom and water column. The swirls get larger and less pronounced as p_i increases, eventually settling into two unswerving lines on both sides of the imaginary axis. The depths at which the modes are active—whether in the water (200 m thick), bottom (2000 m), or ice (3m)—were determined by plotting the vertical mode functions, and confirmed using the estimated mode spacing (6.4) for evanescent modes at 20 Hz:

$$\begin{aligned} \Delta p &\approx i / (2 \times 20 \times 200) = 0.125i \text{ s/km} && \text{for the water column,} \\ \Delta p &\approx i / (2 \times 20 \times 2000) = 0.0125i \text{ s/km} && \text{for the deep bottom plate,} \\ \Delta p &\approx i / (2 \times 20 \times 3) = 8.333i \text{ s/km} && \text{for the thin ice plate,} \end{aligned} \quad (6.5)$$

These agree with vertical spacings found for the three evanescent mode series in Fig.(6.2),

although Δp for the ice plate cannot be checked at the scale displayed.

A series of proper evanescent plate modes can occur in unbounded waveguides as well as bounded. An ice plate floating on an infinite fluid half space, for example, has an infinite series of evanescent plate modes on the proper Riemann sheet as shown in Fig. (6.3).

From these and other examples not reported here, it would appear that every band of fluid layers, and every band of solid layers, not in contact with an infinitely thick layer of the same media type, gives rise to a distinct series of evanescent modes; close to the imaginary axis for fluids, but on both sides of the axis for solids. The vertical mode functions for high order evanescent modes are confined almost entirely to the band of layers engendering them.

I think this behavior can be explained in the following way. Close to a point source, the field depends more on the elastic properties in the immediate vicinity of the source than on the properties of other layers of the waveguide. Each distinct band of layers therefore requires its own series of evanescent modes to fully represent the near-field dynamics of sources lying within them. Thus, the delta-function singularity of a point source ($\delta(z - z_s)$ on page 140) may be produced by one or another evanescent mode series, depending on which band of layers the source lies in. Near the interface between two distinct bands of layers, the singularity is due to the evanescent mode series of both because the vertical mode functions extend slightly beyond their boundaries. However, in a band of layers in contact with an infinitely thick layer of the same type, which do not have a corresponding evanescent mode series, the singularity is due to the branch line integrals of the infinite layer.

6.1.3 Proper and improper modes

In Section (4.2.4), it was assumed that the cylindrical wave field in an infinitely thick basement layer, at depths below all sources, are due to sources and reverberation in layers above. Thus, the schematic diagram Fig.(4.7) shows a down-going transmission matrix (T_{3L}) directed into a infinite basement, with the up-going wave set to zero ($\mathbf{v}_6^- = \mathbf{0}$).

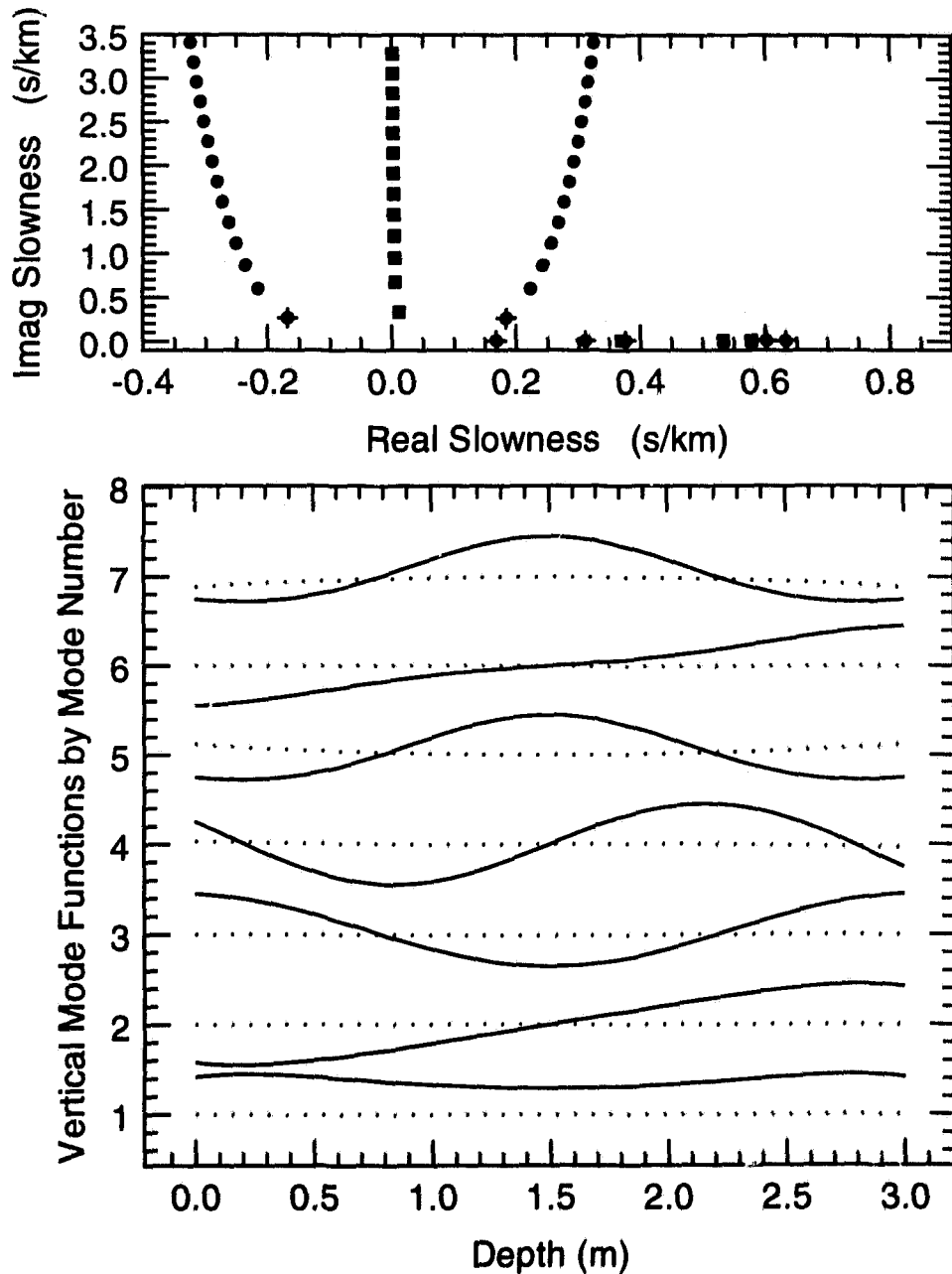


Figure 6.1: Top: The P-SV (circular dots) and SH (square dots) modes for a free ice plate: $\alpha = 3300 - 30.0i$ m/s, $\beta = 1730 - 20.0i$ m/s, $\rho = 900$ kg/m³, thickness $H = 3.0$ m, and $f = 750.0$ Hz. Bottom: The vertical mode functions for the first 7 P-SV modes marked by crosses above, ordered by decreasing real slowness. Shown are the real (solid line) and imaginary (dotted line) parts of the vertical displacement U for each mode.

SAMPLE: Complex Slowness Plane

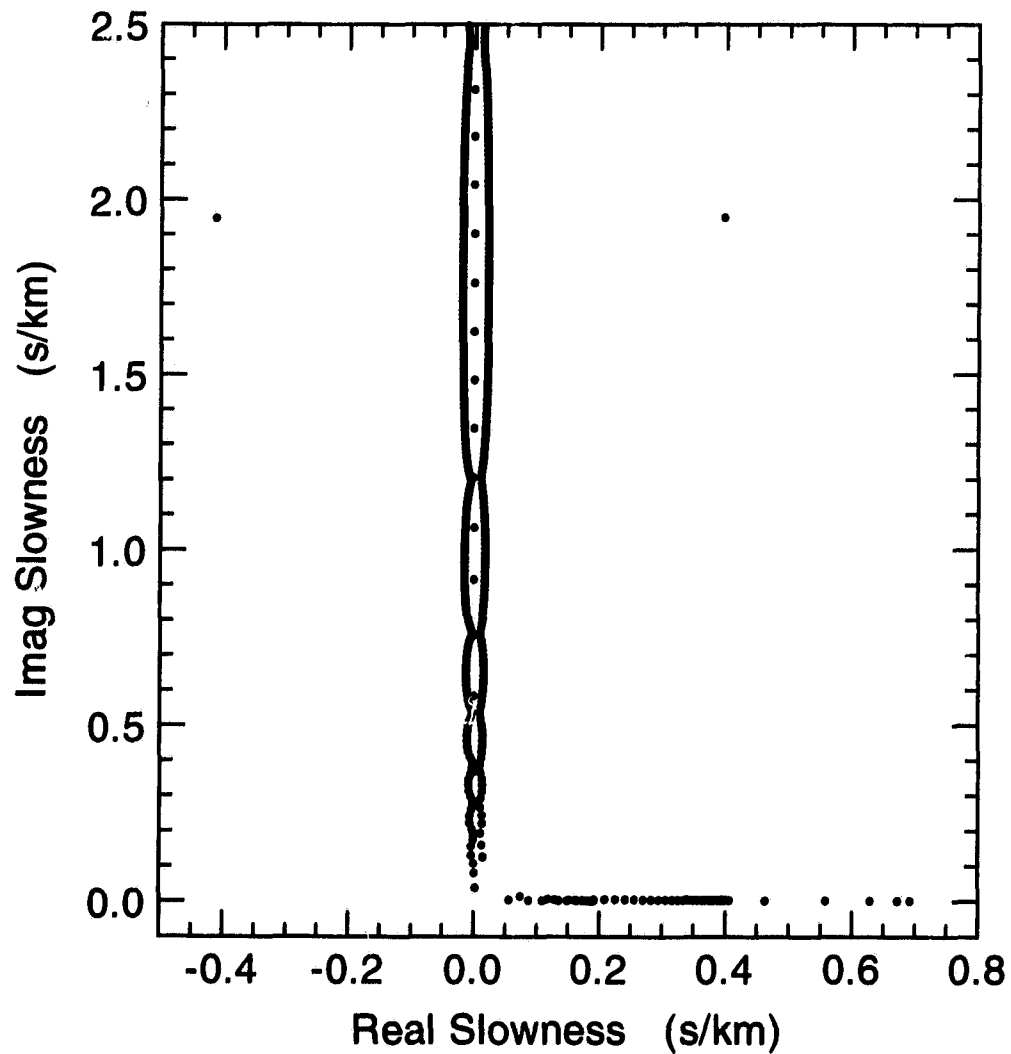


Figure 6.2: P-SV modes in the Arctic waveguide at 20 Hz. The evanescent modes separate into three series: one for the water column (the widely spaced modes along the imaginary axis), one for the deep basement (the closely spaced modes swirling around the imaginary axis), and one for the floating ice plate (the isolated pair of modes on both sides of the imaginary axis are the start of this plate mode series).

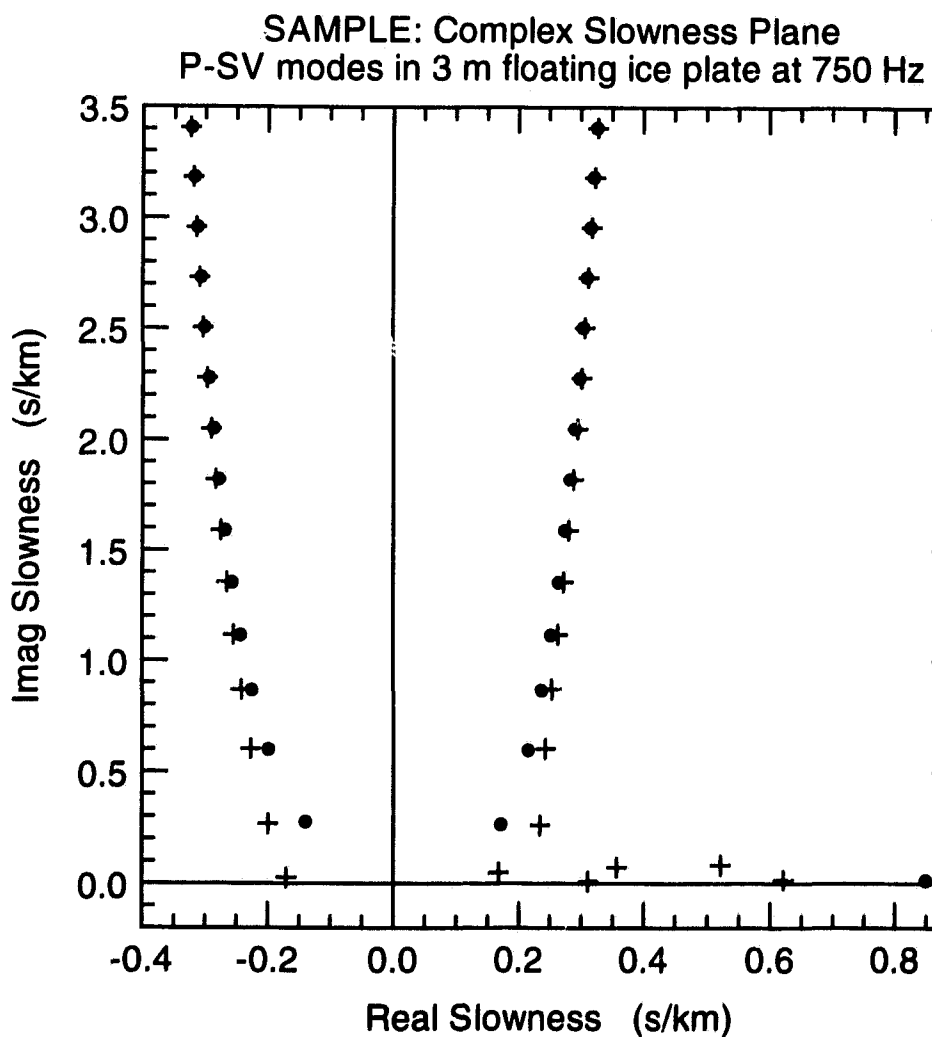


Figure 6.3: The P-SV modes for a 3 m floating ice plate: $\alpha = 3300 - 30.0i$ m/s, $\beta = 1730 - 20.i$ m/s, $\rho = 900$ kg/m³, thickness $H = 3.0$ m, and $f = 750.0$ Hz. Proper modes are shown using circular dots, and improper by crosses. Low P-wave speed in the supporting water, $\alpha = 1460$ m/s, $\rho = 1000$ kg/m³, changes the first propagating P-SV mode of the free ice plate into a Scholte mode at the ice-water interface, and the others into improper leaky modes (compare Fig.(6.1) top). An infinite series of evanescent plate modes still appears on the proper Riemann sheet as in the free plate.

The vertical depth dependence of waves in the basement therefore behaves like

$$e^{i\omega qz} = e^{i\omega q_r z} e^{-\omega q_i z}. \quad (6.6)$$

Recall, however, that the sign of the vertical slowness q depends on our choice of Riemann sheet. Each sheet therefore yields a different system of cylindrical waves: one with down-going waves in the basement layer, and the other with up. Furthermore, if the EJP branch cut is used, then $q_i > 0$ when p lies on the *proper* Riemann sheet (giving exponential decay of the waves with depth in the basement), and $q_i < 0$ on the *improper* (giving exponential growth).⁵ So long as we use the EJP cuts, as we did when the residue theorem was used to separate the field into a discrete (mode sum) and continuous (branch-line integrals) spectrum in Section (5.1), the discrete spectrum consists entirely of well-behaved *proper* modes.

But we can deform the branch cuts, possibly into straight lines directed vertically upwards from the branch point, which is how the Pekeris branch cuts are taken [125]. Moving the branch changes how the residue theorem is applied. Not only is the path of the branch line integral in (5.4) changed, but poles that were hidden on the improper Riemann sheet may now be encircled by the integration contour, adding *improper modes* to the discrete spectrum. At times this is an advantage because the contribution of dominant improper (leaky) modes may be included more efficiently as part of the discrete spectrum, rather than through the EJP branch cuts [125]. The disadvantage is that improper modes cannot be normalized by integrating vertically through the entire waveguide as we did in Section (5.5) because the mode function becomes infinitely large with depth.⁶

When the basement is an infinitely thick solid layer, there are four different types of proper and improper modes. These can be distinguished according to the Riemann sheet

⁵See Section (4.2.4).

⁶The integral identity (5.10) still applies for improper modes, but z_A and z_B must always be taken at some finite value in the unbounded waveguide, making its left side non-zero. Following much the same method, then, we could derive somewhat more complicated normalizations for improper modes, but this is beyond the scope of my project.

they lie on when the EJP branch cuts are used:

- sheet 1 = proper sheet for P waves and proper sheet for S waves,
- sheet 2 = proper sheet for P waves and improper sheet for S waves,
- sheet 3 = improper sheet for P waves and proper sheet for S waves,
- sheet 4 = improper sheet for P waves and improper sheet for S waves.

All proper modes lie on sheet 1, and all improper modes on sheets 2, 3, or 4.

6.1.4 Vertical energy flux

In Section (5.6) we saw that the sign of the real vertical slowness determines the direction of vertical energy flow for a *propagating mode*. Since the vertical slowness q is related to the horizontal slowness p according to (6.2), the sign of its real part q_r is determined by the location of p relative to the EJP branch cut and the choice of Riemann sheet as shown in Fig. (4.1). In an infinitely deep basement layer, at depths below all sources, we have naturally assumed that the field has only down (+) going waves; hence, the measure of the vertical flux \mathcal{Y} in (5.41) is simply

$$\mathcal{Y} = \mathcal{Y}^P + \mathcal{Y}^S = \frac{q_{\alpha r}}{2|q_{\alpha}|} |P^+|^2 + \frac{q_{\beta r}}{2|q_{\beta}|} |S^+|^2 \quad (6.7)$$

for P-SV waves. And if p for a mode were located in a region of the complex plane where q_r is negative, it would mean that the waves of its vibrations in the infinite basement are actually flowing in reverse, upwards from infinite depth, for \mathcal{Y} would be negative. At first this may seem impossible, for it implies that energy is propagating upwards from depths below all sources and all reflecting interfaces in apparent violation of the radiation condition, but this upward flow actually occurs in the following way.

Upward energy flow in a lower half space

Consider a lossless waveguide for which the propagating modes lie directly on the real p axis (because they do not suffer energy loss), and for which the EJP branch cuts for an infinitely thick basement layer lie along the real and imaginary p -axis. If absorption is added to layers above the basement while keeping the basement media lossless, then the

propagating modes drift upwards in the complex plane, away from the real axis because they now lose energy in the upper layers, whereas the EJP cuts for the basement remain fixed to the axes because they depend only on the basement media. By inspection of Fig. (4.1), then, we see that proper modes lying above the EJP cut have a small negative q_r in the infinite basement; that is, the "down going" wave a lower half space is actually transporting its energy slightly upwards.

This surprising behavior can be explained in physical terms. The wave disturbance at the source has excited a mode whose vibrations extend downwards into the lower half space. The mode loses energy as it propagates due to absorption in the upper layers, but how can the vibrations in the bottom lose energy if the bottom is lossless? The only possibility is for the waves to send their energy upwards for dissipation in the lossy layers. Indeed, the energy flows upward at precisely the rate needed to preserve the shape of the mode function through all layers, for the relative shape of the mode function must always be the same in a range independent waveguide—the mode cannot decay more quickly with range in lossy layers than in lossless layers for instance, for that would alter the shape of the mode function during propagation. More generally, this upward energy flow can occur whenever the duct trapping a mode is particularly lossy compared to an infinite half space, just as ocean sediment layers are usually much more lossy than an underlying rock basement, for example.

To illustrate, consider the *Scholte mode* at 50 Hz, in a 10 m sand layer lying on top of a limestone base in the sea floor described in Table (6.1). The mode function and vertical energy flux for the mode is plotted in Fig.(6.4). The net energy flow is upwards at depths where the real vertical flux is negative. In this case, energy in the infinitely deep limestone layer is drawn upwards by the relatively high absorption losses in the sand at precisely the rate needed to preserve the relative shape of the mode function as the mode propagates.

The real vertical energy flow can also be in opposite directions for P and S waves in an infinite basement. In an S-leaky mode, for example, the high rate of energy loss due to S wave energy radiation into the infinite basement can force p for the S-leaky mode to lie above the P-wave branch cut where q_r for proper P waves is negative. In physical terms,

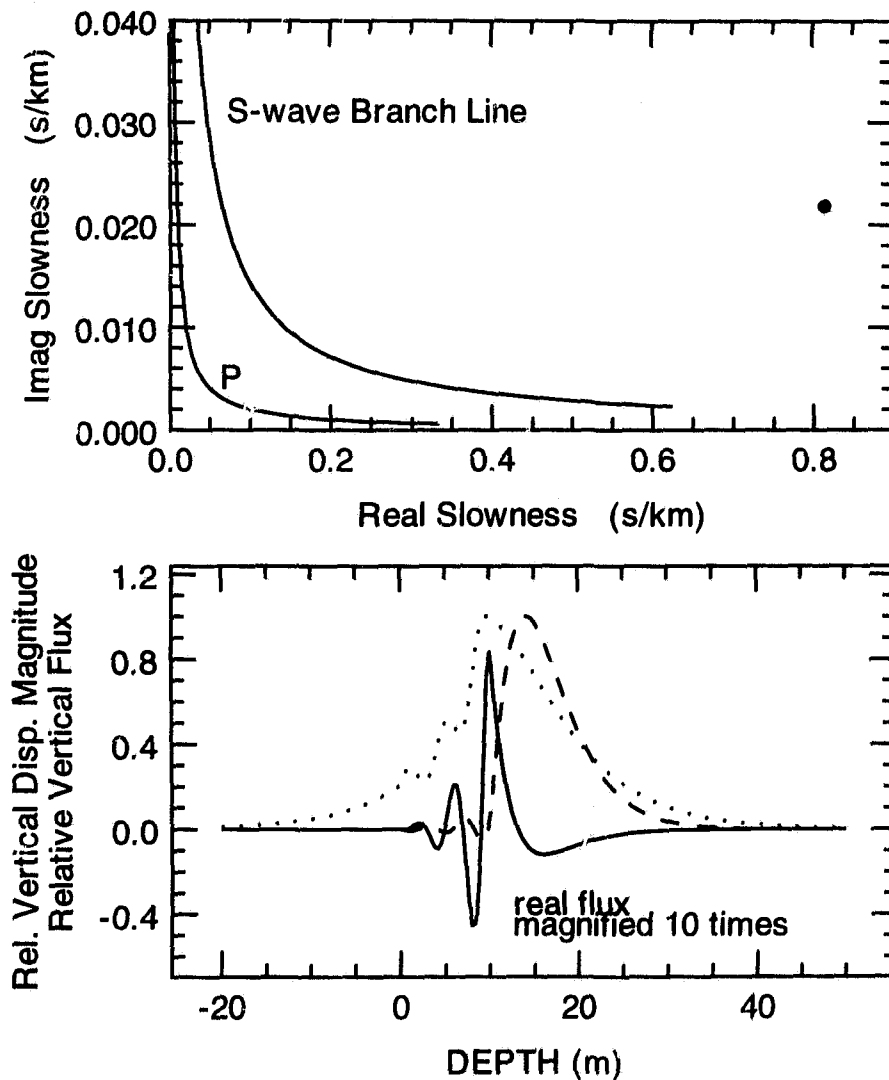


Figure 6.4: Upward energy flow in an infinite basement layer. Top: The Scholte mode location in the complex slowness plane at 25 Hz. Energy loss due to absorption in the 10 m sand layer forces the proper mode above the P- and S-wave branch points for the limestone basement, which makes the real vertical slowness negative in the limestone, and reverses the assumed direction of energy flow in the infinite basement. Bottom: Upward energy flow occurs where the real vertical flux (solid line) is negative. Slight upward energy flow in the basement layer ($z > 10$ m) occurs at precisely the rate needed to preserve the relative shape of the mode function as the mode propagates (dotted line shows the magnitude of the vertical displacement). The imaginary (reactive) vertical flux is also shown (dashed line).

| layer no. | z upper (m) | z lower (m) | α (m/s) | β (m/s) | ρ (kg/m ³) |
|--------------|---------------------|---------------------|---------------------|---------------------|--------------------------------|
| 1 | $-\infty$ | 0.0 | 1500.0 | 0.0 | 1000. |
| 2 | 0.0 | 10.0 | 1650.-50.0 <i>i</i> | 200.0-20.0 <i>i</i> | 1900. |
| 3 | 10.0 | ∞ | 3000.-5.50 <i>i</i> | 1600.-5.86 <i>i</i> | 2400. |

Table 6.1: 10 m sand layer on a limestone sea floor.

the basement P-wave energy flows upwards to the top of the basement where it is partially converted to a downward S by reflection from the interface. In a lossless waveguide, upward energy flow is the only loss mechanism available to the basement P waves for an S-leaky mode.

6.2 Mode trapping mechanisms

In Section (5.3.1) we saw that modes tend to lie in the “L”-shaped region enclosing the EJP cuts for all layers in the waveguide (possible exceptions being *interface modes* whose vibrations are confined to a single interface, and *plate modes* in a thin distinct layer). To estimate the mode locations more exactly, we must consider the two mechanisms that are responsible for trapping modes, both of which have already been introduced: 1) repeated reflection from layer interfaces and waveguide boundaries, and 2) the intrinsic resonance of an interface between dissimilar media. The distinction between the two trapping mechanisms is not always clear. The vibrations of an interface mode may extend through several layers, in which case repeated reflections play a role in the interface mode.

6.2.1 Modes trapped by constructive reflection

Reflection traps a mode whenever the repeated reflections of waves interfere constructively. This is what the condition for modes (5.5) says when interpreted using rays as in (4.69).

Duct modes

The band of layers bounding a phase speed minimum can trap a mode, for at some range of ω and p the cylindrical waves undergo total internal reflection as they travel into the bounding high speed layers. A good example of a duct is the deep sound channel in ocean acoustics [17]. It is a simple matter to estimate where propagating modes so trapped must lie since

1. the modes lie close to the real p axis because their cylindrical waves are efficiently trapped by total internal reflection at the duct boundaries;
2. the waves must be vertically evanescent in the bounding high-speed layers, again because the modes are trapped by total internal reflection, which restricts the modes to the right of $p = 1/c_{\text{bound}}$, where c_{bound} is the smallest phase speed at the upper and lower boundaries of the duct;
3. the imaginary part of the vertical slowness q of the waves inside the duct must be small enough for the waves to traverse the duct without significant vertical decay, which restricts the modes to the left of the point $p = 1/c_{\text{min}}$, where c_{min} is the minimum phase speed in the duct;
4. the frequency ω must be high enough that the P or S wavelengths in the duct are less than about twice the thickness of the duct, otherwise the waves are too long to be strongly affected by the duct.

Conditions 1 to 3 imply the duct modes lie close to the real slowness axis, in the range

$$1/c_{\text{bound}} < p < 1/c_{\text{min}}. \quad (6.8)$$

Condition 4 implies that a duct cannot trap modes below a certain cutoff frequency. The spacing of duct modes in the complex plane depends strongly on the layer profile and the frequency, and it cannot be estimated in a generally applicable way.

At times, a duct may be bounded on one side by a perfect reflector such as the upper boundary of the waveguide in the case of the ocean surface duct [130] [17]. To

illustrate, let us return to the Gutenberg earth model in Fig. (5.11), which has a phase speed minimum at depth $z = 140$ km, where $\alpha_{\min} = 7850$ and $\beta_{\min} = c_{\min} = 4350$ m/s. This creates a duct bounded above by the impenetrable interface with the atmosphere, and below by the infinitely deep basement layer with $\alpha = 11350$ and $\beta = c_{\text{bound}} = 6320$ m/s. The condition for propagating duct modes (6.8) is therefore

$$0.158 \text{ s/km} < p < 0.230 \text{ s/km}, \quad (6.9)$$

which is confirmed in Fig. (5.13), for there are 10 propagating modes found in that range. All of the other modes are *leaky modes*, except for the Rayleigh *interface mode* (mode 1). In a similar way, by inspection of the Arctic profile in Table (5.1), we see there is a duct in the water extending from the surface to the sea floor, with $c_{\min} = 1436.3$ m/s and $c_{\text{bound}} = 2500.0$ m/s; hence

$$0.400 \text{ s/km} < p < 0.696 \text{ s/km},$$

which is confirmed in Fig. (5.6), for there are 6 propagating modes in that range. All of the other modes are *radiation modes*,⁷ except for the fundamental ice-plate mode (mode 1). A consequence of the fourth condition for a duct (item 4 above) is that distinct layers—conspicuous for their sharply contrasting elastic parameters—can be ignored when choosing the bounding layers for the duct provided they are much thinner than wavelength. Thus, the ice and sediment layers in the Arctic profile and the shallow surface duct in the Gutenberg model do not significantly affect the ducts at the frequencies considered.

Leaky modes

Although the cylindrical waves of a mode reverberate constructively within a band of layers, their repeated reflections may not be perfect, causing the mode to leak energy out of the duct.⁸ These *leaky modes* usually occur when the P or S wave speeds in a thick basement layer are less than the speeds in other layers of the waveguide, for the low phase

⁷See Section(6.2.2) below.

⁸I disagree with Dr. Frisk [48], who suggests that leaky modes are not the constructive interference of waves. The condition for modes (5.2) is precisely the condition for constructive interference of plane or cylindrical waves. It holds for leaky modes as well as trapped.

speeds prevents total internal reflection at the top interface of the basement. Leaky modes are usually much weaker than propagating modes far from the source due to their energy loss, but they can dominate the field far from the source in the absence of propagating modes [42]. Estimating where leaky modes should lie is more difficult than trapped modes because the lower bound in (6.8) does not apply in the absence of total internal reflection. They are also relatively far from the real slowness axis due to their high energy loss.

There are three types of *leaky modes* named according to the leaking wave type:⁹ if the basement layer is solid, there are *S-leaky* modes, and *PS-leaky* modes; if the basement layer is a fluid, there are only *P-leaky* modes. P-leaky modes do not occur with solid basements for S waves invariably leak when P waves do since $\alpha > \beta$. In lossless media, all leaky modes lie on improper Riemann sheets—S-leaky modes on Riemann sheet 2, PS-leaky on sheet 4, and P-leaky on sheet 3—causing their mode functions to grow exponentially with depth. For when the basement is lossless, its EJP cuts lie along the real and imaginary axes of the complex p -plane, and the dual requirement that the mode lose energy ($p_i > 0$) and that the radiated energy travel downwards in the basement ($q_r > 0$), imply that p lie on an improper Riemann sheet as shown by Fig. 4.1). Improper leaky modes only occur in unbounded waveguides because the impenetrable boundaries of the bounded waveguide ultimately trap the energy radiated out of the duct. But in a deep bounded waveguide there are *radiation modes* that correspond very closely to the leaky modes in the unbounded case as we might expect.¹⁰

Proper leaky modes

It was surprising to find that leaky modes can be transferred to the proper Riemann sheet by absorption in the infinite basement layer. Recall that energy absorption is added to a half space by adding a small negative imaginary part to the P and S phase speeds,¹¹ which shifts the EJP branch cuts away from the real p axis. If the absorption is great enough, it is possible for the branch cut to pass over some leaky modes, transferring them from the improper sheet to the proper sheet. In effect, the exponential growth due to

⁹The suggestion to name leaky modes this way is due to Zhang [137].

¹⁰See Section (6.2.2).

¹¹See Section(2.2).

leakage in a lossless half space is overcome by exponential decay due to energy absorption. The relatively high absorption typical of low-speed shear waves in ocean sediment layers is often sufficient to place the dominant S-leaky modes on the proper Riemann sheet. All of the S-leaky modes reported by Tindle and (N.R.)Chapman [126] are proper modes for this reason,¹² as are the modes reported by Ellis and (M.F.)Chapman [42]. Though instances of proper leaky modes can be found in the literature, they have appeared without specific mention, presumably because leaky modes are always assumed to be improper modes, as they are in the lossless waveguide commonly used in introductory treatments.

Proper leaky modes are of interest for modeling purposes, for normal mode programs designed for proper modes with complex p , which ordinarily cannot handle leaky modes due to their poorly behaved mode functions, should be able to handle proper leaky modes without modification. In fact, it may be justified to add artificially high absorption in the basement to make a leaky mode environment amenable to a proper mode program.

We have already encountered proper leaky modes in the Gutenberg earth model in Fig. (5.13), where the artificial absorption added to the basement layer displaced the S-wave branch line far enough to pass over some S-leaky modes, transferring them from the improper Riemann sheet to the proper. For a more realistic example for ocean acoustics, consider the two layer leaky-mode environment used by Ellis and Chapman [42], detailed in Table (6.2). The mode locations at 200 Hz are shown in Fig. (6.5). In this case the realistic S-wave absorption of the chalk sea floor is enough to transfer all of the leaky modes to a proper Riemann sheet for S-waves (Riemann sheet 1 or 3). The exponential decay with depth of a proper leaky mode is evident in Fig. (6.6). In the absence of absorption in the basement they would grow exponentially with depth.

¹²Tindle and Chapman call the five modes left of the P-wave branch point in their Fig.(2) "trapped modes" since, lying close to the real axis, the modes suffer little energy loss. But the modes are S-leaky nonetheless, for they are imperfectly trapped by the low shear wave speed in the bottom half space: $\beta = 550$ m/s with absorption 0.2 dB/ λ in the basement, compared with $\alpha = 1500$ m/s in the water column. The leakage is very weak because the large $\alpha : \beta$ contrast prevents the leaking shear waves in the bottom from being strongly excited. In the absence of absorption in the bottom, these modes would be improper modes because the EJP branch cut for S-waves would slip down over these modes, transferring them to the improper Riemann sheet 2.

SAMPLE: Complex Slowness Plane

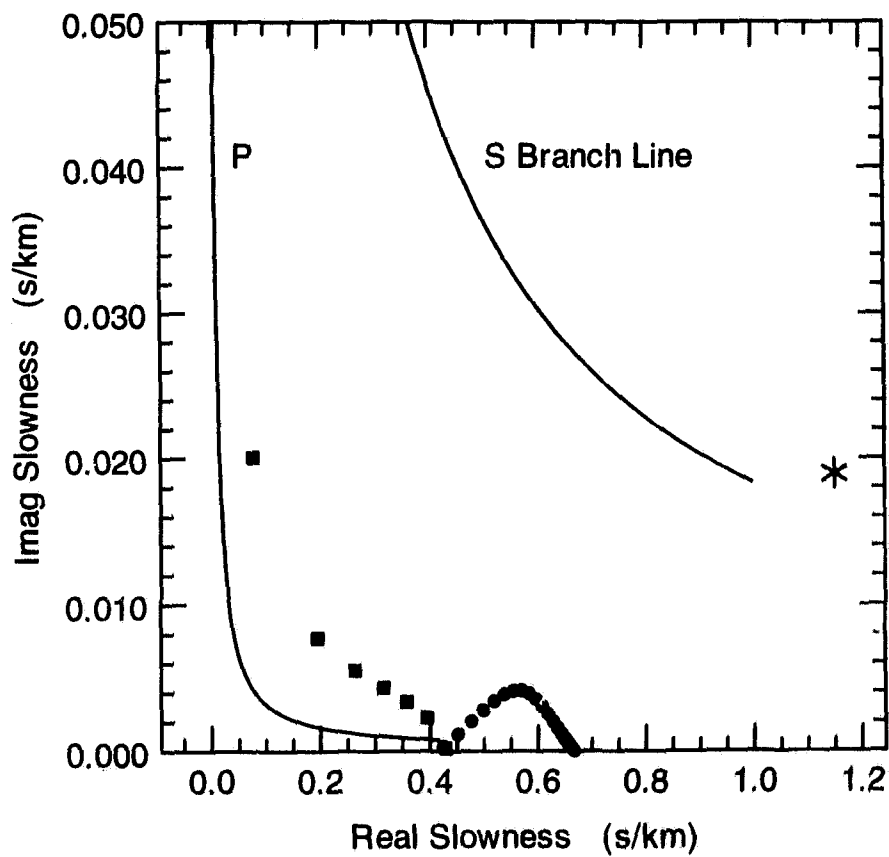


Figure 6.5: The P-SV mode locations for the two-layer leaky mode environment at 200 Hz. 22 proper S-leaky modes (circular dots), 7 improper PS-leaky modes (square dots), and the bottom Scholte interface mode (star) are shown. The S-leaky modes are proper because S-wave absorption in the chalk basement has pushed the S-wave branch line upwards, transferring them from the improper to proper Riemann sheet.

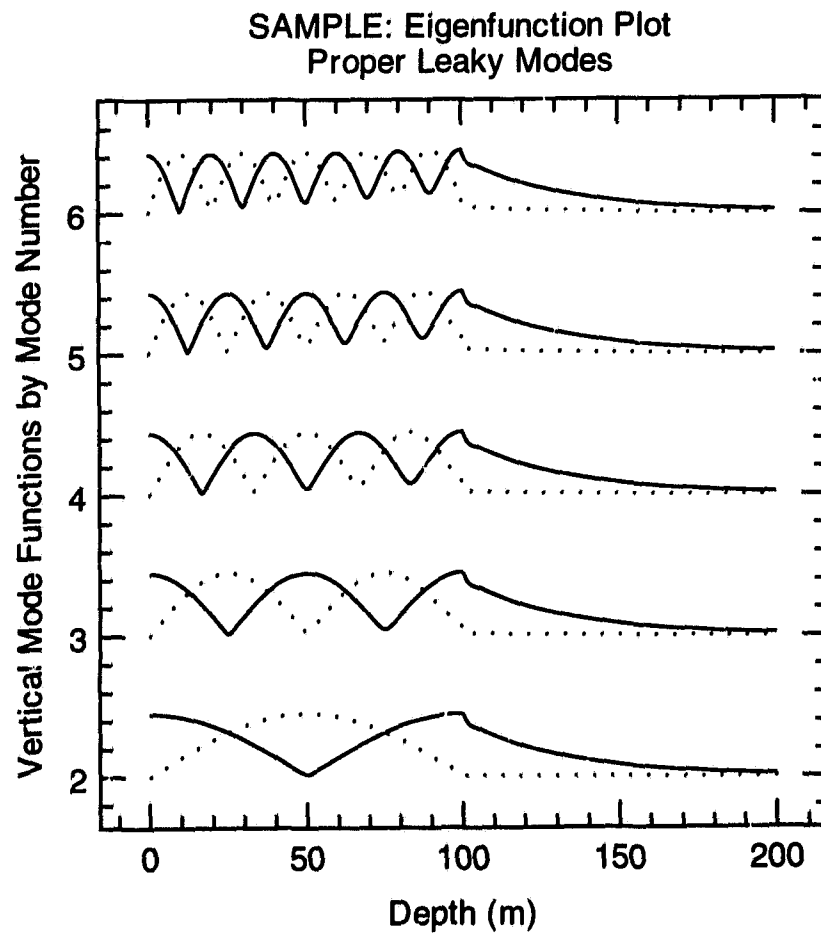


Figure 6.6: The vertical mode functions for proper S-leaky modes at 200 Hz. Shown are the relative magnitudes of the vertical displacement U (solid line) and horizontal displacement V (dashed line). The modes decay exponentially with depth as all proper modes in infinitely deep waveguides do.

| layer no. | z upper (m) | z lower (m) | α (m/s) | β (m/s) | ρ (kg/m ³) |
|--------------|---------------------|---------------------|-------------------|------------------|--------------------------------|
| 1 | 0. | 100.0 | 1500.0 | 0.0 | 1000. |
| 2 | 100.0 | ∞ | 2400.-4.40i | 1000.0-18.32i | 2200. |

Table 6.2: The two-layer leaky mode environment used by Ellis and Chapman (1985). The upper interface is a traction free boundary. The chalk basement layer is infinitely thick. This is a leaky mode environment because the shear speed in the basement is less than the compressional speed in the water.

6.2.2 Modes in bounded waveguides

The impenetrable boundaries of a bounded waveguide trap waves that traverse its entire thickness. Like resonant modes in a duct, these top and bottom interacting modes tend to have small imaginary vertical slowness q_i for P or S waves in the thickest layers traversed by vibrations, otherwise they would suffer significant decay due to vertical evanescence before spanning the waveguide. Since total internal reflection is not involved, however, there is no lower bound on the estimated mode locations (6.8). Indeed, there is an infinite series of modes located roughly along the EJP branch lines of the thickest layers. A good example of this, cited earlier for evanescent modes in Section (6.1.2), is the infinite series of modes in the elementary oceanic waveguide, in which all of the modes lie directly on the EJP branch line for P waves its fluid layer [17], [66]. In this way, the EJP branch lines continue to play an important role in bounded waveguides, even though there are no branch line integrals to consider.

Radiation modes in deep bounded waveguides

An infinitely deep waveguide is sometimes modeled using a corresponding bounded waveguide, identical in every respect except that it is bounded below by a deep perfectly reflecting boundary. Here “deep” means that the bottom layer is much thicker than the wavelength for P and S waves, and much thicker than the combined thickness of all the

| layer no. | z upper (m) | z lower (m) | α (m/s) | β (m/s) | ρ (kg/m ³) |
|--------------|---------------------|---------------------|-------------------|------------------|--------------------------------|
| 1 | 0. | 200.0 | 1500.0 | 0.0 | 1000. |
| 2 | 200.0 | 1700. | 3000.-16.49i | 1732.-11.0i | 2000. |

Table 6.3: A simple deep bounded waveguide. The upper interface is a traction free boundary, and the bottom boundary is rigid in welded contact.

other layers in the waveguide. Bounding the waveguide results in a proliferation of bottom interacting modes that lie close to the EJP branch lines for the bottom layer where $q_i \approx 0$; otherwise they could not traverse the entire bottom layer. These are often called *radiation modes* because they radiate into the bottom layer [24] [5]. There is at least one series of radiation modes for P-waves in the bounded waveguide, but two series—for P and S waves—if the basement is solid.

Ways of estimating the location and spacing of radiation modes, which are helpful when directing a mode search, are considered below in Section (6.4). The correspondence between the deep bounded and unbounded waveguide is examined there as well. To illustrate radiation modes here, I will use a simple two-layer ocean model in Table (6.3). Figure (6.7) shows the mode locations for the both the unbounded and deep bounded waveguides at 100 Hz. The modes in the unbounded waveguide also appear in the deep bounded, but with their locations slightly perturbed (not noticeable at the scale of the figures) due to the finite basement thickness. The perturbation increases as the deep bounded waveguide is made thinner.

Leaky modes become radiation modes when the waveguide is bounded

When switching from the unbounded waveguide to the corresponding deep bounded waveguide, the role of leaky modes is taken on by the radiation modes. That is, radiation modes in the deep bounded waveguide are pulled away from a branch line to be located near the slowness p of the leaky modes for the unbounded waveguide. This is evident in Fig.(6.7) for the two-layer model, where the role of (proper) S-leaky modes in the unbounded wave-

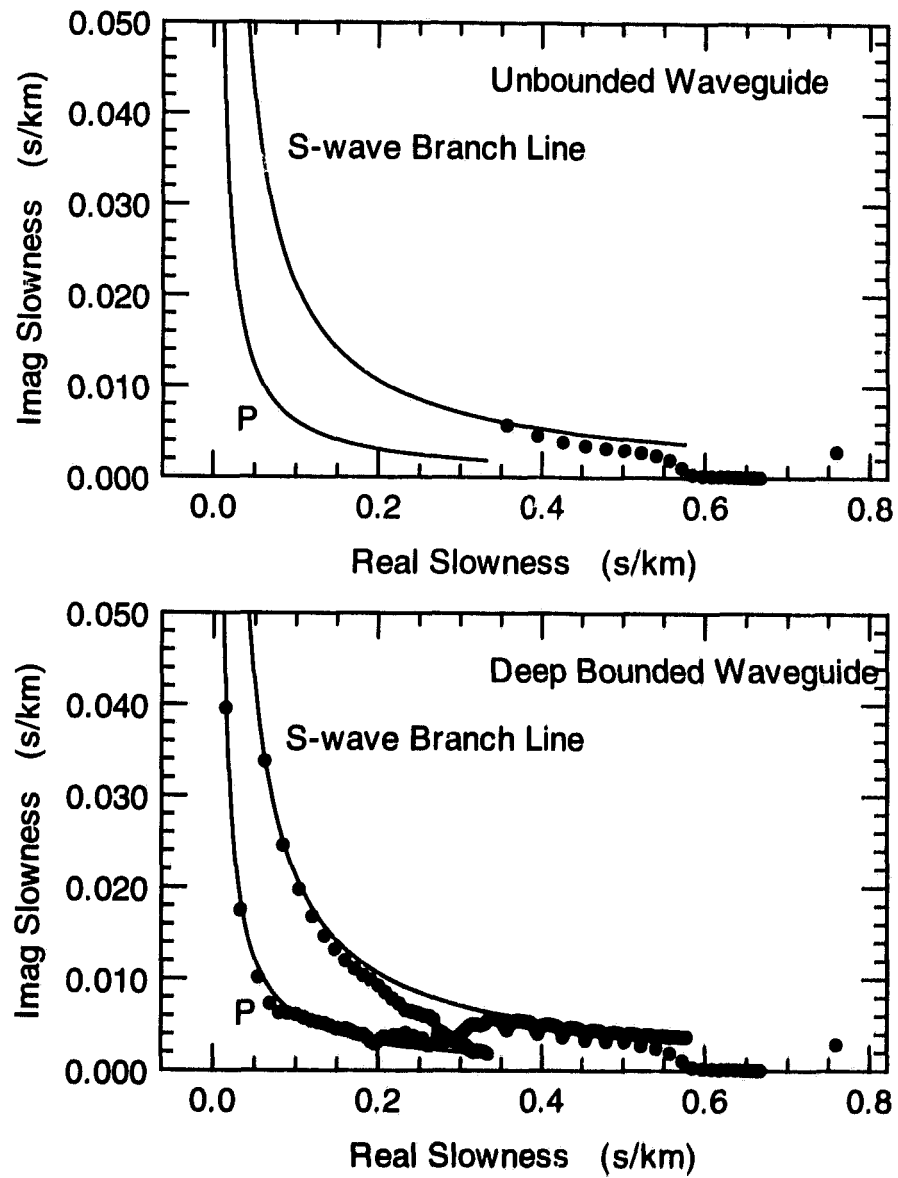


Figure 6.7: P-SV modes in the complex slowness plane for the unbounded and corresponding deep bounded waveguides at 100 Hz. In the bounded waveguide, there is a proliferation of radiation modes along the P- and S-wave branchlines of the basement media.

uide is taken on by radiation modes in the deep bounded waveguide. Fig.(6.8) shows that the vertical mode function for one proper leaky mode and its corresponding radiation mode are virtually identical. A similar correspondence occurs between dominant improper leaky modes lying above the S-wave branch line, and radiation modes pulled upwards away from the line to fill the role of the leaky mode. This correspondence suggests that improper leaky modes in an unbounded waveguide, whose mode function grow exponentially with depth, could be replaced by closely matched radiation modes of the corresponding deep bounded waveguide, whose mode function is well behaved with depth.

6.2.3 Interface modes

An interface mode is the resonance of an interface due to a discontinuity in the layered media, rather than the repeated constructive reflection of waves between interfaces. Like gravity waves at the surface of water, they entail elliptical particle motion in a vertical plane parallel to the direction of travel[66, sect. 8.4.3] [127]. This precludes interface modes consisting of strictly P waves in fluid media since their motion is irrotational, and of SH waves in solid since their motion is horizontal, leaving only the possibility of P-SV interface modes. The characteristic vibrations of an interface mode are maximal at the reverberating interface.

Rayleigh mode

An interface mode due to a traction free boundary on a solid is called a *Rayleigh mode*. The free boundary of a homogeneous solid half space always supports one, and only one, propagating Rayleigh mode. It is nondispersive, and its horizontal slowness of the mode typically lies in the range¹³

$$1.05 \frac{1}{\beta} < p < 1.2 \frac{1}{\beta}. \quad (6.10)$$

The situation is more complicated when the mode interacts with other layers in the waveguide because the wave is then dispersive. An oceanic waveguide having an infinitely deep solid bottom, for example, supports a Rayleigh mode at very low frequencies (below 1 Hz)

¹³The phase speed is typically 0.85 to 0.95 times the minimum phase speed c_{min} in either medium [127].

SAMPLE: Eigenfunction Plot

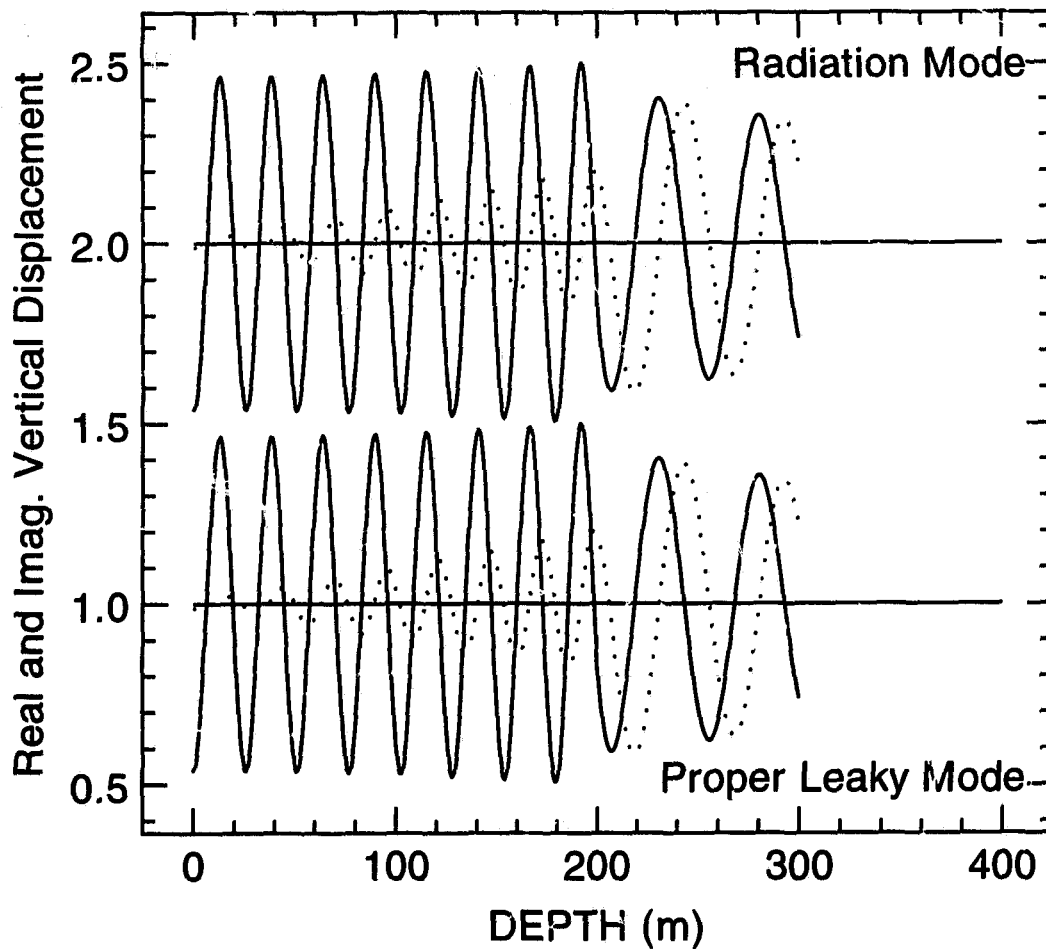


Figure 6.8: A proper S-leaky mode in the unbounded waveguide and its corresponding radiation mode in the deep bounded waveguide. Shown are the real (solid line) and imaginary (dotted line) parts of the vertical displacement U in the vertical mode functions. The locations of the modes are almost identical: $p = (5.406443 + 0.024069i) \times 10^{-4}$ s/m for the S-leaky mode in the unbounded waveguide, and $p = (5.4064281 + 0.024048i) \times 10^{-4}$ s/m for the radiation mode in the deep bounded waveguide. The mode normalizations are also almost identical; their proportions being (S-leaky : radiation) = 1.0056 : 1.0000.

when the water column is thin compared with the wavelength, in which case β in (6.10) must be taken from deep within the solid bottom. At higher frequencies, however, the same Rayleigh mode is likely to become a *Scholte mode* (considered below) confined to the ocean floor. We have already encountered a Rayleigh mode in the Gutenberg earth model in Section (5.8).

Scholte modes

An interface mode due to the discontinuity at a fluid-solid interface is called a *Scholte mode*. The interface between a fluid and solid half space always supports just one propagating Scholte mode. It is nondispersive, and its horizontal slowness must be

$$p > \frac{1}{\min \{ \alpha_{\text{solid}}, \beta_{\text{solid}}, \alpha_{\text{fluid}} \}} \quad (6.11)$$

or else it radiates (leaks) energy. Thus, each fluid-solid interface in a waveguide supports a Scholte mode when the wavelength is considerably less than the thickness of the adjacent layers. At longer wavelengths, however, the Scholte mode interacts with other parts of the waveguide, and is likely to become a different mode altogether, possibly a *duct* or *radiation mode*. We have already encountered a dispersive Scholte mode spanning a lossy sand layer on the sea floor in Fig.(6.4).

Stonely modes

An interface mode due to the discontinuity at a solid-solid interface is called a *Stonely mode*. Unlike Rayleigh and Scholte modes, Stonely modes rarely occur; they only exist for narrow ranges of elastic parameters α , β , and ρ for both media [6]. They have not been found in seismology [127], nor have I encountered one in the course of this research.

Rayleigh mode of the second kind

An interface mode due to a rigid boundary in welded contact with a solid also exists, though it is always a leaky mode. This mode appears in geoacoustics in an indirect way, when the waveguide is bounded below by a rigid impenetrable reflector. Since the waveguide is bounded, this leaky interface mode appears as a radiation mode at roughly

| layer no. | z upper (m) | z lower (m) | α (m/s) | β (m/s) | ρ (kg/m ³) |
|--------------|---------------------|---------------------|-------------------|------------------|--------------------------------|
| 1 | 0. | 200.0 | 1500.0 | 0.0 | 1030. |
| 2 | 200.0 | 1200 | 1704.5-0.532i | 200.0-0.0733i | 1150. |

Table 6.4: The two-layer leaky mode environment used by Arvelo et al. (1992). The upper interface is a traction free boundary, and the bottom boundary is rigid in welded contact.

the same location. Recall from (4.49) for the reflection matrix for P-SV waves at a rigid, welded contact boundary, the boundary wave occurs when M^\pm are singular. By setting $|M^+|$ or $|M^-| = 0$, we can show that the horizontal slowness for a Rayleigh wave of the second kind at a rigid boundary homogeneous solid half space lies at $p = 1/\sqrt{\alpha^2 + \beta^2}$. The mode is leaky because $p < 1/\alpha$ and $1/\beta$. Mode mode appears in a bounded waveguide in Table (6.4) studied by Arvelo et al. [5], though they make no mention of it. The upper figure in Fig.(6.9) duplicates their own figure 4, but I have used the complex slowness plane rather than horizontal wavenumber.¹⁴ The fourth mode at $p_r = 0.5895 \times 10^{-3}$ s/m ($k_r = 0.9260 \times 10^{-1}$ m⁻¹) corresponds to the Rayleigh mode of the second kind, made a proper radiation mode in the bounded waveguide, which agrees well with the theoretical estimate $p = 1/\sqrt{\alpha^2 + \beta^2} = 1/\sqrt{1704.5^2 + 200.0^2} = 0.5827 \times 10^{-3}$ s/m, which is exact when the basement layer is infinitely deep. The vibrations of the mode are confined to the bottom interface as shown in Fig. (6.9).

¹⁴Arvelo, et al. [5] report P and S wave absorption rates of 0.1 dB/m-Hz in the solid basement, whereas I can only duplicate their results using 0.01 dB/m-Hz. Their figure 4 shows 29 of the 37 modes they found, with the unplotted modes lying off scale. Unfortunately, mode number 4, which corresponds to the Rayleigh mode of the second kind, is among those left off the diagram. I also find 37 modes close to the real axis in the range of real of real slowness they consider, but there are many other modes further along the real axis, and higher above the region considered. These are mostly S-wave radiation modes along the S-wave branchline for the basement media, and there are very many of them because the S wavelength is small relative to the thickness of the basement layer. There is also the Scholte mode trapped at the seafloor.

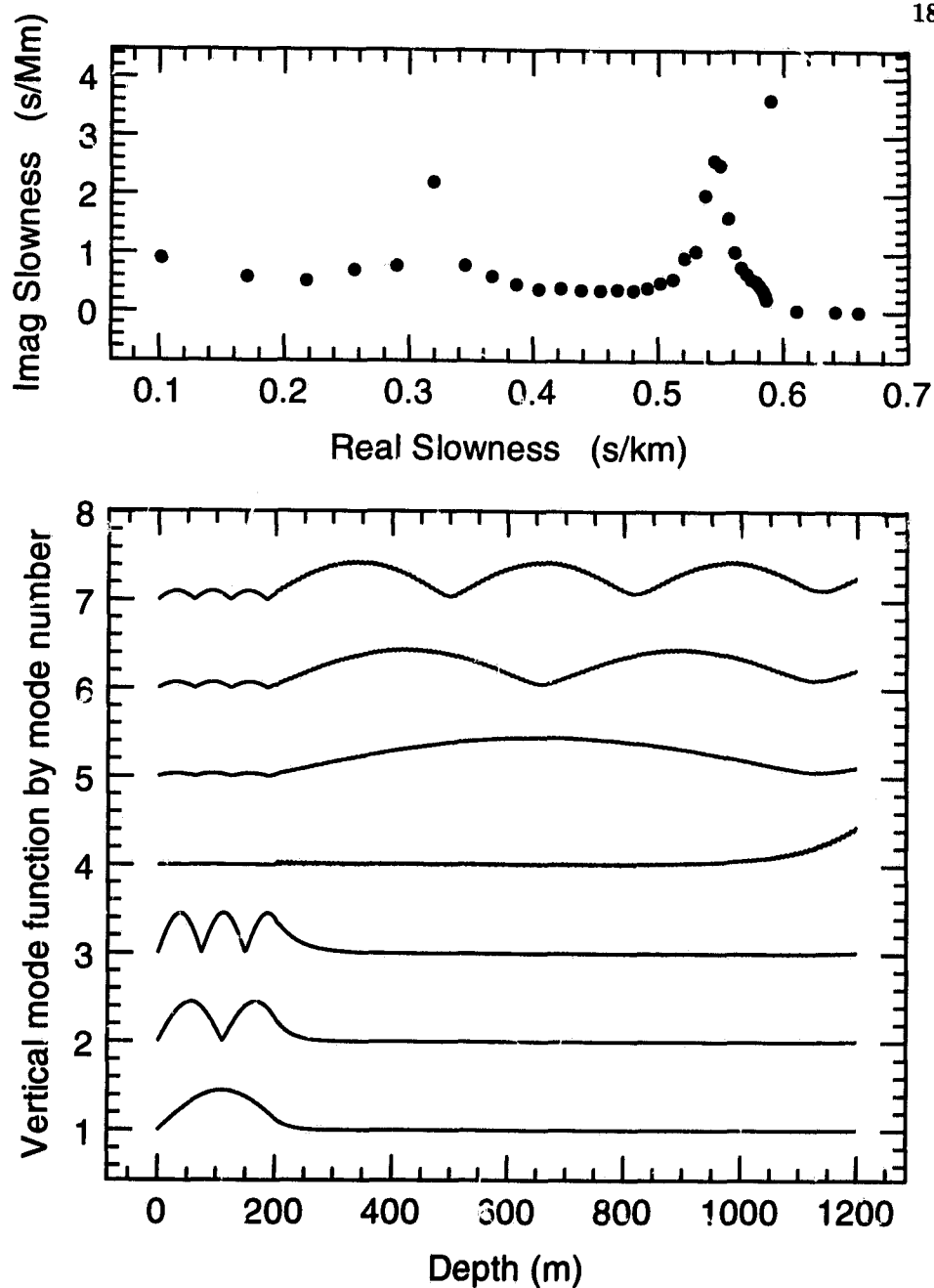


Figure 6.9: Top: P-SV modes for the two-layer bounded waveguide at 25 Hz. All modes are proper because the waveguide is bounded. Note that the vertical scale has been greatly amplified. Bottom: The vertical mode functions for the first seven modes, ordered by descending real slowness. The relative magnitude of the normal stress P in the mode functions has been plotted. Mode four corresponds to the Rayleigh mode of the second kind at the bottom interface. The small ripples are due to short wavelength shear waves in the bottom.

6.3 Identifying channels in the channel matrix method

The purpose of the channel matrix method is to accelerate the mode search by compressing the global matrix before computing its singular values, by combining components (layers and interfaces) in the schematic diagram together using the numerically stable scattering matrix method. The only difficulty is to ensure that the compressed matrix remains sensitive to modes trapped at any depth in the waveguide. This requires that the unknown wave vector for the compressed matrix sample the field at depths within the channel of every possible mode, where the vertical mode function for the mode will be significantly large. This can be done following two simple rules when combining elements.

Earlier in this chapter we saw that the boundary of an efficient duct occurs where the cylindrical waves undergo total internal reflection, which is where the waves switch from being vertically propagating inside the duct (mostly real vertical slowness q), to being vertically evanescent outside (mostly imaginary q). The first rule, then, is to retain the unknown wave vectors at every interface across which the P- or S-wave vertical slowness change from being mostly real in one layer to mostly imaginary in the other, for in this way we ensure that the compressed matrix will be sensitive to modes trapped in any duct. A second rule is to retain the unknown wave vectors at all interfaces that could possibly support an interface mode—impenetrable interfaces, and all interfaces between solid and fluid layers—because the vibrations of an interface mode are certain to be significantly large at the interface trapping it.

We could, for example, start at the top of the waveguide, and work downwards, combining layers and their interfaces into a single scattering matrix using the combination rules (4.65). Whenever the complex nature of the vertical slowness in the next layer changes—from dominantly real to imaginary at the boundary of a duct—the combination process is stopped and a new element is begun to retain the wave vector at the transmission depth as an unknown in the reduced ladder diagram for the waveguide. A new combined element would also be started whenever the media changes from solid to fluid. The combined elements are coupled using the continuity equation (4.42) for the interfaces between them. To ensure interface modes are detected at impenetrable boundaries, their boundary

conditions for P-SV waves would be enforced using the basic forms: (4.46) for rigid boundaries, and (4.48) for free. Since the vertical slowness depends on the horizontal slowness p , the depths between components will change throughout a mode search.

In this way, the Arctic profile in Table (5.1) is reduced to as few as five different components—the free boundary, the ice plate, the water column, the solid sea floor, and the deep rigid bottom, depending on the slowness p ; rather than sixteen components in the uncompressed waveguide: the free boundary, fourteen layers, and the deep rigid bottom. The time savings due to compression are considerable. In this case, the time taken for a search for modes along the real slowness axis is almost exactly ten times longer using the global matrix than the channel matrix method.

6.4 Deep bounded waveguides—Theory

An unbounded oceanic waveguide is sometimes modeled by a corresponding bounded waveguide identical in every respect except that it is bounded below by a deep perfectly reflecting boundary. To approximate the unbounded case, the bounded basement layer must be much thicker than the wavelength for P and S waves in the basement media, and much thicker than the combined thickness of all the other layers in the waveguide. The modes characteristic of the deep bounded waveguide and its correspondence with the unbounded waveguide are examined here.

6.4.1 Radiation modes close to the EJP branch lines

Fig.(6.10) is a schematic diagram for the deep bounded waveguide when the wave vectors are sampled at the top and bottom of the basement layer. The upper reflection matrix \mathbf{R}^- is due to the layer structure above the basement layer (including the top interface of the basement layer), and the lower reflection matrix \mathbf{R}^+ is due to the impenetrable bottom. Up and down going wave vectors are transmitted equally through the homogeneous basement layer by the transmission matrix (4.40)

$$\mathbf{T} = \begin{bmatrix} e^{i\omega q_\alpha H} & 0 \\ 0 & e^{i\omega q_\beta H} \end{bmatrix}, \quad (6.12)$$

where q_α or q_β are the P and S wave vertical slownesses in the basement media with $\text{Im}\{q\} \geq 0$. By inspection of the diagram, the equation for the wave vector component \mathbf{v}_1^+ is

$$\mathbf{v}_1^+ = \mathbf{R}^- \mathbf{v}_1^- = \mathbf{R}^- \mathbf{T} \mathbf{v}_2^- = \mathbf{R}^- \mathbf{T} \mathbf{R}^+ \mathbf{v}_2^+ = \mathbf{R}^- \mathbf{T} \mathbf{R}^+ \mathbf{T} \mathbf{v}_1^+; \quad (6.13)$$

hence

$$(\mathbf{I} - \mathbf{R}^- \mathbf{T} \mathbf{R}^+ \mathbf{T}) \mathbf{v}_1^+ = \mathbf{0}, \quad (6.14)$$

and the characteristic equation for modes traversing the entire basement layer to interact with the deep impenetrable bottom is

$$|\mathbf{I} - \mathbf{R}^- \mathbf{T} \mathbf{R}^+ \mathbf{T}| = 0. \quad (6.15)$$

In the limit as H becomes large,

$$\lim_{H \rightarrow \infty} e^{i\omega q H} = e^{i\omega q_r H} \left(\lim_{H \rightarrow \infty} e^{-\omega q_i H} \right) = 0 \quad (6.16)$$

unless the imaginary part $q_i \rightarrow 0$ simultaneously. Thus,

$$\lim_{H \rightarrow \infty} \mathbf{T} = \begin{cases} \mathbf{0} & \text{if } \text{Im}\{q_\alpha\} \text{ and } \text{Im}\{q_\beta\} \neq 0, \\ \begin{bmatrix} e^{i\omega q_\alpha H} & 0 \\ 0 & 0 \end{bmatrix} & \text{if } q_\alpha \text{ is real and } \text{Im}\{q_\beta\} \neq 0, \\ \begin{bmatrix} 0 & 0 \\ 0 & e^{i\omega q_\beta H} \end{bmatrix} & \text{if } q_\beta \text{ is real and } \text{Im}\{q_\alpha\} \neq 0; \end{cases} \quad (6.17)$$

and

$$\lim_{H \rightarrow \infty} |\mathbf{I} - \mathbf{R}^- \mathbf{T} \mathbf{R}^+ \mathbf{T}| = \begin{cases} 1 & \text{if } \text{Im}\{q_\alpha\} \text{ and } \text{Im}\{q_\beta\} \neq 0, \\ 1 - R_{11}^- R_{11}^+ e^{2i\omega q_\alpha H} & \text{if } q_\alpha \text{ is real and } \text{Im}\{q_\beta\} \neq 0, \\ 1 - R_{22}^- R_{22}^+ e^{2i\omega q_\beta H} & \text{if } q_\beta \text{ is real and } \text{Im}\{q_\alpha\} \neq 0, \end{cases} \quad (6.18)$$

indicating two possible sets of modes, called *radiation modes*, along the P and S branch lines.

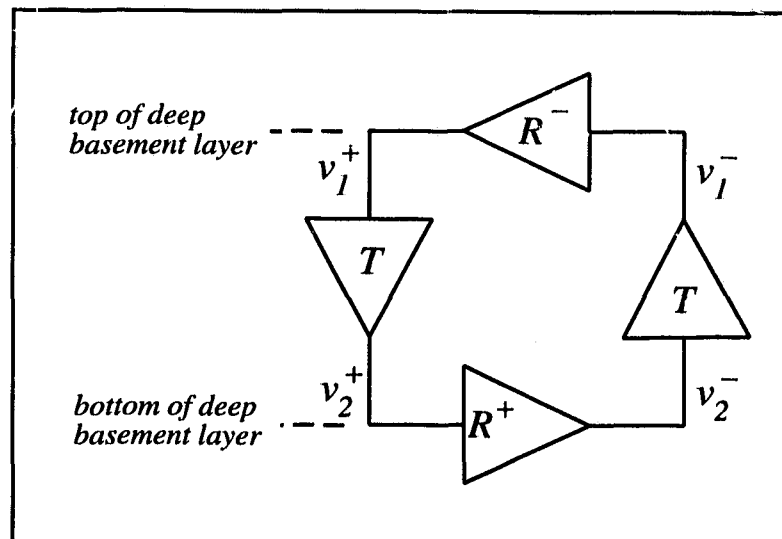


Figure 6.10: The reduced schematic ladder diagram for a deep basement layer. The upper reflection matrix represents all layers except the basement, and the lower reflection from the impenetrable bottom interface. Transmission through the basement is simply that of a homogeneous layer.

6.4.2 The spacing of radiation modes

Since H is large, the phase terms $e^{2i\omega q_{\alpha,\beta}H}$ change considerably over a small step Δq along a branch line, whereas the reflection matrix components R_{ij}^{\pm} change very little. If a radiation mode exists at some value of q , neighboring modes should lie along the branch line at $q \pm \Delta q$ where

$$2\omega\Delta qH \approx 2\pi. \quad (6.19)$$

Using $\Delta q \approx (dq/dp)\Delta p = -(p/q)\Delta p$, the estimate of the mode spacing along a branch line is

$$\Delta p \approx -\frac{\pi q}{\omega H p}. \quad (6.20)$$

The estimate improves as H is made larger.

Notice that the modes can be very close together near the branch point where $q \approx 0$. By analogy with the elementary oceanic waveguide, let us assume that the first radiation mode on a branch line—the mode closest to the branch point—occurs when a quarter P or S wavelength λ fits vertically inside the basement layer

$$H \approx \frac{\lambda}{4} = \frac{1}{4fq} \quad (6.21)$$

Furthermore, assuming that $p \approx 1/c$ near the branch point, the estimated mode spacing (6.20) gives

$$\Delta p \approx -\frac{c}{8f^2H^2} \quad (6.22)$$

near the branch point, where $c = \alpha$ or β according to the branch line. The search resolution needed to resolve radiation modes near the branch point must be somewhat smaller than this.

Radiation modes are further apart away from the branch point. The largest Δp occurs near $p = 0$, at the knee in the EJP branch line. In fact, the estimate (6.20) may break down at the knee because it assumes Δp is small. Following the EJP branch line high along the positive imaginary axis, however, $q = \sqrt{1/c^2 - p^2} \rightarrow p$, and the mode spacing approaches a constant independent of the elastic media

$$\Delta p \approx \frac{i}{2fH}. \quad (6.23)$$

The radiation modes trail indefinitely along the imaginary axis with roughly this spacing. This result also applies for high-order evanescent *plate modes* which might be viewed as a special case of radiation modes trapped in a distinct plate-like structure.

6.4.3 Estimating the number of radiation modes

Let us estimate the number of propagating radiation modes close to the real p axis, along the horizontal portion of the branch line. For simplicity, neglect the small imaginary part of the phase speed c (α or β), then the branch line follows the real slowness axis from $p = 1/c$ to 0, where $q = 0$ and $1/c$, respectively. For waves travelling the circuit from top to bottom to top again in the basement layer, the change in vertical phase along this horizontal part of the branch line (ignoring changes in R_{ij}^{\pm} in (6.18)), is roughly $2\omega\Delta qH \approx 2\omega H/c$. Dividing this total change of phase into 2π steps gives an estimate of the minimum number of propagating radiation modes for one branch line

$$N_p \approx \frac{2\omega H}{2\pi c} = 2fH/c = 2H/\lambda; \quad (6.24)$$

λ being the wavelength of P or S waves in the bottom, depending on which branch line is under consideration. Notice there are proportionally fewer propagating modes at low frequencies than at high because the mode spacing is inversely proportional to frequency (6.20).

Applying the estimate to the two-layer oceanic model considered earlier in Chapter 6, Table(6.3), we have

$$\begin{aligned} H &= 1500 \text{ m,} \\ \lambda_\alpha &= \alpha/f = 3000./100 = 30.00 \text{ m,} \\ \lambda_\beta &= \beta/f = 1732./100 = 17.32 \text{ m;} \end{aligned} \quad (6.25)$$

hence

$$\begin{aligned} N_p &\approx 100 && \text{P-wave radiation modes,} \\ N_p &\approx 173 && \text{S-wave radiation modes,} \\ \text{Total} &= 275 \end{aligned} \quad (6.26)$$

which compares well with the total of 255 radiation modes actually found near the horizontal branch lines in Fig. (6.7), in the range $0 < p_r < 1/1732 = 0.577 \text{ s/km}$, and $0 < p_i < 0.02$

s/km.

Applying the estimate to a more realistic model, the Arctic waveguide considered earlier in Table (5.1), we have

$$\begin{aligned} H &= 2000 \text{ m,} \\ \lambda_\alpha &= \alpha/f = 5250/20 = 262.5 \text{ m,} \\ \lambda_\beta &= \beta/f = 2500/20 = 125.0 \text{ m;} \end{aligned} \tag{6.27}$$

hence

$$\begin{aligned} N_p &\approx 15 && \text{P-wave radiation modes,} \\ N_p &\approx 32 && \text{S-wave radiation modes,} \\ \text{Total} &= 47 \end{aligned} \tag{6.28}$$

which compares well with the total of 45 radiation modes actually found near the horizontal branch lines in Fig. (5.6).

It is important to know roughly how many evanescent radiation modes may be required to compute the field in the bounded waveguide to a specified relative precision ϵ . To this end, let us assume, as in the convergence test (5.42), that the radiation mode series has converged when

$$p_i \approx -\frac{\ln(\epsilon)}{2\pi f r}. \tag{6.29}$$

Dividing by the magnitude of the asymptotic spacing (6.23) gives the number of evanescent modes

$$N_e \approx -\frac{H \ln(\epsilon)}{\pi r}. \tag{6.30}$$

At small ranges the number of modes may be prohibitively large. At very large ranges, no evanescent modes may be required. Unlike the propagating modes, the number of evanescent radiation modes N_e needed at close ranges is independent of frequency because both the maximum imaginary slowness spanned by the significant evanescent modes (6.29), and the asymptotic mode spacing, are inversely proportional to frequency.

6.4 4 Correspondence with the unbounded waveguide

Radiation modes of the bounded waveguide presumably approximate the contribution of the branch line integrals of the unbounded. Frisk demonstrates the correspondence

for a two-layer fluid (Pekeris) waveguide [48]. The extension to elastic media will not be attempted here, except to point out that the branch line mode spacing (6.20) vanishes as $H \rightarrow \infty$, as it must if the series approaches an integral in the limit; and that the field for each radiation mode can be written in terms of down and up going waves in the basement layer, as it must if the series represents the integral along both sides of the EJP branch cut simultaneously.

For modeling purposes, it is important to know when the deep bounded waveguide accurately models the unbounded case. One rule of thumb can be derived by viewing the branch line mode series as a numerical approximation to the branch line integrals. Obviously the modes cannot be too far apart or the integrand will not be adequately sampled along the branch line. Indeed, there should only be a small change in the complex phase $e^{i\omega p r}$ between modes

$$\omega |\operatorname{Re}\{\Delta p\}| r \ll 2\pi. \quad (6.31)$$

Assuming a lossless bottom medium, Δp is pure real along the EJP branch line from the branch point to the origin, and using (6.20), (6.31) becomes

$$\frac{r}{2H} \ll \frac{p'}{q'}, \quad (6.32)$$

where p' is the slowness of the mode closest to the origin where $|\Delta p|$ is maximal. This limit has a physical interpretation, for equality of both sides in (6.32) is the condition of the first bottom bounce of "rays" having horizontal and vertical slowness, p' and q' . And as the range from the source increases from zero, it is the bottom reflections of the mode with the most vertically directed rays—the mode at the knee of the branch line—that first ruins the correspondence between the unbounded and deep bounded waveguides, as we might have expected.

Unfortunately, p' for the mode at the knee of the branch line cannot be estimated in a general way, and the limit on r can only be estimated once the mode has been found. Nevertheless, it is reasonable to take $q' = \sqrt{1/c^2 - (p')^2} \approx 1/c$ since p' lies near the origin, where $|\Delta p|$ is a maximum, so that (6.32) simplifies to

$$r \ll 2Hp'c, \quad (6.33)$$

where $c = \alpha$ or β according to the branch line.

Adding absorption to the bottom media improves the correspondence with the unbounded waveguide. By pushing the propagating radiation modes away from the real p axis, the contribution of the higher order modes at the knee of the branch line decreases, relaxing the condition (6.32) somewhat. More importantly, absorption makes all of the propagating radiation modes decay more quickly with range, effectively turning them off at large ranges. If the dominant radiation modes near the branch point become negligible due to energy loss, then

$$e^{-\omega p_i r} \leq \epsilon, \quad (6.34)$$

for some small ϵ , taking

$$p \approx 1/c = 1/(c_r + ic_i) \approx 1/c_r - ic_i/c_r^2 \quad (6.35)$$

near the branch point, where $c_i \leq 0$ and $|c_i| \ll c_r$, we find

$$r \geq \frac{c_r^2 \ln(\epsilon)}{2\pi f c_i}. \quad (6.36)$$

Thus, the effect of absorption in the basement is to eliminate the offending bottom bounce (propagating radiation) modes beyond this range. When the basement is solid, the largest bound for P-SV waves results using the P-wave phase speed α for c , because α is larger than β .

To summarize, then, the correspondence between the unbounded and deep bounded waveguide is best in the near field, at ranges satisfying (6.33) where p' is the slownesses for the highest order propagating radiation mode; and best in the far field, when absorption is included in the basement media, at ranges defined by (6.36). Ideally, these two conditions would overlap to give good correspondence between the two waveguides at all ranges.

To illustrate, let us return to the two-layer oceanic waveguide considered earlier, in Table (6.3). From the P-SV mode locations in Fig.(6.7), we see that the modes closest to the knee of the P and S-wave branch lines are roughly $p_r = 0.065$ and 0.080 s/km, respectively, for which the first condition for correspondence (6.33) is

$$\begin{aligned} r &\ll 2Hp\alpha = 2 \times 1500 \times 0.065 \times 10^{-3} \times 3000 \approx 585 \text{ m} && \text{for P waves,} \\ r &\ll 2Hp\beta = 2 \times 1500 \times 0.080 \times 10^{-3} \times 1732 \approx 416 \text{ m} && \text{for S waves.} \end{aligned} \quad (6.37)$$

Assuming precision $\epsilon = 0.01$, the second condition is

$$r \geq \frac{\alpha_r^2 \ln(\epsilon)}{2\pi f \alpha_i} = \frac{3000^2 \ln(0.01)}{2\pi \times 100 \times (-16.49)} \approx 4000 \text{ m.} \quad (6.38)$$

Fig.(6.11) shows the normal stress due to an explosive point source at $z = 25.0$ m and $f = 20.0$ Hz, computed for the waveguide when it is infinitely thick, and when the basement layer 1500.0 m thick. Good correspondence is achieved throughout, but it does look as though the correspondence worsens beyond $r = 585$ m, then improves again towards 4000 m. Also shown is the field close to the source when the bounded basement is lossless. The near field correspondence is good for $r \ll 416$ m, as predicted for shear waves, beyond which bottom bounces obviously ruin the correspondence, as shown by the rapid variations. Repeated bottom bounces continue to all greater ranges since the condition for restored correspondence (6.36) is $r = \infty$ for a lossless basement.

6.5 Weakly coupled sound channels—Theory

To illustrate how close mode pairs occur in weakly coupled channels,¹⁵ consider the two-channel system in Fig.(6.12). The upper and lower reflection components \mathbf{R}_A^- and \mathbf{R}_B^+ represent reflection from the upper and lower channels A and B respectively. The intervening scattering matrix network, with reflection and transmission partitions \mathbf{R}_e^\pm and \mathbf{T}_e^\pm , represents a band of evanescent layers that weakly couples the two channels. From the schematic diagram we can immediately write the channel matrix equation, omitting sources because we are concerned with modes,

$$\begin{bmatrix} \mathbf{I} & -\mathbf{R}_A^- & \mathbf{0} & \mathbf{0} \\ -\mathbf{R}_e^+ & \mathbf{I} & \mathbf{0} & -\mathbf{T}_e^- \\ -\mathbf{T}_e^+ & \mathbf{0} & \mathbf{I} & -\mathbf{R}_e^- \\ \mathbf{0} & \mathbf{0} & -\mathbf{R}_B^+ & \mathbf{I} \end{bmatrix} \begin{bmatrix} \mathbf{v}_A^+ \\ \mathbf{v}_A^- \\ \mathbf{v}_B^+ \\ \mathbf{v}_B^- \end{bmatrix} = \mathbf{0}. \quad (6.39)$$

¹⁵The study of modes in weakly coupled systems finds application in many (linear) physical problems, and the analysis in each is much the same. Perhaps the simplest instance is that of weakly coupled pendula in classical physics [119]. Even closer to the geoacoustic problem is that of weakly coupled internal wave modes in the ocean, which has been studied in detail by Dawson (1988) [30].

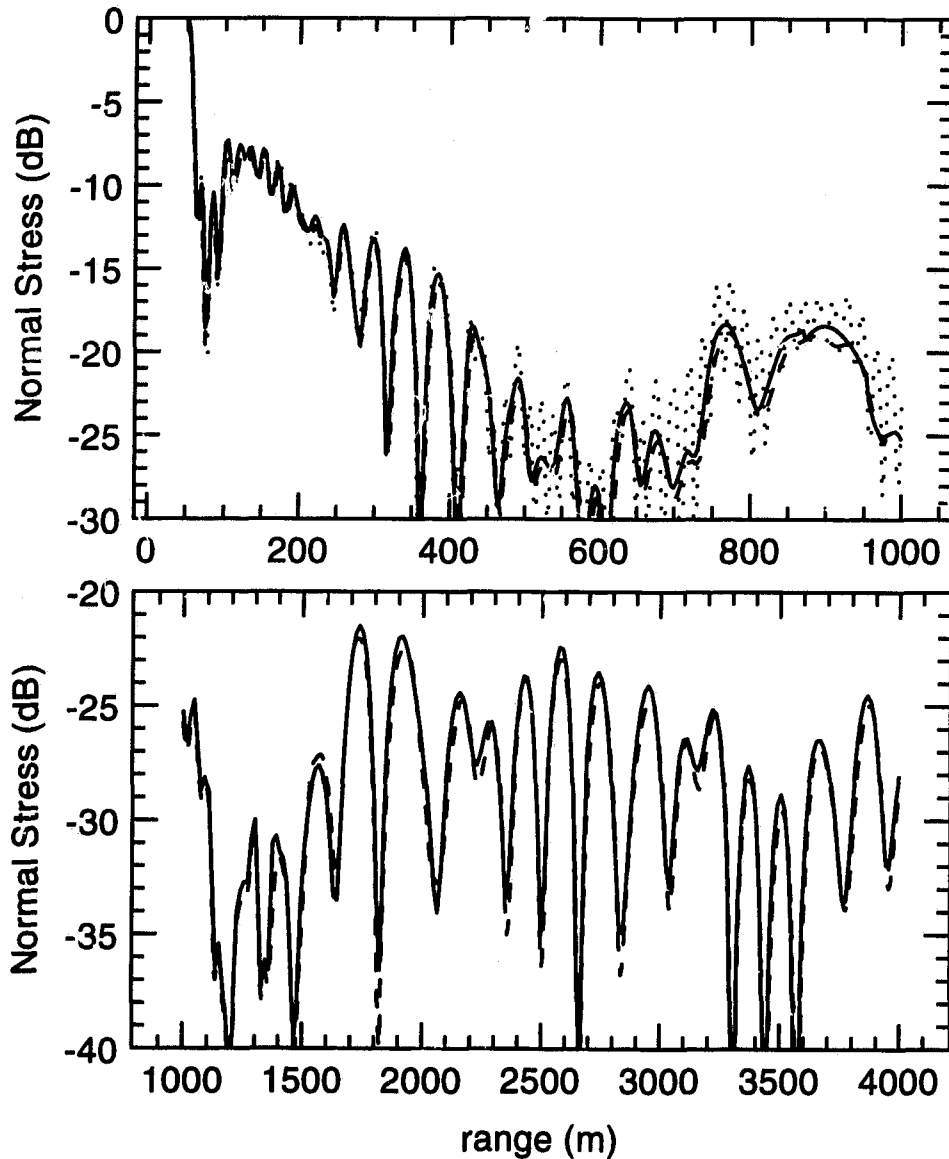


Figure 6.11: Normal stress τ_{zz} as a function of range, at depth $z = 25.0$ m, in the infinitely deep waveguide (dashed line), computed using contour integration, and in the corresponding deep bounded waveguide (solid line), computed using mode summation. **Top:** Near field. The field for the lossless bounded waveguide is also plotted (dotted line). **Bottom:** Far field. The source, also at depth $z = 25.0$ m, is operating at $f = 20.0$ Hz.

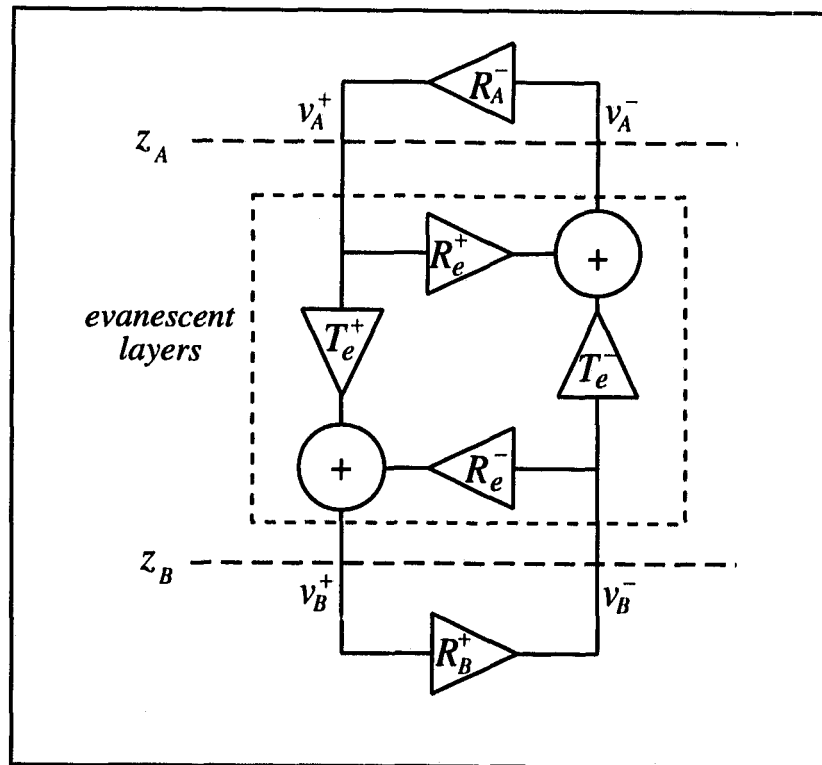


Figure 6.12: The reduced schematic ladder diagram for a waveguide supporting two weakly coupled channels at once. z_A lies inside the upper channel, and z_B within the lower.

The decoupling of channels is evident when the transmission \mathbf{T}_e^\pm goes to zero due to strong vertical evanescence. At the same time, the determinant of the matrix goes to

$$\begin{vmatrix} \mathbf{I} & -\mathbf{R}_A^- \\ -\mathbf{R}_e^+ & \mathbf{I} \end{vmatrix} \cdot \begin{vmatrix} \mathbf{I} & -\mathbf{R}_e^- \\ -\mathbf{R}_B^+ & \mathbf{I} \end{vmatrix} - \epsilon = |\mathbf{I} - \mathbf{R}_A^- \mathbf{R}_e^+| \cdot |\mathbf{I} - \mathbf{R}_e^- \mathbf{R}_B^+| - \epsilon, \quad (6.40)$$

where $\epsilon = \epsilon(\omega, p)$ is a small number whose magnitude is less than some upper bound given by

$$|\epsilon| < C \|\mathbf{T}_e^+\| \|\mathbf{T}_e^-\|, \quad (6.41)$$

where C is a positive real constant and $\|\mathbf{T}_e^\pm\|$ denotes a norm of the transmission matrices. In the scalar case for P waves, for example, when z_A and z_B lie in fluid layers, the reflection, transmission, and identity partitions in (6.39) are all scalars, giving

$$|\epsilon| = |\mathbf{R}_A^- \mathbf{R}_e^+| |\mathbf{T}_e^+| |\mathbf{T}_e^-| \quad (6.42)$$

In the limit of total decoupling $\|\mathbf{T}_e^\pm\| \rightarrow 0$, hence $\epsilon \rightarrow 0$, and the condition for a mode—that (6.40) be zero—becomes

$$|\mathbf{I} - \mathbf{R}_A^- \mathbf{R}_e^+| \cdot |\mathbf{I} - \mathbf{R}_e^- \mathbf{R}_B^+| = \epsilon \approx 0. \quad (6.43)$$

At a mode, either

$$\begin{aligned} |\mathbf{I} - \mathbf{R}_A^- \mathbf{R}_e^+| &\approx 0, \\ |\mathbf{I} - \mathbf{R}_e^- \mathbf{R}_B^+| &\approx 0, \end{aligned} \quad (6.44)$$

or both determinants are simultaneously small. These determinants are the characteristic equations for modes in each channel considered separately, so the modes of the weakly coupled channels are located near the modes of each channel considered independently, as expected.

Close mode pairs occur when both conditions (6.44) are satisfied simultaneously. The slowness p and frequency ω of the modes must be a point on the dispersion curves where the curves for each channel would cross if the channels were totally decoupled. In the vicinity of such a crossing point p_c , the left sides of (6.44) can be approximated by a Taylor series expansion

$$\begin{aligned} |\mathbf{I} - \mathbf{R}_A^- \mathbf{R}_e^+| &= 0 + \lambda_A (p - p_c) + O((p - p_c)^2), \\ |\mathbf{I} - \mathbf{R}_e^- \mathbf{R}_B^+| &= 0 + \lambda_B (p - p_c) + O((p - p_c)^2), \end{aligned} \quad (6.45)$$

where λ_A and λ_B are the first derivatives of the left sides of (6.44) evaluated at p_c .¹⁶ Substituting these into (6.43) and retaining only the first order terms, gives the characteristic equation for the weakly coupled channels near the crossing point p_c

$$\lambda_A \lambda_B (p - p_c)^2 = \epsilon. \quad (6.46)$$

Solving for p , we find a pair of modes for the coupled system

$$p = p_c \pm \sqrt{\epsilon / \lambda_A \lambda_B} = p_c \pm \Delta p / 2. \quad (6.47)$$

The spacing between a mode pair $|\Delta p| = 2 \left| \sqrt{\epsilon / \lambda_A \lambda_B} \right|$ can be very small indeed since $\epsilon \rightarrow 0$ exponentially due to vertical evanescence. An extensive search at the resolution needed to distinguish the pair would usually not be feasible, but they can be identified and resolved using the singular values of the channel matrix during the mode search function as described in Section (5.3.3).

The mode functions for a close mode pair are approximately anti-symmetric, just as the modes for the classic mode problem for weakly coupled pendula are anti-symmetric [23]

$$\begin{bmatrix} \mathbf{v}_A^+ \\ \mathbf{v}_A^- \\ \mathbf{v}_B^+ \\ \mathbf{v}_B^- \end{bmatrix} \approx \begin{bmatrix} \mathbf{v}_A^+ \\ \mathbf{0} \\ \mathbf{0} \\ \mathbf{v}_B^- \end{bmatrix} \quad \text{or} \quad \begin{bmatrix} \mathbf{v}_A^+ \\ \mathbf{0} \\ \mathbf{0} \\ -\mathbf{v}_B^- \end{bmatrix}. \quad (6.48)$$

Thus, both modes must be almost equally excited when the source lies in just one channel to achieve cancellation in the other channel. But at large distances from the source, the slightly different horizontal slownesses for a mode pair causes the mode functions to interfere (beat) with each other. Assuming a range phase dependence $e^{i\omega p r}$ characteristic of cylindrical waves in the far field, for example, the sum of the two equally excited modes can be written

¹⁶Here I have assumed that λ_A and λ_B are not zero, which could only occur if the mode in either system was itself a double (or higher) mode, meaning that there are actually three or more resonant modes at slowness p —a very unlikely situation in naturally occurring waveguides.

as

$$e^{i\omega(p_c + \Delta p/2)r} \begin{bmatrix} \mathbf{v}_A^+ \\ \mathbf{0} \\ \mathbf{0} \\ \mathbf{v}_B^- \end{bmatrix} + e^{i\omega(p_m - \Delta p/2)r} \begin{bmatrix} \mathbf{v}_A^+ \\ \mathbf{0} \\ \mathbf{0} \\ -\mathbf{v}_B^- \end{bmatrix} = \begin{bmatrix} 2\mathbf{v}_A^+ e^{i\omega p_c r} \cos \omega \Delta p r / 2 \\ \mathbf{0} \\ \mathbf{0} \\ 2i \mathbf{v}_B^- e^{i\omega p_c r} \sin \omega \Delta p r / 2 \end{bmatrix} \quad (6.49)$$

The interference causes the sound energy of both modes together to transfer between the channels over a cycle distance $D = 2\pi / (\omega \operatorname{Re} \{\Delta p\}) = (f \operatorname{Re} \{\Delta p\})^{-1}$ in range. The situation is analogous to the transfer of pendulum motion in the coupled pendula problem. Motion in just one pendulum is in time transferred to its resonant partner, originally stationary, then back again, and so repeatedly transferring the vibration energy between the two pendula. What happens in time between resonant pendula, happens in range between resonant channels in the waveguide: waves travelling in one channel are over long distances transferred to the other, and the back again, with cycle distance D .

To illustrate, consider the almost symmetric fluid waveguide in Table (6.5), contrived for demonstration of weakly coupled resonant modes. Fig. (6.13) shows the first and second singular values in the search for propagating modes along the real axis at 12 Hz. Close to a mode pair, the search functions follow the form described earlier in Fig. (5.4), which is evident for the second pair (modes 3 and 4, spacing $\Delta p = .003475$ s/km), though not for the first pair (1 and 2, spacing $\Delta p = .0002484$ s/km) at the scale of the figure. The antisymmetric nature of the vertical mode functions is evident in the bottom figure. Fig. (6.14) shows the transfer of sound energy between the two channels with range for modes 3 and 4 alone. The source is an explosive point source (12 Hz) in the upper channel at $z = 50$ m.

Resonant sound channels may be encountered occasionally when modeling waves of one frequency in a range independent waveguide. In practice, the frequency band of an acoustic signal may span several resonances, and slowly varying layer thicknesses and elastic properties may cause channels to tune in and out of resonance as the sound propagates, making the coupled channels much more likely, possibly resulting in a partial transfer of energy between weakly coupled channels, though without ongoing repetition.

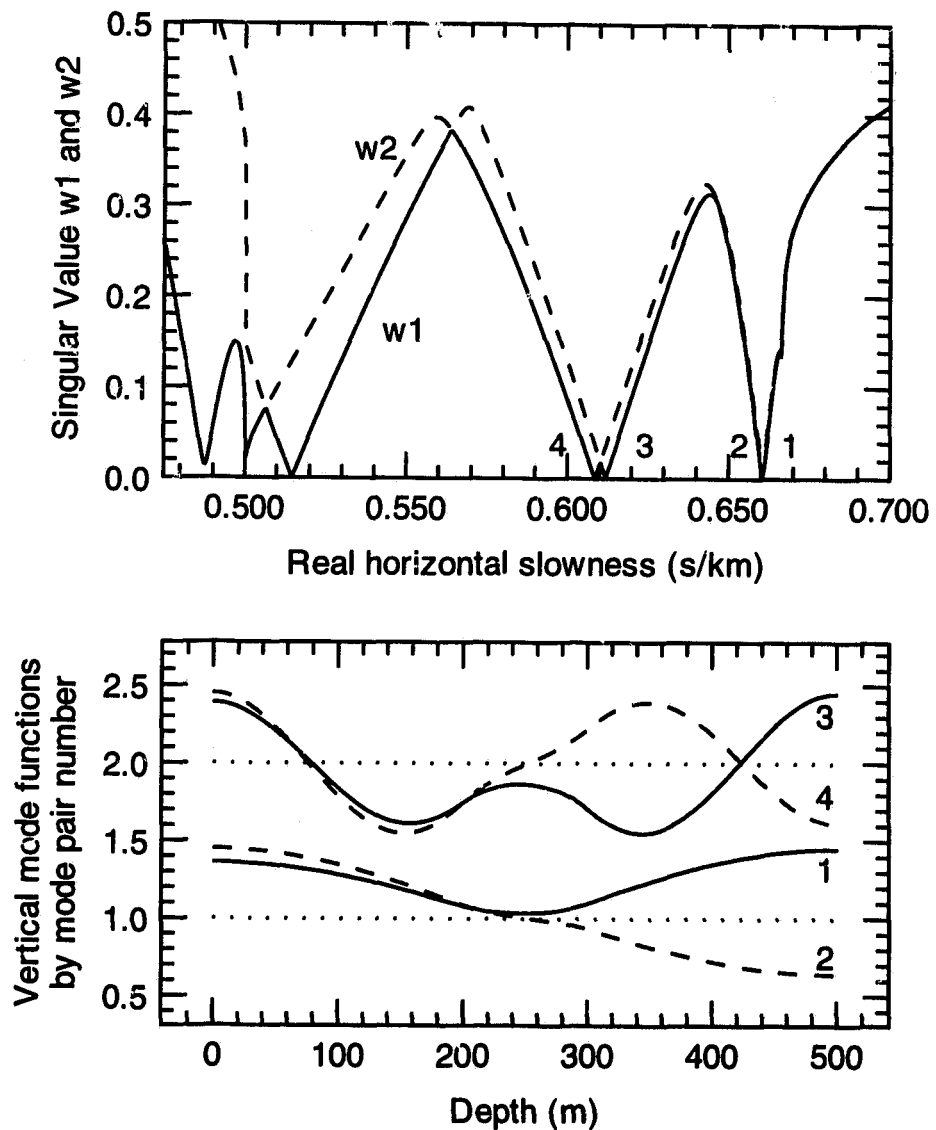


Figure 6.13: Weakly coupled sound channels: **Top:** The mode search functions along the real axis at 12 Hz. Deep minima in the second smallest singular value w_2 indicate the presence of a close mode pair. **Bottom:** The vertical mode functions for close mode pairs are roughly antisymmetric. Here the real part of the normal stress P in the stress-displacement vector has been plotted for the first two mode pairs (by decreasing p_r).

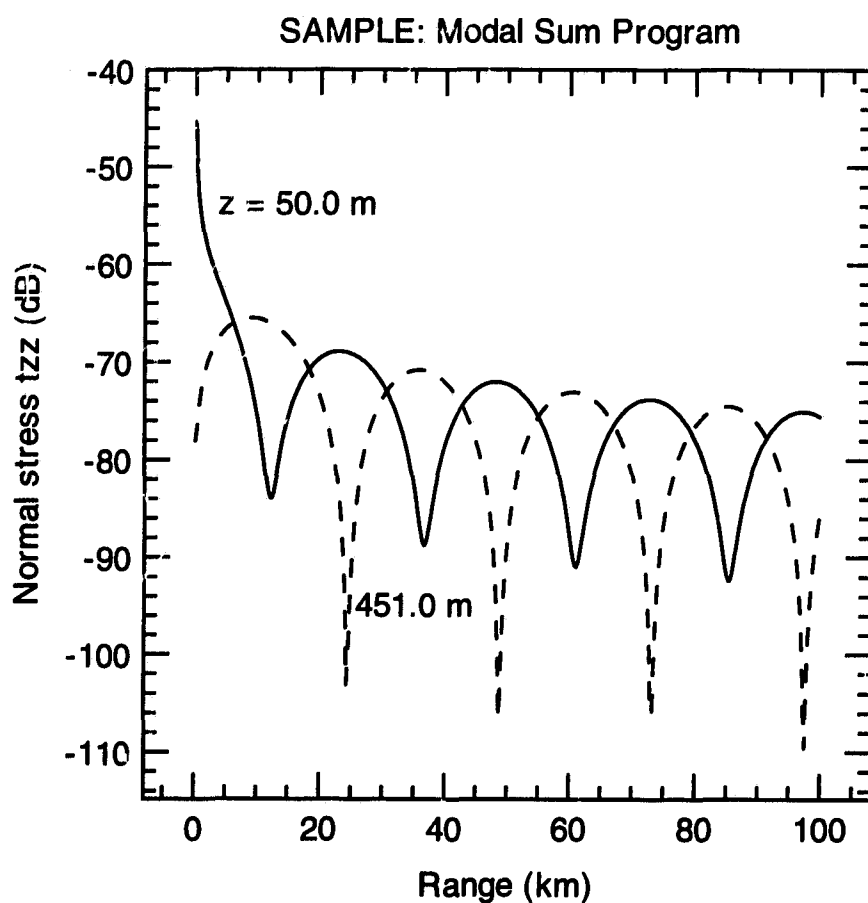


Figure 6.14: Repeated transfer of sound energy between weakly coupled sound channels. The source lies in the upper channel at $z = 50.0$ m. Plotted is the normal stress as a function of range in the upper (solid line) and lower (dashed line) sound channels for the sum of modes 3 and 4 alone. The cycle distance determined from their mode spacing is 23.98 km.

| layer no. | z upper (m) | z lower (m) | α (m/s) | β (m/s) | ρ (kg/m ³) |
|--------------|---------------------|---------------------|-------------------|------------------|--------------------------------|
| 1 | 0.0 | 200.0 | 1500.0 | 0.0 | 1000. |
| 2 | 200.0 | 300.0 | 2000.0 | 0.0 | 1000. |
| 3 | 300.0 | 501.0 | 1500.0 | 0.0 | 1000. |

Table 6.5: Almost symmetric fluid waveguide. The top and bottom of the waveguide are bounded by a rigid plane.

Chapter 7

BIE method for layered media

I have so far developed a new indirect BIE method for the scattering of elastic waves and a normal mode method for numerically computing the complete Green's function for layered media. It remains to unite them in a single model of elastic wave scattering. This is a straightforward task from a programmer's perspective, for we need only make the modal summation subroutine available to the existing Green's function subroutine. The matter is much more complicated from the user's perspective, for, as we will see, one part of the scattering problem cannot be freely specified without regard for another since there are several competing parameters that must be balanced for the model to run successfully. As in BIE methods generally, the kinds of problems that can be solved are biased towards low frequency scattering, for the wavelength cannot be too small compared to the dimensions of the inclusion or the number of elements needed to represent its boundary will exceed a practical limit. In layered media, when using mode summation for the Green's function, the low-frequency bias appears in another way, for the wavelength cannot be too small compared to the thickness of the waveguide or there will be a proliferation of significant modes beyond a practical limit. These constraints are reviewed below.

7.0.1 Constraints due to element size

We have seen that the size of the boundary elements must be small compared to the wavelengths in their vicinity. Frequency and phase speed therefore constrain the

maximum size of the elements, which in turn determines the minimum number of elements needed to cover a given scattering inclusion. On the other hand, limitations on the available computer memory and execution time place a maximum limit on the number of boundary elements, because increasing the number of elements increases the number of nodes, which in turn increases the number of unknowns and equations in the dense partitions of the BIE coefficient matrix. Both constraints must be satisfied to solve a scattering problem. Similar constraints apply in almost all numerical scattering models, whether or not BIE method is used or layered media are included.

When specifying the element size, both the P and S wavelengths must be considered. Sea floor sediments pose particular difficulty since the S wave speeds in the upper sediment layers can be very small, perhaps 200 to 300 m/s, whereas the P wave speed may be somewhat higher than that of water, 1500 m/s. This makes the P wavelength roughly 7.5 times larger than the S. In scattering from a sphere, for example, when $kr = 3.0$ for P waves, it may be 22.5 for S, which is rather large for any three-dimensional full-wave model to handle. Thus, low speed sediments can only be included in the waveguide if the scattering inclusion does not pass through them.

Finally, tall vertical sides to the scattering inclusion should be avoided in the indirect BIE method for layered media, because the integral coefficients for all elements above and below a surface computation point are troublesome due to poor convergence in the mode series, whereas perhaps only as many as six troublesome elements can be handled reliably.¹ Hence, a vertical side wall cannot be much greater than the smallest wavelength near the inclusion.

7.0.2 Constraints due to mode proliferation

We have seen that a complete normal mode treatment of the Green's function is only possible for waveguides that are bounded top and bottom by an impenetrable plane boundaries. Moreover, as the bounded waveguide is made thicker, or frequency is increased, there is a proliferation of *radiation modes* that must be included in the mode series,² which

¹The indirect method becomes numerically unstable as the number of troublesome elements in an equation increases; see Section (3.5.1).

²See Section (6.2.2).

can make the mode search tedious, and the modal summation intolerably slow. The rules for estimating the number of propagating and evanescent radiation modes in terms of the frequency and waveguide thickness are given in Section (6.4). It must be remembered that there may be more than one evanescent mode series, since each plate-like structure in the waveguide is likely to have its own *plate modes* trailing along both sides of the imaginary slowness axis. Fortunately, the vertical mode functions of evanescent plate modes are confined within the plate-like structure that engenders them, so entire series of evanescent plate modes can be omitted if the scattering inclusion lies outside the plate.

7.1 The particular solutions for layered media

It is important to note that, unlike homogeneous domains, the point sources generating the particular solutions in layered media cannot lie within, or directly above or below the scattering inclusions, again because of poor convergence in the mode series when computing the particular solution (unscattered incident field) at the boundary. To accommodate those source locations, while still using a truncated mode series, we would have to derive a new delta-function sifting term ζ for the incident field term,³ by excluding the source using a vanishingly small exclusion cylinder, positioned vertically, reaching from the top to the bottom of the waveguide and piercing through the scattering inclusion. Although I have had some success along these lines, I have nothing conclusive at the time of writing.

It is best to use particular solutions that excite both P-SV and SH waves (in solid layers) in significant proportions, to provide as much information to the indirect solution as possible. This can be done in layered media by exciting both a horizontal twisting source plus a randomized point force. The horizontal twisting source is a source of SH waves that can be imagined as horizontal rotational oscillations of a point in welded contact about its vertical axis. It consists of a moment tensor in (4.54) having the form

$$M = \begin{bmatrix} 0 & M_{12} & 0 \\ -M_{12} & 0 & 0 \\ 0 & 0 & 0 \end{bmatrix}. \quad (7.1)$$

³See Section(2.4).

7.2 Interfaces and edges

We have seen that the displacement tangential to an interface with a fluid can be discontinuous. When the boundary of the scattering inclusion is smooth and passes through the plane interface adjoining a fluid layer, the component of displacement tangential to both the plane interface and the inclusion boundary (the horizontal component of displacement tangential to the boundary) can therefore be discontinuous as well. To permit a displacement discontinuity, we can treat the line of contact between the interface and boundary using double nodes along the line [8, sect. 7.2.3]. To place nodes on this line of discontinuity, it must be a dividing line between boundary elements. And to place double nodes on the line, the nodes from elements on both sides of the line must be treated as separate nodes, even if they are coincident. Coupling of the field can be enforced between double nodes using additional coupling equations in the coefficient matrix (3.8) that relate double nodes in the same perspective. For instance, assuming that the interface between a fluid and solid layer lies outside the boundary, the continuity equations between double nodes would equate the traction vector, the vertical displacement, and the horizontal displacement normal to the boundary, while leaving the horizontal component of the tangential displacement discontinuous. If there is an interface both outside and inside the boundary, however, as there will be in the free-field test in layered domains, the continuity of the horizontal displacement normal to the line of discontinuity should not be enforced.

The traction vector will be discontinuous across an edge in the boundary, because the traction depends on the normal vector. The discontinuity in traction can also be handled using double nodes and additional coupling equations. Here again, the coupling conditions depend on the media, whether fluid or solid, both inside and outside the scattering inclusion. Matters become rather complicated if an edge is coincident with an interface between a fluid and solid layer.

I will not attempt a general treatment of lines of discontinuity here. When in doubt, it seems the best policy is to enforce no coupling between double nodes and let the BIE solution resolve discontinuities itself. Instead of using coincident double nodes, for example, we could stagger the nodes across the line of discontinuity, in which case no

coupling is the only possibility. The worst policy is to force continuity where it should not be, for, like the error of welded contact with fluids (Section (2.3.2) and (3.2.4)), it forces the BIE method to solve the wrong—if not a meaningless—boundary value problem. Examples of edges and extension of the inclusion through a fluid-solid interface are among the demonstrations given below.

7.3 Demonstration of the BIE method for layered media

After a particular scattering problem has been carefully planned, and it has been determined that the number of modes and boundary elements are practicable, the new model proceeds in this way:

1. the modes must be found, and their vertical mode functions computed;
2. the source locations for the particular solutions, and their fields \mathbf{u} and \mathbf{t} at the boundary element nodes must be computed and saved for quick access;
3. the surface- and null-field computation points must be chosen, and the coefficients for their corresponding integral equations computed (using the particular solutions to compute troublesome coefficients indirectly) and verified using consistency tests and the free-field test;
4. the integral equations, together with the boundary and continuity conditions, must be solved for \mathbf{u} and \mathbf{t} at the boundary nodes, then verified using the null-field test;
5. the displacement \mathbf{u} can be computed at points off the boundary using the whole-field equation.⁴

It need hardly be mentioned that the new model, like most three-dimensional models of scattering, requires considerable time and effort to setup and run, especially in its earliest stages of development. It also requires many utility programs to specify the boundary elements, automatically choose points of one kind or another, verify test

⁴Components of the stress tensor τ could also be computed as noted in Section (3.2.5).

results, and plot the boundary and elastic field. It is impossible to review all of this in detail. Instead, my aim is to show that the method works in elastic waveguides, and to indicate the diverse range of problems it can undertake, such as scattering from penetrable, impenetrable, and mixed inclusions that cross a layer interface.

To demonstrate that a model works is one task, but to analyze the corresponding physics is quite another. At this early stage in the model development, I will not venture far into the analysis of scattering, by hypothesizing general rules governing scattering in such cases for example, for that requires considerably more detail than a demonstration requires, plus many more simulations for verification. Without knowing beforehand what direction such rules about scattering may take, I hope the demonstrations will be complete enough to allow readers (and myself at a later date) to make preliminary judgments about scattering, or to find confirmation of principles derived in other ways.

Three demonstrations will be given, ordered by increasing complexity; they are scattering by 1) a cavity in an ice plate, 2) a half-buried sphere on the sea floor in a shallow ocean, and 3) a circular ice dome in a floating ice plate in an Arctic environment.

7.3.1 Hemispherical cavity in an ice plate

To begin, let us consider scattering from a 1 m radius hemispherical cavity on the floor of a 3 m free ice plate. For simplicity, the ice, frequency (750 Hz) and modes are the same as for the free plate considered earlier in Fig. (6.1). Details of the BIE setup are summarized in Table (7.1). Twenty boundary elements cover the hemisphere as shown in Fig. (7.1). The sources generating particular solutions for the indirect coefficient computations are positioned as shown in Fig. (7.2), the excitation for each source being the sum of a randomly oriented point force and horizontal twisting source (7.1). More than enough modes have been found as shown in Fig. (7.3), where the relative strength of each mode has been plotted, when evaluated at the edge of the close neighborhood in which indirect computations are performed.

1 m Hemispherical Cavity

| | |
|------------------------|-------------------------------------|
| No. boundary elements: | 20 |
| No. boundary nodes: | 89 |
| Avg. node spacing: | 0.375 m |
| Symmetry assumed: | Bilateral symmetry in $y = 0$ plane |

Ice plate and modes

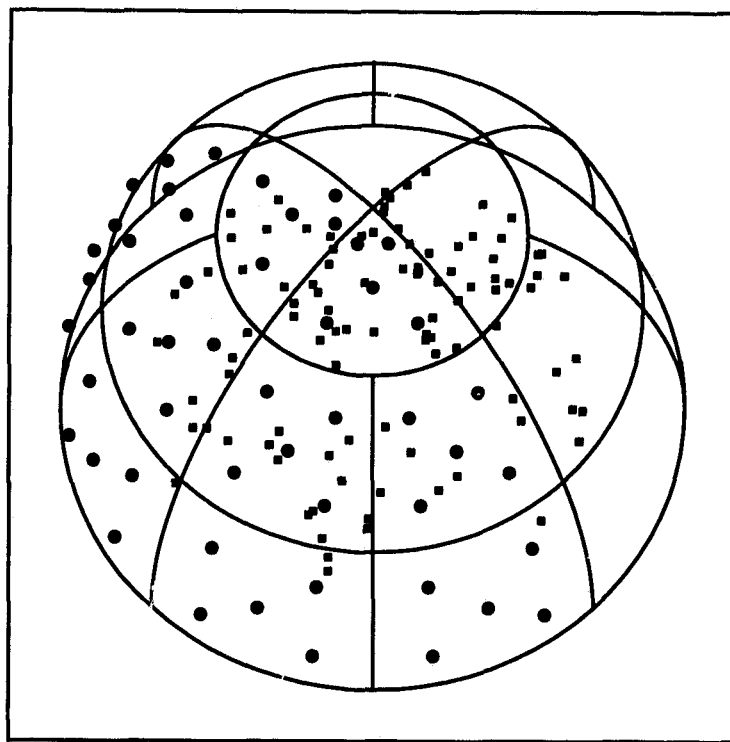
| | |
|--------------------|--|
| α | $3300 - 33.0i$ m/s |
| β | $1730 - 20.0i$ m/s |
| ρ | 900.0 kg/m ³ |
| H | 3.0 m |
| Upper interface: | traction free; $\mathbf{t} = \mathbf{0}$ |
| Lower interface: | traction free; $\mathbf{t} = \mathbf{0}$ |
| No. of P-SV modes: | 5 propagating; 894 evanescent (max. $p_i = 0.1s/m$) |
| No. of SH modes: | 3 propagating; 448 evanescent (max. $p_i = 0.1s/m$) |

Equations for ice domain: Perspective 0

| | |
|----------------------------------|--|
| No. surface computation points: | 50 points; 5 per element on half the boundary |
| No. interior computation points: | 100 scattered randomly inside cavity |
| Straightforward integration: | 10 by 10 Gaussian quadrature scheme for each boundary element |
| Close neighborhood of elements: | $\epsilon = 0.15$ m |
| No. particular solutions: | 428 |
| Boundary Conditions: | $\mathbf{t} = \mathbf{0}$ |

Table 7.1: Setup for scattering from a hemispherical cavity on the floor of an ice plate. There is only one penetrable domain, the 3 m ice plate outside the hemisphere, and therefore only one perspective for the boundary integral equations, perspective 0.

Boundary Element Plot



Oblique projection: Viewer in quadrant 1

Figure 7.1: 20 boundary elements cover the hemispherical cavity. Surface-field computation points (circular dots) are distributed evenly over half the boundary, but not at the element nodes, with the remainder made up using bilateral symmetry. 100 null-field points (square dots) are randomly distributed inside the cavity. Traction-free boundary conditions are applied to the cavity and the top and bottom interfaces of the ice plate. The center of the spherical boundary is at $(x, y, z) = (0, 0, 3)$ m.

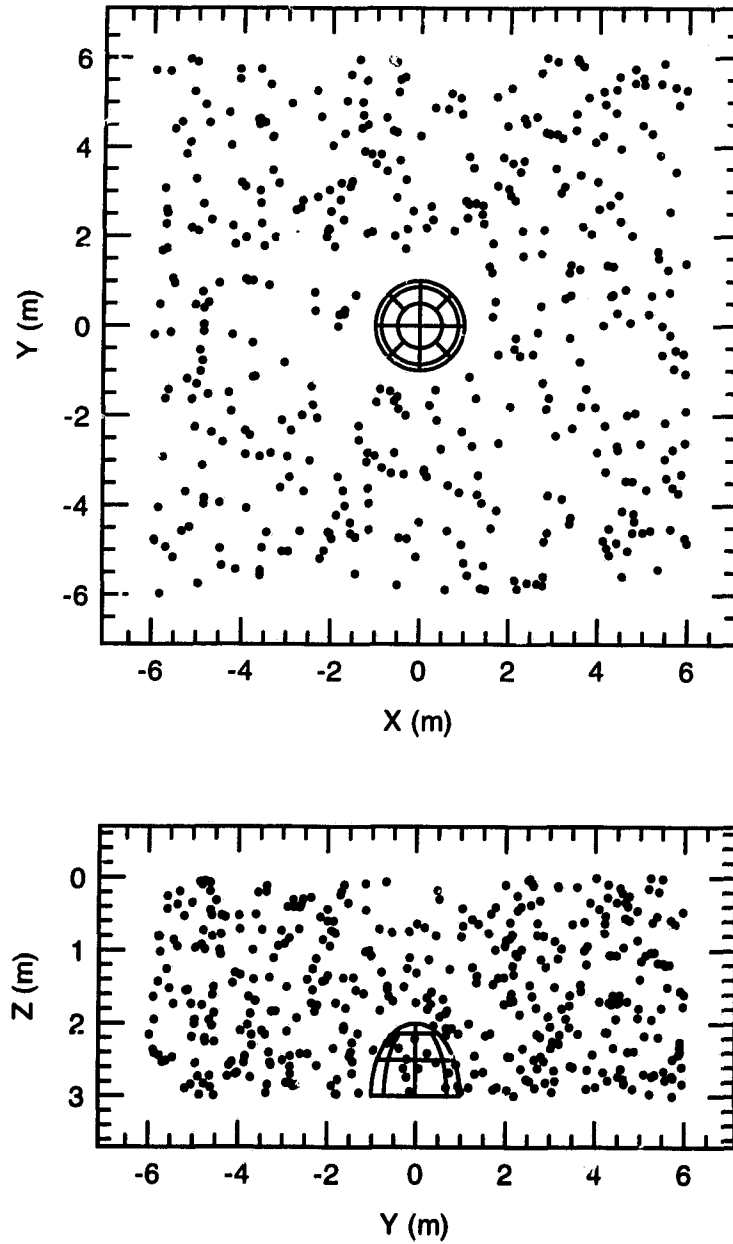


Figure 7.2: 428 sources generating particular solutions are distributed randomly in the 3 m ice plate. No sources lie inside or directly above the hemispherical cavity. **Top:** View along z axis. **Bottom:** View along x axis.

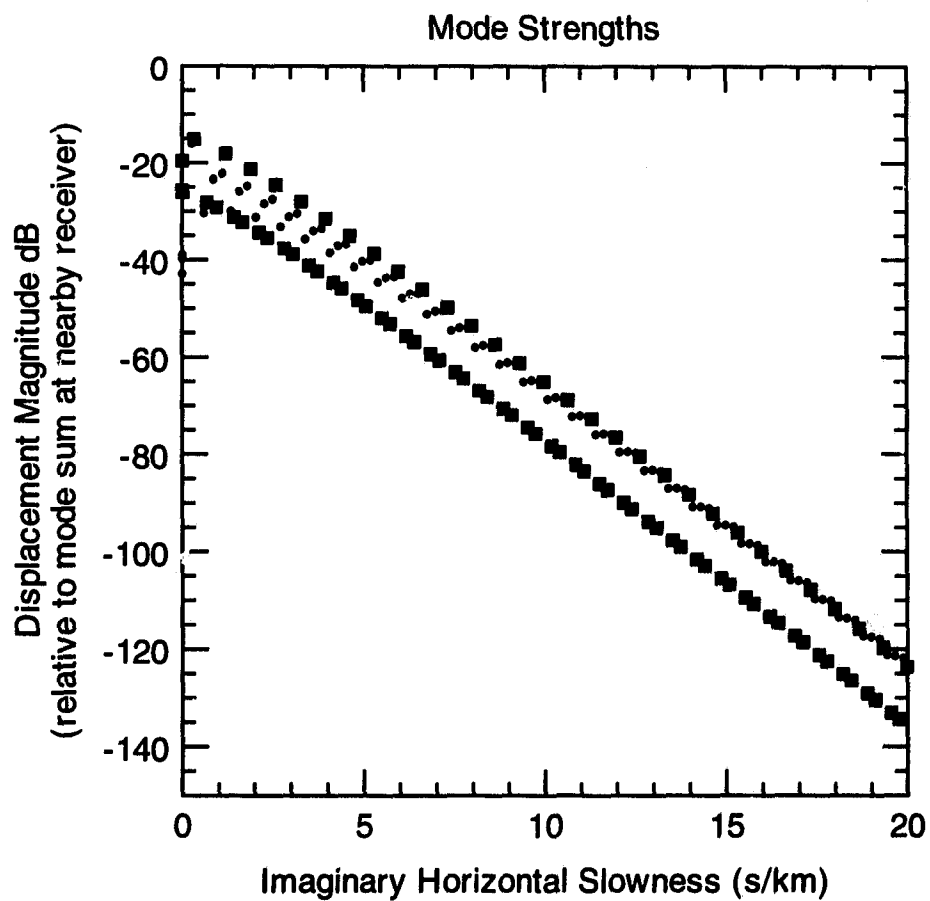


Figure 7.3: The relative strength of evanescent modes in the P-SV (circular dots) and SH (square dots) mode series decay exponentially with increasing imaginary slowness. Here the source is a point source at $z = 2.0$ m, and the receiver is just $\epsilon = 0.15$ m away, at the same depth. The source excitation is a combined vertical point source (P-SV waves only) plus horizontal twisting source (SH waves only).

Incident P-SV waves

The free-field test was used to verify the BIE setup and the integral equations computed for the scattering problem. Using boundary condition equations, the traction at each node was set to the free-field traction due to a vertical point force—a source of P-SV waves alone—acting at $(x, y, z) = (50.0, 0.0, 0.01)$ m in the ice plate, and the BIE method was used to compute the unassigned displacement. The error in the displacement at the nodes was found to be ⁵

$$\begin{aligned} \text{Avg. err}_1 &= 2.61 \%, \\ \text{Max. err}_1 &= 9.25 \%, \\ \text{err}_2 / \text{err}_1 &= 1.19 \end{aligned} \tag{7.2}$$

Fig. (7.4) shows both the BIE computed and exact displacement fields on the boundary for the test. Notice that we are solving an equation of the second kind in displacement alone because the traction at the boundary element nodes is known from the outset, as will be the case when solving the actual scattering problem.⁶

Then the scattering boundary conditions $\mathbf{t} = \mathbf{0}$ were restored, and the boundary field for the cavity was computed using the BIE method for the same P-SV incident field. The result was verified using the null-field test in Fig. (7.5).⁷ Recall that the total field (incident plus scattered) should ideally drop discontinuously to zero in the exterior domain (inside the cavity); hence, the scattered field should be the negative of the incident inside the cavity, and their magnitudes (plotted in the figure) should be equal there. Note that indirect coefficient computations were used at all interior points because they lie directly below the boundary elements.

Once the boundary field is available, the field can be computed at any point off the boundary. Fig. (7.6) shows the incident field in the vertical $y = 0$ plane through the axis of the cavity and the source. The scattered field is weak, roughly 18 dB lower than the incident field as shown in Fig. (7.7). Fig. (7.8) shows a far-field polar plot of the P-SV (u_r and u_θ) and SH (u_ϕ) components of the scattered displacement field at the top and bottom

⁵The errors err_1 and err_2 are defined in Section (3.8).

⁶The nature of the integral equation, whether of the first or second kind, was considered in Section (2.7) and (3.2.2).

⁷The null-field test was described in Section (3.7).

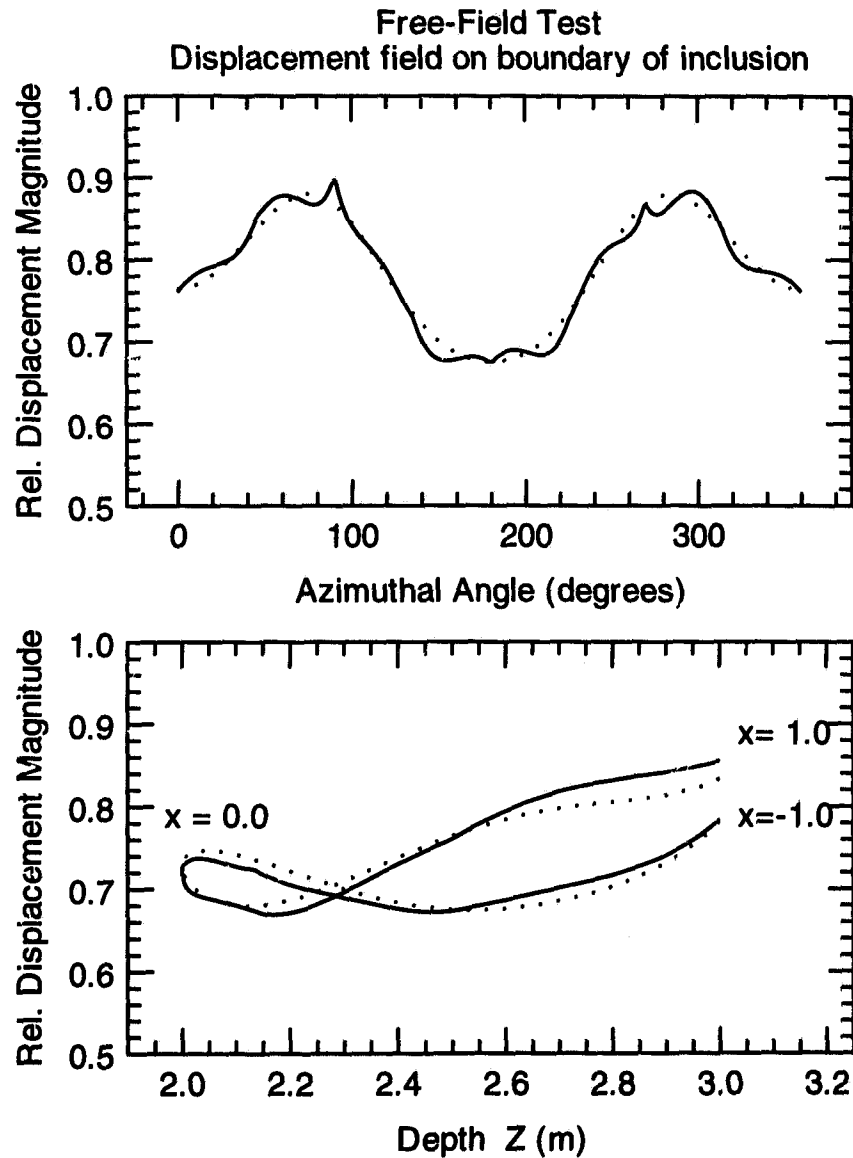


Figure 7.4: The BIE method was used to compute the free-field displacement on the boundary (solid line) due to a vertical point force at $(x, y, z) = (50.0, 0.0, 0.01)$ m (dotted line, exact). **Top:** Displacement magnitude on a horizontal line around the walls of the false cavity at depth $z = 2.5$ m, as a function of azimuthal angle ϕ about its vertical axis. The incident field approaches from $\phi = 0.0$. **Bottom:** The displacement on the walls in the vertical plane $y = 0$ as a function of depth.

of the waveguide. The SH contribution is zero in the $y = 0$ plane as required by symmetry. Fig.(7.9) shows the field along a horizontal line along the surface of the waveguide in the $y = 0$ plane. Indirect coefficient computations were needed to compute the field directly above the scattering inclusion.

Incident SH waves

The computations were repeated for a source of SH waves, a horizontal twisting source (7.1), positioned at $(x, y, z) = (50.0, 0.0, 2.0)$ m, operating once again at 750 Hz. This time bilateral symmetry was not used assumed because the plus-minus symmetry needed for the SH incident field was not implemented in the BIE program. Instead, additional surface-field equations were computed at points evenly distributed on elements that went without surface-field points when bilateral symmetry was used before. The results of the free-field test were

$$\begin{aligned} \text{Avg. err}_1 &= 2.17 \%, \\ \text{Max. err}_1 &= 8.25 \%, \\ \text{err}_2 / \text{err}_1 &= 1.37 \end{aligned} \tag{7.3}$$

The computed and exact fields for the free-field test are shown in Fig. (7.10).

The incident field due to the source is shown in Fig. (7.11), and the scattered field due to the cavity is shown in Fig. (7.12). Now the effects of scattering are somewhat larger, lying roughly 13 dB below the incident field, presumably because the incident field consists purely of S waves. These interact more strongly with the relatively small cavity since their wavelengths are about half as long as the P wavelengths generated by the vertical point force. The polar plot in Fig.(7.13) shows the conversion from incident SH waves, which have no vertical displacement u_z , to P-SV waves that do. Fig. (7.14) shows the field along a horizontal line along the surface of the plate. Here again, indirect coefficient computations were needed at points directly above the cavity. Finally, Fig. (7.15) and (7.16) show the total and vertical displacement at the surface of the ice. The vertical displacement is a purely scattered field since the incident field consists only of horizontal SH waves.

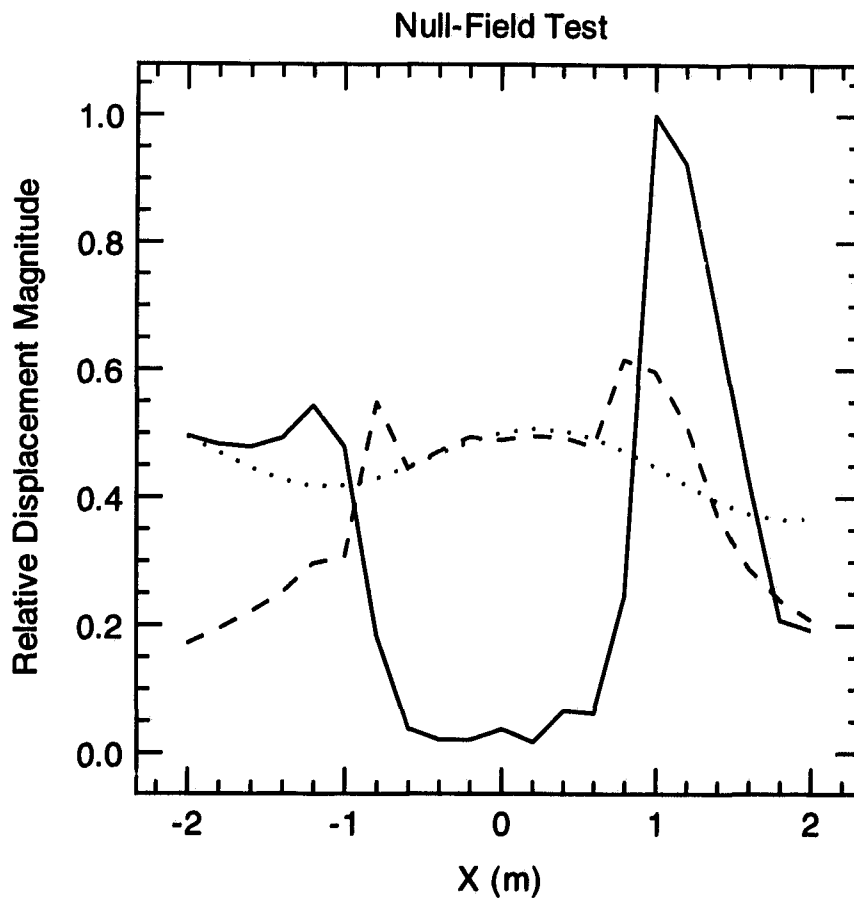


Figure 7.5: The BIE solution for scattering from the cavity was tested using the null-field test. Here the magnitude of the total displacement (incident plus scattered, solid line) is plotted along a horizontal line $(y, z) = (0.0, 2.95)$ m, passing through the boundary between $x \approx -1$ to $+1$ m. Ideally the total field should drop to zero inside the cavity where the boundary integral gives the null-field result. This requires that the magnitude of the incident field (dotted line) equal that of the scattered field (dashed line) inside the inclusion.

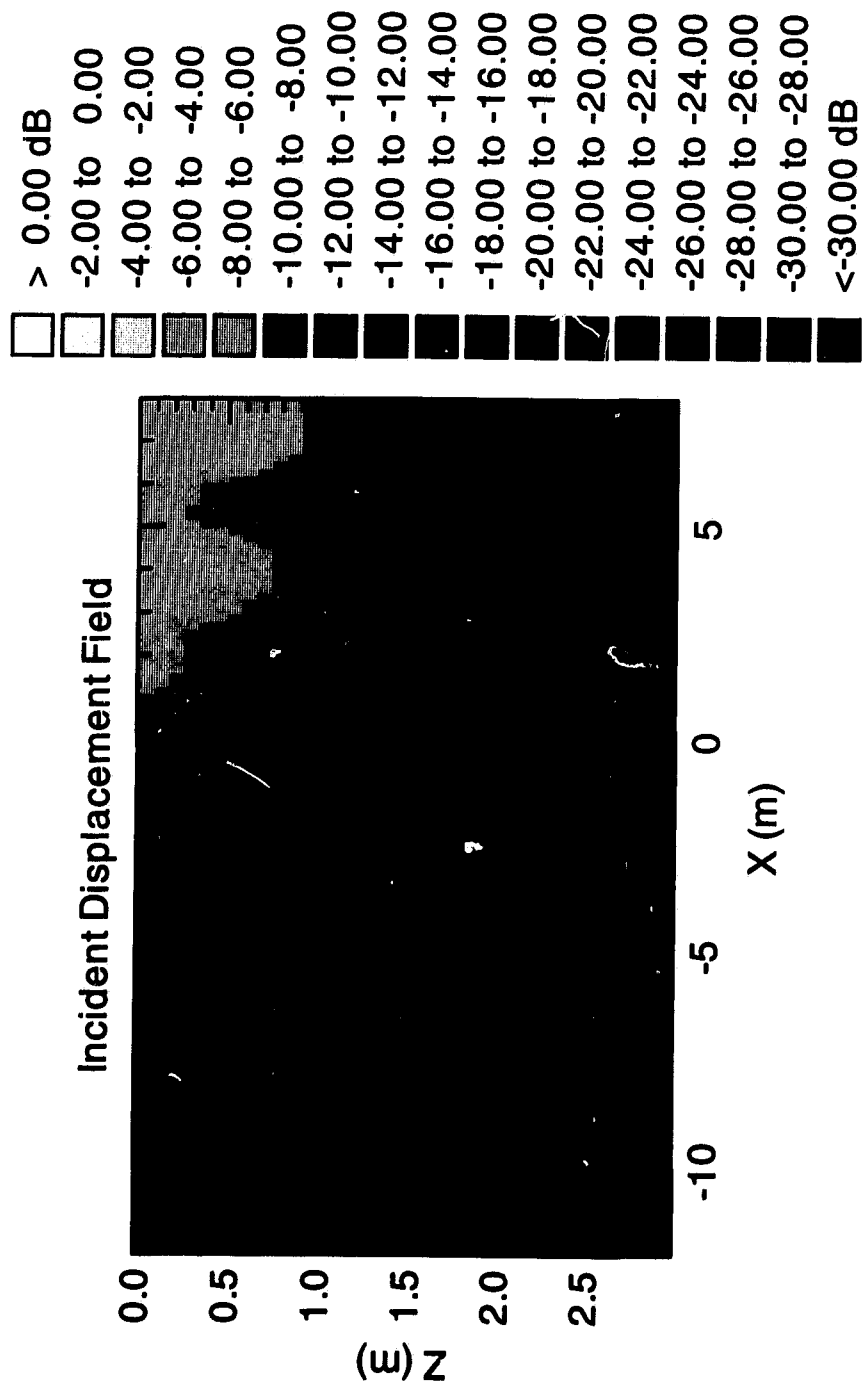


Figure 7.6: Incident Field (plotted laterally): The magnitude of the incident displacement field in the vertical $y = 0$ plane, due to a vertical point force at the surface of the ice at $(x, y, z) = (50.0, 0.0, 0.01)$ m.

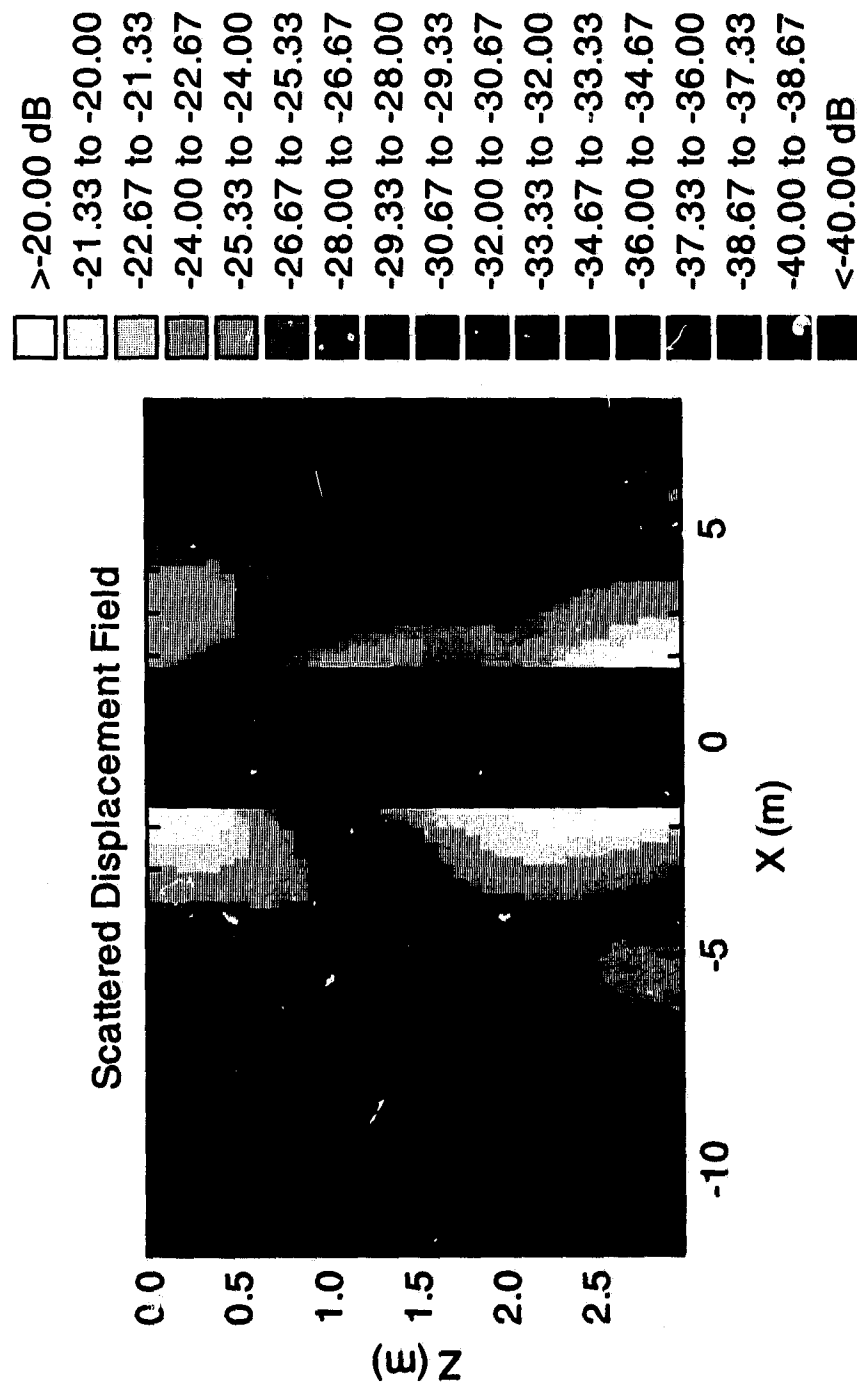


Figure 7.7: Scattered Field (plotted laterally): The magnitude of the scattered displacement field in the vertical $y = 0$ plane. The dark band is the zone in which indirect coefficient computations are required, but were omitted to reduce the computation time. The incident field is that of a vertical point force at the surface of the ice at $(x, y, z) = (50.0, 0.0, 0.01)$ m.

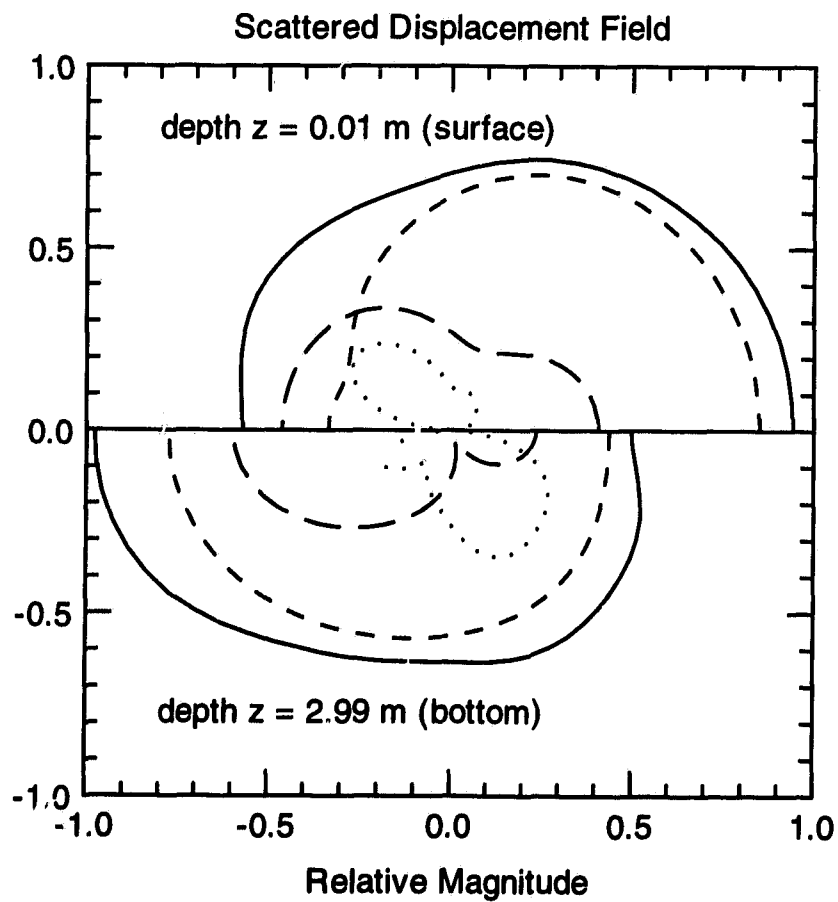


Figure 7.8: A polar plot of the scattered field in a horizontal plane at a radial distance 25.0 m from the axis of the cavity. The magnitude of the displacement vector is the solid line, vertical u_z , the small dashed, radial u_r , the long dashed, and azimuthal u_ϕ the dotted. The incident field due to a vertical point force approaches the cavity from the right.

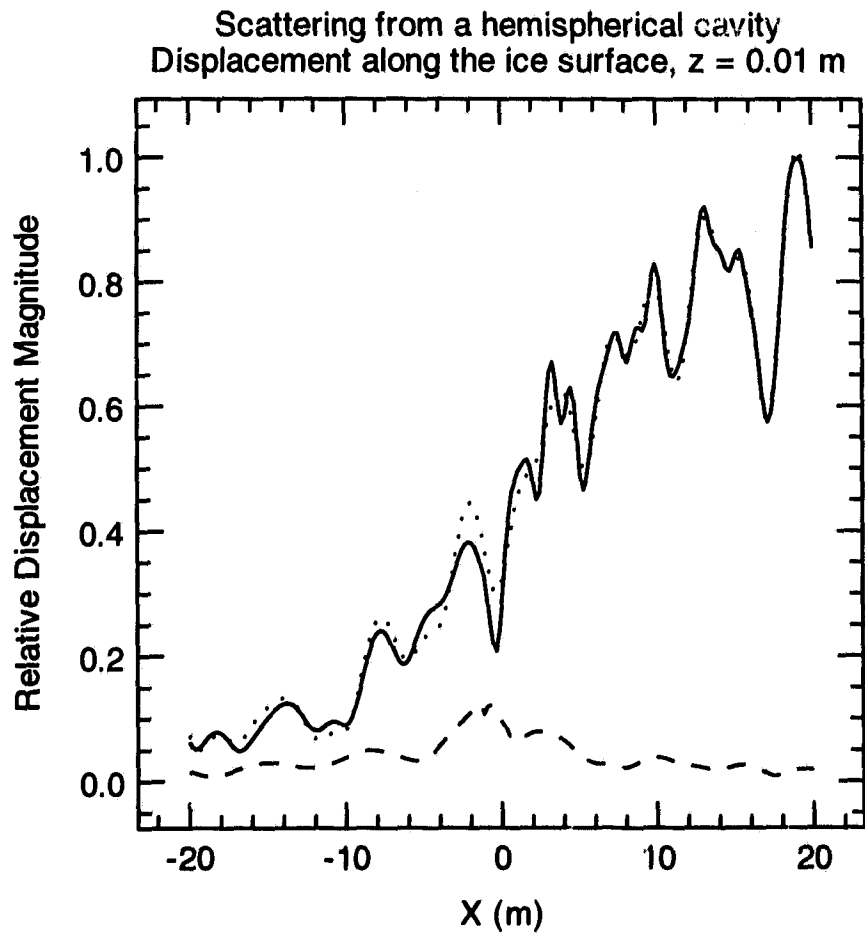


Figure 7.9: The displacement field along a horizontal line $(y, z) = (0, 0.01)$ passing over the scattering cavity. The total field is the solid line, the incident the dotted, and the scattered the dashed. Indirect coefficient computations were used at points directly above the cavity, between $x = -1$ to $+1$.

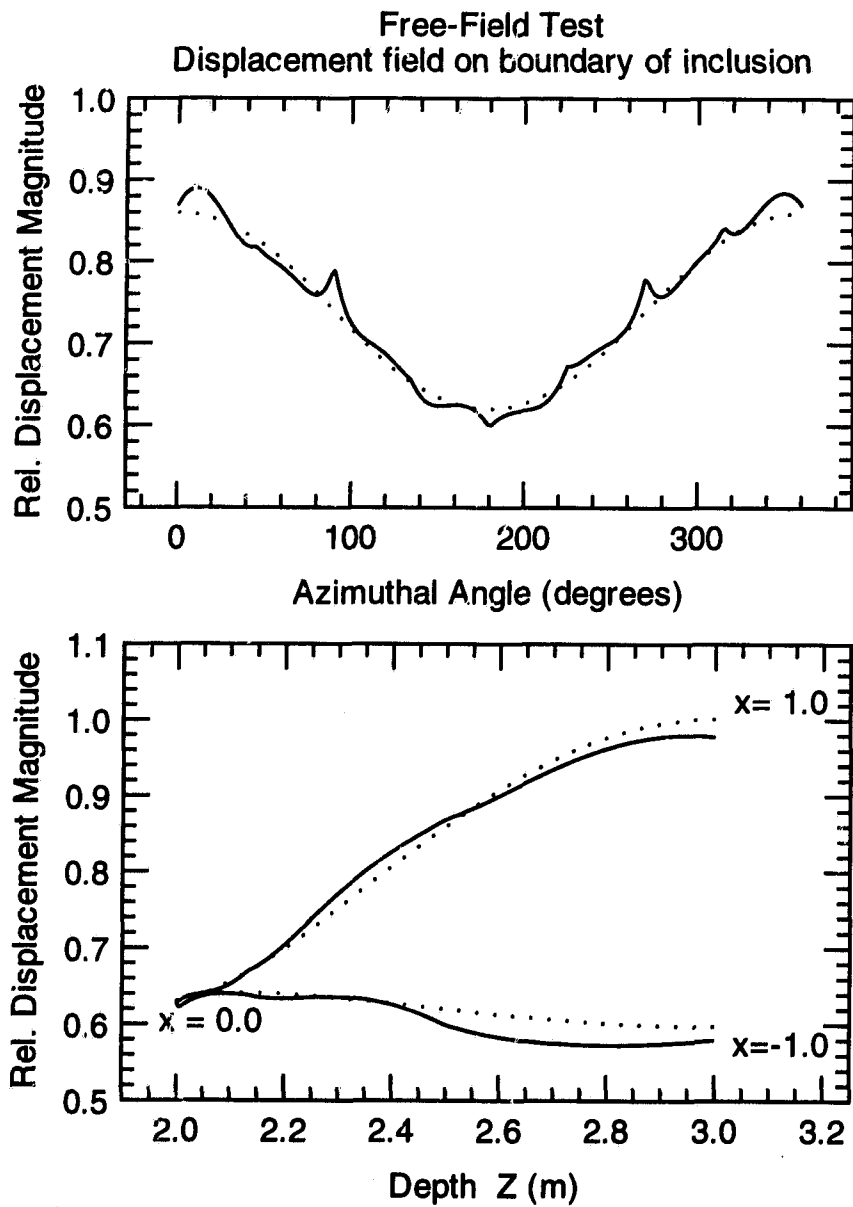


Figure 7.10: The BIE method was used to compute the free-field displacement on the boundary (solid line) due to a horizontal twisting source of SH waves at $(x, y, z) = (50.0, 0.0, 2.0)$ m (dotted line, exact). Top: Displacement magnitude on a horizontal line on the walls of the false cavity at depth $z = 2.5$ m as a function of azimuthal angle ϕ about its vertical axis. The incident field approaches from $\phi = 0$. Bottom: The displacement on the walls in the vertical plane $y = 0$ as a function of depth z .

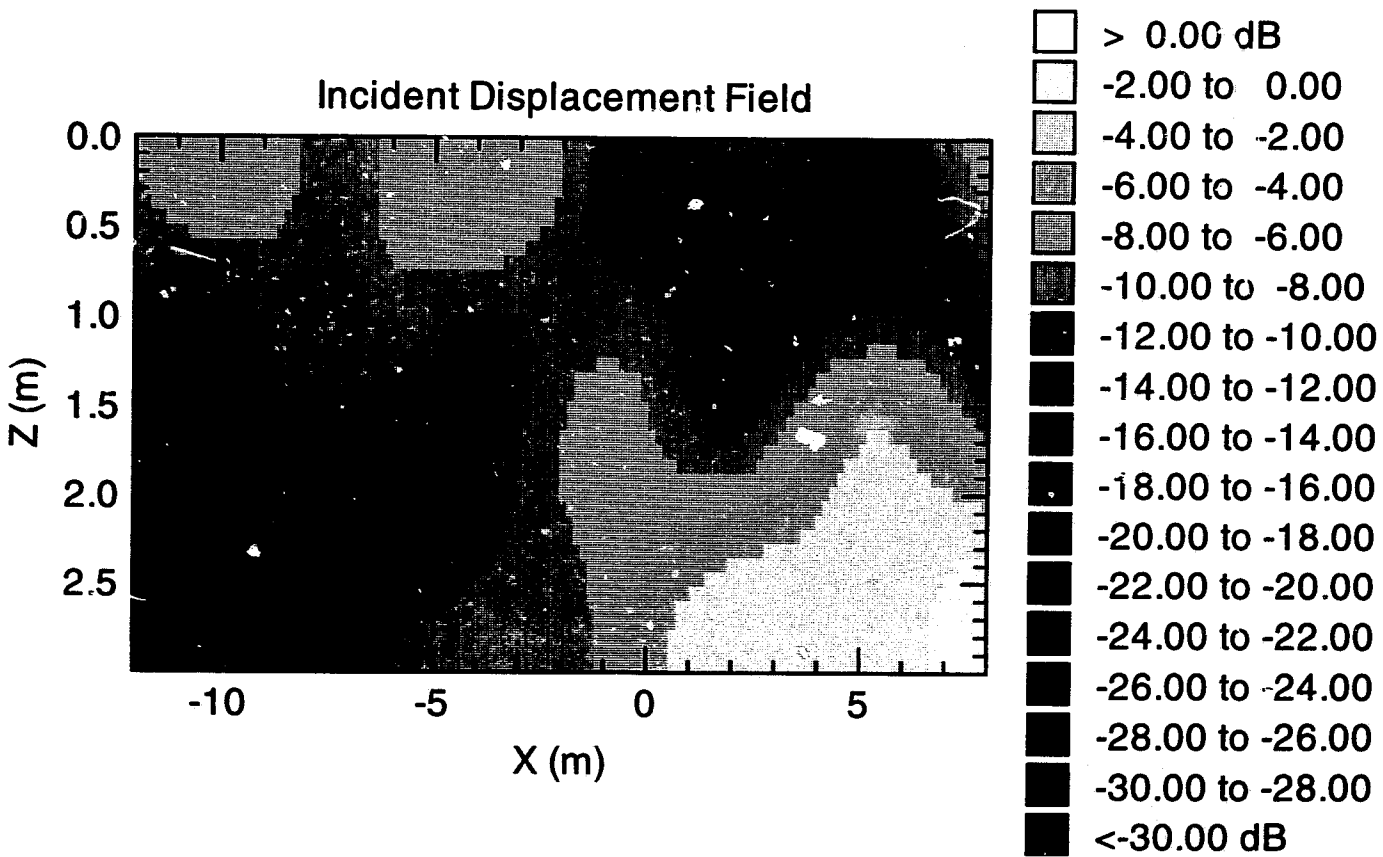


Figure 7.11: Incident Field (pivoted laterally): The magnitude of the incident displacement field in the vertical $y = 0$ plane, due to a horizontal twisting source of SH waves at $(x, y, z) = (50.0, 0.0, 2.0)$ m.

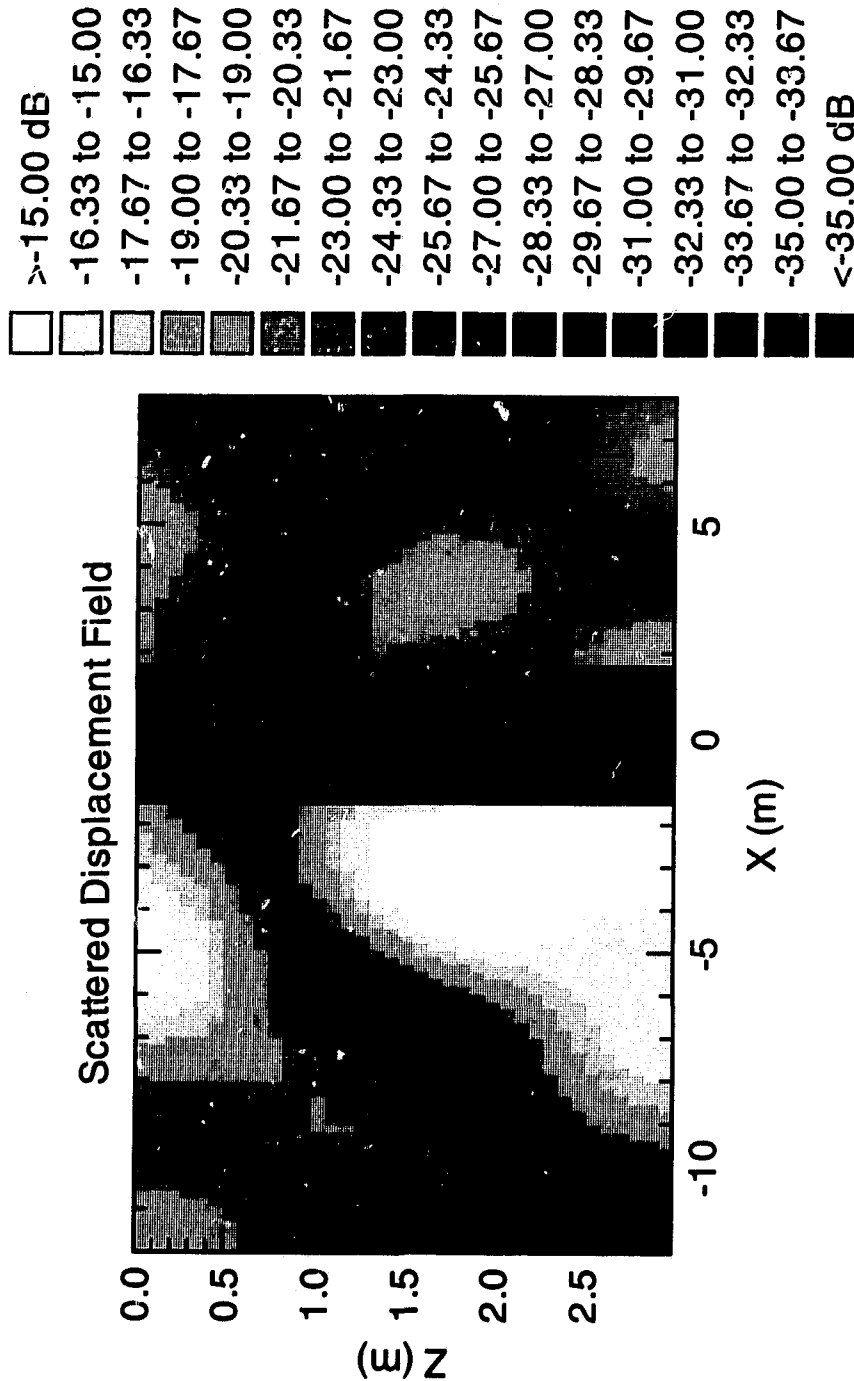


Figure 7.12: Scattered Field (plotted laterally): The magnitude of the scattered displacement field in the vertical $y = 0$ plane. The dark band is the zone in which indirect coefficient computations are required, but were omitted to reduce the computation time. The incident field is that of a horizontal twisting source of SH waves at $(x, y, z) = (50.0, 0.0, 2.0)$ m.

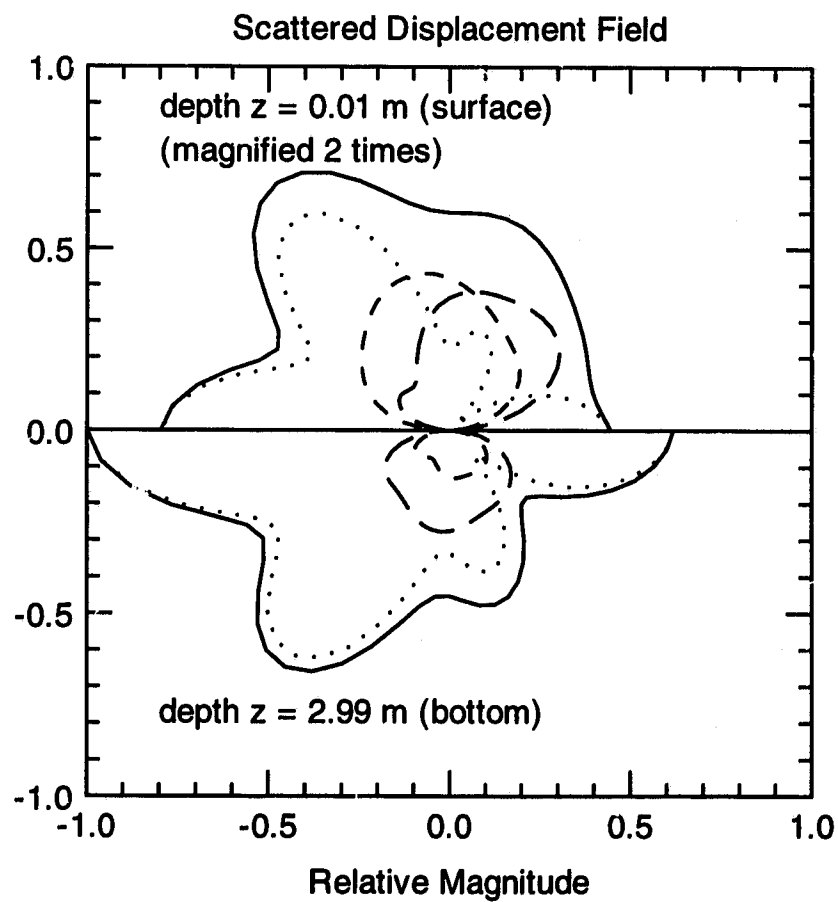


Figure 7.13: A polar plot of the scattered field in a horizontal plane at a radial distance 25.0 m from the axis of the cavity. The magnitude of the displacement vector is the solid line, vertical u_z the small dashed, radial u_r the long dashed, and azimuthal u_ϕ the dotted. The incident SH waves due to a horizontal twisting source approaches from the right.

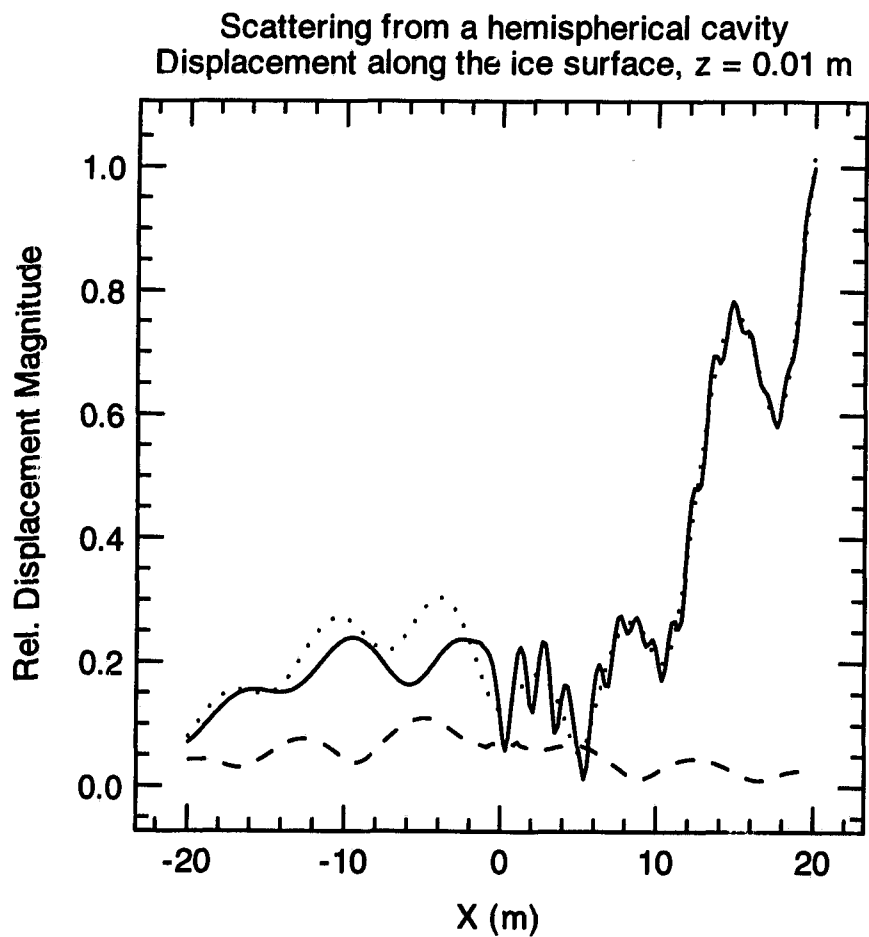


Figure 7.14: The displacement field plotted along a horizontal line $(y, z) = (0, 0.01)$ passing over the scattering cavity. The total field is the solid line, incident the dotted, and scattered the dashed. Indirect coefficient computations were used at points directly above the cavity, from $x = -1$ to $+1$. The incident field is due to a horizontal twisting source of SH waves at $(x, y, z) = (50.0, 0.0, 2.0)$.

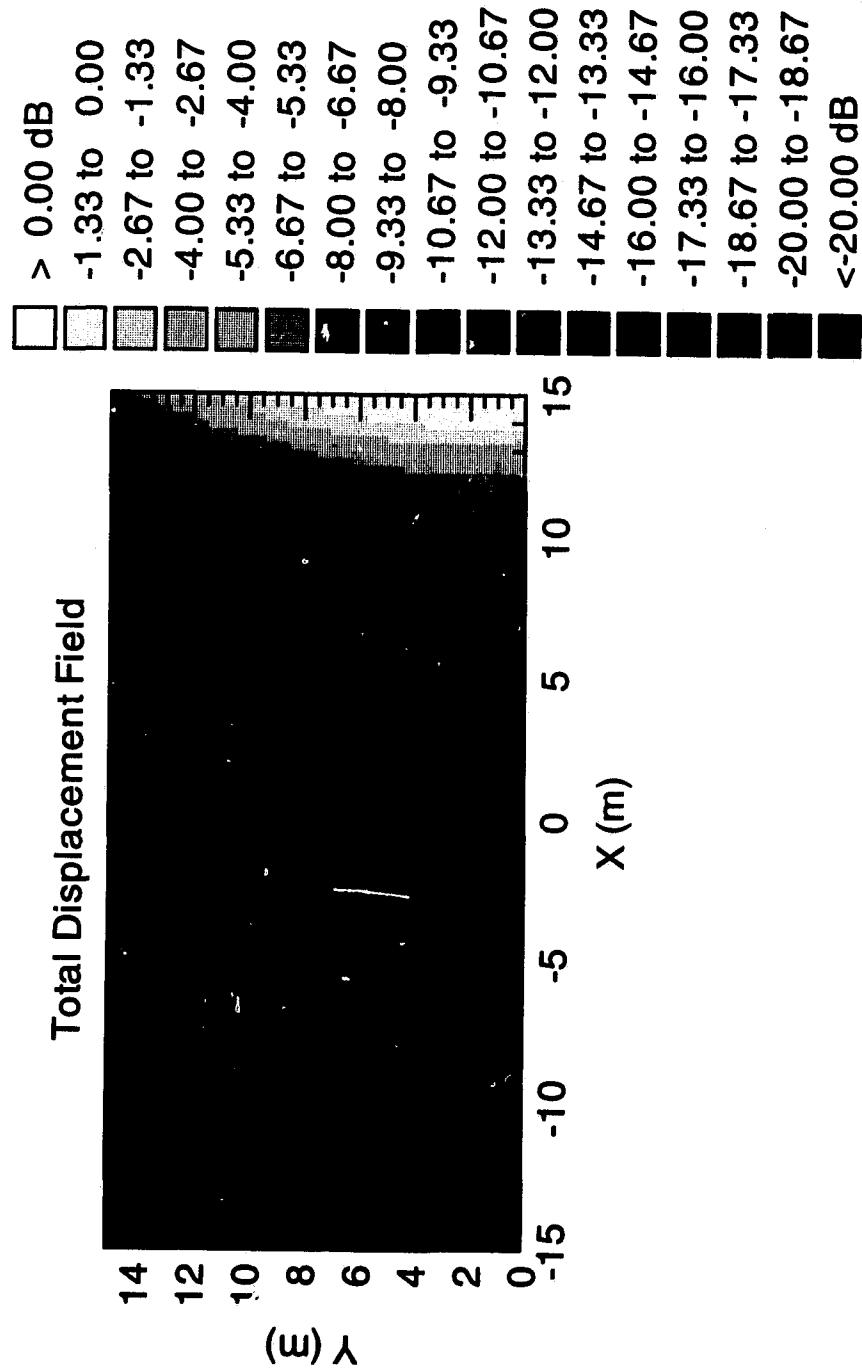


Figure 7.15: Total Field (plotted laterally): The magnitude of the total (incident plus scattered) displacement field at the surface of the ice $z = 0.01$ m. The incident field is that of a horizontal twisting source of SH waves at $(x, y, z) = (50.0, 0.0, 2.0)$ m.

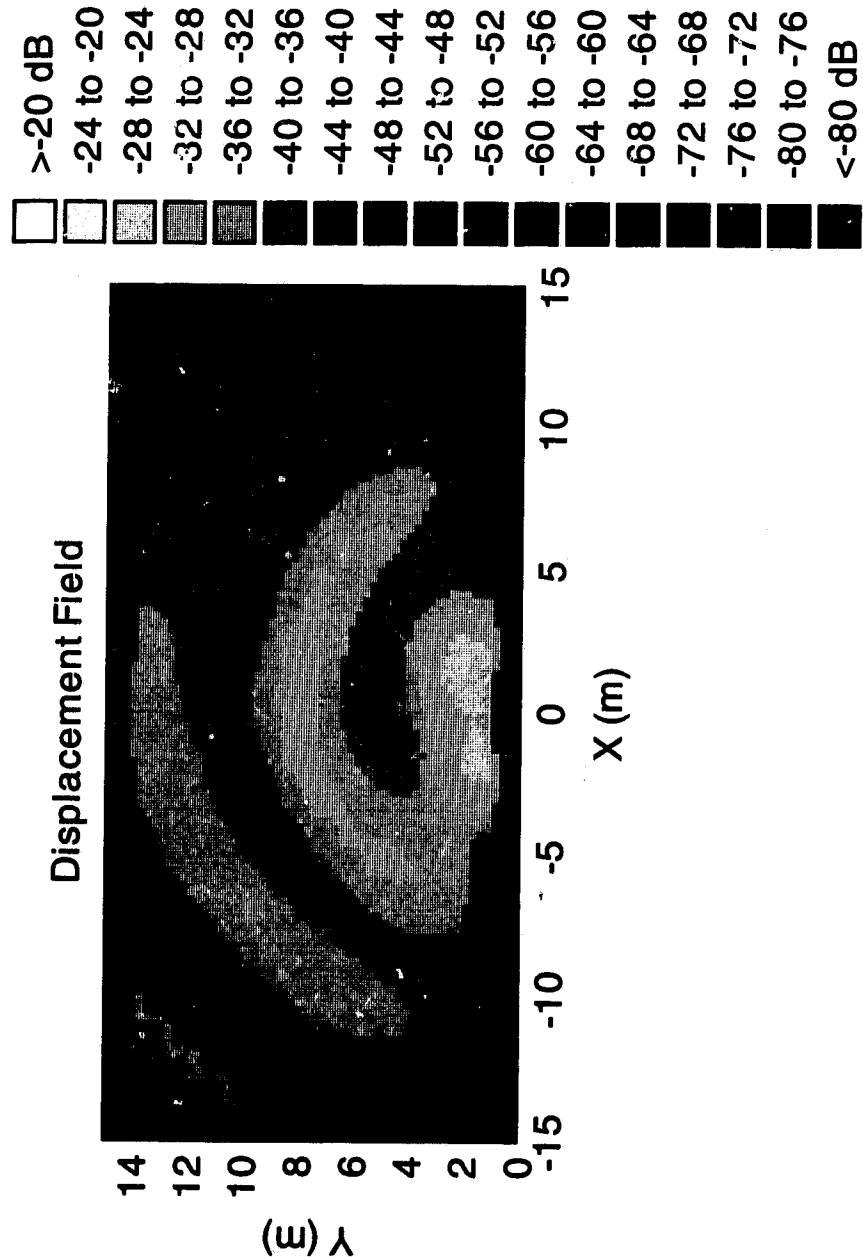


Figure 7.16: Scattered Field u_z (plotted laterally): The magnitude of the vertical component total of the scattered displacement field at the surface of the ice $z = 0.01$ m. The incident field is that of a horizontal twisting source of SH waves at $(x, y, z) = (50.0, 0.0, 2.0)$ m. u_z is due entirely to scattering by the cavity since the incident field consists purely of SH waves.

1.193 m Rigid Sphere

| | |
|------------------------|-----------------------------------|
| No. boundary elements: | 12 in water, 44 in sand |
| No. boundary nodes: | 57 in water, 201 in sand |
| Avg. node spacing: | 0.396 m in water, 0.211 m in sand |
| Symmetry assumed: | Bilateral symm. in $y = 0$ plane |

Modes

| | |
|--------------------|------------------------------|
| No. of P-SV modes: | 1922 (max. $p_i = 0.08s/m$) |
| No. of SH modes: | 200 (max. $p_i = 0.1s/m$) |

Equations for ocean domain: Perspective 0

| | |
|----------------------------------|---|
| No. surface computation points: | 168 total; 5 per element on half boundary and 1 central point per element on other half |
| No. interior computation points: | 30 scattered randomly inside cavity |
| Straightforward integration: | 7 by 7 Gaussian quadrature scheme for each boundary element |
| Close neighborhood of elements: | $\epsilon = 0.15$ m |
| No. particular solutions: | 440 |
| Boundary Conditions: | $\mathbf{u} \cdot \mathbf{n} = 0$ |

Table 7.2: Setup for scattering from a rigid sphere half buried in a sand layer. There is only one penetrable domain, the shallow ocean outside the sphere, and therefore only one perspective for the boundary integral equations, perspective 0.

7.3.2 Rigid sphere half buried in sand

The next demonstration is of scattering from a small rigid sphere half buried in sand on the floor of a shallow ocean, as shown in Fig. (7.17). Details of the BIE setup are summarized in Table (7.2). 56 boundary elements cover the hemisphere as shown in Fig. (7.18). Since the sphere crosses the water-sand interface—a line of discontinuity in the horizontal displacement—the perimeter of the boundary elements must lie along that interface, and double nodes used across it. The sources generating the particular solutions are shown in Fig. (7.19). The P-SV and SH modes for the waveguide at 200 Hz are shown in Figures (7.20) and (7.21), respectively.

The free-field test was used again to verify the BIE setup and the integral equations computed for the scattering problem. The displacement at each node was assigned the displacement of the Scholte mode at the sand-water interface excited by an explosive source at $(x, y, z) = (20, 0, 50.1)$ m. The BIE method was then used to compute the unassigned free-field traction. Notice that we are solving an equation of the first kind in traction alone because the displacement vector at the boundary element nodes is known from the outset. Double nodes across the line of discontinuity on the boundary were left totally uncoupled, permitting both a displacement and traction discontinuity on the boundary across the sand-water interface. The errors in traction at the boundary element nodes were

$$\begin{aligned} \text{Avg. } \text{err}_1 &= 2.51 \%, \\ \text{Max. } \text{err}_1 &= 7.5 \%, \\ \text{err}_2 / \text{err}_1 &= 5.83 \end{aligned} \tag{7.4}$$

Fig. (7.22) compares the computed and exact fields on the boundary for the test. Recall that the test is somewhat better at points off the boundary due to the smoothing operation of the whole-field integral equation.⁸

Then the boundary conditions for the impenetrable rigid sphere were restored, and the BIE method was used to compute the unknown parts of the boundary field: the traction at all nodes, and the tangential components of the displacement at nodes in the water. Fig. (7.23) shows the incident and scattered field in the vertical $y = 0$ plane through the axis of the sphere and the source. Fig. (7.24) and (7.25) show the total and scattered field in a horizontal plane just below the top of the sand layer. Fig. (7.26) is a far-field polar plot of the P-SV and SH components of the scattered displacement field at the top and bottom of the waveguide.

⁸See Section (3.2.2).

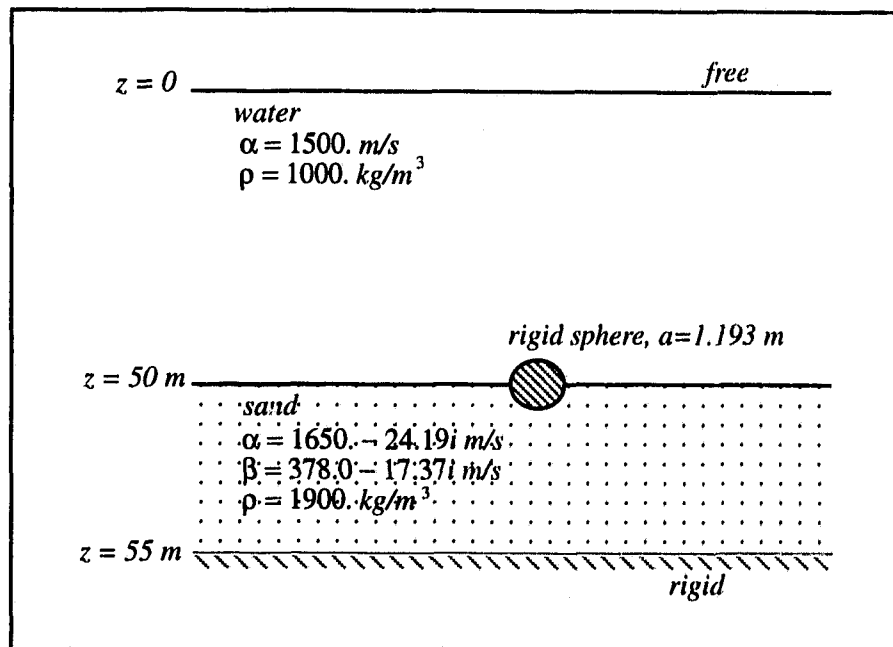
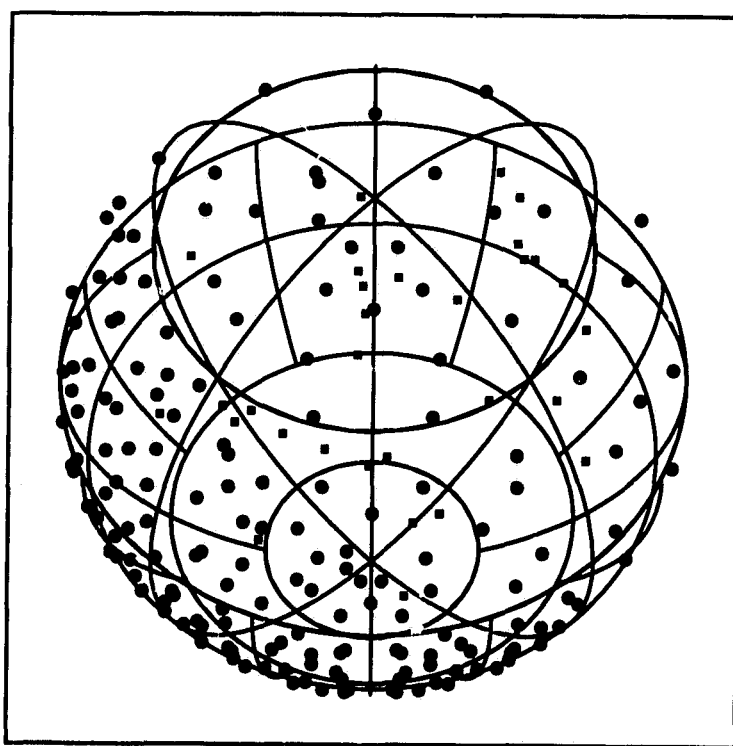


Figure 7.17: Schematic diagram of half-buried rigid sphere. The ocean is 50 m deep, and the sand layer 5 m. The surface of the ocean is a traction-free boundary, and the bottom of the sand layer is rigid (welded contact).

Boundary Element Plot



Oblique projection: Viewer in quadrant 1

Figure 7.18: The radius of the half-buried rigid sphere is 1.193 m. There are 12 boundary elements in the upper hemisphere touching the water, and 44 on the lower touching the sand where the S wavelegth is relatively small. The equator is a line of field discontinuity at the sand-water interface where double nodes are needed. There are 168 surface-field computation points (circular dots) and 30 randomly placed interior null-field points (square dots).

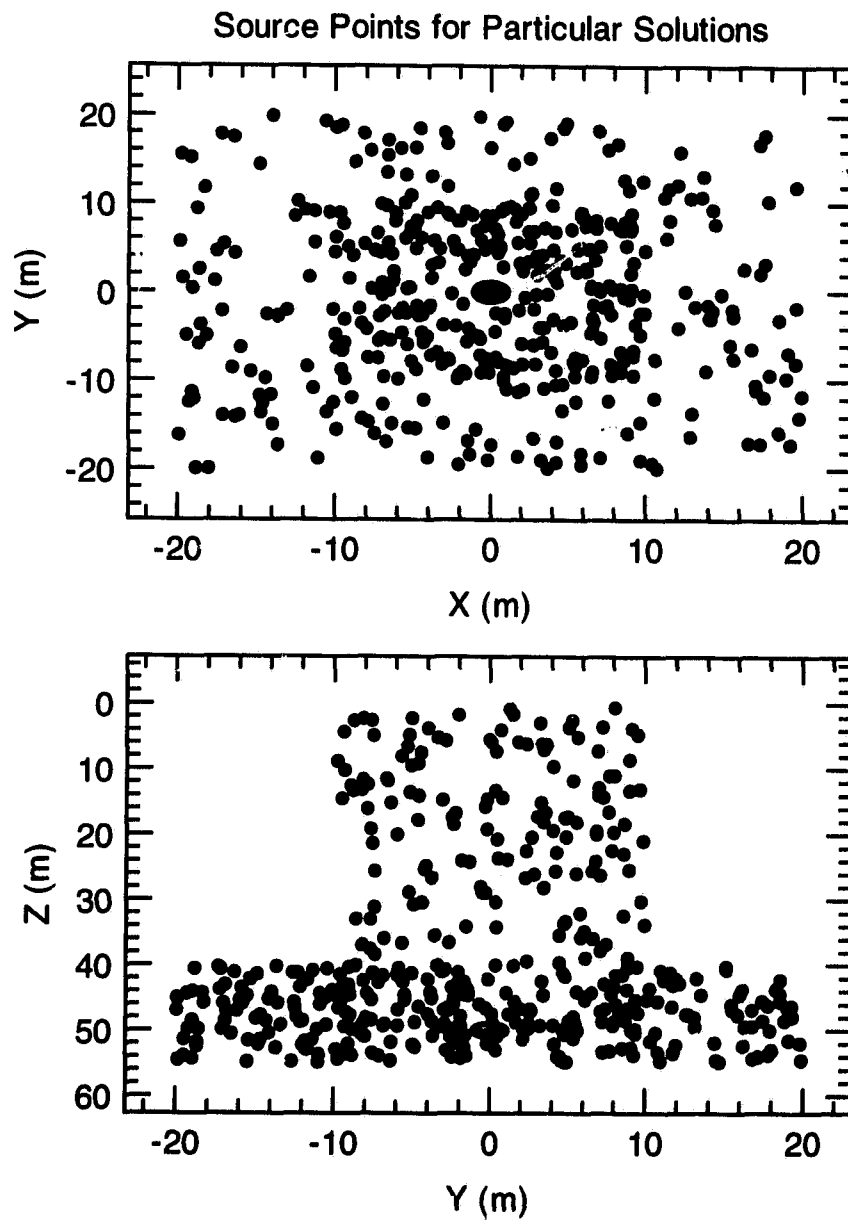


Figure 7.19: There are 440 point sources generating particular solutions for the half-buried sphere. **Top:** View along z axis. **Bottom:** View along z axis. The sources are randomly positioned; the region covered being roughly two P wavelengths in the z and y directions. There are no sources directly above, below, or inside the sphere.

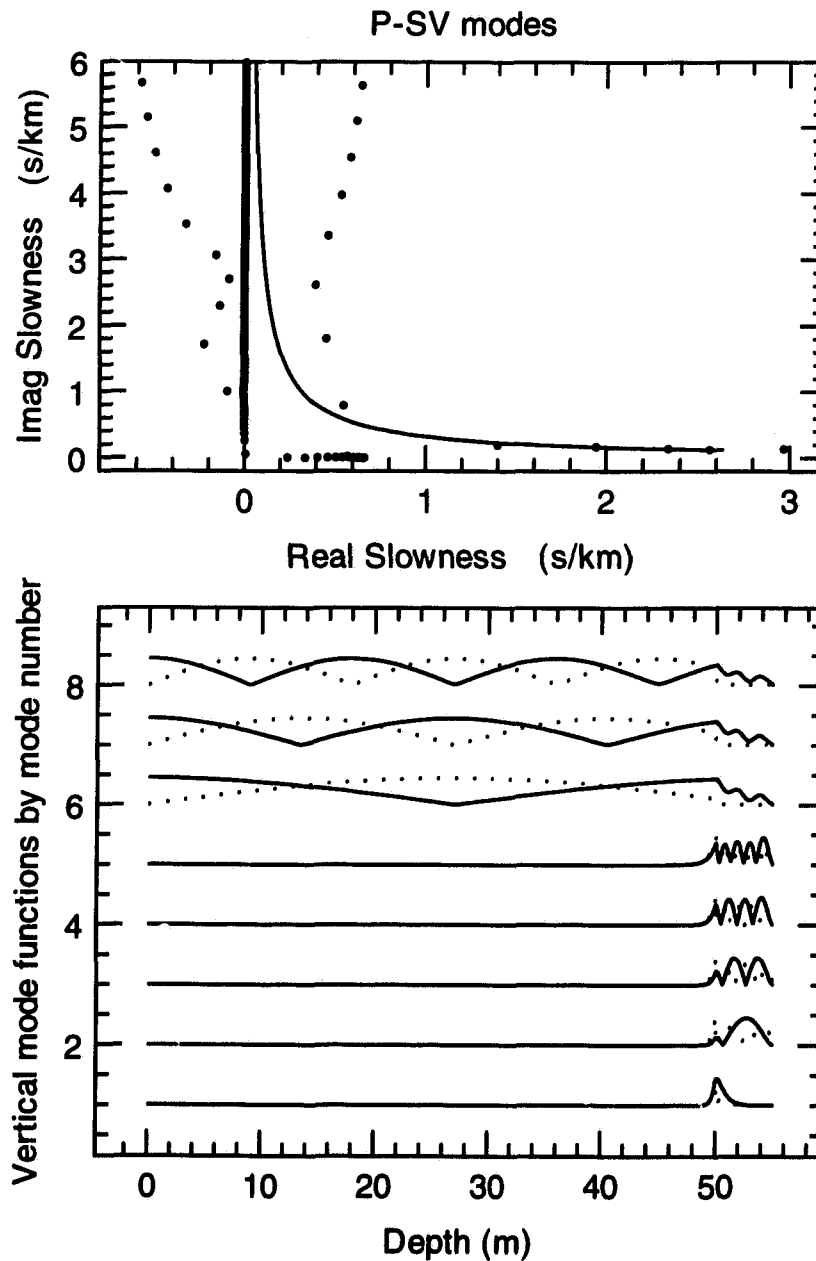


Figure 7.20: P-SV modes for the shallow ocean waveguide at 200 Hz. **Top:** Mode locations in the complex slowness plane. Notable are the Scholte mode at the sand-water interface ($p_r = 2.970$ s/km); propagating modes trapped in the sand layer on the S-wave branch line (solid line); propagating radiation modes ($p_r < 0.667$ s/km); a series of water-born evanescent modes along the imaginary axis; and a series of evanescent plate modes for the sand layer on both sides of the imaginary axis. **Bottom:** The vertical mode functions for the first eight propagating modes in order of decreasing p_r : vertical displacement U is the solid line, and horizontal V is dotted. The relative magnitudes are plotted.

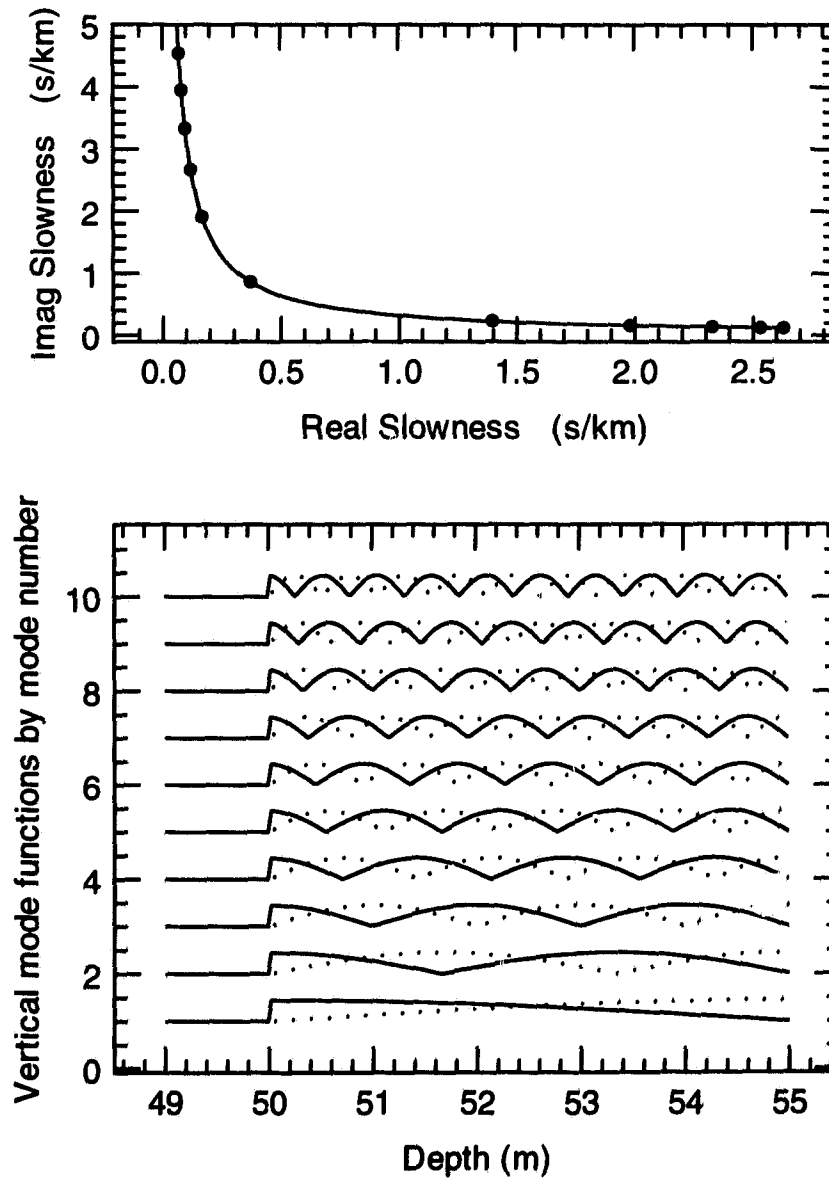


Figure 7.21: SH modes in the 5 m sand layer at 200 Hz. **Top:** The SH modes lie along the S-wave branch line (solid line) of the sand layer. **Bottom:** The vertical mode functions for the first ten propagating modes in order of decreasing p_r : horizontal displacement W is solid line, shear stress T is dotted.

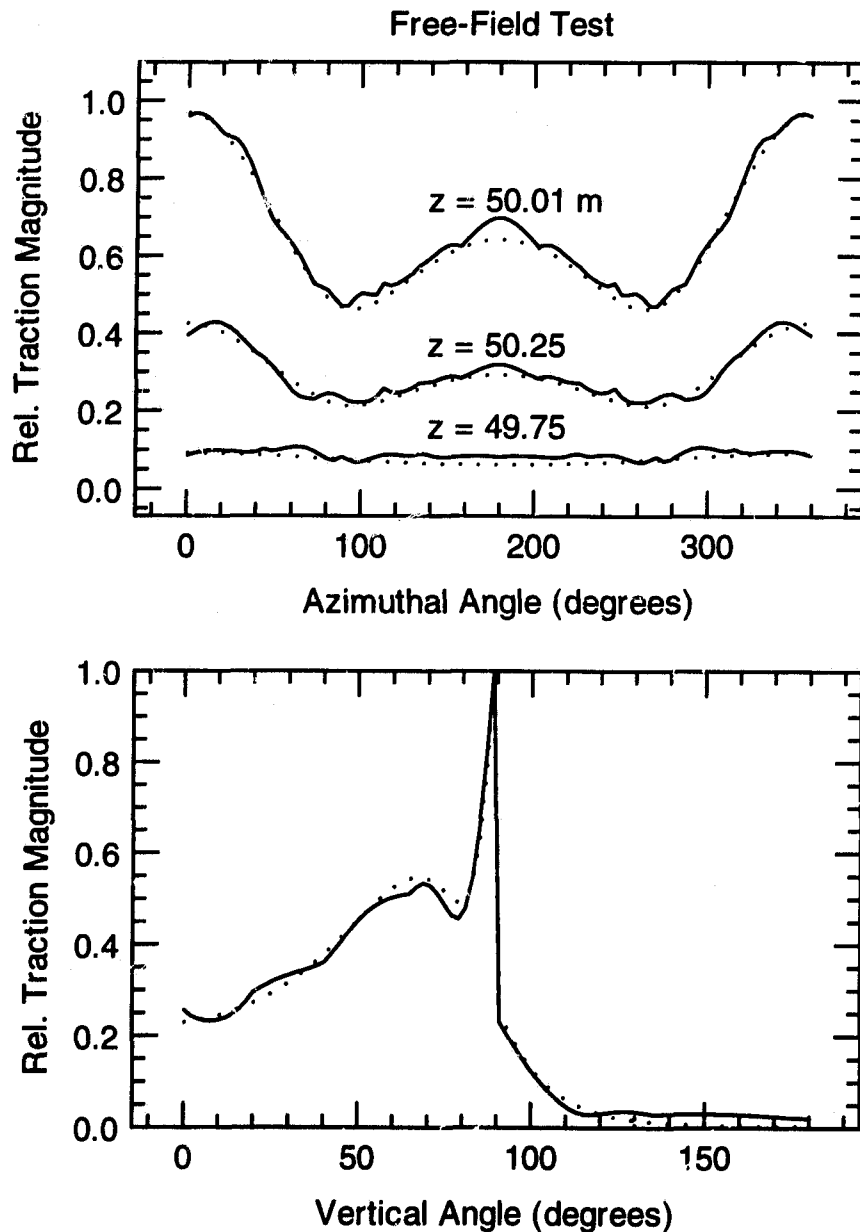


Figure 7.22: Free-Field Test: The BIE method was used to compute the free-field traction (solid line) at the boundary due to an incident Scholte mode (dotted line, exact). **Top:** Traction magnitude on three horizontal lines around the walls of the false sphere as a function of azimuthal angle ϕ . The incident Scholte mode approaches from $\phi = 0.0$. **Bottom:** Traction in the vertical $y = 0$ plane as a function vertical angle θ from the center for the sphere; $\theta = 0$ points vertically downwards. The sand-water interface is evident from the discontinuity at 90 degrees due to the edge at the ice-water interface, $z = 3.0$ m.

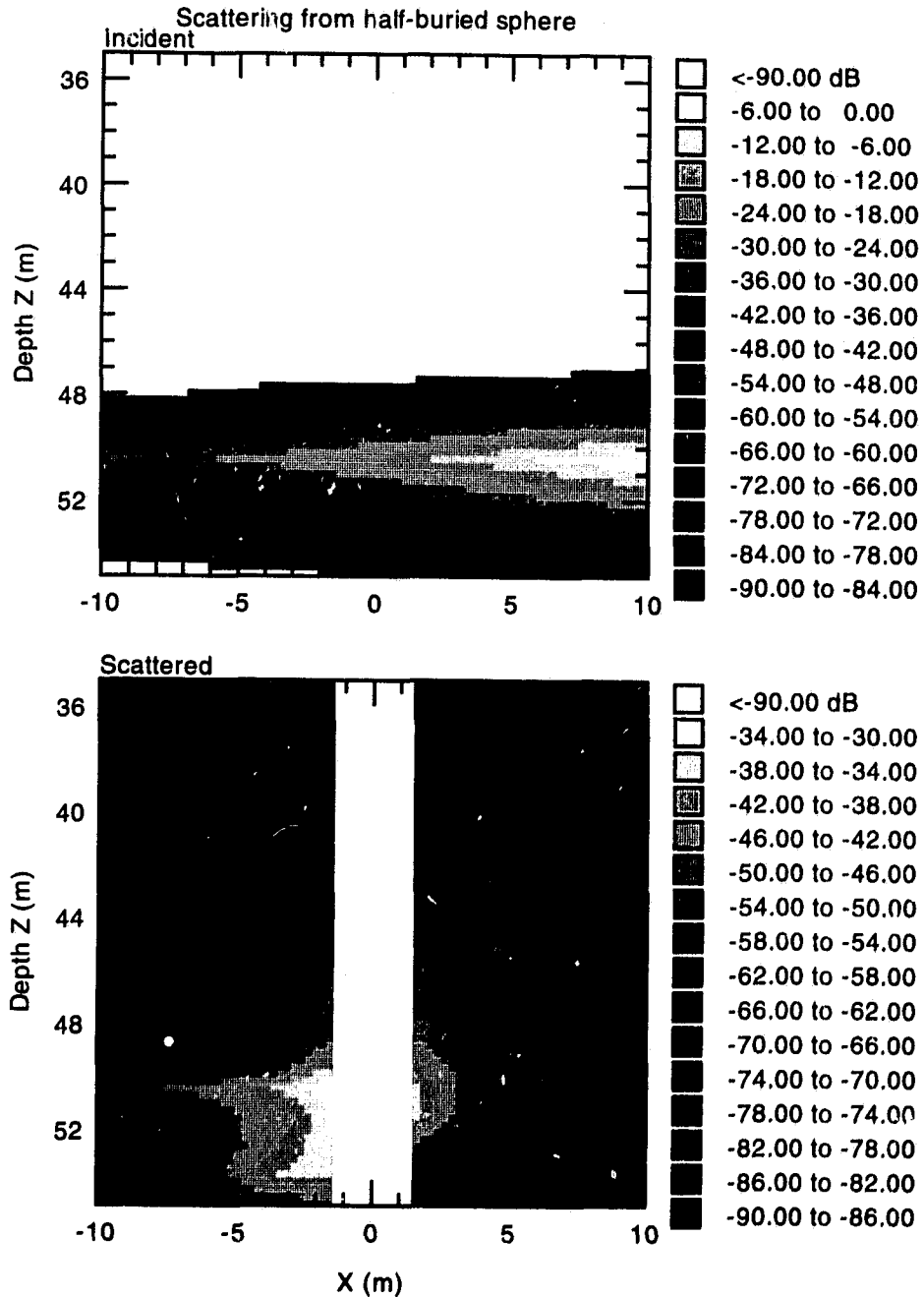


Figure 7.23: Scattering from the half-buried sphere. Top: Magnitude of the displacement due to the incident Scholte mode in the vertical plane $y = 0$. Bottom: Magnitude of the displacement in the field scattered from the half-buried sphere. The white band is the zone in which indirect coefficient computations are required, but were omitted to reduce the computation time.

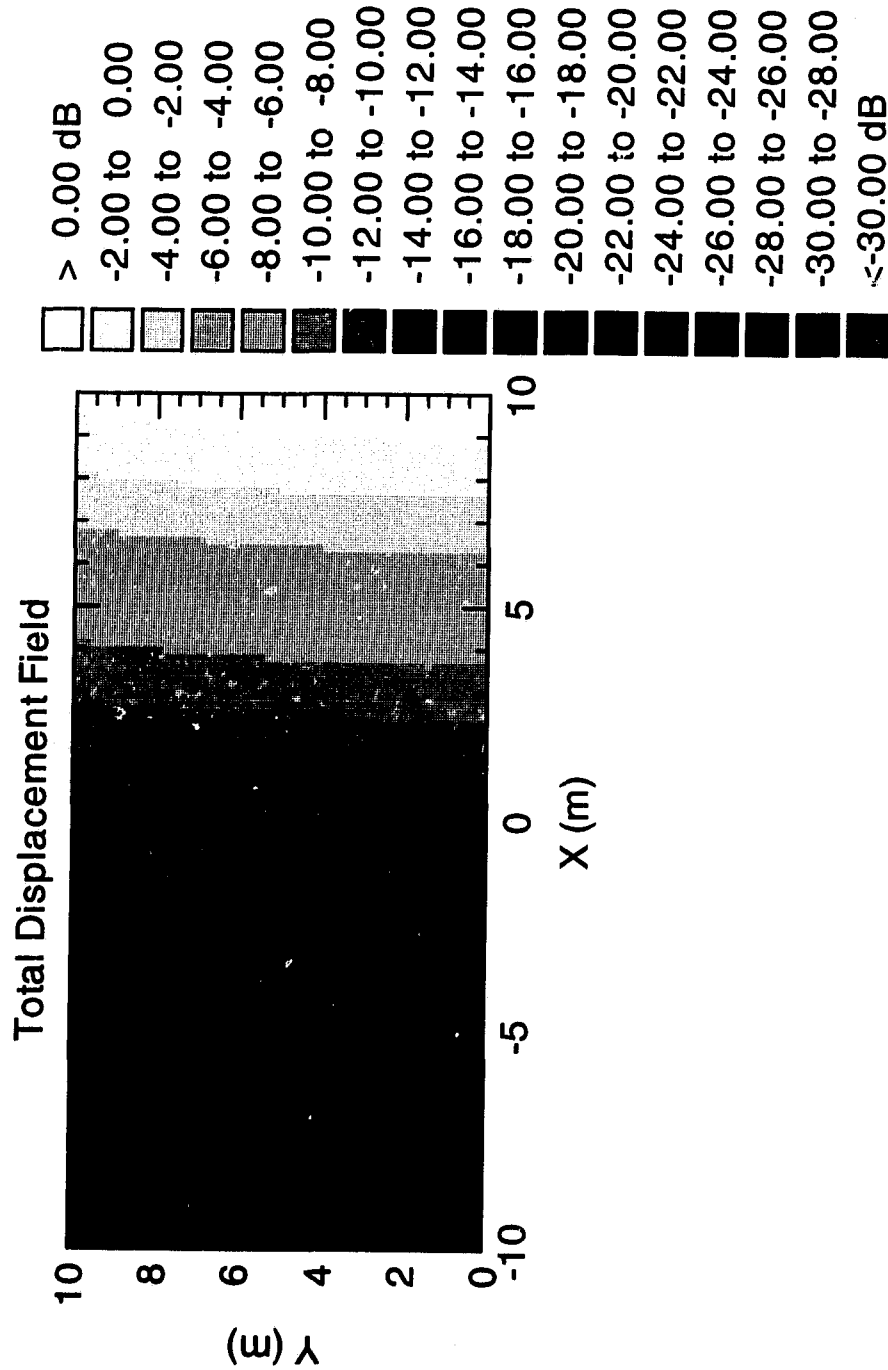


Figure 7.24: Total Field (plotted laterally): The magnitude of the total displacement field (incident plus scattered) at the top of the sand layer $z = 50.01$ m. The incident field is a Scholte mode approaching from the right.

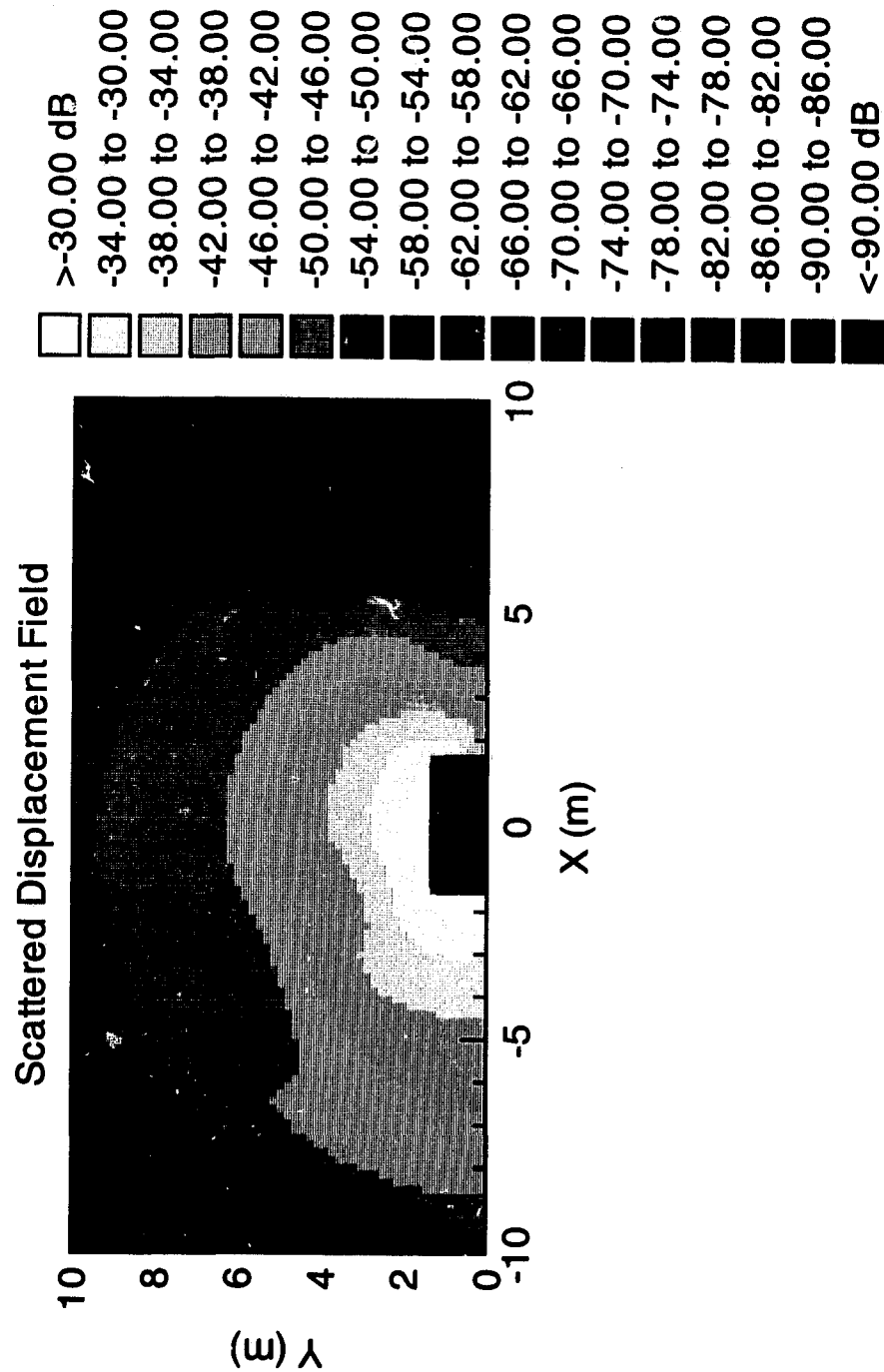


Figure 7.26: Scattered Field (plotted laterally): The magnitude of the scattered displacement field at the top of the sand layer at $z = 50.01$ m. The incident field is a Scholte mode approaching from the right.

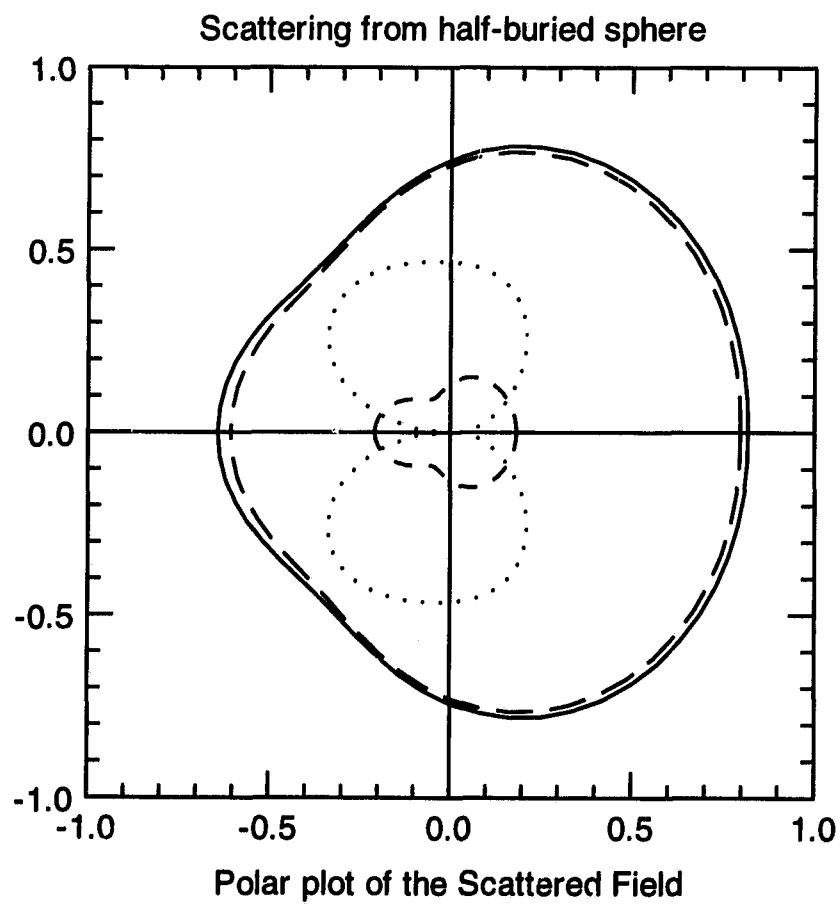


Figure 7.26: A polar plot of the scattered field in a horizontal plane just below the top of the sand layer $z = 50.01$ m, at a radial distance 150.0 m from the axis of the rigid sphere. The magnitude of the scattered displacement vector is the solid line, vertical u_z the small dashed, radial u_r the long dashed, and azimuthal u_ϕ magnified 10 times the dotted. The incident field is a Scholte mode approaching from the right.

7.3.3 Circular ice dome

The final demonstration is of scattering from a circular ice dome in a 3 m ice plate. A schematic of the model is shown in Fig. (7.27). The ice dome extends 2 m spherically up out of the waveguide, and 4 m down below the ice, into the water, as detailed in Fig. (7.28). The details for the BIE method are summarized in Table (7.3). There are two penetrable domains, hence, two perspectives for the integral equations: the exterior waveguide (perspective 0) and the interior of the ice dome (perspective 1). The two perspectives share 15 boundary elements inside the ice layer and sea water, and the field is coupled across those elements using continuity conditions applied at the nodes. Perspective 1 needs 9 additional impenetrable elements to close the upper part of its boundary outside the waveguide, where traction free $\mathbf{t} = \mathbf{0}$ boundary conditions apply; hence, the interior domain is a mixture of both penetrable and impenetrable boundary elements.

The Green's function for perspective 0 is for the Arctic waveguide considered earlier in Table (5.1). The Green's function for perspective 1 is for an unbounded homogeneous ice domain. The P-SV modes for the Arctic profile at 20 Hz have been reported earlier: the propagating in Fig.(5.6) and evanescent in (6.2). The SH modes for the ice plate at 20 Hz are shown in Fig. (7.29). SH modes in the sediments and bottom of the ocean are not needed because their vibrations do not enter the water. Each perspective has its own set of null-field points in their respective interior domain, as shown in Fig. (7.30). Each also has its own set of particular solutions for the indirect BIE method; those of perspective 0 lying within the waveguide—though not inside or directly below the scattering inclusion—, as shown in Fig. (7.31), and those for perspective 1 distributed uniformly around the inclusion in every direction, as shown in Fig. (7.32).

The free-field test was used to test the integral equations and BIE setup for both perspectives. The free-field was due to a vertical point force acting at $(x, y, z) = (200, 0, 0.01)$ m for both perspectives. Two tests were made for each perspective. In the first the free-field boundary displacement was assigned to the nodes using boundary condition equations, and the BIE method was used to compute the unassigned traction vector (equation of the first kind); in the second, traction was assigned and displacement was

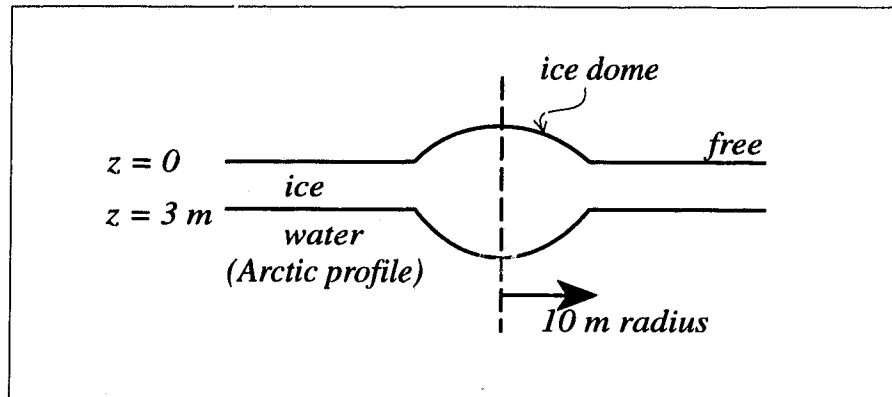


Figure 7.27: Schematic diagram of an ice dome in a 3m ice plate. The waveguide below the ice dome is the Arctic waveguide.

computed (equation of the second kind). Fig. (7.33) and Fig. (7.34) compare the exact and computed boundary traction for the tests.

The boundary field was then computed for the scattering problem, using the same integral equations used in the free-field tests, plus the coupling equations between the common nodes of the two perspectives, plus the coupling equations for vertical displacement u_z across the edges in each perspective, plus the traction-free boundary conditions for the top of perspective 1. Fig. (7.35) shows the incident and total displacement fields in a horizontal plane at the surface of the ice. Fig. (7.36) and (7.37) show the scattered displacement and its three vector components in cylindrical coordinates centered on the axis of the ice dome. Finally, Fig. (7.38) shows the far-field polar plot of the scattered field at the ice surface, at a radius 500 m from the axis of the dome.

Perspective 0: Arctic waveguide

| | |
|----------------------------------|--|
| No. boundary elements: | 15 |
| No. boundary nodes: | 79 |
| Symmetry assumed: | Bilateral symm. in $y = 0$ plane |
| No. of P-SV modes: | 1168 (max. $p_i = 0.08s/m$) |
| No. of SH modes: | 26 in ice plate only (max. $p_i = 0.2s/m$) |
| No. surface computation points: | 38 |
| No. interior computation points: | 100 |
| No. particular solutions: | 480 |
| Straightforward integration: | 7 by 7 Gaussian quadrature scheme for each boundary element |
| Close neighborhood of elements: | $\epsilon = 0.95$ m |

Perspective 1: ice dome

| | |
|----------------------------------|--|
| No. boundary elements: | 24 |
| No. boundary nodes: | 122 |
| Symmetry assumed: | Bilateral symm. in $y = 0$ plane |
| α | 3300. – 33.0 <i>i</i> m/s |
| β | 1730. – 20.0 <i>i</i> m/s |
| ρ | 900 kg/m ³ |
| No. surface computation points: | 73 |
| No. interior computation points: | 194 |
| No. particular solutions: | 400 |
| Straightforward integration: | 7 by 7 Gaussian quadrature scheme for each boundary element |
| Close neighborhood of elements: | $\epsilon = 0.95$ m |

Table 7.3: Setup for scattering ice dome in a floating ice plate.

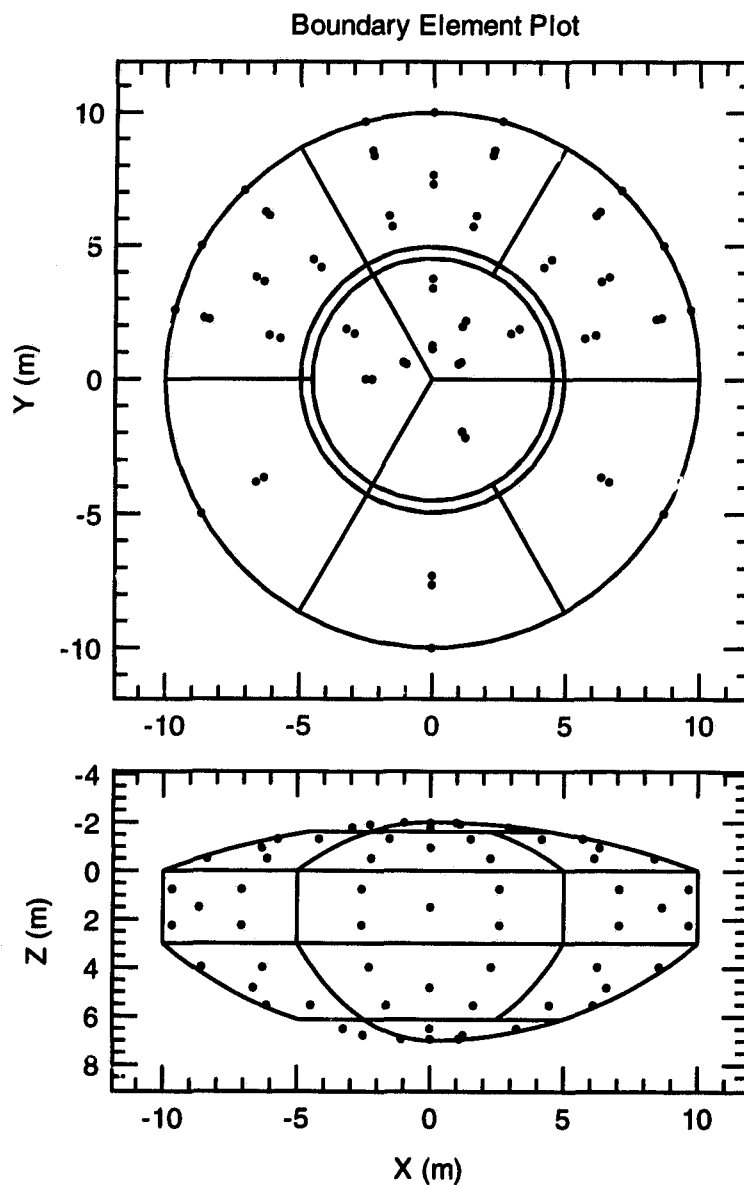


Figure 7.28: There are 24 boundary elements in the ice dome. The ice layer spans depths $z = 0$ to 3 m. **Top:** View along z axis. **Bottom:** View along y axis. Perspective 0 requires only 15 elements to enclose the dome extending into the waveguide ($z > 0$). Perspective 1 requires all 24 elements. The surface-field computation points (circular dots) are the same for both perspectives on their common boundary elements. The edges of the dome are lines of discontinuity where double nodes are required. Bilateral symmetry was assumed in the computations.

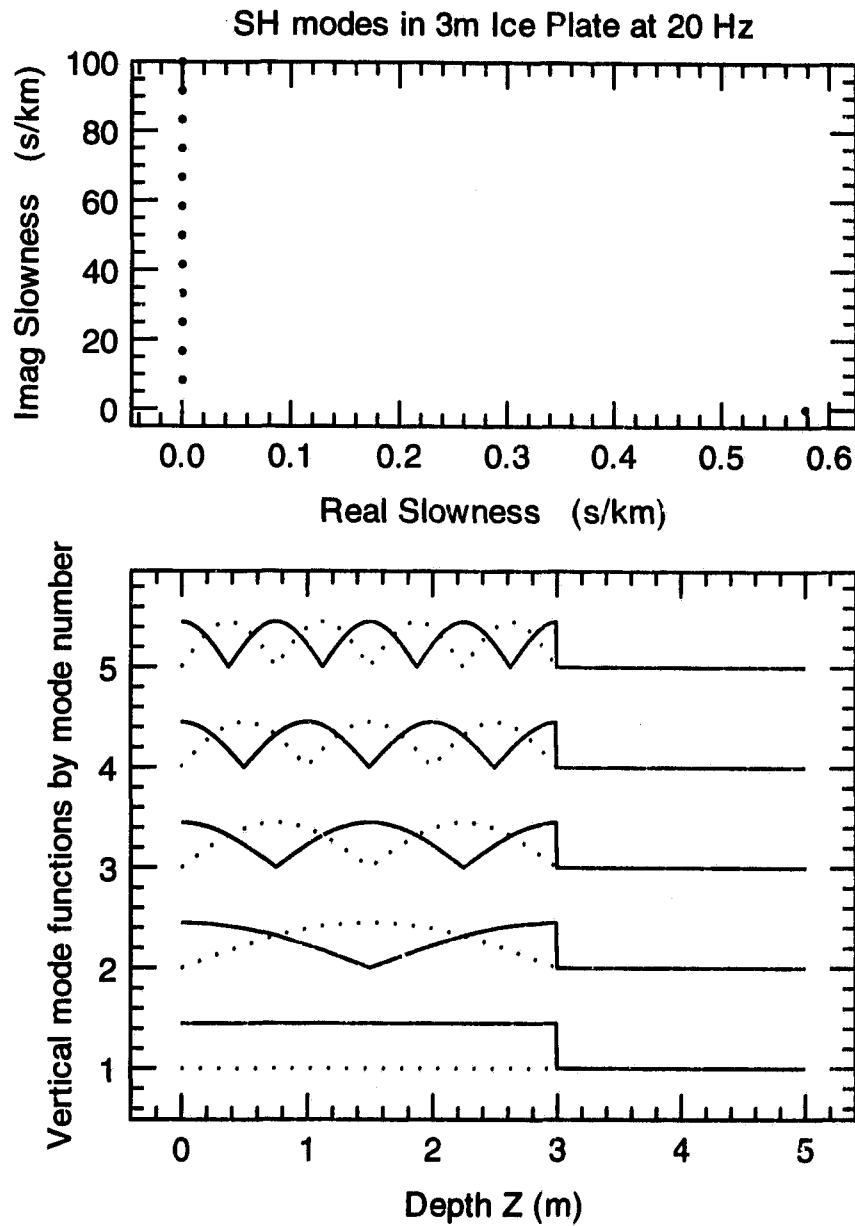
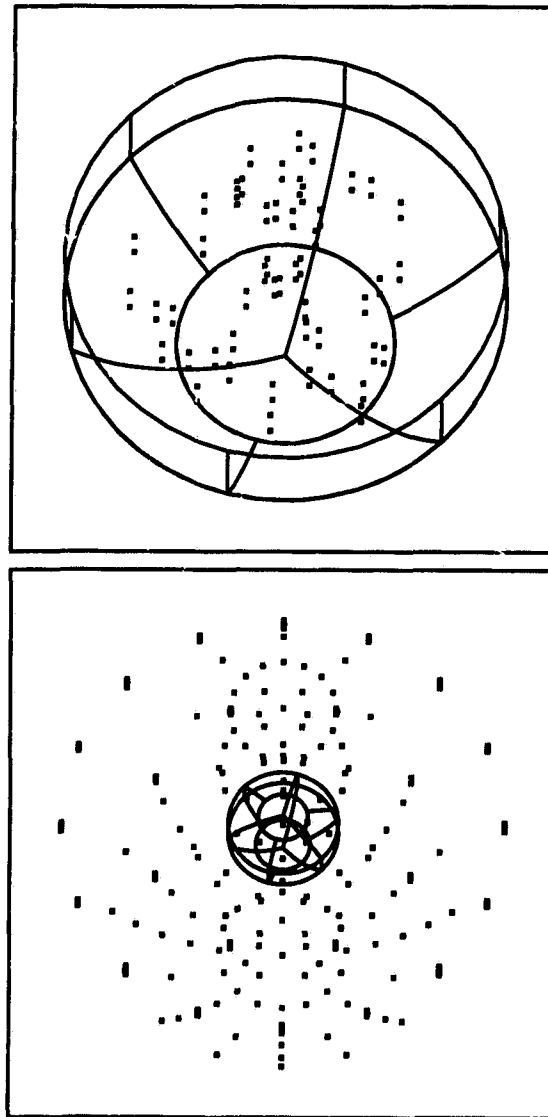


Figure 7.29: SH modes for the 3 m ice plate at 20 Hz. **Top:** The location of the SH modes in the complex plane. There is only one propagating SH mode at this relatively low frequency. **Bottom:** The vertical mode functions for the first 5 modes ordered by decreasing p_r . Shown are the relative magnitudes of the shear displacement W (solid line) and stress T (dotted line).



Oblique projection: Viewer in quadrant 1

Figure 7.30: Interior point locations: Each perspective has its own set of null-field computation points in their interior domain. Top: Perspective 0 has 100 interior points inside the ice dome for $z > 0$. Bottom: Perspective 1 has 194 null-field points distributed uniformly in a spherical domain outside the ice dome.

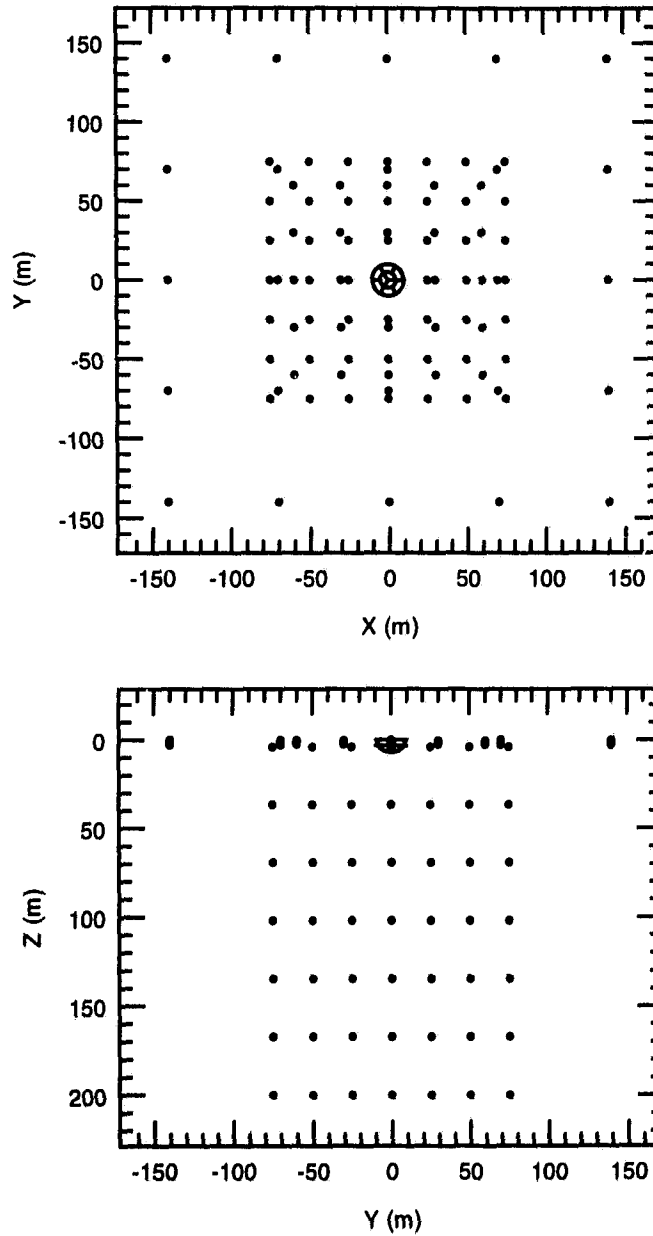


Figure 7.31: Sources for Particular Solutions, Perspective 0: 480 sources generate the particular solutions for the waveguide. They have been positioned in two regular sets: one set for the ice, and one for the water column. There are no sources above, below, or inside the ice dome. There are no sources in the sea floor because the ice dome is far from the bottom. Top: View along z axis. Bottom: View along z axis.

Sources for Particular Solutions
Perspective 1

248

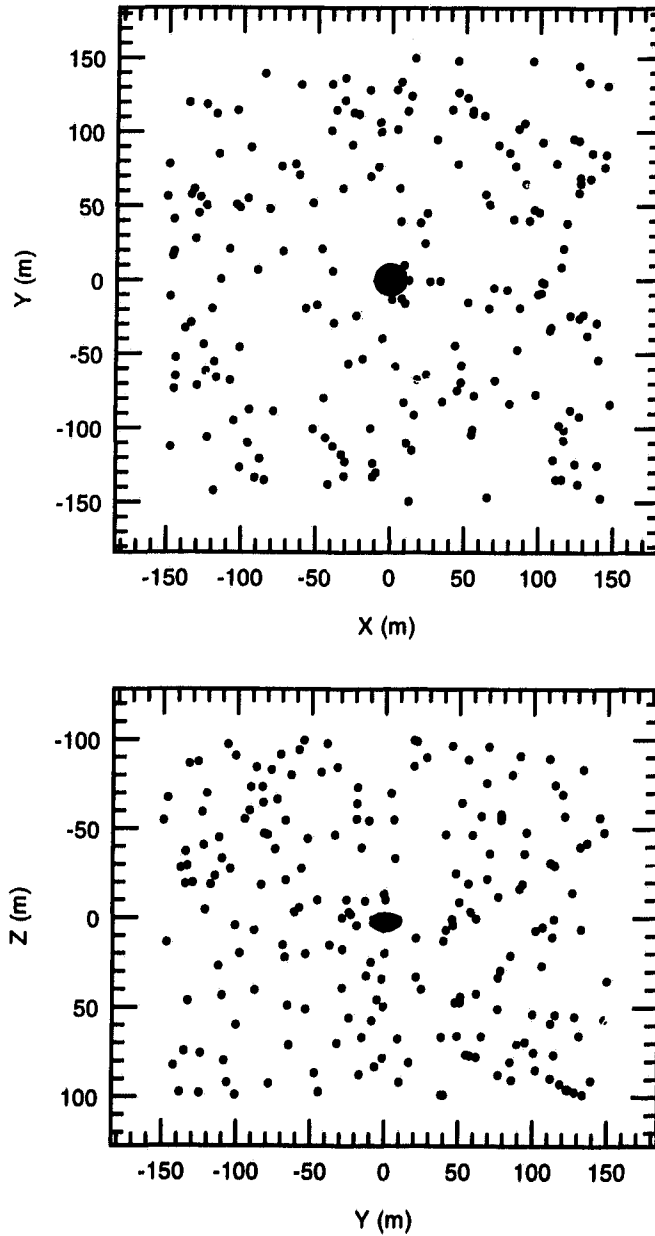


Figure 7.32: Sources for Particular Solutions, Perspective 1: 400 sources located randomly inside and outside the ice dome generate the particular solutions for perspective 1. There are few restrictions on the source location since this perspective uses the Green's function for a homogeneous unbounded domain. Top: View along z axis. Bottom: View along x axis.

Free-Field Test
Plot of field on boundary

249

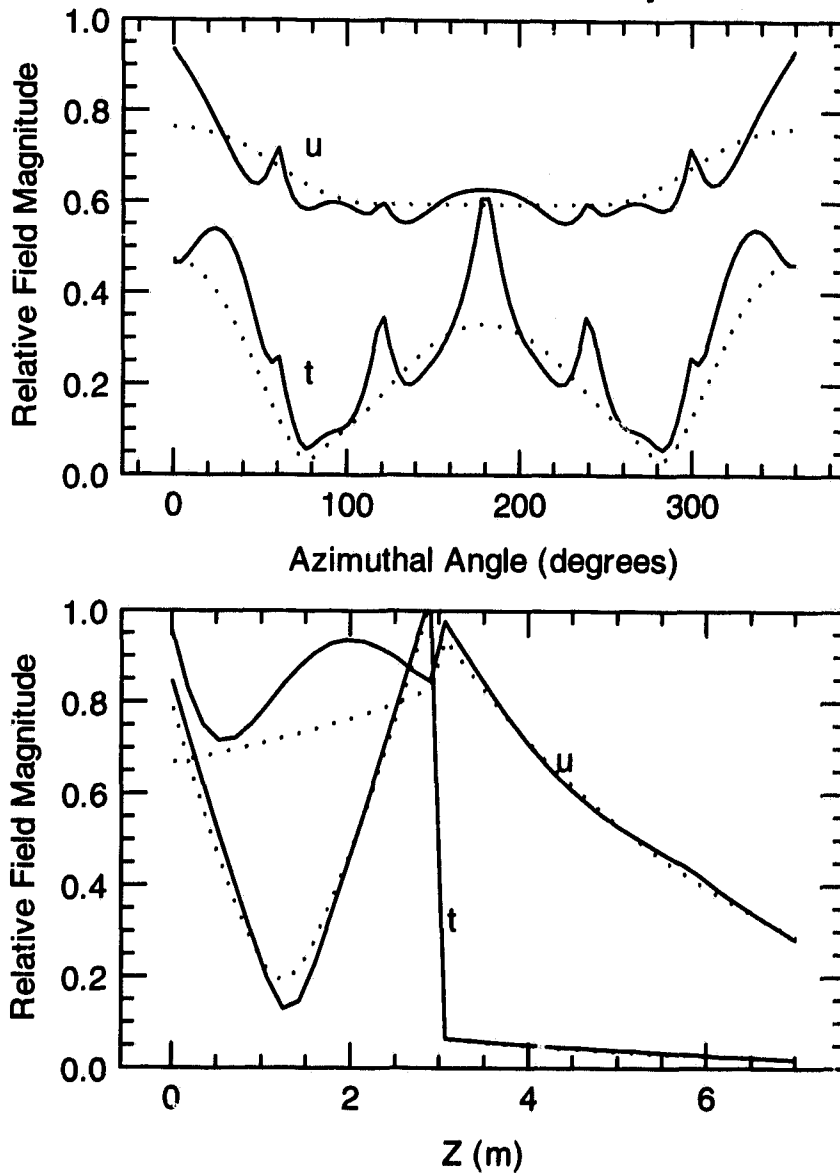


Figure 7.33: Free-Field Test, Perspective 0: The BIE method was used to compute the free-field on the "false" boundary of the dome (solid line) due to an explosive point source at $(x, y, z) = (50, 0, 1)$ (dotted line, exact). The test was performed twice: first the displacement u was computed from the free-field traction, then the traction t was computed from the free-field displacement. **Top:** Magnitude of u and t on a horizontal line around the wall of the false dome as a function of azimuthal angle ϕ at depth $z = 2.0$ m. **Bottom:** The same on a line in the vertical plane $y = 0$ ($x > 0$) as a function of depth.

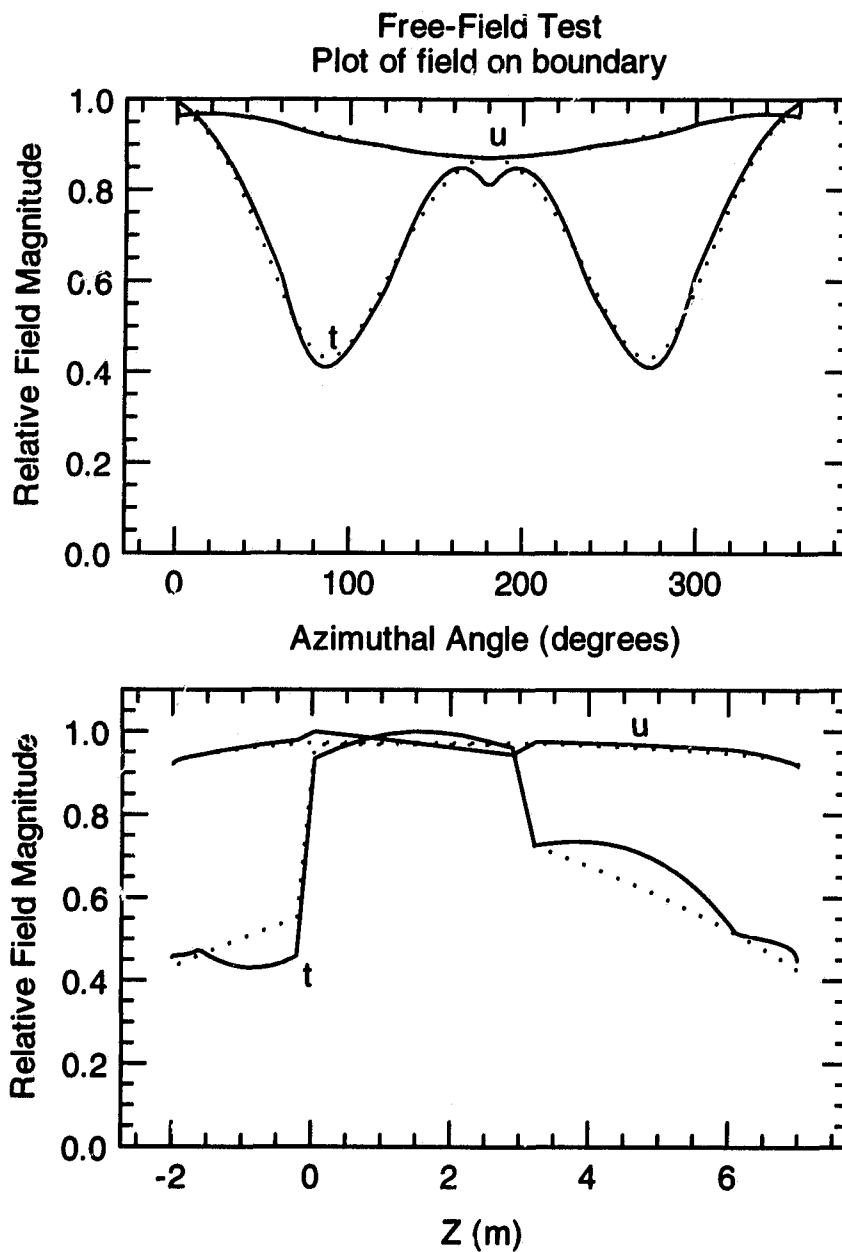


Figure 7.34: Free-Field Test, Perspective 1: The BIE method was used to compute the free-field (solid line) on the false boundary of the dome due to a distant vertical point force at $(x, y, z) = (200, 0, 0)$ (dotted line, exact). The test was performed twice: first the displacement u was computed from assigned free-field traction, then the traction t was computed from assigned free-field displacement. **Top:** Magnitude of u and t on a horizontal line around the wall of the false dome as a function of azimuthal angle ϕ at depth $z = 2.0$ m. **Bottom:** The same on a line in the vertical plane $y = 0$ ($x > 0$) as a function of depth.

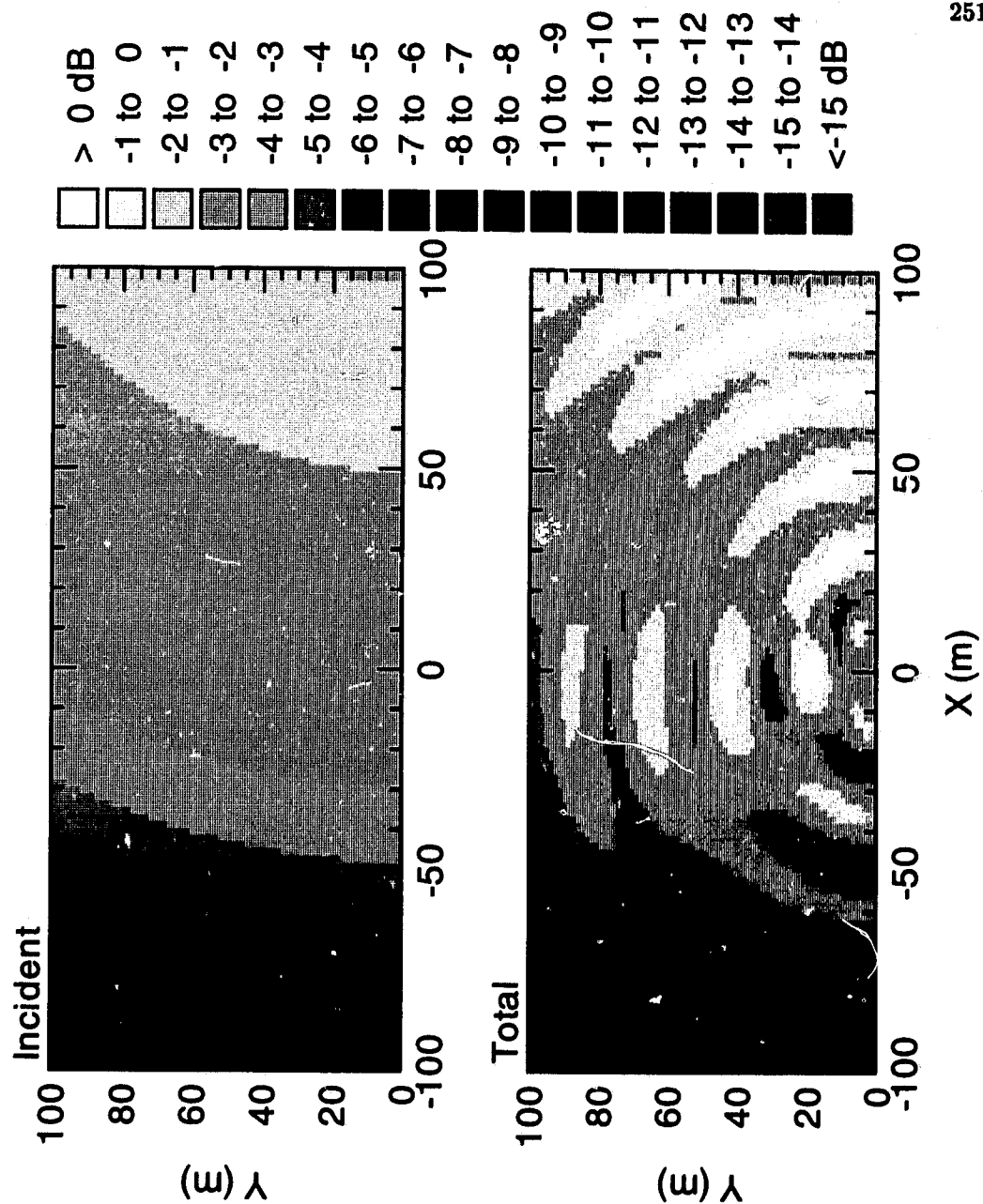


Figure 7.35: Incident and Total Field (plotted laterally): The magnitude of the incident and total (incident plus scattered) displacement field at the surface of the ice, $z = 0.01$ m. The incident field is that of a distant vertical point force at $(x, y, z) = (200, 0, 0.01)$ m operating at 20 Hz. Scattering is due to the 10 m radius ice dome at $(x, y) = (0, 0)$.

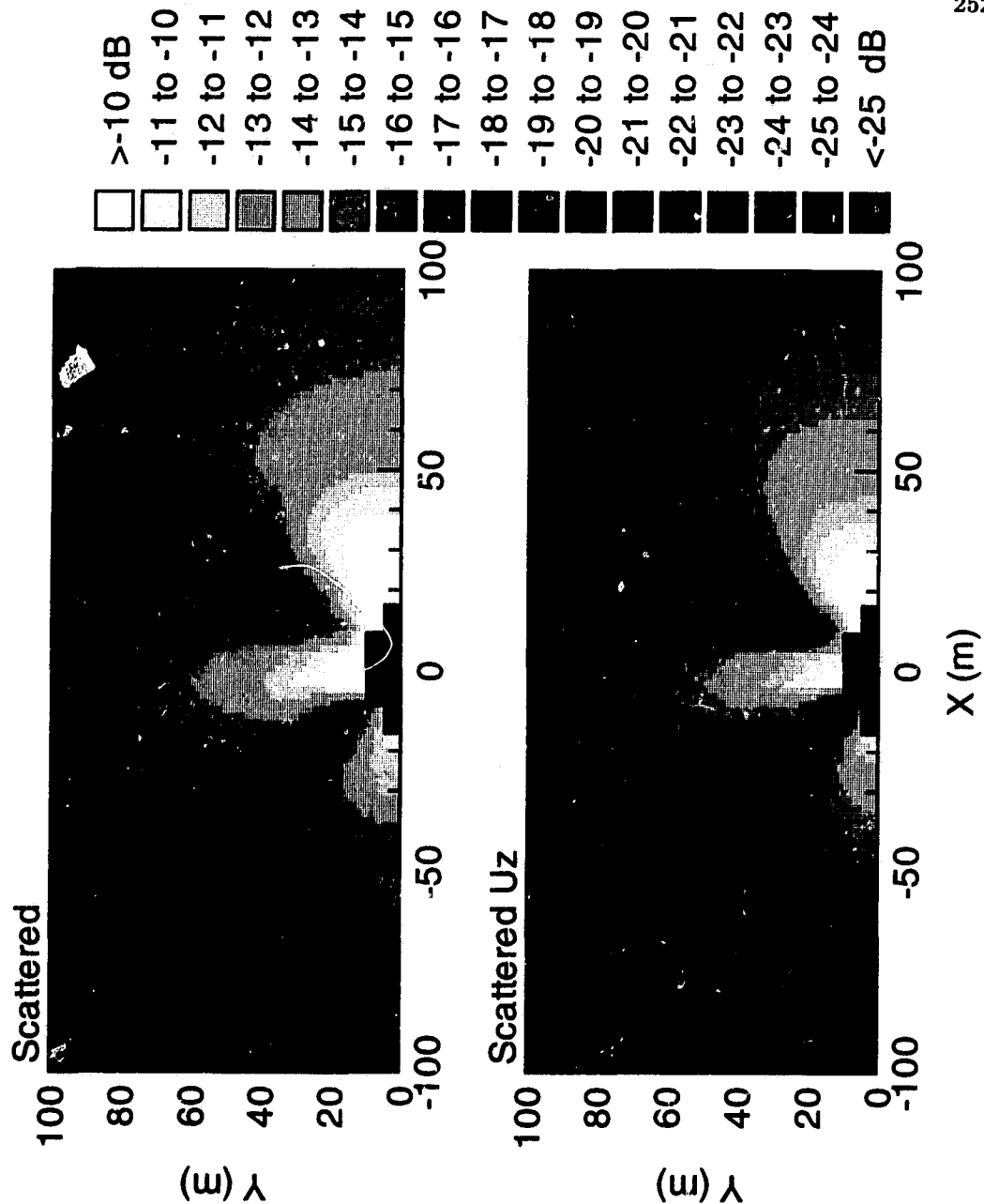


Figure 7.36: Scattered Field (plotted laterally): The magnitude of the scattered displacement vector and its vertical u_z component at the surface of the ice, $z = 0.01$ m. The incident field is that of a distant vertical point force at $(x, y, z) = (200, 0, 0.01)$ m operating at 20 Hz. Scattering is due to the 10 m radius ice dome at $(x, y) = (0, 0)$. The dark region at the dome marks the zone in which indirect coefficient computations were required, but were omitted to reduce the computation time.

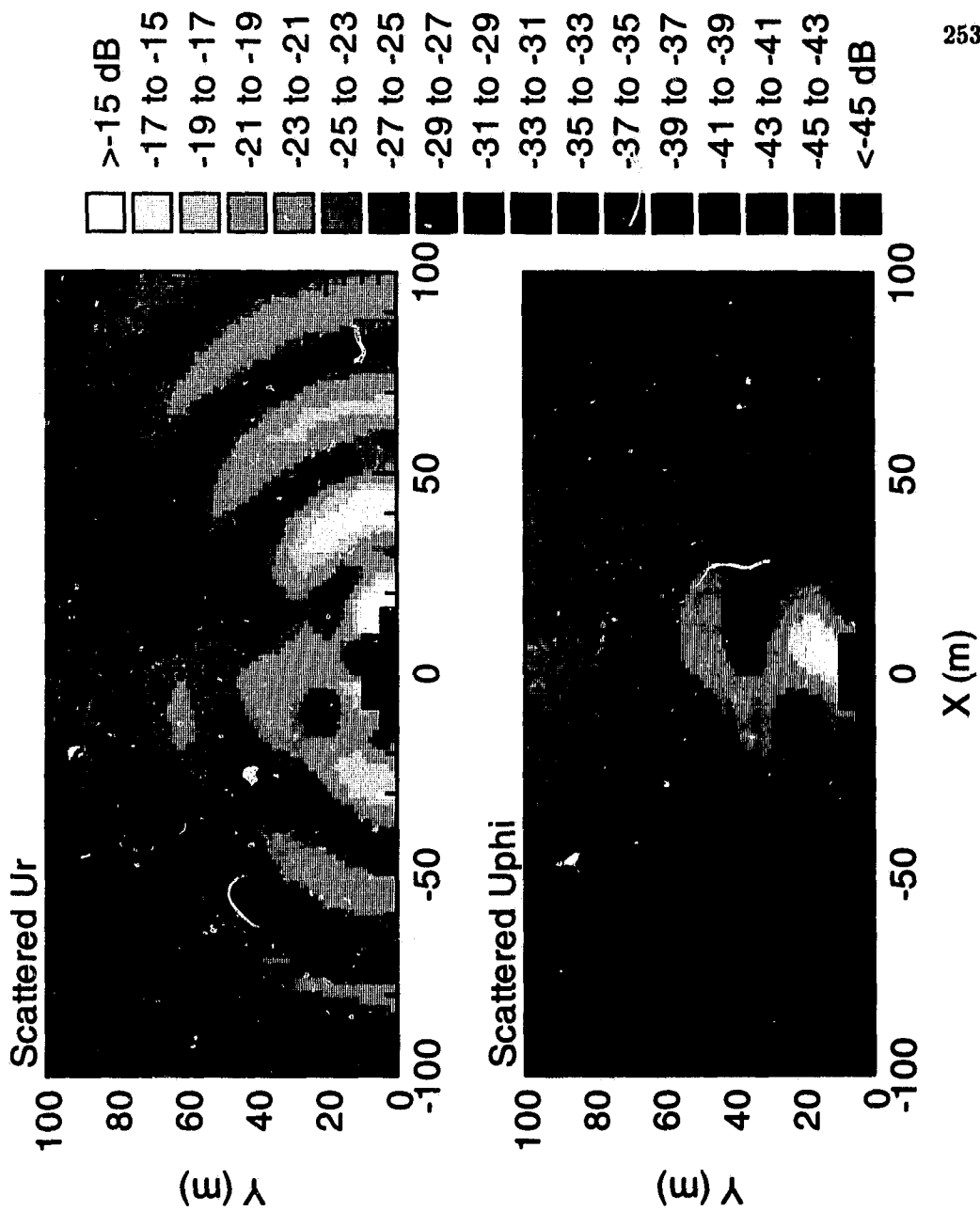


Figure 7.37: Scattered Field (plotted laterally): The magnitude of the horizontal radial u_r and azimuthal u_ϕ components of the scattered displacement vector at the surface of the ice, $z = 0.01$ m. The incident field is that of a distant vertical point force at $(x, y, z) = (200, 0, 0.01)$ m operating at 20 Hz. Scattering is due to the 10 m radius ice dome at $(x, y) = (0, 0)$. The dark region at the dome marks the zone in which indirect coefficient computations were required, but were omitted to reduce the computation time.

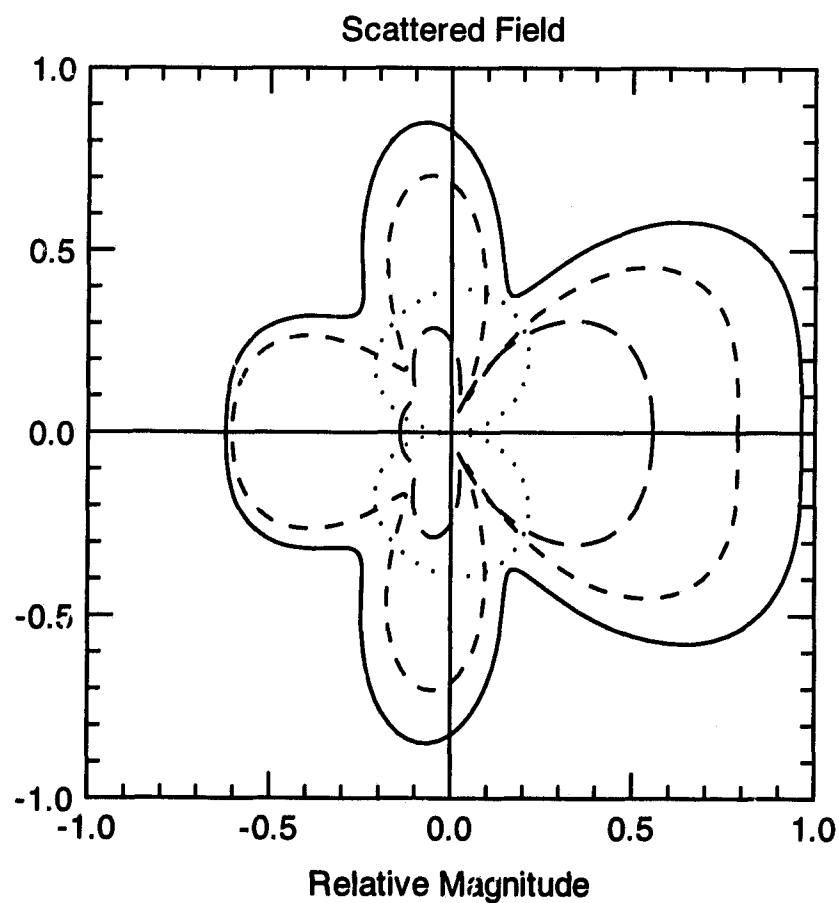


Figure 7.38: Scattered Field: A polar plot of the scattered field at the ice surface $z = 0.01$ m, at a radial distance 500 m from the axis of the ice dome. The magnitude of the displacement vector is the solid line, vertical u_z the small dashed, radial u_r the long dashed, and azimuthal u_ϕ the dotted. The incident field, due a distant vertical point force at $(x, y, z) = (200, 0, 0.01)$ operating at 20 Hz, approaches from the right.

Chapter 8

Conclusions

I have followed two paths towards a three-dimensional scattering model for layered media. The first followed Huygens' principle, which lead to a physical interpretation of the BIE method in terms of wavelet superposition, then to an indirect method for computing troublesome integral coefficients using particular solutions in the absence of scattering, and finally to several numerical tests for every application of the BIE method—the consistency, free-field and null-field tests. The second followed the schematic diagram for layered media, which first lead to the scattering matrix method for cylindrical waves, then to the channel matrix and SVD method for carrying out an exhaustive search for normal modes that was implemented by the SAMPLE program, which in turn lead to some discoveries regarding modes. The two paths met in a three-dimensional scattering model for layered media.

When faced with a complicated model, we must ask whether the same results could be achieved in a simpler way. I believe there is just one minor point in which the present model might have been simplified, and that is by limiting the problem to a single scattering inclusion rather than generalizing to multiple inclusions. As it happened, computer limitations on the number of boundary elements discouraged me from attempting the multiple body problem here. Beyond this, further simplifications could only be made by sacrificing one of the three features I set out to include from the beginning; by simplifying as others have done, using strictly fluid media instead of layered elastic media, impenetrable inclusions instead of penetrable, or two dimensions instead of three. Each step towards greater

realism engenders greater complexity in the model. There is no escape from this general rule of modeling.

The main developments made in the course of this work are summarized below.

8.1 Conclusions regarding layered media

The elastic field due to a general class of seismic point sources, some of which are not axially symmetric, was derived here for arbitrarily layered media in terms of the Fourier-Bessel transform. This topic has been covered by others in geophysics, and to a lesser extent in ocean acoustics, but my own contribution has been to

1. bring together fluid and solid media in a single comprehensive analysis;
2. press the analysis to completion, to give all nine components of the field—three components of displacement, and six of stress—as required by the BIE method;
3. develop a schematic ladder diagram for layered media, based upon the numerically stable scattering matrix method for two-port networks;
4. develop a robust normal mode search routine which, under the direction of the user, can perform an exhaustive search for modes in the complex plane.

The upshot of these advances are reviewed below.

8.1.1 Schematic ladder diagram

By treating the waveguide as a linear system whose components and interaction are easy to visualize and understand, the schematic ladder diagram forms a conceptual bridge between the physics of cylindrical or plane waves in layered media, and the more abstract matrix operations needed to compute the field due to a point source. Indeed, the diagram resembles the schematics an engineer might use to analyze a linear system, and the corresponding matrix can be written directly by inspection. The scattering matrix method at the heart of the diagram is an extension of Kennett's numerically stable recursive scheme [71].¹

¹The schematic diagram was developed step by step in Chapter 4, beginning in Section (4.2).

8.1.2 Normal modes and SVD

A mode occurs at frequencies ω and horizontal slownesses p at which the global matrix representing vertical propagation of cylindrical (or plane) waves through the layers is singular.² The smallest singular value w_1 of the global matrix was used as the mode search function, for the zeros of w_1 indicate singularity. To speed up the search for roots, the dimensions of the global matrix were compressed to give the channel matrix, in a way that ensures that the search remains sensitive to modes trapped at any depth in the waveguide. The main advantages of using w_1 as the search function are that

1. SVD is a robust matrix operation for nonsingular and singular matrices alike;
2. SVD gives the (un-normalized) vertical mode function for a mode;³
3. the second smallest singular value w_2 can be used to identify and resolve uncommonly close mode pairs (double roots) that can occur when the waveguide supports two weakly coupled sound channels.⁴

Using still other singular values in the search, the method could also be extended to check for close mode triplets and so forth, in the rare event that the waveguide supports three or more modes in as many sound channels at virtually the same ω and p .

8.1.3 The mode search program SAMPLE

A channel matrix and SVD method for the mode search was implemented in a program called SAMPLE, which undertakes the mode computations needed for the rigorous demands of the BIE method. Under the direction of the user, SAMPLE can perform an exhaustive search for all of the different types of modes that occur in layered media: whether P-SV or SH, propagating or evanescent, trapped or leaky, proper or improper (found on various Riemann sheets), or duct or interface modes. SAMPLE furthermore computes all nine components of the elastic wave field ($u_r, u_\phi, u_z, \tau_{rr}, \tau_{r\phi}, \tau_{rz}, \tau_{\phi\phi}, \tau_{\phi z}, \tau_{zz}$) due to a class of

²Section (5.2).

³Section (5.2.1).

⁴Section (5.3.3).

seismic point sources comprising general point forces, and couples with and without moment. The proper mode series is a complete representation of the field in a bounded waveguide. By including a long series of evanescent modes in a bounded waveguide, SAMPLE can compute the field very close to an ideal point source, within a small fraction of a wavelength, and that is essential for the BIE method.

SAMPLE includes many utilities that make it an excellent tool for the analysis of modes. It plots the location of modes and EJP branch lines in the complex slowness or wavenumber plane, plots vertical mode functions, computes group velocity, tracks modes with changing frequency, computes vertical energy flux in a mode function, and sorts modes in a number of useful ways. It also incorporates three important tests for mode computations:

1. verification of each mode using Rayleigh's principle;⁵
2. verification of part or all of the mode series using contour integration and the residue theorem;⁶
3. and verification of the dominant modes in the medium to far field the spectral FFT—a special form of contour integration.⁷

Further possibilities for SAMPLE

The following additions to SAMPLE may prove helpful:

1. Airy functions: SAMPLE now supports homogeneous solid and fluid layers. Another possibility for fluid layers is to make the square of the phase slowness for P waves vary linearly with depth in a layer, for which the vertical propagation is governed by Airy functions [66, sect. 2.5.1]. In this way, the sound speed profile in the water column can be approximated using fewer layers for greater program efficiency.
2. Pekeris branch cuts: SAMPLE now uses the EJP branch cuts when computing vertical slowness,⁸ but the Pekeris cuts (extending vertically from the branch point) are

⁵See Section (5.4.4).

⁶See Section (5.4.2).

⁷See Section (5.8).

⁸See Fig. (4.1).

convenient for leaky mode environments, when the search is liable to cross the EJP cuts several times [125]. They could be included as an option in SAMPLE.

3. **Improper mode normalization:** Although SAMPLE can find improper modes, it cannot use them in the mode series because the integral identities used to normalize a mode function have only been implemented for proper modes. Improper modes could be normalized using modified integral identities.⁹
4. **Optimization:** As with most modeling programs in the development stage, SAMPLE could be optimized using specialized computation routines. In particular, an SVD routine for banded matrices may speed up the mode search for waveguides having many channels.
5. **Anisotropy:** Following the method of Takeuchi and Saito [122] it is possible to include anisotropy in the solid layers, where the phase speeds for waves travelling horizontally are different from waves travelling vertically.

Items 2 and 3 above are never needed for bounded waveguides because they do not have improper modes.

8.1.4 The properties of modes

SAMPLE made it possible to investigate modes in great detail, revealing little-known properties of modes that are of interest in their own right. These properties are summarized below.

Upward energy flow from an infinite halfspace

Modes in infinitely deep waveguides sometimes carry energy upwards from depths below all sources and reflecting interfaces.¹⁰ This apparent contradiction to the radiation condition is actually an energy loss mechanism for the vibrations of waves trapped in the basement media, when the rate of decay of the mode due to energy loss exceeds the P or S

⁹See note regarding improper mode normalization on page 167.

¹⁰Section (6.1.4).

wave absorption rate in the bottom. The upward flow is slight, but it may be the cause of alarm to the conscientious modeler.

Proper leaky modes

It is generally assumed that leaky modes in unbounded waveguides must be improper modes whose vertical mode functions grow exponentially with depth. But leaky modes radiating into a lossy infinite half space may also be proper modes, with mode functions that decay with depth.¹¹ This happens when the exponential vertical decay due to absorption overcomes the exponential growth characteristic of leaky modes in lossless media. The shear wave absorption used to model ocean sediments is often enough to make S-leaky modes proper.

Proper leaky modes are of interest for modeling purposes, since normal mode programs designed for proper modes with complex horizontal slowness should be able to handle proper leaky modes without modification. At times it may be justified to add artificially high absorption in the basement to make a leaky mode environment amenable to a proper mode program.

Radiation modes in deep bounded waveguides

A waveguide having a deep bounded basement layer is often used to model the corresponding unbounded case. Since the basement layer is thick, there is a proliferation of radiation modes close to the P and S branch lines.¹² The range of good agreement between the two was estimated in Section (6.4). It was also shown that isolated radiation modes in an unbounded waveguide approximate the dominant leaky modes of the corresponding unbounded waveguide.

Rayleigh mode of the second kind

It was shown that a leaky interface mode can be trapped at the rigid boundary in welded contact with a solid layer. This mode can appear as a proper mode in deep bounded

¹¹Section (6.2.1).

¹²Section (6.2.2).

waveguides, when a thick solid basement layer is bounded by a rigid interface.¹³

8.2 The indirect BIE method

The indirect BIE method infers numerically troublesome integral coefficients from many particular free-field solutions of the boundary integral equations needed for the intended scattering problem.¹⁴ The main advantages of the indirect method are that:

1. it makes the BIE method possible in layered media when the Green's function is computed using mode summation, for there is presently no other way to avoid poor convergence of the mode series at the close ranges routinely encountered in the BIE method;
2. all troublesome integral coefficients are treated in the same way, whether troublesome due to the singularity in the surface-field equation, poor convergence in the Green's function, or for any other reason.

In addition, the indirect BIE method includes features that could be included in any BIE method for scattering. Most important are the three tests it supports:

1. the free-field test, which is a comprehensive test of all aspects of the BIE method for each application;¹⁵
2. the null-field test, which tests the boundary field computed by the BIE method;¹⁶
3. the consistency test, which verifies that the integral coefficients for a boundary integral equation have been accurately computed at the time of computation.¹⁷

Of secondary importance is its unprecedented flexibility, for the new method permits

¹³Section (6.2.3).

¹⁴The new indirect BIE method was first described in Chapter 3, then applied to layered media in Chapter 7.

¹⁵See Section (5.4.2).

¹⁶Section (3.7).

¹⁷Section (3.3).

1. any combination of surface-field and null-field equations when determining the boundary fields;
2. any number of surface-field computation points, placed anywhere on the boundary, rather than just at the element nodes;
3. multiple penetrable, impenetrable and actively vibrating inclusions;
4. lines of discontinuity in the field; in the displacement field where the inclusion crosses an interface with a fluid layer, or in the traction at an edge on the boundary.

By experimenting with the number of computation points and their location, it is sometimes possible to improve the numerical stability of the BIE solution.

The main disadvantage of the method is that it is computationally intensive. Many particular solutions are needed to infer troublesome coefficients indirectly, and in layered media, computing the particular solutions at the boundary element nodes takes considerable time, making it best to compute and save them for ready access. This of course increases the computer disk space used by the model. To judge how slow (or fast) the indirect method may be relative to other three-dimensional BIE methods for layered media, we must wait until alternative models are developed.

8.2.1 Future research

The next step is to use the new model to explore general principles of scattering, by applying it to particular instances of scattering. To say, for example, when and to what degree scattering from a series of ice keels is a significant loss mechanism for long range propagation in the Arctic ocean, or whether Scholte modes could be used to detect objects buried in the sea floor. The model could also be used in the development of faster approximate treatments of scattering, along the lines of the Kirchhoff or Born approximations.

The model itself could be improved by

1. making provisions for the computation of the scattered stress field, especially the normal stress in fluids commonly used in ocean acoustics;¹⁸

¹⁸Section (3.2.5).

2. permitting layered media inside a penetrable inclusion as well as outside;
3. testing its use with multiple scattering inclusions;
4. conducting a thorough analysis of the continuity conditions for lines of discontinuity on the boundary: edges and interfaces between layers;
5. and by a theoretical analysis into the stability of integral equations that are both of the first and second kind.¹⁹

8.3 Closing Remarks

I close on a cautionary note for modelers. The BIE method for scattering, whether or not the indirect method described here is used, supports several excellent tests: the consistency test, null-field test, and especially the free-field tests. In numerical modeling it is rare to have such comprehensive tests available. All three tests for the BIE methods have been reviewed here, though the null-field and free-field tests have appeared elsewhere in the literature. It would appear, however, that such tests have rarely been used to verify results published in the literature, probably because the tests are little known. I find that worrisome, for my own experience has been that it is not enough to prove the BIE method by successfully solving a problem that others have solved another way. Rather, every application of the BIE method must be tested because changes in the boundary, frequency, elastic media, and boundary conditions, invite a host of difficulties that may lie quiescent in a benchmark test. This is particularly true for scattering in layered media. The tests do not require much extra effort, provided they have been included in the overall plan for the BIE model from the outset.

¹⁹Section (2.7).

Bibliography

- [1] **Aki, K., and P.G. Richards**, *Quantitative seismology*, Vol. 1, Freeman, San Francisco (1980).
- [2] **Abramowitz, M., and I.A. Stegun**, *Handbook of Mathematical Functions*, National Bureau of Standards, Applied Mathematics Series 55, Washington DC (1965).
- [3] **Aliabadi, M.H., W.S. Hall, and T.G. Phemister**, "Taylor expansions for singular kernels in the boundary element method," *International Journal for Numerical Methods in Engineering*, 21, (1983): 2221-2236.
- [4] **Arfken, G.**, *Mathematical methods for physicists*, Third Ed., Academic Press, Toronto (1985).
- [5] **Arvelo, J.I., M. Talmant, and H. Uberall**, "A normal mode model of underwater propagation including shear effects in a layered ocean floor," *Computational Acoustics*, 3 (1990): 131-150.
- [6] **Auld, B.A.**, *Acoustic fields and waves in solids*, Vol. 1, John Wiley and Sons (1973).
- [7] **Baker, B.B., and E.T. Copson**, *A mathematical theory of Huygens' principle*, 2nd ed., Oxford at the Clarendon Press (1949).
- [8] **Banerjee, P.K., and R. Butterfield**, *Boundary element methods in engineering science*, McGraw-Hill, Maidenhead, Brekshire, England (1981).

- [9] **Bartberger, C.**, "Normal mode solutions and computer programs for underwater sound propagation," Part II-Prog. for Arbitrary Velocity Profiles, Naval Air Development Center, Report No. NADC-72002-AE (April 4 1973).
- [10] **Batchelor, G.K.**, *An introduction to fluid dynamics*, Cambridge University Press (1967).
- [11] **Benthien, G.W., and D. Barach**, CHIEF user's manual, Naval Ocean Systems Center, San Diego, California, NOSC TD 970 (Feb 1987).
- [12] **Bhatia, A.B.**, "Ultrasonic Absorption," Dover Publications, New York (1985).
- [13] **Bhatia, A.B., and R.N. Singh**, *Mechanics of deformable media*, Adam Hilger, Bristol (1986).
- [14] **Bolt, B.A.**, Editor, Seismic surface waves, in *Methods in computational physics*, vol. 11, Academic Press, New York (1972).
- [15] **Brebbia, C.A., J.J. Rego Silva, and P.W. Partridge**, Chapt. 2 Computational Formulation, in *Boundary element methods in acoustics*, ed. R.D. Ciskowski and C.A. Brebbia, co-published by Computational Mechanics Publications, Southampton, and Elsevier Science Publishers Ltd., New York (1991).
- [16] **Brekhovskikh, L.**, *Waves in layered media*, 2nd ed., Academic Press, New York (1980).
- [17] **Brekhovskikh, L.**, and Y. Lysanov, *Fundamentals ocean acoustics*, Springer-Verlag, Berlin (1982).
- [18] **Brooke, G.H., and J.M. Ozard**, "In-situ measurements of elastic properties of sea ice," *Underwater acoustic data processing*, Ed. Y.T. Chan (1989): 113-118.
- [19] **Burns, D.R., and R.A. Stephen**, "Three-dimensional numerical modeling of geoacoustic scattering from seafloor topography," *Journal of the Acoustical Society of America*, 88 (1990): 2338-2345.

- [20] **Burns, D.R.**, "Acoustic and elastic scattering from seamounts in three dimensions—a numerical study." *Journal of the Acoustical Society of America*, 92 (1992): 2784-2791.
- [21] **Burridge, R., and L. Knopoff**, "Body force equivalents for seismic dislocations," *Bulletin of the Seismological Society of America*, 54 (1964): 1875-1888.
- [22] **Burton, A.J.**, "The solution of Helmholtz' equation in exterior domains using integral equations", National Physical Laboratory, Report NAC 30 (January 1973).
- [23] **Byron F.W., and R.W. Fuller**, *Mathematics of classical and quantum physics*, Dover Publications, New York (1969).
- [24] **Chew, W.C.**, "*Waves and fields in inhomogeneous media*," Van Nostrand Reinhold, New York (1990).
- [25] **Chin, R.C., G.W. Hedstrom and L. Thigpen**, "Matrix methods in synthetic seismograms," *Geophysical Journal of the Astronomical Society*, 77 (1984): 483-502.
- [26] **Chin-Bing, S.A. , D. B. King, and J. D. Boyd**, "The effects of ocean environmental variability on underwater acoustic propagation forecasting," in *Oceanography and acoustics*, Ed. A. R. Robinson and D. Lee (1994).
- [27] **Ciskowski, R.D. and C.A. Brebbia**, Editors, *Boundary element methods in acoustics*, Computational Mechanics Publications, Elsevier Applied Science, London (1991).
- [28] **Clay, C.S., and H. Medwin**, *Acoustical oceanography: principles and applications*, John Wiley and Sons (1977).
- [29] **Colton, D., and R. Kress**, *Integral equation methods in scattering theory*, John Wiley and Sons (1983).
- [30] **Dawson, T.W.**, "The DREP internal wave normal mode model - theoretical background," Technical Memorandum 88-7, Defence Research Establishment Pacific, Esquimalt, Canada (1988).

- [31] **Dawson, T.W., and J.A. Fawcett**, "A boundary integral equation method for acoustic scattering in a waveguide with nonplanar surfaces," *Journal of the Acoustical Society of America*, 87 (1990): 1110-1124.
- [32] **Dawson, T.W.**, "Scattering matrix and boundary integral equation methods for long range propagation in an acoustic waveguide with repeated deformations," *Journal of the Acoustical Society of America*, 90 (1991): 1560-1574.
- [33] **Dawson, T.W.**, "Scattering matrix and boundary integral equation methods for acoustic propagation over a slope," *Journal of the Acoustical Society of America*, 90 (1991): 1575-1581.
- [34] **Dawson, T.W.**, "Acoustic scattering in a three-dimensional oceanic waveguide using boundary integral equation methods," *Journal of the Acoustical Society of America*, 90 (1991): 2609-2622.
- [35] **Dawson, T.W., and R.T. Kessel**, *SAMPLE: A Seismo-Acoustic Mode Program for Layered Environments. Theoretical Background*, Defence Research Establishment Atlantic (Canada) Technical Memorandum DREA/TM/95/225 (October 1995).
- [36] **DeSanto, J.A.**, *Scalar wave theory, Green's functions and applications*, Springer-Verlag, Berlin (1992).
- [37] **Diachok, O.S.**, "Effects of sea-ice ridges on sound propagation in the Arctic Ocean," *Journal of the Acoustical Society of America*, 59 (1976): 1110-1120.
- [38] **DiNapoli, F.R. and R.L Davenport**, "Numerical models of underwater acoustic propagation," Chapter 3 in *Ocean Acoustics, Topics in Current Physics, Volume 8*, Edited by J.A. DeSanto, Springer-Verlag, Berlin (1979).
- [39] **Doornbos, D.J.**, ed., *Seismological Algorithms: computational methods and computer programs*, Academic Press, London (1988).
- [40] **Dougherty, M.E., and R.A. Stephen**, "Geoacoustic scattering from seafloor features in the ROSE area," *Journal of the Acoustical Society of America*, 82 (1987): 238-256.

- [41] **Eliseevnin, V.A., and Y.I. Tuzhilkin**, "Diffraction of a sound field at a plane rectangular vertical screen in a waveguide," *Acoustical Physics*, 41 (1995): 214-218.
- [42] **Ellis, D.D., and M.F. Chapman**, "A simple shallow water propagation model including shear wave effects," *Journal of the Acoustical Society of America*, 78 (1985): 2087-2095.
- [43] **Etter, P.C.**, *Underwater acoustic modeling: principles techniques and applications*, Elsevier Science Publishers (1991).
- [44] **Ewing, W.M., W.S. Jardetsky and F. Press**, *Elastic waves in layered media*, McGraw-Hill, New York (1957).
- [45] **Evans, R.B.**, "A coupled mode solution for propagation in a waveguide with stepwise depth variations of a penetrable bottom," *Journal of the Acoustical Society of America*, 74 (1983): 188-195.
- [46] **Fawcett, J.A., and T.W. Dawson**, "Fourier synthesis of three-dimensional scattering in a two-dimensional oceanic waveguide using boundary integral equation methods", *Journal of the Acoustical Society of America*, 88 (1990): 1913-1920.
- [47] **Ficke, J.R.**, "Acoustic scattering from elemental Arctic ice features: numerical model results," *Journal of the Acoustical Society of America*, 93 (1993): 1784-1796.
- [48] **Frisk, G.V.**, *Ocean and seabed acoustics, a theory of wave propagation*, Prentice Hall, New Jersey (1994).
- [49] **Gilbert, F., and G.E. Backus**, "Propagator matrices in elastic wave vibration problems," *Geophysics*, Vol. 31 (1966): 326-332.
- [50] **Gerstoft, P., and H. Schmidt**, "A boundary element approach to ocean seismoacoustic facet reverberation," *Journal of the Acoustical Society of America*, 89 (1991): 1629-1642.
- [51] **Graff, K.F.**, *Wave motion in elastic solids*, Dover Publications, New York (1975).

- [52] **M. Guiggiani and A. Gigante**, "A general algorithm for multidimensional Cauchy principal value integrals in the boundary element method," *Transactions of the ASME*, 57 (1990): 906-915.
- [53] **Guiggiani, M.**, "Computing principle-value integrals in 3-D BEM for time harmonic elastodynamics - a direct approach," *Communications in Applied Numerical Methods*, 8 (1992): 141-149.
- [54] **Hamilton, E. L.**, "Geoacoustic modeling of the sea floor", *Journal of the Acoustical Society of America*, 68 (1980): 1313-1340.
- [55] **Harkrider, D.G.**, "Surface waves in multi-layered elastic media I: Rayleigh and Love waves from buried sources in a multilayered halfspace," *Bulletin of the Seismological Society of America*, 54 (1964): 627-679.
- [56] **Haskell, N.A.**, "The dispersion of surface waves on multilayered media," *Bulletin of the Seismological Society of America*, 43 (1953): 17-34.
- [57] **Haskell, N.A.**, "Radiation pattern of surface waves from point sources in a multilayered medium," *Bulletin of the Seismological Society of America*, 54 (1964): 377-393.
- [58] **Heise, U.**, "The calculation of Cauchy principal values in the integral equations for boundary value problems of the plane and three-dimensional theory of elasticity," *Journal of Elasticity*, 5 (1975): 99-110.
- [59] **Heppenheimer, T.A.**, *Anti-submarine warfare: the threat, the strategy, the solution*, Pasha Publications Inc., Arlington (1989).
- [60] **Hudson, J.A.**, "A quantitative evaluation of seismic signals as teleseismic distances - Radiation from point sources," *Geophysical Journal of the Astronomical Society*, 18 (1969): 233-249.
- [61] **Hudson, J.A.**, *The excitation and propagation of elastic waves*, Cambridge University Press, Cambridge (1980).

- [62] **Huygens, C.**, *Treatise on Light*, trans. S P. Thompson, in Great Books of the Western World, Volume 34, Encyclopedia Britannica, Chicago (1952).
- [63] **Ingenito, F.**, "Scattering from an object in a stratified medium," *Journal of the Acoustical Society of America*, 82 (1987): 2051-2059.
- [64] **Jackson, J.D.**, *Classical Electrodynamics*, John Wiley and Sons (1975).
- [65] **Jensen, F.B., and M.C. Ferla**, "SNAP: The SAACLANTCEN normal mode acoustic propagation model," SAACLANT ASW Research Center, La Spezia, Italy, January 15 (1979).
- [66] **Jensen, F.B., W.A. Kuperman, M.B. Porter and H. Schmidt**, *Computational ocean acoustics*, American Institute of Physics Press, New York (1994).
- [67] **Kawase, H.**, "Time domain response of a semi-circular canyon for incident SV, P and Rayleigh waves calculated by the discrete wavenumber boundary element method," *Bulletin of the Seismological Society of America*, 78 (1988): 1415-1437.
- [68] **Kellogg, O.D.**, *Foundations of potential theory*, Dover Publications (1953).
- [69] **Kennett, B.L.N., and N.J. Kerry**, "Seismic waves in a stratified halfspace," *Geophysical Journal of the Astronomical Society*, 57 (1979): 557-583.
- [70] **Kennett, B.L.N.**, "Elastic wave propagation in stratified media," in *Advances in Applied Mechanics*, Vol. 21, ed., C.S. Yih, Academic Press, New York (1981).
- [71] **Kennett, B.L.N.**, *Seismic wave propagation in stratified media*, Cambridge University Press, Cambridge (1983).
- [72] **Kerry, N.J.**, "Synthesis of seismic surface waves," *Geophysical Journal of the Astronomical Society*, 64 (1981): 425-446.
- [73] **Kessel, R.T.**, "The exterior Helmholtz integral equation and its approximate solution for acoustic radiation problems," Master's Thesis, Dept. of Physics, University of Waterloo, Ontario (1989).

- [74] **Kim, J.S.**, *Radiation from directional seismic sources in laterally stratified media with application to Arctic ice cracking noise*, PhD Thesis, Massachusetts Institute of technology (May 1989).
- [75] **Korneev, V.A., and L.R. Johnson**, "Scattering of elastic waves by a spherical inclusion - I," *Geophysical Journal International*, 115 (1993): 230-250.
- [76] **Kress, R.**, *Linear integral equations*, Springer Verlag, New York (1989).
- [77] **Kuo, J.T.**, "The influence of the elasticity of the bottom on wave propagation," *Computational Acoustics: Wave Propagation*, D. Lee, R.L. Strenberg, and M.H. Schultz Editors, Elsevier Science Publishers B.V. (1988).
- [78] **Kupradze, V.D.**, *Potential methods in the theory of elasticity*, trans. H. Gutfreund, ed. I. Meroz, Isreal Program for Scientific Translations, Monson, Jerusalem (1965).
- [79] **Lachat, J.C., and J.O. Watson**, "Effective numerical treatment of boundary integral equations: a formulation for three-dimensional elastostatics," *International Journal for Numerical Methods in Engineering*, 10 (1976): 991-1005.
- [80] **Levinson, S.J., E.K. Westwood, R.A. Koch, S.K. Mitchell, and C.V. Shepard**, "An efficient and robust method for underwater acoustic normal-mode computations," *Journal of the Acoustical Society of America*, 97 (1995): 1576-1585.
- [81] **Lighthill, M. J.**, *Waves in fluids*, Cambridge University Press, Cambridge (1978)
- [82] **Lim, R., J.L. Lopes, R.H. Hackman, and D.G. Todoroff**, "Scattering by objects buried in underwater sediments: theory and experiment," *Journal of the Acoustical Society of America*, 93 (1993): 1762-1783.
- [83] **Love, A. E. H.**, *A treatise on the mathematical theory of elasticity*, 4th ed., Dover Publications, New York (1944).
- [84] **Lu, I.T. , L.B. Felsen and A.H. Kamel**, "Eigenreverberations, eigenmodes and hybrid combinations: a new approach to propagation in layers multiwave media", *Wave Motion*, 6 (1984): 435-457.

- [85] **Lu, I.T., and L.B. Felsen**, "Ray, mode, and hybrid combinations for source-excited propagation in a elastic plate," *Journal of the Acoustical Society of America*, 78 (1985): 701-704.
- [86] **Lu, I.T.**, "Analysis of acoustic wave scattering by scatterers in layered media using the hybrid ray-mode (boundary integral equation) method," *Journal of the Acoustical Society of America*, 86 (1989): 1136-1142.
- [87] **Manolis, G.D.**, "A comparative study on three boundary element method approaches to problems in elastodynamics," *International Journal for Numerical Methods in Engineering*, 19 (1983): 73-91.
- [88] **Manolis, G.D. and D.E. Beskos**, *Boundary element methods in elastodynamics*, Unwin Hyman, London, (1988).
- [89] **Marschall, R.A.**, "Boundary element solution of a body's exterior acoustic field near its internal eigenvalues," *Journal of Computational Acoustics*, 3 (1993): 335-353.
- [90] **Miklowitz, J.**, *The theory of elastic waveguides*, Paperback Edition, North-Holland, Amsterdam (1984).
- [91] **Morse, P.M. and K.U. Ingard**, *Theoretical acoustics*, McGraw-Hill, New York (1968).
- [92] **Mossessian, T.K., and Dravinski, M.**, "Scattering of elastic waves by three-dimensional surface topographies," *Wave Motion*, 11 (1989): 579-592.
- [93] **Munk, W.H., R.C. Spindel, A. Baggeroer, and T.G. Birdsall**, "The Heard Island feasibility test," *Journal of the Acoustical Society of America*, 96 (1994): 2330-2484.
- [94] **Niku, S.M., and C.A. Brebbia**, "Implicit evaluation of boundary element influence integrals using particular solutions," *Engineering Analysis with Boundary Elements*, 10 (1992): 333-335.

- [95] **Panza, G.F., F.A. Schwab and L. Knopoff**, "Channel and crustal Rayleigh waves," *Geophysical Journal of the Astronomical Society*, 30 (1972): 273-280.
- [96] **Pao, Y., and V. Varantharajulu**, "Huygen's principle, radiation conditions, and integral formulas for the scattering of elastic waves," *Journal of the Acoustical Society of America*, 59 (1976): 1361-1371.
- [97] **Pekeris, C.L.**, "Theory of propagation of explosive sound in shallow water," *Geological Society of America Memoirs*, 27 (1948).
- [98] **Porter, M.B., and E.L. Reiss**, "A numerical method for ocean-acoustic normal modes," *Journal of the Acoustical Society of America*, 76 (1984): 244-251.
- [99] **Porter, M.B.**, "*The KRAKEN normal mode program*," NRL/MR/5120-92-6920, Naval Research Laboratory, Washington, D.C. (May 22, 1992).
- [100] **Press, W.H., B.P. Flannery, S.A. Teukolsky and W.T. Vettering**, *Numerical recipes*, Cambridge University Press, Cambridge (1986).
- [101] **Rizzo, F.J., D.J. Shippy and M. Rezayat**, "A boundary integral equation method for radiation and scattering of elastic waves in three dimensions," *International Journal for Numerical Methods in Engineering*, 21 (1985): 115-129.
- [102] **Rubenstein, D., and R. Greene**, "Modeling the acoustic scattering by under-ice ridge keels," *Journal of the Acoustical Society of America*, 89 (1991): 666-672.
- [103] **Sanchez-Sesma, F.J., and M. Camillo**, "Diffraction of P, SV and Rayleigh waves by topographic features: a boundary integral formulation," *Bulletin of the Seismological Society of America*, 81 (1991): 2234-2253
- [104] **Schafbuch, P.J., F.J. Rizzo, and R.B. Thompson**, "Boundary element method solutions for elastic wave scattering in 3D", *International Journal for Numerical Methods in Engineering*, 36 (1993): 437-455.
- [105] **Schechter, M.**, *Principles of functional analysis*, Student Edition, Academic Press, New York (1971).

- [106] **Schenck, H.A.**, "Improved integral formulation for acoustic radiation problems," *Journal of the Acoustical Society of America*, 77 (1968): 41-58.
- [107] **Schmidt, H., and F.B. Jensen**, "A full wave solution for propagation in multi-layered viscoelastic media with application to Gaussian beam reflection at fluid-solid interfaces," *Journal of the Acoustical Society of America*, 77 (1985): 813-825.
- [108] **Schmidt, H., and J. Glattetre**, A fast field model for three-dimensional wave propagation in stratified environments based on the global matrix method, *Journal of the Acoustical Society of America*, 78 (1985): 2105-2114.
- [109] **Schmidt, H.**, *SAFARI: Seismo-acoustic fast field algorithm for range independent environments*, SR 113, SACLANT ASW Research Center, La Spezia, Italy (1987).
- [110] **Schmidt, H.**, "Numerical modelling of three-dimensional reverberation from bottom facets", in *Ocean Reverberation*, ed., D.D. Ellis, J.R. Preston and H.G. Urban, Kluwer Academic Publishers, Dordrecht (1993).
- [111] **Schmidt, H.**, *OASES version 1.7, Application and upgrade notes*, Dept. of Ocean Engineering, Massachusetts Institute of Technology, Feb. 20 (1996).
- [112] **Schuster, G.T., and L.C. Smith**, "Modelling scatterers embedded in plane-layered media by a hybrid Haskell-Thomson and boundary integral equation method," *Journal of the Acoustical Society of America*, 78 (1985): 1387-1394.
- [113] **Segel, L.A.**, *Mathematics applied to continuum mechanics*, Dover Publications, New York (1987).
- [114] **Seybert, A.F., and T.K. Rengarajan**, "The use of CHIEF to obtain unique solutions for acoustic radiation using boundary integral equations," *Journal of the Acoustical Society of America*, 81 (1987): 1299-1306.
- [115] **Seybert, A.F., and D.K. Casey**, "An integral equation method for coupled fluid/fluid scattering in three dimensions", *Journal of the Acoustical Society of America*, 84 (1988): 379-384

- [116] **Seybert, A.F., and T.W. Wu**, "Modified Helmholtz integral equation for bodies sitting on an infinite plane," *Journal of the Acoustical Society of America*, 85 (1989): 19-23.
- [117] **Sheriff, R.E.**, *Geophysical methods*, Prentice Hall, New Jersey (1989).
- [118] **Skudrzyk, E.**, "The foundations of acoustics," Springer Verlag, New York (1971).
- [119] **Sommerfeld, A.**, *Mechanics: Lectures on theoretical physics*, Vol. 1, Academic Press, New York (1952).
- [120] **Stefanick, T.**, *Strategic antisubmarine warfare and naval strategy*, Lexington Books, D.C. Heath Company, Lexington, Massachusetts (1987).
- [121] **Stickler, D.C.**, "Normal mode program with both discrete and branch line contributions," *Journal of the Acoustical Society of America*, 57 (1975): 856-861.
- [122] **Takeuchi, H., and M.Saito**, Seismic surface waves, in *Methods in computational physics*, vol. 11, ed. B.A. Bolt, Academic Press, New York (1972).
- [123] **Theocaris, P.S., N. Karayanopoulos, and G. Tsamasphyros**, "A numerical method for the solution of static and dynamic three-dimensional elasticity problems," *Computers and Structures*, 16 (1983): 777-784.
- [124] **Thomson, W.T.**, "Transmission of elastic waves through a stratified solid medium," *Journal of Applied Physics*, 21 (1950): 89-93.
- [125] **Tindle, C.T., and Z.Y. Zhang**, "Continuous modes and shallow water sound propagation", IEEE Oceans 1993, Engineering in harmony with the ocean, Proceedings, Volume 1 (1993): I-81.
- [126] **Tindle, C.T., and N.R. Chapman**, "A phase function for finding normal mode eigenvalues over a layered elastic bottom," *Journal of the Acoustical Society of America*, 96 (1994): 1777-1782.
- [127] **Tolstoy, I.**, *Wave propagation*, McGraw-Hill, New York (1973).

- [128] **Tolstoy, I., and C.S. Clay**, *Ocean acoustics: theory and experiment in underwater sound*, Acoustical Society of America Publication by the American Institute of Physics, New York (1987).
- [129] **Tricomi, F.G.**, *Integral Equations*, Dover Publications Inc, New York, 1985.
- [130] **Urich, R.J.**, *Sound propagation in the sea*, Peninsula Publishing, Los Altos, California (1982).
- [131] **Westwood, E.K.**, *ORCA version 1.0 Users Guide*, Draft Copy, Applied Research Laboratories, University of Austin Texas (Feb 1996).
- [132] **Wu, T.W., W.L. Li, and A.F.Seybert**, "An efficient boundary element algorithm for multi-frequency acoustic analysis", *Journal of the Acoustical Society of America*, 94 (1993): 447-452.
- [133] **Wu, T.W.**, "On computational aspects of the boundary element method for acoustic radiation and scattering in a perfect waveguide," *Journal of the Acoustical Society of America*, 96 (1994): 3733-3743.
- [134] **Xie, Y.**, "An acoustic study of the properties and behaviour of sea ice," Doctoral Thesis, Dept. of Oceanography, University of British Columbia, Canada (1991).
- [135] **Xu, Y., and Y. Yan**, "An approximate boundary integral method for acoustic scattering in shallow oceans," *Journal of Computational Acoustics*, 1 (1993): 61-75.
- [136] **Xu, Y., and Y. Yan**, "A boundary integral method for acoustic source localization in a waveguide with inclusions," *Journal of Computational Acoustics*, 2, (1994): 133-145.
- [137] **Zhang, Z.Y.**, "Approximations for acoustic reflection from solid sea beds," Ph.D. Thesis, University of Auckland (Feb 1993).

VITA

Surname: Kessel

Given names: Ronald T.

Place of Birth: Kitchener, Ontario, Canada

Educational Institutions Attended:

| | |
|-------------------------|--------------|
| University of Victoria: | 1991 to 1996 |
| University of Waterloo: | 1986 to 1989 |
| University of Waterloo: | 1979 to 1984 |

Degrees Awarded:

| | | | |
|---------|---------------|------------------------|------|
| Ph.D. | (Physics) | University of Victoria | 1996 |
| M.Sc. | (Physics) | University of Waterloo | 1989 |
| B.A.Sc. | (Engineering) | University of Waterloo | 1984 |

Honours and Awards:

| | |
|---|------|
| Dean's Award of Merit (Master's Thesis) | 1989 |
|---|------|

Work Experience:

Consultant: Numerical Decisions Group (NDG), Victoria 1996
Research Assistant: SACLANT Centre, Le Spezia, Italy Fall 1993
Optical Design Engineer: Lighting Sciences Canada, 1984-86
Engineer in training: Two years engineering work experience 1979-84
through the cooperative degree program at the Univ. of Waterloo

PARTIAL COPYRIGHT LICENSE

I hereby grant the right to lend my dissertation to users of the University of Victoria Library, and to make single copies only for such users or in response to a request from the Library of any other university, or similar institution, on its behalf or for one of its users. I further agree that permission for extensive copying of this dissertation for scholarly purposes may be granted by me or a member of the University designated by me. It is understood that copying or publication of this thesis for financial gain shall not be allowed without my written permission.

Title of Dissertation:

**Scattering of Elastic Waves in Layered Media:
A Boundary Integral—Normal Mode Method**

Author:

**Ronald T. Kessel
April 19 1996**